GEÇİCİ KAPAK

Kapak tasarımı devam ediyor.

BİDGE Yayınları

Advanced Manufacturing, Materials, and Structural Engineering Applications

Editor: HASAN KÖTEN

ISBN: -

1st Edition
Page Layout By: Gözde YÜCEL
Publication Date: 2025-12-25
BİDGE Yayınları

Certificate No: 71374

www.bidgeyayinlari.com.tr - bidgeyayinlari@gmail.com
Krc Bilişim Ticaret ve Organizasyon Ltd. Şti.
Güzeltepe Mahallesi Abidin Daver Sokak Sefer Apartmanı No: 7/9 Çankaya / Ankara

İÇİNDEKİLER

CHAPTER 1
CHAPTER

Applications of Metal-Core Wires in 3D Additive Manufacturing (WAAM) Processes

Ferit ARTKIN[1]

Introduction

The use of Metal-Cored Wires (MCW) in Wire Arc Additive Manufacturing (WAAM) is a major change in the manufacturing of high-performance, large-scale metallic components. Although solid wires have historically dominated the WAAM industry, metal-cored wires have particular benefits for robotic 3D printing due to their unique physical and metallurgical design. Metal-cored wires are composite tubular electrodes made of ferro-alloys and high-purity metallic powders encased in a metallic sheath. In a WAAM process,

[1] Lect.Dr., Kocaeli University, Hereke Asimkocabiyik Vocational School, Department of Machinery and Metal Technologies, Machinery Programme, Kocaeli/Türkiye, Orcid: 0000-0002-8543-6334, artkinf@kocaeli.edu.tr

the wire is injected into a plasma or GMAW electric arc, where it melts and deposits material layer by layer. The "skin effect" refers to the fact that, in contrast to solid wires, the current in MCWs is mostly focused in the outer sheath.

The wide, cone-shaped arc produces a flatter bead profile that enhances interlayer fusion and lowers the possibility of "lack-of-fusion" flaws. MCWs are especially widely used in WAAM in sectors that requires large, structural components with intricate metallurgical requirements. MCWs make it possible to create "tailor-made" alloys. Researchers can print components with certain qualities like radiation shielding or high-temperature creep resistance that are not commercially accessible in solid wire form by changing the powder composition in the core. WAAM parts for the mining and tool-and-die industries are made using the powder core's flexibility. A metal-cored wire enhanced with chromium or tungsten carbides can be used to "clad" components with a wear-resistant surface layer after they have been printed with a robust structural core.

Decreased Post-Processing: MCWs' flatter bead crown and less splatter provide a smoother "as-printed" surface, which drastically cuts down on CNC machining time and expense. Superior feedability and a constant "cast and helix" are features of seamless metal-cored wires that guarantee the robot deposits material precisely where the path-planning software desires. This is essential for preserving dimensional tolerances in three-dimensional constructions.

Methods of Metal-Core Wires in 3D Additive Manufacturing (WAAM)

Metal-Cored Wires (MCW) are used in Wire Arc Additive Manufacturing (WAAM) through a structured engineering process that incorporates improved metallurgical control, optimum arc

physics, and robotic route planning. MCWs are perfect for large-scale industrial components because they enable greater deposition speeds and customized alloy compositions, in contrast to solid wires (Harati, E., et al., 2024). MCW in WAAM relies on striking a balance between the part's cooling pace and the wire's rapid melting rate.

To ascertain the ideal connection between Wire Feed Speed (WFS), Voltage (V), and Travel Speed (TS), researchers employ Response Surface Methodology (RSM) or Taguchi Methods (Vora J.,et al., 2022). In order to attain the same bead height, metal-cored wires sometimes require lower currents than solid wires, which helps control heat buildup in big constructions (Lin Z., et al., 2019)

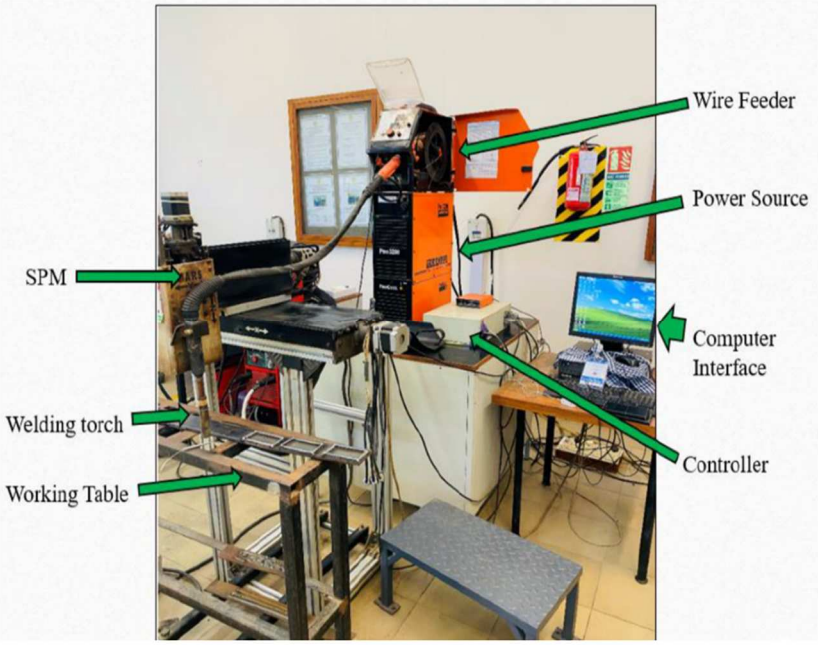

Figure 1. Experimental setup of the WAAM process (Vora J.,et al., 2022).

Metallurgical Control Methods

Compared to solid wires, MCWs have a more flexible approach for influencing the final material characteristics since they are made of a metal sheath that is filled with powder. The capacity to employ "tailor-made" wires is one of the most effective techniques. In the event that a certain aerospace or marine alloy is unavailable as a solid wire, a bespoke metal-cored wire can be produced using a powder core that, when melted, produces the required chemistry. An Intrinsic Heat Treatment (IHT) technique is used since WAAM requires repeatedly heating earlier layers. To guarantee a consistent hardness profile, engineers can manage the phase changes (e.g., from Austenite to Martensite or Bainite) by regulating the Interpass Temperature, which is usually kept below 350 ^{0}C for high-strength steels (Treutler K.,et al., 2022).

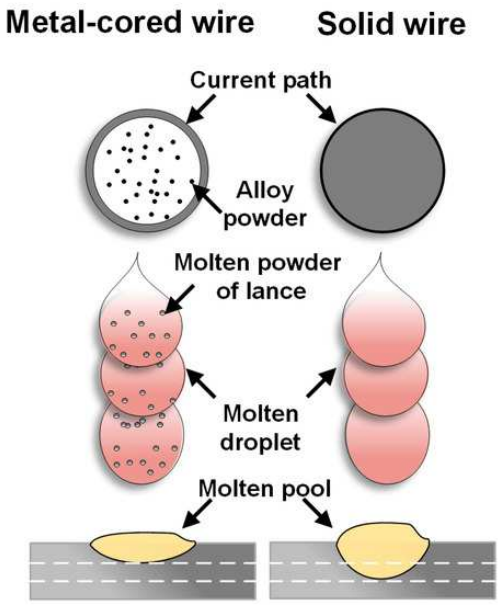

Figure 2. Comparison of the cross section and the metal transfer mode of a metal-cored wire and solid wire under short-circuit transfer mode (Lin Z., et al., 2019).

The stiffness of solid wires is not provided by metal-cored wires, which have a powder core and a solid sheath (Figure 2) (Boothroyd, G., et al., 1994). Metal-cored wires carry current exclusively via the sheath during a deposition, increasing the current density. The arc melts the powder inside the sheath, creating a powder lance that moves in the direction of the base. Nevertheless, less energy is needed to melt the same volume of the metal-cored wire than the solid wire since there is no energy transfer through the powder lance. As a result, the WAAM component's heat input is decreased, which helps to lower penetration.

Characterization and Testing Methods

Testing and Characterization Techniques To confirm its structural integrity, the part must go through extensive testing when the deposition is finished. Non-Destructive Testing (NDT): Techniques like X-ray Diffraction (XRD) are used to quantify

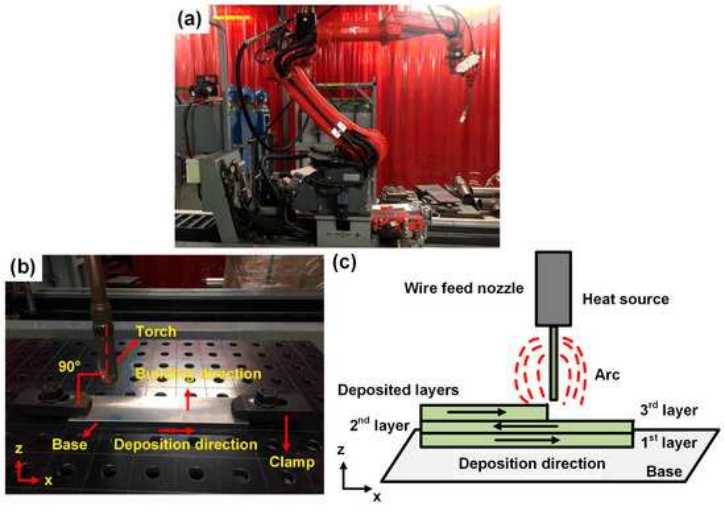

Figure 3. Robotic wire and arc additive manufacturing (WAAM) set-up, (b) experimental set-up, (c) deposition tool path applied in this study (Lin Z., et al., 2019).

near-surface residual stresses, and CT scans are utilized to check for interior porosity, which is often lower in MCW constructions because of cleaner metal transfer. Mechanical Features:Tensile Testing: To examine anisotropy, specimens are sliced in both horizontal (longitudinal) and vertical (build) directions. Fractography: To make sure the component satisfies safety requirements, the fracture surfaces (such as dimple structures for ductile failure) are examined using Field Emission Scanning Electron Microscopy (FESEM).

Table I. Summary Table of MCW WAAM Methods (*meltio3d.com, 2025)*

Method Phase	**Key Action / Tool**	**Purpose in WAAM**
Pre-Processing	CAD Modeling and Slicing	Defines the layer thickness and robot path.
Deposition	Pulsed Spray Transfer	Minimizes spatter and stabilizes the arc.
Monitoring	Infrared Thermography	Real-time monitoring of layer cooling/ interpass temp.
ValidationHardness	Hardness Mapping	Ensures uniform properties from the base to the top.

Advantages of Metal-Core Wires in 3D Additive Manufacturing (WAAM)

The considerable improvement in deposition efficiency is MCW's most immediate benefit. The "skin effect" causes the current to be focused in the outer metal sheath, which causes the wire to melt more quickly than a solid wire with the same diameter and amperage. 20–30% Increase in Deposition: Studies show that when MCWs are used instead of solid wires, deposition rates can increase by up to 30%. quicker Travel Speeds: The robotic system can function at quicker travel speeds because to the greater melting rate, which shortens the lead time for large-scale components (hobartbrothers.com, 2025), (Iqbal, H., 2025). Reduced Heat Input: In order to minimize residual stress and distortion in 3D-printed walls, MCWs can achieve comparable deposition speeds to solid wires while requiring less heat input overall (Zhai W., et al., 2022), (Iqbal, H., 2025).

Superior Interlayer Fusion and Bead Geometry
In WAAM, structural integrity is based on bead morphology. When it comes to layer stacking, MCWs offer a clear advantage. Wide, Cone-Shaped Arc: In contrast to solid wires' "finger-like" penetration, MCWs create a wide, parabolic arc profile. For overlapping layers and avoiding "lack of fusion" flaws, this produces a flatter bead with improved tie-in at the edges. Minimal Spatter: MCWs' spray transfer mode produces almost little spatter, guaranteeing a cleaner "as-printed" surface and lowering the requirement for post-weld grinding in between layers. Gap Bridging: The technique is more resilient to substrate defects or small path-planning mistakes because of the broad arc's superior gap-bridging capabilities (hobartbrothers.com, 2025a), (Iqbal, H., 2025). Metallurgical Tailoring and Design Flexibility: The ability to alter the core powder to produce "designer" alloys that are not available as commercial solid wires is a special benefit of MCWs. Custom Alloy Development: By altering the powder core, manufacturers may create bespoke chemical wires in small quantities. The use of MCWs to print medium carbon steels, such as

Grade XC-45, particularly for aerospace components has been effectively established by research. Cermets and Composites: During the WAAM process, metal-matrix composites (Cermets) may be made by filling the core with non-melting ceramic particles. This is almost impossible with solid wire feedstock (labsolda.ufsc.br, 2025). Uniform Hardness: Research comparing WAAM-deposited MCW components to conventionally cast or forged components discovered that MCWs provided a more consistent hardness distribution throughout the structure (Lin Z., et al., 2019), (Iqbal, H., 2025).

Metallurgical Safety: Smooth Low-Hydrogen Utilization Moisture-induced hydrogen cracking is a major challenge for essential structural applications (like offshore or aerospace).Protection from Hermetic: Seamless metal-cored wires are pulled from a closed tube or laser-sealed to keep moisture out of the core. By ensuring ultra-low diffusible hydrogen levels (sub-H4, < 3 ml/100g), high preheat temperatures are not necessary to reduce the danger of cold cracking (Lin Z., et al., 2019), (hyundaiwelding.com, 2025).

Industrial Applications of Metal-Core Wires in 3D Additive Manufacturing (WAAM)

Metal-Cored Wires (MCW) are now a common option for industrial-scale Wire Arc Additive Manufacturing (WAAM), having previously been specialized consumables.In order to address the "three pillars" of additive manufacturing deposition rate, material flexibility, and hydrogen control industrial behemoths in the fields of aerospace, energy, and marine engineering are increasingly using metal-cored versions of classic solid wires, which were the original norm.

Producing parts with high "buy-to-fly" ratios that satisfy forged-level mechanical criteria is the main problem in the aircraft industry.

Application: Using Medium Carbon Steel (Grade XC-45) and High-Strength Low-Alloy (HSLA) steels, large-scale engine mounts and structural landing gear components are produced. The MCW Advantage: Alloys that are not available as commercial solid wires may be created on demand using custom metal-cored wires. For aircraft parts that need particular fatigue and creep resistance, this is essential. Finding: When compared to conventionally treated materials, parts made with MCW-WAAM show more consistent hardness from the bottom to the top layer, guaranteeing consistency in crucial flight gear (Lin Z., et al., 2019).

Oil and Gas: Pressure Vessels and Subsea ManifoldsHydrogen-induced cracking (HIC) is a deadly issue for the offshore sector since components must endure high pressures and corrosive conditions.Application: Production of heavy-duty valves, pressure-retaining housings, and subsea manifolds on demand.The MCW Benefit Hermetically sealed seamless metal-cored wires offer a "Zero-Hydrogen" barrier (H < 4 ml/100g). This removes the requirement for costly pre-heating and post-print baking procedures, which are frequently unfeasible for large subsea components.Finding: Research indicates that MCW technology is economically feasible for large-scale energy infrastructure since it shortens manufacturing times by 43% and boosts deposition rates by up to 74% when compared to solid wire alternatives.

Marine Engineering: Massive Rudders and Propellers The marine industry, which has historically been sluggish to embrace 3D printing, has led the way in using WAAM to fabricate some of the biggest additive parts in the world. Application: Quick production of massive rudder shafts and stainless steel and bronze propellers (such as the Damen Shipyards "WAAMpeller"). The MCW Advantage: Flatter beads with superior side-wall tie-in are produced by the wider, cone-shaped arc of metal-cored wires. This is crucial for maritime propellers since any interior lack-of-fusion flaw might result in catastrophic failure due to cavitation forces.

Finding: Compared to conventional casting and subtractive machining from solid billets, using MCW results in 70% material savings and 80% shorter lead times (huntingdonfusion.com, 2025).

Wear-Resistant "Cermets" for Heavy Tooling and Mining Parts are subjected to severe impact and abrasion in the mining and heavy equipment industries. Application: Bimetallic cutting tools, crushing plates, and excavator teeth manufacturing and repair. The MCW Advantage: Filling the powder core with ceramic particles (such as tungsten carbides) that do not melt in the arc is one of MCW's special capabilities. As a result, the 3D-printed component develops a Cermet (Ceramic-Metallic) structure, offering surface hardness that beyond what is achievable with solid wire feedstock. Finding: MCW-WAAM enables Functionally Graded Materials (FGM), in which the robot prints a durable, ductile core for the outer "hardfaced" shell before switching to a metal-cored wire that is resistant to wear in a single continuous operation (labsolda.ufsc.br, 2025).

Conclusion

The results of research and industrial use of Metal-Cored Wires (MCW) in Wire Arc Additive Manufacturing (WAAM) show that this technology is now a better option for large-scale, high-performance manufacturing rather than merely a substitute for solid wires. The assurance that MCW-WAAM is the most effective arc-based additive method currently in use is the most important outcome.For industrial-scale products, the total cost of ownership (TCO) is much cheaper because to the reduction in total "arc-on" time and post-weld machining, even if the wire cost per kilogram is slightly greater. The hazards connected to tubular wires in the past have been eliminated with the switch to seamless MCW. WAAM is now feasible for high-strength steels in the offshore and military industries without preheating thanks to the "hermetic seal" of next-generation wires, which has set a new bar for H4 (ultra-low hydrogen) printing. Because of the constant chemistry of the powder core and the steady heat cycles of the robotic process, MCW-

WAAM deposits exhibit a more uniform hardness distribution and greater tensile strength than casting or forging. The industry is shifting toward "tailor-made" metallurgy and Functionally Graded Materials (FGM). For certain aerospace or energy applications where solid wire melts are not economically viable, MCW is the sole method that enables researchers to produce small quantities of unique alloy wires (such as tool steels or complicated concentrated alloys). The MCW arc's stability in conjunction with AI-powered closed-loop sensors is making it possible to produce large parts like crane booms and ship propellers in a completely autonomous, round-the-clock manner.

Acknowledge

I would like to thank my thesis advisor, Prof. Dr. Mustafa KOÇAK, for his invaluable help and support in determining the thesis topic that forms the basis of this study.

REFERENCES

Boothroyd, G., Dewhurst, P., Knight, W.A., Product design for manufacture and assembly; M. Dekker: New York, NY, USA, 1994.

Harati, E., Jose, B., & Igestrand, M. (2024). Wire arc additive manufacturing using high-strength steel tubular and solid wires. Welding International, 38(5), 329–334. doi.org/10.1080/09507116.2024.2337163.

https://huntingdonfusion.com/case-studies/3d-printing-for-the-marine-industry- a-case-study-on- wire-and-arc-additive-manufacturingwaam/#:~:text=However%2C%20recent%20advancements%20in%20Wire,tooling%20and%20lengthy%20production%20times, Accessed 23 December, 2025.

https://labsolda.ufsc.br/public/resumos/926-advantages-of-the-intrinsic-metal-cored-wires-production-flexibility-targeted-for-wire-arc-additive-manufacturing Accessed 23 December, 2025.

https://labsolda.ufsc.br/public/resumos/926-advantages-of-the-intrinsic-metal-cored-wires-production-flexibility-targeted-for-wire-arc-additive manufacturing#:~:text= An%20additional%20 advantage%20is%20the,metal%20matrix%2C%20forming%20a% 20Cermet, Accessed 23 December, 2025.

https://meltio3d.com/wire-arc-additive-manufacturing-key insights/#:~:text=Post%2Dprocessing%20steps%20such%20as,stre sses%20in%20the%20printed%20components Accessed 23 December, 2025.

https://www.hobartbrothers.com/resources/technical-articles/metal-cored-wire-and-robotic-welding-a-combination-for-productivity/ Accessed 23 December, 2025(a).

https://www.hobartbrothers.com/resources/technical-articles/the-benefits-of-metal-cored-welding-wire/ Accessed 23 December, 2025.

https://www.hyundaiwelding.com/data/file/download/brochures/H YUNDAI_FCAW_SL-71%20(BROCHURE)_eng.pdf Accessed 23 December, 2025.

Iqbal, Hambal. (2025). Wire-arc additive manufacturing (WAAM): investigation of process dynamics, material insights, and application prospects. 10.48676/unibo/amsdottorato/11835.

Lin Z., Goulas C., Ya W., Hermans MJM., Microstructure and Mechanical Properties of Medium Carbon Steel Deposits Obtained via Wire and Arc Additive Manufacturing Using Metal-Cored Wire. Metals. 2019; 9(6):673. https://doi.org/10.3390/met9060673.

Treutler K., Lorenz S., Hamje J., Wesling V., Wire and Arc Additive Manufacturing of a CoCrFeMoNiV Complex Concentrated Alloy Using Metal-Cored Wire—Process, Properties, and Wear Resistance. Applied Sciences. 2022; 12(13): 6308. https://doi.org/10.3390/app12136308.

Vora J., Parikh N., Chaudhari R., Patel VK., Paramar H., Pimenov DY., Giasin K.,Optimization of Bead Morphology for GMAW-Based Wire-Arc Additive Manufacturing of 2.25 Cr-1.0 Mo Steel Using Metal-Cored Wires. Applied Sciences. 2022; 12(10):5060. https://doi.org/10.3390/app12105060.

CHAPTER 2

SCALABLE SIMULATION OF MICROCAVITY FLOWS VIA MEMORY EFFICIENT EVENT DRIVEN MOLECULAR DYNAMICS

VOLKAN RAMAZAN AKKAYA[1]

Introduction

Molecular Dynamics (MD) is an essential computational methodology for deriving the macroscopic transport properties from microscopic interactions. Although Time-Driven Molecular Dynamics (TDMD) is extensively utilized for dense fluids, it is computationally inefficient for rarefied gases, where molecular interactions are infrequent. In such regimes, Event-Driven Molecular Dynamics (EDMD) has emerged as a more effective alternative by advancing the simulation time asynchronously from one discrete collision event to the next, rather than employing fixed time steps.

The validity of employing Event-Driven Molecular Dynamics (EDMD) to assess long-term dynamic properties necessitates particular consideration, because of the inherently chaotic nature of n-body systems. Although molecular trajectories in event-driven simulations are susceptible to Lyapunov instability,

[1] Asst.Prof.Dr., Muğla Sıtkı Koçman University, Orcid: 0000-0002-5052-8554

which makes individual particle paths extremely sensitive to their initial conditions, this characteristic does not influence averaged structural and dynamic properties (Rapaport, 2009). In contrast to continuous potential simulations, which depend on approximate numerical integration over a fixed time step (Δt), EDMD advances through a precise, time-ordered sequence of discrete events, such as collisions and cell crossings. This methodology ensures that the trajectories are computed with full computer precision, theoretically eliminating the truncation errors associated with finite difference methods. Although the apparent absolute precision is constrained by the rounding errors of floating-point arithmetic, the absence of systematic integration drift renders EDMD a physically robust approach for modeling the macroscale behavior of complex systems.

In addition to its theoretical robustness, the versatility of Event-Driven Molecular Dynamics (EDMD) encompasses a broad spectrum of physical systems characterized by discrete or "hard" interaction potentials. As highlighted byBannerman, Sargant, & Lue (2011), while systems with continuous "soft" potentials require approximate time-stepping integration, EDMD is particularly adept at modeling complex discontinuous systems, including granular materials, square-well fluids, and helix-forming polymers. Furthermore, the method exhibits significant efficacy in replicating the equilibrium properties of simple molecular systems, such as hydrocarbons, alcohols, and carboxylic acid mixtures.

In the field of fluid dynamics, Yakunchikov & Kosyanchuk (2018) demonstrated the applicability of this method to rarefied gas dynamics, particularly for flows involving arbitrary and moving boundaries. Their study underscores the capability of EDMD to address classical problems, such as supersonic flow past a cylinder, while also extending its utility to complex engineering challenges, including the separation of multicomponent gas mixtures in devices with oscillating elements. This ability to generalize moving

boundaries without compromising precision establishes EDMD as an essential tool for investigating free-molecular and transitional flow regimes, where continuum assumptions are no longer valid.

Event-Driven Molecular Dynamics (EDMD) is a significant tool in the simulation of rarefied gas flows, where the mean free path of the molecules is comparable to the characteristic length of the system. Under these low-density conditions, traditional time-driven methods are computationally expensive owing to the unnecessary integration of ballistic trajectories between infrequent collisions. Valentini & Schwartzentruber (2009b)addressed this inefficiency proposing a hybrid event-driven/time-driven (ED/TD) algorithm. Their research demonstrated that the integration of event-driven logic facilitates the precise simulation of high-speed nonequilibrium phenomena, such as Mach 9 shock waves in argon, producing results consistent with both Direct Simulation Monte Carlo (DSMC) data and experimental observations.

Following the achievements of hybrid approaches in hypersonic and transitional flow studies, pure Event-Driven Molecular Dynamics (EDMD) implementations have shown similar levels of reliability in capturing rarefied gas dynamics. Akkaya & Kandemir (2015) validated this method for hard-sphere gas flows in microchannels, illustrating that EDMD accurately predicts the velocity profiles in both shear-driven (Couette) and pressure-driven flows. Their findings aligned closely with solutions from the linearized Boltzmann equation and DSMC benchmarks, validating EDMD as a reliable tool for microfluidic applications. Furthermore, Koc, Kandemir, & Akkaya (2021) expanded the scope to the transition regime in porous media, specifically for Knudsen numbers between 0.1 and 10. By calculating complex transport parameters like dynamic viscosity, tortuosity, and permeability, they showed that EDMD's discrete treatment of interactions enables the simulation of

larger systems over longer periods than traditional time-stepping methods.

Building on this theoretical framework, the computational advantages of EDMD are well-documented. Donev (2009) showed that asynchronous event processing can be up to two orders of magnitude more efficient than traditional MD, particularly when detailed solvent structures are not required. Similarly, Valentini & Schwartzentruber (2009a) noted that by bypassing the redundant integration of ballistic trajectories between collisions, EDMD can perform hundreds to thousands of times faster than TDMD in rarefied gas simulations. From an algorithmic perspective, Akkaya & Kandemir (2015) further optimized the method by combining cell partitioning with priority queues. Their approach reduces the total computational complexity to linear scaling, *O(N)*, positioning EDMD as a robust competitor to the Direct Simulation Monte Carlo (DSMC) method in both accuracy and speed.

Despite these algorithmic efficiencies, implementing high-performance EDMD engines on modern hardware remains a significant challenge. Unlike TDMD, which benefits from predictable linear memory access, EDMD relies on random access to particle data due to the unpredictable timing of collision events. In modern CPU architectures, this leads to frequent cache misses that severely hamper performance.

Historical implementations clearly illustrate the trade-offs necessitated by hardware constraints. For instance, Kandemir & Kaya (2011) utilized Fortran-based systems capable of handling large particle counts; however, maintaining *O(N)* complexity required high cell occupancy ratios, typically eight molecules per cell. While effective for memory management, this approach inherently limits the spatial resolution of the grid. Conversely, implementations in managed object-oriented languages like C# Akkaya & Kandemir (2015) often struggle with memory

fragmentation and Garbage Collection overhead. In these cases, representing molecules and cells as individual heap objects disrupts data locality, creating significant performance bottlenecks that are absent in lower-level implementations.

The primary aim of this study is to reconcile the theoretical efficiency of EDMD with the performance requirements of contemporary hardware. To this end, we present a scalable EDMD engine implemented in Rust. By leveraging ownership model of Rust and adopting Data-Oriented Design (DoD) principles, such as Arena Allocation and Stable Indexing, this engine effectively mitigates the memory fragmentation and cache misses that hinder traditional implementations.

Furthermore, we introduce a Lazy Update mechanism designed to minimize grid-induced numerical drift. This approach preserves physical fidelity while maintaining linear scalability ($O(N)$), enabling the simulation of millions of particles without compromising accuracy.

Data Architecture: A Data-Oriented Approach

In managed languages like C#, traditional object-oriented implementations typically allocate molecules and cells as individual reference-type objects on the heap. While this approach aligns with standard design principles, it creates pointer-heavy memory layouts where particle data are accessed indirectly. Given that memory latency now outweighs clock speed as a performance bottleneck, this *pointer chasing* significantly degrades spatial locality and leads to poor CPU cache utilization (Drepper, 2007).

To address these limitations, this study employs a Structure of Arrays (SoA) data layout, a strategy widely advocated for molecular dynamics (Anderson, Lorenz, & Travesset, 2008). Unlike reference-based or Array of Structures (AoS) models, SoA groups individual particle attributes such as position or velocity components

into contiguous memory regions. This arrangement ensures sequential access patterns and improves cache line efficiency, allowing computational kernels to utilize memory bandwidth more effectively. For large-scale simulations, this shift to SoA significantly reduces memory overhead and accelerates overall computation.

This architectural distinction in data layout and memory access patterns serves as the primary performance differentiator between the legacy C# implementation (Akkaya & Kandemir, 2015) and the newly developed engine, proving more significant than the choice of programming language alone. Rust was selected for this study because it integrates the low-level hardware control of C/C++ with stringent memory safety assurances (Perkel, 2020). By utilizing Rust's ownership model, the engine manages memory at compile-time to effectively bypass the need for a Garbage Collector. This eliminates the latency spikes typically found in managed environments and ensures a consistent, high data-processing throughput throughout the simulation.

This methodology organizes data into contiguous memory blocks to enhance cache efficiency and reduce computational latency. By leveraging Rust's borrowing rules, the system maintains memory safety without the performance overhead associated with traditional managed languages. Consequently, this design significantly improves scalability while facilitating the predictable memory access patterns essential for optimizing parallel workloads. The explicit control over memory layout afforded by Rust allows for the fine-tuning of data structures, which minimizes cache misses and maximizes throughput in a way that aligns with the demands of modern hardware architectures.

Managing Graph Structures via Arena Allocation

In conventional Event-Driven Molecular Dynamics (EDMD) implementations, the interaction between cells and molecules is typically bidirectional. In such designs, a cell maintains a collection of references to its constituent molecules while each molecule retains a reference to its parent cell. While this cyclic reference graph is easily managed in garbage-collected environments, it conflicts with Rust's stringent ownership and borrowing rules. Specifically, Rust's memory safety guarantees prohibit multiple simultaneous mutable references to the same data, making a direct representation of these cyclic dependencies unfeasible. This restriction complicates the bidirectional linking of cells and molecules because it requires concurrent mutable access from both entities.

To resolve this architectural challenge without the runtime overhead of reference counting or the risks associated with raw pointers, an index-over-pointers strategy integrated with Arena Allocation was employed. This approach ensures that all molecules are stored within a contiguous memory block, such as a *Vec<Molecule>,* where relationships are maintained exclusively through *usize* indices. By substituting pointers with indices, the data remain packed in memory, which maximizes CPU cache hit rates and minimizes the latency associated with traditional object-oriented layouts. The fundamental architectural divergence between the legacy pointer-based approach and the newly developed engine is illustrated in Figures 1 and 2, while the resulting memory layout visualization is further detailed in Figure 3.

Figure 1 Traditional OOP Approach (High Heap Fragmentation)

```
// C# Style
class Cell {
    List<Molecule> Molecules; // References scattered in heap
}

class Molecule {
    Cell OwnerCell; // Cyclic reference loop
    Vector3 Position;
}
```

Figure 2 Data-Oriented Rust Implementation

```
// Rust: Contiguous Memory Layout
struct Simulation {
    molecules: Vec<Molecule>, // Arena: All data in one contiguous block
    cells: Vec<Cell>,
}

struct Cell {
    member_ids: Vec<usize>, // Stable indices, lightweight and safe
}

struct Molecule {
    owner_cell_id: usize, // Decoupled relationship via index
    position: [f64; 3],
}
```

Figure 3 Memory Layout Visualization

```
(a) OOP Memory Layout (Pointer Chasing & Cache Misses)
[Cell Object] -> [List Ptr] -> [Node] -> [Molecule A @ 0x0E12] (Random Address)
                               [Node] -> [Molecule B @ 0x9A42] (Random Address)
                               ...

(b) Data-Oriented Layout (Contiguous & Cache Friendly)
[Molecules Arena (Vec)] | [Mol A] | [Mol B] | [Mol C] | [Mol D] | ...
                        ^         ^         ^         ^
Indices (usize):        0         1         2         3
```

Free List Strategy

In open systems, where particles frequently enter or exit the domain, dynamic memory allocation can become a significant performance-limiting factor. To address this, a Free List mechanism was implemented to recycle memory efficiently by managing

molecular indices within a reusable pool. Rather than deallocating an index when a molecule exits the system, the index is retained and added to a collection of available IDs. This approach enables new particles entering the system to utilize existing indices, thereby bypassing the overhead typically associated with frequent allocation and deallocation.

By maintaining this pool of free indices, the system mitigates memory fragmentation and reduces computational costs, a design choice that is particularly vital for large-scale simulations requiring performance consistency. Furthermore, by ensuring the main simulation loop operates entirely without dynamic memory allocation, the system achieves deterministic frame times. This stability ensures that each simulation step executes within predictable intervals, which is crucial for maintaining real-time performance and synchronization across extensive simulations. Ultimately, this framework enhances both the reliability and the scalability of the proposed EDMD engine.

Efficient Cell Membership Management

A subtle yet significant limitation of traditional C# implementations is the management of dynamic lists within cells. The removal of a molecule from a *List<T>* typically incurs an *O(N)* cost, as standard collections maintain order by shifting all subsequent elements in memory. In simulations involving millions of cell crossings per second, this constant memory reorganization imposes a substantial burden on CPU resources. Since the order of molecules inside a cell does not affect collision detection logic, the swap-remove method available in Rust was utilized. When a molecule exits a cell, the last element in the vector is swapped into the vacated position and the vector length is decremented. This operation is strictly *O(1)* and eliminates the need for memory shifting. Furthermore, the underlying capacity of the cell vector is

preserved, which prevents repeated heap allocations as molecules continuously enter and exit cells.

Domain Discretization and Ghost Cells

The spatial partitioning of the simulation domain into a grid of $N_x \times N_y \times N_z$ cells is an effective strategy for optimizing neighbor search by reducing its computational complexity from $O(N^2)$ to $O(N)$. This approach organizes particles into discrete spatial regions, allowing the algorithm to limit neighbor checks to a smaller subset of cells rather than the entire domain. However, implementing boundary conditions, such as periodic or reflective boundaries, typically introduces conditional branching within the particle update routines. These conditional statements, often expressed as if-else blocks, can interrupt the smooth flow of CPU instruction pipelines, leading to performance degradation owing to branch mispredictions and pipeline stalls.

To address this issue, the Ghost Cell technique was employed. This method involves adding a conceptual grid with an extra layer of cells around the original domain (indices 1 to N_x), effectively creating a border of ghost cells (indices 0 and N_x+1). While this increases the total number of cells to $(N_x+2) \times (N_y+2) \times (N_z+2)$, these additional cells replicate the necessary boundary information, allowing particle updates near the edges to proceed without explicit boundary verifications. By incorporating ghost cells, the simulation avoids costly conditional branching during neighbor searches and particle movement, thereby maintaining efficient CPU instruction pipelining.

Molecules exiting the physical domain initially interact with these ghost cells rather than requiring immediate boundary checks. For example, under periodic boundary conditions, a molecule entering a ghost cell is mapped onto the corresponding physical cell on the opposite side. This architectural design simplifies the core

collision-detection loop by standardizing boundary interactions as routine cell-transfer events, which significantly enhances the overall computational throughput.

Lazy Update Mechanism for Time Integration

In conventional Event-Driven Molecular Dynamics (EDMD), the spatial subdivision of the domain introduces a subtle but critical source of error. When a molecule crosses a virtual cell boundary, standard algorithms typically update its position vector to the calculated intersection point on the cell face. Although analytically correct, the finite precision of floating-point arithmetic causes repeated updates at arbitrary boundary points to introduce truncation errors (Rapaport, 2004). This accumulation of numerical noise disrupts the deterministic nature of EDMD and alters the prediction of future collisions. Such a *butterfly effect* can reorder events in the priority queue, leading to a sequence of interactions that diverges from the physical model. Consequently, the simulation trajectories become artifacts of the grid resolution, resulting in grid-induced numerical divergence. Unlike Time-Driven MD, where errors stem from integration approximations such as the Verlet algorithm, this structural error in EDMD compromises physical validity regardless of algorithmic complexity.

To mitigate this, the algorithm illustrated in Figure 4 employs a Lazy Update mechanism to logically separate cell transitions from physical position updates. This decoupling eliminates the need for intermediate position calculations at virtual boundaries, which mathematically preserves the true trajectory of the molecule with full floating-point precision. By separating cell-crossing logic from the update of physical coordinates, the computational load is reduced, and precise, grid-density-independent ballistic trajectories are achieved. This approach ensures that the physical accuracy of the

simulation remains robust, even as the system scales to millions of particles.

Figure 4 Event Processing with Lazy Update Strategy

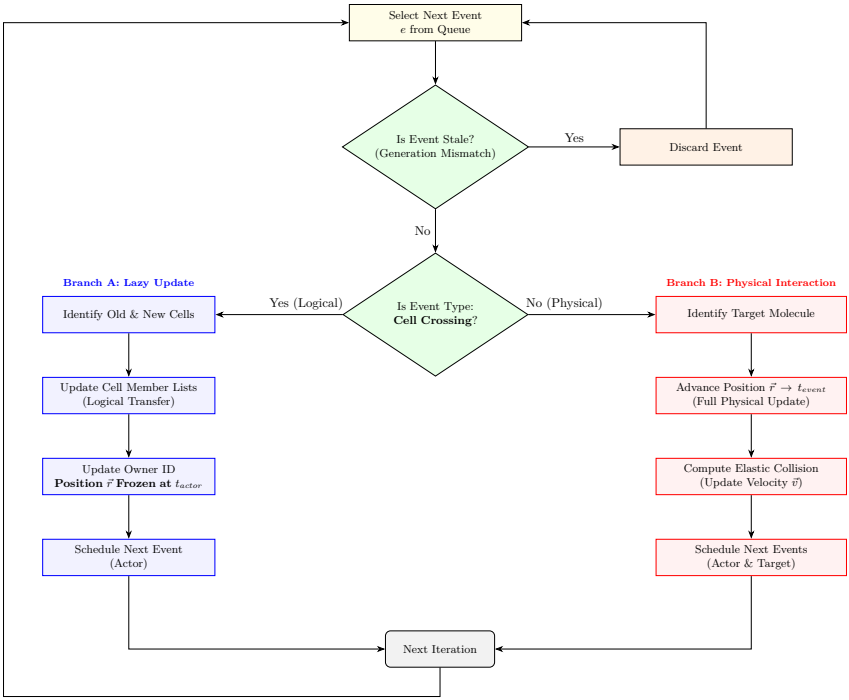

Efficient Event Scheduling and Queue Management

The precision and throughput of Event-Driven Molecular Dynamics (EDMD) simulations are largely determined by the efficiency of the priority queue. Historically, researchers have concentrated on reducing the algorithmic complexity of event insertion and extraction, often proposing complex structures such as Calendar Queues to achieve *O(1)* amortized access times (Paul, 2006). Although theoretically advantageous, these pointer-intensive structures frequently exhibit poor cache coherency on modern hardware due to dispersed memory access patterns.

In the present work, standard *BinaryHeap* of Rust was employed, which implements a complete binary tree structure arranged contiguously in memory as an array-based heap (Figure 5). Although the theoretical complexity of heap operations is *O(logN)*, the array-based layout ensures a high cache hit rate by eliminating pointer chasing. This data-oriented approach renders the *BinaryHeap* practically superior to more complex *O(1)* structures for system sizes typical in molecular dynamics, ranging from 10^3 to 10^7 particles, as the cost of cache misses in node-based trees often surpasses any algorithmic advantage.

Figure 5 Structural mapping of BinaryHeap.
(a) Logical hierarchy representing event priorities as a CBT
(b) Actual linear memory layout (contiguous array)

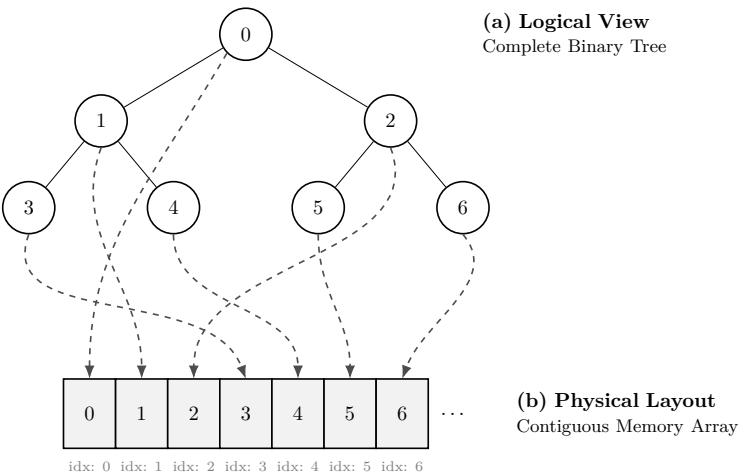

A major challenge in EDMD involves managing invalidated events, which occur when a molecule engages in a different interaction before its previously anticipated collision time. The linear removal of such obsolete events from a queue is computationally expensive, typically incurring an *O(N)* cost. To mitigate this issue, a lazy deletion strategy using generation counters was implemented. Each molecule is associated with a monotonic

generation counter (*u32*), and when an event is scheduled, the current generation of the involved molecules is recorded. Upon extraction from the queue, the engine compares the stored generation of the event with the live generation of the molecule; if they do not match, the event is discarded as stale with an *O(1)* cost. This approach effectively decouples the event-cancellation overhead from the queue size, thereby ensuring the scalability of the simulation engine.

Computational verification by grid independence

Prior to conducting an analysis of grid independence, it is crucial to specify the physical parameters and the system of units employed. The simulation utilizes a system of identical hard spheres in which all physical quantities are rendered dimensionless. The molecular diameter (L) and molecular mass (m) serve as the fundamental scales for length and mass, respectively; consequently, the size of the simulation domain (L) and all spatial coordinates are expressed in units of d.

In this verification study, a system consisting of N=100,000 molecules was simulated within a cubic domain with an edge length of $L=176.0d$. This configuration resulted in a global number density of $n^*=N/V\approx0.018d^{-3}$, corresponding to a solid volume fraction of $\phi\approx1\%$. This density regime was deliberately selected to represent a dilute gas, thereby minimizing multi-body correlation effects while ensuring a sufficient collision frequency for statistical sampling. Periodic boundary conditions were applied to all faces of the cubic domain to eliminate wall effects and isolate the impact of the spatial grid on particle trajectories.

To evaluate the accuracy and robustness of the Lazy Update algorithm, four distinct grid scenarios were examined across a broad range of cell occupancy ratios, defined as $\rho_{cell}=N_{mol}/N_{cells}$. The domain was first conceptualized as a singular cell ($N_{cells}=1$),

requiring the algorithm to evaluate $O(N^2)$ pairs for collision prediction, which served as the benchmark for physical accuracy. When using a coarse grid, the domain was partitioned into $17 \times 17 \times 17$ cells, resulting in a cell size of approximately $10.35d$ ($\rho_{cell} \approx 20.3$). In the medium-grid scenario, the domain was divided into $44 \times 44 \times 44$ cells with a cell size of $4.0d$, representing a unit density case ($\rho_{cell} \approx 1.17$), which is typically considered optimal for cell-linked list algorithms. Finally, the fine grid divides the domain into $88 \times 88 \times 88$ cells with a cell size of $2.0d$, representing a sparse scenario ($\rho_{cell} \approx 0.15$) in which molecules frequently traverse cell boundaries.

Table 1 lists the simulated physical time (t_{sim}) achieved upon the completion of 1,000,000 physical collisions. The variations in the simulated time compared with the reference no-grid scenario were minimal (less than 0.15%), thereby confirming that the spatial discretization did not introduce a statistical bias into the event calendar. These results affirm the grid-independent nature of the lazy update algorithm.

Performance Analysis and Memory Management

From a computational standpoint, the transition from a brute-force methodology to a spatially partitioned strategy yielded a speedup factor of approximately 121. Notably, the Rust engine exhibited superior performance, particularly at low cell occupancy ratios. As demonstrated in Table 1, the fine grid scenario ($\rho_{cell} \approx 0.15$) outperforms the medium grid ($\rho_{cell} \approx 1.17$), indicating an optimal range of 0.3 to 0.5 molecules per cell for this specific architecture.

This optimal range represents a significant deviation from traditional EDMD implementations. In previous studies utilizing linear search algorithms for event scheduling, the optimal occupancy was reported to be $\rho_{cell} \approx 8$. Within those architectural frameworks, maintaining a coarser grid was crucial for balancing the

computational cost of cell-crossing events against the overhead of neighbor searching.

Table 1 Simulation Time and Performance Comparison for Grid Independence Test (10^6 Collisions)

Metric	**No grid**	**Coarse**	**Medium**	**Fine**
Grid Layout (N^3)	1	17	44	88
Total Cells (N_{cells})	1	4,913	85,184	681,472
Occupancy (N_{mol}/N_{cells})	100	~20.35	~1.17	~0.15
Simulated Time (t_{sim})	2.619.198	2.622.432	2.622.540	2.620.611
Relative Error (ϵ)	-	0.12%	0.13%	0.05%
Wall Clock Time (s)	3823.21	48.49	33.69	31.53

A prior implementation in C# encountered scalability limitations in low-occupancy scenarios due to the overhead associated with managed memory. Increasing the number of cells to achieve a finer grid resolution necessitated dynamic object instantiation for each cell, which resulted in significant memory bloat and garbage collection delays as N_{cells} approached N_{mol}.

The current implementation in Rust addresses these historical challenges by employing a zero-cost abstraction model with a deterministic memory layout. In this model, the total memory requirement is pre-allocated and remains constant regardless of the grid resolution. This approach enables the engine to exploit the theoretical efficiency of sparse grids ($\rho_{cell}<1$) without incurring the algorithmic penalties of linear searches or the memory penalties typically associated with managed languages.

Physical Validation: Lid-Driven Cavity Flow

A series of parametric simulations was conducted using the classical Lid-Driven Cavity flow problem to rigorously validate the physical accuracy of the developed Rust code under non-equilibrium conditions. This flow configuration is widely used as a standard

benchmark for rarefied gas dynamics because it demonstrates complex coupled phenomena, such as viscous heating, compressibility, and thermal creep, within a simple geometry. The primary objective of this section is to evaluate the capability of the code to accurately resolve the momentum and energy transport in the transition regime by referencing the established results of previous studies (Kandemir & Kaya, 2011).

All validation cases utilized a standardized computational domain measuring $160.0d \times 160.0d \times 4800.0d$, comprising $N=1,000,000$ molecules. A substantial extension of the domain along the periodic axis, with an aspect ratio of 30, was intentionally selected to reduce statistical noise by enlarging the sampling volume while preserving the nominal two-dimensional nature of the flow.

The spatial domain was discretized into a uniform grid consisting of $55 \times 55 \times 1650$ cells, yielding an optimal spatial resolution of approximately $2.9d$. Given the effective number density ($n \approx 0.008d^{-3}$), the mean free path of the gas molecules was calculated as $\lambda=40d$. This results in a Knudsen number of $Kn=\lambda/L=0.25$ (where $L=160.d$), situating the flow distinctly within the transition regime where continuum assumptions are no longer valid.

To ensure statistical convergence, the system was equilibrated for 100×10^6 collisions, followed by a sampling phase of 5×10^6 collisions to extract the macroscopic field variables, including number density, streamlines, temperature, and pressure.

Four distinct test cases were simulated to isolate specific physical effects by varying the boundary conditions of the moving lid at $y=H$. The Reference Case established a subsonic baseline with $U_{lid}=0.8$ and $T_{lid}=1.0$ to verify the fundamental vortex topology and the kinetic shift of the vortex center. The High Mach Case involved a supersonic condition with $U_{lid}=1.6$ and $T_{lid}=1.0$, which was

designed to stress-test the engine under elevated shear rates and analyze compressibility effects, particularly the density accumulation at the stagnation point. Additionally, two thermal variation scenarios were considered, designated as hot ($T_{lid}=2.0$) and cold ($T_{lid}=0.5$), to validate the implementation of the diffuse reflection kernel by assessing the system response to strong thermal gradients and the consequent modification of the flow field owing to temperature-dependent viscosity.

The impact of the lid velocity on the macroscopic flow structure is depicted in Figure 6 (a), which contrasts the streamlines and scalar fields of the reference and high-Mach-number cases. In the subsonic reference scenario, where $U_{lid}=0.8$, the primary vortex center shifted downstream towards the upper-right corner ($x>0.5L$). This deviation from the geometric center, which is clearly visible in Figure 6 (a), corresponds to the kinetic shift phenomenon characteristic of rarefied transition flows at $Kn=0.25$. Such an observation confirms the solver's capability to capture non-equilibrium effects that exist beyond the scope of continuum hydrodynamics.

When the lid velocity is increased to $U_{lid}=1.6$ in the high Mach case, compressibility effects become pronounced. As illustrated in Figure 6 (b), significant density accumulation is observed near the stagnation point at the top-right corner, where high-momentum molecules collide with the stationary vertical wall. This local density build-up creates a sharp pressure gradient that opposes the flow, resulting in a slight vertical compression of the primary vortex compared with the reference case. Despite the high local collision rates in this region, the event-driven algorithm maintained stability without any energy drift.

Figure 6 Flow Topology and Compressibility
(a) Reference Case (U=0.8) showing the kinetic shift of the vortex
(b) High Mach Case (U=1.6) highlighting density accumulation at the stagnation point

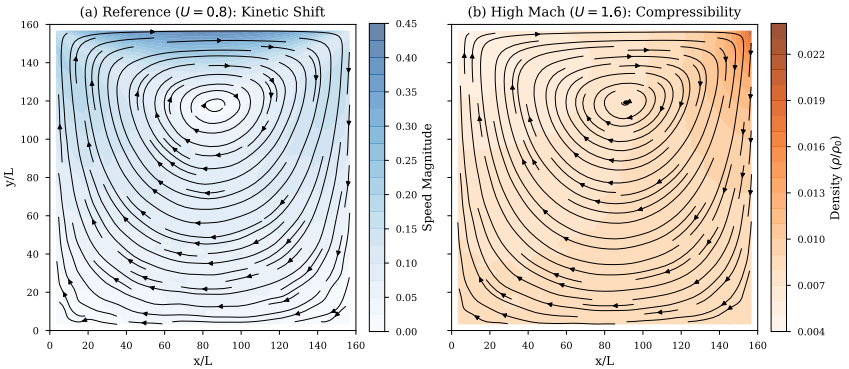

The interaction between heat transfer and momentum transport was examined using cold ($T_{lid}=0.5$) and hot ($T_{lid}=2.0$) lid scenarios, as shown in Figure 7. The temperature contours illustrate the transmission of thermal energy via molecular collisions. In the cold lid scenario depicted in Figure 7 (a), the moving wall functioned as an energy sink and established a thermal boundary layer where the gas temperature decreased significantly below the bulk temperature ($T<1.0$). In contrast, the hot lid scenario shown in Figure 7 (b) introduced energy into the system, elevating the local temperature and consequently increasing the gas viscosity near the lid. This temperature-dependent viscosity influenced the shear stress distribution, thereby altering the circulation strength of the primary vortex.

Figure 8 presents a quantitative comparison of the vertical profiles of the horizontal velocity (u) and temperature (T) along the cavity centerline ($x=0.5L$) with established results from the literature. The velocity profiles in Figure 8 (a) demonstrate the

characteristic velocity slip at the moving lid ($y/L=1.0$), where the gas velocity at the wall is less than the wall velocity ($u/u_{max}<1.0$). This observation is consistent with predictions for a high Knudsen number (Kn).

Figure 7 Thermal Non-Equilibrium Fields for hot and cold lids

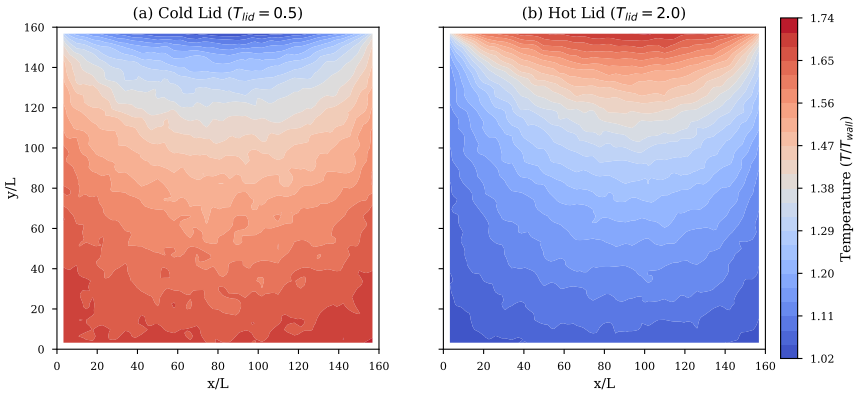

Figure 8 Centerline Profiles at x=0.5L
(a) Normalized horizontal velocity (b) Normalized temperature

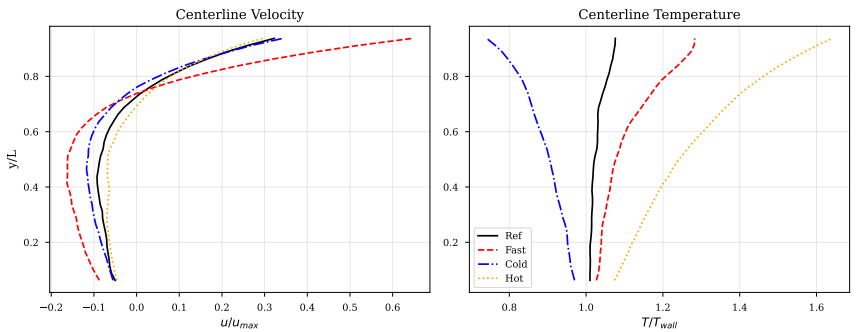

The temperature profiles in Figure 8 (b) display clear temperature jumps, or thermal slip, at both the moving and stationary bottom walls. In addition, the high Mach number case, represented by the red dashed line, shows a nonlinear temperature bulge within the bulk fluid that deviates from the linear conduction profile. This bulge results from viscous heating owing to the dissipation of kinetic

energy from the high-shear flow into heat, a phenomenon that is accurately modeled by the developed code.

Conclusion

This chapter demonstrates the effectiveness of a data-oriented Event-Driven Molecular Dynamics (EDMD) framework specifically developed for simulating rarefied gas flows within the transition regime. By integrating an exact event-driven methodology with contemporary computational architectures, the approach proved to be a robust and superior alternative to traditional time-driven methods for systems characterized by Knudsen numbers in the range of $0.1 \leq Kn \leq 10$.

The key findings highlight the accurate representation of non-equilibrium phenomena demonstrated through validation against benchmark cases such as the Lid-Driven Cavity flow. This validation confirms the capability of the framework to capture the critical effects of rarefied gas dynamics, including velocity slip, temperature jump, and the kinetic displacement of vortex centers. This method reliably resolves the physics of the Boltzmann equation without the statistical noise typical of stochastic techniques, provided that hard-sphere collisions dominate the interaction landscape.

The preservation of ballistic molecular trajectories is achieved through the introduction of the Lazy Update algorithm, which effectively separates spatial discretization from particle propagation. This decoupling prevents truncation errors at virtual cell boundaries and maintains the precise ballistic trajectories that are essential for accurately predicting the transport coefficients of dilute gases.

Regarding computational efficiency, the event-driven architecture exploits gas sparsity to reduce computational costs, particularly in low-density regimes. Unlike conventional methods

hindered by neighbor-search overheads in sparse systems, this approach achieves optimal performance in fine grid configurations where the cell occupancy is less than one ($\rho_{cell}<1$). This characteristic enables high-resolution spatial sampling without incurring excessive computational penalties.

In the future, the deterministic and high-throughput nature of this framework will be instrumental in addressing complex microfluidic challenges. Planned extensions include the modeling of multi-component gas mixtures and the incorporation of internal molecular degrees of freedom. These enhancements will facilitate detailed simulations of separation processes in porous media and thermal transpiration phenomena in MEMS devices, where continuum assumptions fail to hold.

References

Akkaya, V. R., & Kandemir, I. (2015). Event-Driven Molecular Dynamics Simulation of Hard-Sphere Gas Flows in Microchannels. *Mathematical Problems in Engineering*, *2015*(1), 842837. https://doi.org/10.1155/2015/842837

Anderson, J., Lorenz, C., & Travesset, A. (2008). General purpose molecular dynamics simulations fully implemented on graphics processing units. *Journal of Computational Physics*, *227*(10), 5342–5359. https://doi.org/10.1016/j.jcp.2008.01.047

Bannerman, M. N., Sargant, R., & Lue, L. (2011). DynamO: a free O(N) general event-driven molecular dynamics simulator. *Journal of Computational Chemistry*, *32*(15), 3329–3338. https://doi.org/10.1002/jcc.21915

Donev, A. (2009). Asynchronous Event-Driven Particle Algorithms. *Simulation*, *85*(4), 229–242. https://doi.org/10.1177/0037549708097881

Drepper, U. (2007). What every programmer should know about memory. *Red Hat, Inc*, *11*(2007), 2007.

Kandemir, I., & Kaya, A. M. (2011). Molecular dynamics simulation of compressible hot/cold moving lid-driven microcavity flow. *Microfluidics and Nanofluidics*, *12*(1–4), 509–520. https://doi.org/10.1007/s10404-011-0892-4

Koc, M., Kandemir, İ., & Akkaya, V. (2021). An Investigation of Transition Flow in Porous Media by Event Driven Molecular Dynamics Simulation. *Journal of Applied Fluid Mechanics*, *14*(01). https://doi.org/10.47176/jafm.14.01.31475

Perkel, J. M. (2020). Why scientists are turning to Rust. *Nature*, *588*(7836), 185–186. https://doi.org/10.1038/d41586-020-03382-2

Rapaport, D. C. (2004). *The art of molecular dynamics simulation*. Cambridge university press.

Rapaport, D. C. (2009). The Event-Driven Approach to N-Body Simulation. *Progress of Theoretical Physics Supplement*, *178*(178), 5–14. https://doi.org/10.1143/PTPS.178.5

Valentini, P., & Schwartzentruber, T. E. (2009a). A combined Event-Driven/Time-Driven molecular dynamics algorithm for the simulation of shock waves in rarefied gases. *Journal of Computational Physics*, *228*(23), 8766–8778. https://doi.org/10.1016/j.jcp.2009.08.026

Valentini, P., & Schwartzentruber, T. E. (2009b). Large-scale molecular dynamics simulations of normal shock waves in dilute argon. *Physics of Fluids*, *21*(6), 066101. https://doi.org/10.1063/1.3149866

Yakunchikov, A., & Kosyanchuk, V. (2018). Application of event-driven molecular dynamics approach to rarefied gas dynamics

problems. *Computers & Fluids*, *170*, 121–127. https://doi.org/10.1016/j.compfluid.2018.05.002

CHAPTER 3

BIOMEDICAL APPLICATIONS OF POLY(LACTIC) ACID

1. AHMET BEYLESANI[1]
2. GULBAHAR TABAKOĞLU[2]
3. RUMEYSA INCESU[3]
4. TARKAN AKDERYA [4]

Introduction

Polymeric materials maintain their industrial significance through extensive application in strategic sectors such as biomedical, textile, automotive, and construction. In particular, poly(lactic acid) (PLA), a biodegradable polymer synthesised from renewable resources such as corn, potatoes, and sugar beets, is currently regarded as one of the most viable alternatives to petroleum-based polymers due to its sustainable nature (Hazar Yoruç & Uğraşkan,

[1] Department of Biomedical Engineering, Faculty of Engineering and Architecture, Izmir Bakırçay University, Menemen, Orcid: 0009-0003-4007-6747
[2] Department of Biomedical Engineering, Graduate Education Institute, Izmir Bakırçay University, Orcid: 0000-0003-0181-8165
[3] Department of Biomedical Engineering, Graduate Education Institute, Izmir Bakırçay University, Orcid: 0000-0002-8781-2428
[4] Assoc. Prof. Dr., Department of Biomedical Engineering, Faculty of Engineering and Architecture, Izmir Bakırçay University, Menemen, Orcid: 0000-0001-6459-386X

2017). PLA is an aliphatic polyester obtained through the polymerisation of lactic acid, possessing biodegradable, bioresorbable, and biocompatible properties (Hussain et al., 2024).

PLA's high biodegradability plays a critical role in tissue engineering by enabling the fabrication of porous scaffold structures that support cell proliferation (Ranakoti et al., 2023). Its bioabsorbability within the body provides a suitable platform for controlled drug delivery systems. Furthermore, its lack of toxic residue during degradation makes it a valuable resource. This polymer has become widespread in the production of surgical sutures, implants, and stents (Hussain et al., 2024). Today, thanks to its high compatibility with additive manufacturing (3D printing) technologies, the production of patient-specific, personalised prostheses and orthopaedic implants has also become possible (Ranakoti et al., 2023).

Despite its vast potential in the biomedical field, pure PLA has some technical limitations. Low ductility and toughness, limited glass transition temperature, slow crystallisation rate, and high sensitivity to moisture are among the disadvantages of the material (Flaris & Singh, 2009). Furthermore, the control of the hydrolytic degradation rate and the challenges encountered in the production processes limit the use of the material in long-term load-bearing applications.

These shortcomings can be overcome with the development of PLA-based composite materials. For example, PLA composites with enhanced mechanical strength and biological interaction, thanks to hydroxyapatite or natural fibre reinforcements, offer more durable solutions in orthopaedic and medical fields (Vishnuvarthanan et al., 2025). This study aims to comprehensively evaluate the use of PLA in biomedical engineering in terms of advantages, disadvantages and future development strategies (Singhvi et al., 2019; Pawar et al., 2014; Ebrahimi & Dana, 2021).

Production Methods and Properties

PLA is an aliphatic polyester obtained by the polymerisation of lactic acid monomers. Lactic acid can be fermented from renewable resources such as corn starch, sugar beets, and sugarcane, making PLA a more sustainable alternative to petrochemical-based polymers. The biodegradation of PLA occurs through hydrolysis of ester bonds (Fig. 1), ultimately yielding carbon dioxide and water, thereby reducing the risk of leaving toxic residues in the body (Ebrahimi & Dana, 2021).

Figure 1 Hydrolysis mechanism of PLA degradation (Ebrahimi & Dana, 2021).

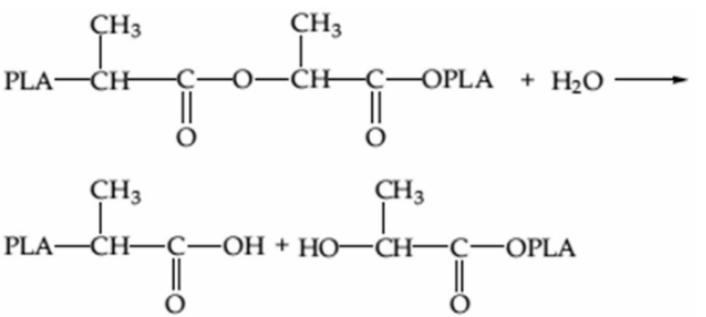

The properties of PLA can vary depending on the chirality ratio of the monomers (the ratio of L-lactic acid to D-lactic acid), molecular weight and polymerisation methods. PLA with high L-lactic acid content (PLLA) exhibits higher crystallinity and, consequently, greater mechanical strength. In contrast, amorphous PLA (PDLA or PLLA/PDLA blends) has a faster degradation rate and lower mechanical strength (Ebrahimi & Dana, 2021; Khouri et al., 2024; Lasprilla et al., 2012).

Various methods exist to produce PLA, with ring-opening polymerisation (ROP) being the most used. ROP involves the

conversion of cyclic lactide monomers into linear polymer chains in the presence of a catalyst. Other methods include direct polycondensation and sol-gel techniques. The production method influences the molecular weight, distribution, and microstructure of PLA, ultimately determining the properties of the final product (Ebrahimi & Dana, 2021; Khouri et al., 2024; Lopes et al., 2014).

Biomedical Applications of PLA

Due to its versatile properties (Fig. 2), PLA has emerged as an auspicious material for various biomedical applications. This section will provide an overview of its utilisation in implants, tissue engineering, drug delivery systems, and 3D-printed biomaterials [6].

Figure 2 Properties of PLA, especially for biomedical applications

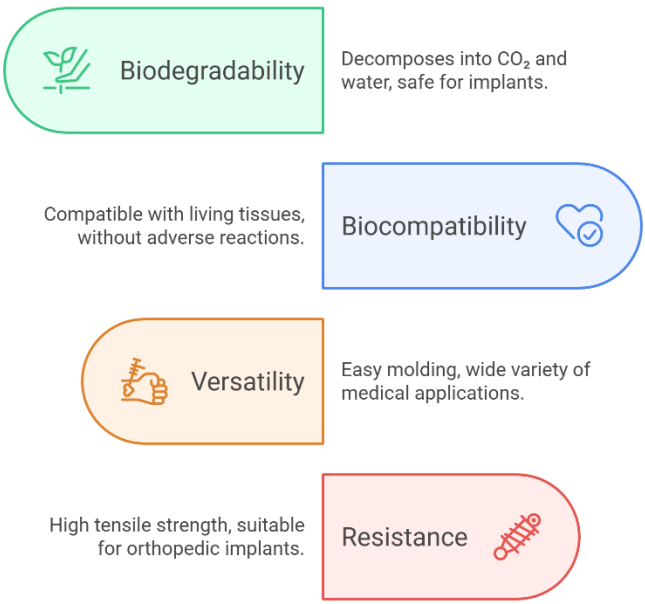

Tissue Engineering

Tissue engineering is an interdisciplinary domain that integrates cellular biology, materials science, and engineering principles to facilitate the repair or regeneration of impaired or diseased tissues and organs. In this context, PLA has emerged as a widely employed scaffold material due to its favourable attributes, including biocompatibility, controlled biodegradability, and tunable porosity, which collectively provide a conducive microenvironment for cellular adhesion, proliferation, and differentiation (Elmowafy et al., 2019; Singhvi et al., 2019; Xiao et al., 2012).

A variety of fabrication techniques have been utilised to engineer PLA-based scaffolds, such as electrospinning, solvent casting, particulate leaching, three-dimensional (3D) printing, and fused deposition modelling (FDM). Electrospinning is particularly advantageous for producing nanofibrous scaffolds with high surface area-to-volume ratios, which enhance cell–scaffold interactions. Solvent casting combined with particulate leaching facilitates the formation of highly macroporous structures, while 3D printing technologies offer exceptional control over scaffold architecture, enabling the creation of complex geometries and precisely defined pore sizes (Pawar et al., 2014; Maleki et al., 2022; Averous, 2012).

PLA scaffolds have been extensively investigated for applications in the engineering of bone, cartilage, skin, neural, and vascular tissues. For bone tissue engineering, PLA is frequently composited with bioactive ceramics such as hydroxyapatite to enhance osteoconductivity, promote osteoblast adhesion, and facilitate mineralised matrix deposition. In cartilage regeneration, PLA scaffolds support chondrocyte proliferation and extracellular matrix production, critical for restoring cartilaginous tissue function. In skin tissue engineering, PLA scaffolds act as a supportive matrix for fibroblast and keratinocyte growth, thus accelerating

epithelialization and wound closure (Averous, 2012; Ebrahimi & Dana, 2021; Ghalia & Dahman, 2017).

Orthopedic Implants

Orthopaedic implants are used in various orthopaedic procedures, including fracture fixation, joint replacement, and tendon repair. Traditional metal implants may present disadvantages such as stress concentration, corrosion, and allergic reactions. PLA has emerged as a promising alternative to metal implants due to its biocompatibility and biodegradability, offering potential advantages in orthopaedic applications (Singhvi et al., 2019; Pawar et al., 2014; Ebrahimi & Dana, 2021).

PLA implants can take various forms, including screws, plates, pins, and nails. The mechanical properties of PLA can be enhanced through reinforcement with composite materials or polymer blending. For instance, PLA composites reinforced with materials such as hydroxyapatite, calcium phosphate, or carbon fibres can provide mechanical properties more closely aligned with those of bone (Singhvi et al., 2019; Pawar et al., 2014; Ebrahimi & Dana, 2021).

PLA implants have been used in a range of orthopaedic applications, including fracture fixation, ligament reconstruction, and cartilage repair. PLA screws and plates are commonly used to stabilise fractured bones and, over time, degrade completely within the body, eliminating the need for a secondary surgical procedure. PLA nails are used in ligament reconstruction to support the attachment of tendons to bone. PLA scaffolds are also utilised in cartilage repair, providing an environment conducive to the growth of chondrocytes and the formation of new cartilage tissue (Singhvi et al., 2019; Pawar et al., 2014; Elmowafy et al., 2019).

Zhang et al. (Zhang et al., 2021) assessed the bone regeneration capacity of PLLA/nHA scaffolds. Hence, the effects of

different HA content on FDM 3D printing technology and the performance of scaffolds were assessed. It was determined that the PLLA/nHA composite ink satisfied the smoothness of printing. Also, the accuracy met the requirements of personalised bone repair applications. During in vivo evaluation, the samples were implanted into the rabbit femurs. It was found that increasing the nHA content could successfully reduce the acidity of the PLLA degradation product. Moreover, the degradation rate could be modified, and the bioactivity improved. It was reported that composite scaffolds with high-loaded nHA (e.g., 50%) had better osteo-regenerative capacity in vivo (Zhang et al., 2021).

Drug Delivery

Controlled drug delivery systems enable the administration of therapeutic agents at a desired rate and duration to target tissues. PLA is a commonly used polymer in drug delivery applications due to its biocompatibility, biodegradability, and ability to encapsulate drugs, making it an ideal matrix material (Tyler et al., 2016; Murariu & Dubois, 2016).

PLA-based drug delivery systems can take various forms, including microparticles, nanoparticles, films, rods, and implants. The drug can be physically encapsulated within the PLA matrix or chemically bound to it. The release rate of the drug depends on several factors, such as the molecular weight, crystallinity, hydrophobicity, and morphology of the PLA. The drug release mechanism can involve the hydrolytic degradation of the polymer, diffusion of the drug, or a combination of both (Ebrahimi & Dana, 2021; Tyler et al., 2016; Murariu & Dubois, 2016).

PLA-based drug delivery systems have been utilised in a wide range of therapeutic applications, including cancer treatment, antibiotic delivery, vaccine distribution, and hormone replacement therapy. For example, PLA nanoparticles have been employed to

deliver chemotherapy drugs directly to cancer cells, reducing systemic toxicity. PLA microparticles have been used to enhance immune responses by slow-release of vaccines. Additionally, PLA implants have been utilised to provide long-term hormone replacement therapy (Singhvi et al., 2019; Ebrahimi & Dana, 2021; Tyler et al., 2016).

Sutures

Sutures are threads used to close surgical incisions or wounds. PLA is commonly utilised as a surgical suture material due to its biocompatibility, biodegradability, and ease of processability, making it an ideal material for this purpose (Singhvi et al., 2019; Maleki et al., 2022).

PLA sutures can be manufactured in either monofilament or multifilament (braided) structures. Monofilament sutures tend to harbour fewer bacteria and have a smoother surface, which reduces tissue trauma during insertion. On the other hand, multifilament sutures offer higher tensile strength and improved knot security. The degradation rate of PLA sutures can be tailored to the postoperative healing timeline, ensuring the material remains intact for the necessary duration before it gradually breaks down (Khouri et al., 2024; Pawar et al., 2014; Maleki et al., 2022).

PLA sutures have been used in a wide range of surgical procedures, including skin closure, internal organ repair, and vascular surgery. The biodegradability of PLA eliminates the need for suture removal, reducing the risk of infection and improving patient comfort. Furthermore, PLA sutures can be loaded with therapeutic agents, such as growth factors or antibiotics, to promote wound healing and prevent infection (Singhvi et al., 2019; Pawar et al., 2014; Khouri et al., 2024).

Shortcomings of PLA and Development Strategies

While PLA offers numerous advantages in biomedical applications, it also presents certain drawbacks. The low mechanical strength, high hydrophobicity, and fast degradation rate of PLA can limit its use in specific applications (Singhvi et al., 2019; Lasprilla et al., 2012).

Several strategies have been developed to improve the mechanical properties of PLA. These strategies include reinforcement with composite materials, polymer blending, crosslinking, and the use of nanocomposites. Reinforcement with composite materials enhances PLA's strength and rigidity, while polymer blending can improve its flexibility and impact resistance. Crosslinking, which forms chemical bonds between PLA chains, can improve both the mechanical properties and the degradation rate of the polymer. Nanocomposites are achieved by incorporating nanoscale reinforcing materials (e.g., carbon nanotubes, clay minerals) into the PLA matrix, thereby enhancing both its mechanical properties and biocompatibility (Singhvi et al., 2019; Elmowafy et al., 2019; Ghalia & Dahman, 2017).

Surface modification techniques can be employed to reduce PLA's hydrophobicity and improve cell adhesion. These techniques include plasma treatment, chemical grafting, protein coating, and the attachment of bioactive molecules. Plasma treatment can reduce the hydrophobicity of PLA by increasing its surface energy. Chemical grafting introduces hydrophilic groups onto the PLA surface, enhancing water absorption and promoting cell attachment. Protein coating, achieved by adsorbing cell-adhesive proteins (e.g., fibronectin, laminin) onto the PLA surface, can promote cell adhesion and proliferation (Ebrahimi & Dana, 2021; Elmowafy et al., 2019; Averous, 2012).

In order to control the degradation rate of PLA, strategies such as adjusting the molecular weight, crystallinity, and monomer ratio can be employed. PLA with high molecular weight and high crystallinity degrades more slowly, whereas PLA with low molecular weight and low crystallinity degrades more rapidly. Altering the ratio of L-lactic acid to D-lactic acid can also influence the degradation rate (Singhvi et al., 2019; Ebrahimi & Dana, 2021; Lasprilla et al., 2012).

Future Perspectives and Conclusion

PLA is a biocompatible and biodegradable polymer with vast potential in biomedical applications. It is found in various fields such as tissue engineering, drug delivery, orthopaedic implants, and suture materials. In the future, PLA is expected to be utilised in more advanced biomedical applications, including gene therapy, diagnostics, and personalised medicine. For instance, PLA nanoparticles may be used to target genes in cells and directly treat genetic disorders. PLA-based biosensors could be developed to detect biomarkers in bodily fluids and enable early disease diagnosis. PLA implants, customised to meet specific patient needs, may be used for personalised orthopaedic treatments. In conclusion, PLA is a versatile material with the potential to revolutionise biomedical engineering. With continuous research and development, the role and significance of PLA in biomedical applications will continue to grow. This review of PLA's advantages, disadvantages, and development strategies helps us better understand the future potential of this polymer in biomedical applications (Ebrahimi & Dana, 2021; Lasprilla et al., 2012; Averous, 2012; Murariu & Dubois, 2016).

References

Averous, L. (2012). Synthesis, properties, environmental and biomedical applications of polylactic acid. *Handbook of Biopolymers and Biodegradable Plastics*, 177-188.

Ebrahimi, F., & Dana, H. R. (2021). Poly lactic acid (PLA) polymers: From properties to biomedical applications. *International Journal of Polymeric Materials and Polymeric Biomaterials*, *71*(15), 1117-1130. https://doi.org/10.1080/00914037.2021.1944140

Elmowafy, E. M., Tiboni, M., & Soliman, M. E. (2019). Biocompatibility, biodegradation and biomedical applications of poly(lactic acid)/poly(lactic-co-glycolic acid) micro and nanoparticles. *Journal of Pharmaceutical Investigation*, *49*(4), 347-380. https://doi.org/10.1007/s40005-019-00439-x

Flaris, V., & Singh, G. (2009). Recent Developments in Biopolymers. *Journal of Vinyl and Additive Technology*, (15), 1-11. https://doi.org/10.1002/vnl.20171

Ghalia, M. A., & Dahman, Y. (2017). Biodegradable poly(lactic acid)-based scaffolds: Synthesis and biomedical applications | Journal of Polymer Research. *Journal of Polymer Research*, *24*(74). https://link.springer.com/article/10.1007/s10965-017-1227-2

Hazar Yoruç, A. B., & Uğraşkan, V. (2017). Green Polymers and Applications. *Afyon Kocatepe University Journal of Sciences and Engineering*, *17*(1), 318-337. https://doi.org/10.5578/fmbd.53940

Hussain, M., Khan, S. M., Shafiq, M., & Abbas, N. (2024). A review on PLA-based biodegradable materials for biomedical applications. *Giant*, *18*, 100261. https://doi.org/10.1016/j.giant.2024.100261

Khouri, N. G., Bahú, J. O., Blanco-Llamero, C., Severino, P., Concha, V. O. C., & Souto, E. B. (2024). Polylactic acid (PLA): Properties, synthesis, and biomedical applications – A review of the literature. *Journal of Molecular Structure*,

1309, 138243. https://doi.org/10.1016/j.molstruc.2024.138243

Lasprilla, A. J. R., Martinez, G. A. R., Lunelli, B. H., Jardini, A. L., & Filho, R. M. (2012). Poly-lactic acid synthesis for application in biomedical devices—A review. *Biotechnology Advances*, *30*(1), 321-328. https://doi.org/10.1016/j.biotechadv.2011.06.019

Lopes, M. S., Jardini, A. L., & Filho, R. M. (2014). Synthesis and characterizations of poly (Lactic Acid) by ring-opening polymerization for biomedical applications. *Chemical engineering transactions*. https://repositorio.unicamp.br/acervo/detalhe/1195260

Maleki, H., Azimi, B., Ismaeilimoghadam, S., Danti, S., Maleki, H., Azimi, B., … Danti, S. (2022). Poly(lactic acid)-Based Electrospun Fibrous Structures for Biomedical Applications. *Applied Sciences*, *12*(6). https://doi.org/10.3390/app12063192

Murariu, M., & Dubois, P. (2016). PLA composites: From production to properties. *Advanced Drug Delivery Reviews*, *107*, 17-46. https://doi.org/10.1016/j.addr.2016.04.003

Pawar, R. P., Tekale, S. U., Shisodia, S. U., Totre, J. T., & Domb, A. J. (2014). Biomedical Applications of Poly(Lactic Acid). *Recent Patents on Regenerative Medicine*, *4*(1), 40-51. https://doi.org/10.2174/2210296504666140402235024

Ranakoti, L., Gangil, B., Bhandari, P., Singh, T., Sharma, S., Singh, J., … Singh, S. (2023). Promising Role of Polylactic Acid as an Ingenious Biomaterial in Scaffolds, Drug Delivery, Tissue Engineering, and Medical Implants: Research Developments, and Prospective Applications. *Molecules*, *28*(2). https://doi.org/10.3390/molecules28020485

Singhvi, M. S., Zinjarde, S. S., & Gokhale, D. V. (2019). Polylactic acid: Synthesis and biomedical applications. *Journal of Applied Microbiology*, *127*(6), 1612-1626. https://doi.org/10.1111/jam.14290

Tyler, B., Gullotti, D., Mangraviti, A., Utsuki, T., & Brem, H. (2016). Polylactic acid (PLA) controlled delivery carriers for biomedical applications. *Advanced Drug Delivery Reviews*, *107*, 163-175. https://doi.org/10.1016/j.addr.2016.06.018

Vishnuvarthanan, M., Prasad, A., & Subha, V. (2025). PLA-Based Composites for Tissue Engineering. Içinde A. Prasad & V. Katiyar (Ed.), *Resorbable Polymers for Bioimplants and Fixation Devices* (ss. 127-162). Singapore: Springer Nature. https://doi.org/10.1007/978-981-96-9306-1_6

Xiao, L., Wang, B., Yang, G., & Gauthier, M. (2012). Poly (lactic acid)-based biomaterials: Synthesis, modification and applications. *Biomedical science, engineering and technology*, *11*, 247-282.

Zhang, B., Wang, L., Song, P., Pei, X., Sun, H., Wu, L., … Zhang, X. (2021). 3D printed bone tissue regenerative PLA/HA scaffolds with comprehensive performance optimizations. *Materials & Design*, *201*, 109490. https://doi.org/10.1016/j.matdes.2021.109490

CHAPTER 4

INVESTIGATION OF MECHANICAL PROPERTIES OF BIOPOLYMERS AND BIOCOMPOSITES

1. MEHMET PAZARLI[1]
2. RUMEYSA INCESU[2]
3. TARKAN AKDERYA[3]
4. CEM GOK[4]

Introduction

Materials science holds a significant place in human history, being at the heart of technological advances and a key element in the development of civilisation. The rapid technological transformations of today have made materials science a dynamic discipline requiring

[1] Department of Intelligent Systems Engineering, Graduate Education Institute, Izmir Bakırçay University, Menemen, Orcid: 0000-0001-9276-4937
[2] Department of Biomedical Engineering, Graduate Education Institute, Izmir Bakırçay University, Menemen, Orcid: 0000-0002-8781-2428
[3] Assoc. Prof. Dr., Department of Biomedical Engineering, Faculty of Engineering and Architecture, Izmir Bakırçay University, Menemen, Orcid: 0000-0001-6459-386X
[4] Prof. Dr., Department of Biomedical Engineering, Faculty of Engineering and Architecture, Izmir Bakırçay University, Menemen, Orcid: 0000-0002-8949-8129

continuous innovation and development. Advances in the healthcare sector have increased the need for materials that are compatible with human biology, safety, and functionality, leading to the use of biomaterials. In this context, biomaterials have become an indispensable element in tissue engineering, implant technologies, and medical device design (Nair & Laurencin, 2007).

Biopolymers and biocomposites, important members of biomaterials, stand out with their biocompatibility, environmental friendliness, and sustainability (Mohanty et al., 2002). As with all materials, the mechanical properties of biopolymers may not always meet the desired high-performance criteria in medical applications. This may necessitate modifications to improve the mechanical capabilities of the material to suit its intended use. In literature, many studies examine the effects of production conditions and applied processes on the behaviour of materials. One of these, Carrasco et al. (2010), in their study on poly(lactic acid) (PLA), one of the most widely used materials among biodegradable polymers, reported that one of the factors that positively improves the yield strength, general mechanical performance, and crystal structure of the material is the heat treatment applied to the material (Carrasco et al., 2010). Similarly, Lim et al. (2008) stated that parameter changes in PLA processing technologies directly shape the final product properties (Lim et al., 2008).

Another method used to improve mechanical performance is material design. Polymers and natural fibres with limited mechanical strength can be transformed into more durable materials by reinforcing them with other materials (John & Thomas, 2008). For example, chitosan, a material with high biocompatibility but low mechanical strength, can be strengthened in terms of tensile and flexural strength by hybridising it with graphene, carbon fibre, or carbon nanotubes. Murariu and Dubois (2016) stated that multifunctional and high-performance biocomposites can be

produced by transferring the unique mechanical, thermal, and electrical properties of graphene to polymer matrices (Murariu & Dubois, 2016). Potts et al. (2011) also showed that graphene-based polymer nanocomposites provide significant improvements in mechanical properties even at much lower rates compared to conventional fillers The final properties of biopolymers and biocomposites are determined by the material recipe as well as variables such as temperature, pressure, cooling rate, and processing time in the production line. Optimising the parameters listed above directly affects the microstructure of the material and therefore its macroscopic mechanical performance. Therefore, considering the mechanical behaviour of materials from a holistic perspective is of great importance for application-specific material design (John & Thomas, 2008; Murariu & Dubois, 2016; Nair & Laurencin, 2007; Potts et al., 2011).

This study aims to systematically examine the factors that determine the mechanical properties of biopolymer and biocomposite materials, in line with the literature data, and to present different modification techniques using a comparative approach. The study is expected to influence the determination of the most accurate materials and production parameters for both academic research and industrial applications.

What are Biopolymers and Biocomposites, and How are They Produced?

Biopolymers

In recent years, biopolymers have gained strategic importance in the development of high-performance and environmentally friendly biocomposites due to their abundance in nature, renewability, and low-density lightweight structures. Research on these materials suggests that they can replace traditional petroleum-derived polymers in optical, biomedical, and engineering

applications. Although biopolymers offer a strong alternative to synthetic polymers, with sustainable and biodegradable structures, they require improvement in mechanical and physical properties, such as impact resistance, tensile strength, permeability, and thermal stability (Pawde & Deshmukh, 2008).

Classification of Biopolymers

Biopolymers are classified based on two main criteria: "source/origin" and "monomeric units," according to their structural complexity and the methods used to obtain them from sustainable sources. Biopolymers are classified as natural and synthetic according to their origin, and as polysaccharides, polypeptides, and polynucleotides according to their monomeric units (A, Ponnuchamy, Jacob, & Kapoor, 2025). This systematic approach, presented in Figure 1, reveals the fundamental building blocks that determine both the biological functions of materials and their potential in engineering applications.

Figure 1. Classification of biopolymers according to their origin and monomeric units.

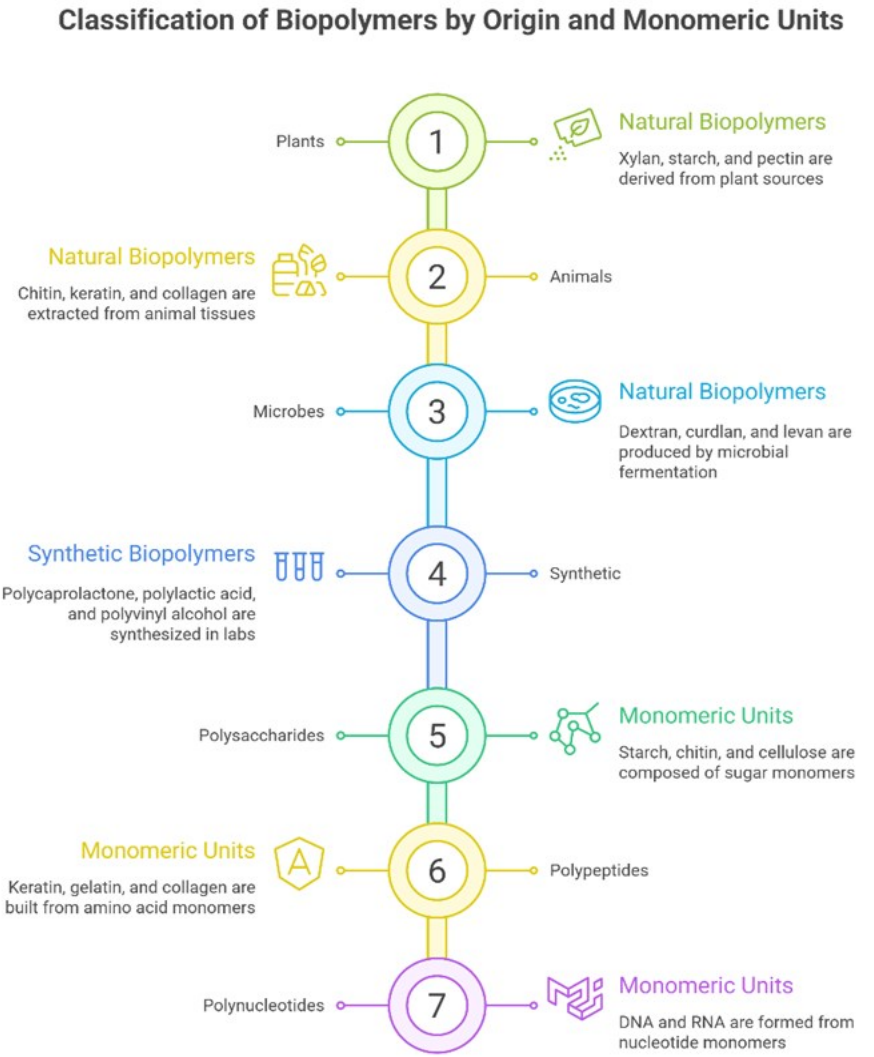

In conclusion, this systematic classification of biopolymers guides the selection of materials suitable for the targeted application area. It forms the basis for establishing the structure-property relationship necessary for biocomposite design.

Application Areas of Biopolymers

The application areas of biopolymeric materials are wide-ranging, in line with the unique physical and biological properties of the material and sustainability criteria. Industrial polymers, despite their superior technical properties, cause severe environmental pollution because they do not degrade through natural processes and can be disposed of only through costly recycling processes (Hazar et al., 2017). However, the fact that these polymers are derived from limited fossil resources, such as petroleum, has necessitated new searches for sustainability and environmental compatibility in the polymer sector. Biopolymers, in contrast to these disadvantages of industrial polymers, stand out as a strategic alternative in many areas, especially in the packaging sector (Flaris & Singh, 2009).

However, the most striking application area of biopolymers is the biomedical sector. These biocompatible materials with controllable degradation rates can serve as fundamental building blocks for the production of tissue-engineering scaffolds, controlled drug-delivery systems, surgical instruments, and temporary implants. Parameter optimisation in the production method is of primary importance in determining the required mechanical strength and biological interaction levels in these application areas (Sin et al., 2012). Table 1 presents, in detail, the production sites and main application areas of some biopolymers classified according to their natural, synthetic, and monomeric units, prepared in light of the literature data.

Table 1. Origins and application areas of biopolymers.

Biopolymers	Origin	Areas of Application	Source
Alginate	Brown algae	The use of stabilisers to extend the shelf life of fruits and vegetables, and for freezing.	(Frent et.al., 2022)
Carrageenan	Cell wall matrix of red seaweed	Anticoagulant and antithrombotic activity	(Valado et.al., 2022)
Keratin	Hair, nails, wool, horns, and feathers	Drug delivery systems, biomedical products, electrode materials, and absorbers.	(Sharma & Gupta, 2016)
Cellulose	Plant tissue	Cellophane films, thickeners, packaging materials, and adhesives.	(Grujic et al., 2017; Yadav et al., 2015; Zaman et al., 2020)
Guar gum	Cyamopsis tetragonolobus or *Cyamopsis psoraloides*	Emulsifier, bioadhesive, bulking laxative and film-forming agent.	(Tripathy & Das, 2013)
Collagen	Cuticles and cell walls of invertebrates	Dental composites, skin resurfacing templates, and biodegradable matrices.	(Kim, 2020)
Gelatine	Fish, cowhide, and bones	Thickener, texture regulator, stabiliser and emulsifier.	(Noor et. al., 2021)

Chitin	Cuticles of shellfish	Applications include drinking water purification, coagulation agents, biological treatment of phenolic compounds, and treatment of skin burns.	(Alborzi et al., 2021; Upadhye et al., 2022)
Hyaluronic acid	Fermentation liquids of Streptococcus and other bacteria obtained from rooster combs.	Cosmetic products and drug delivery systems	(Upadhye et.al., 2022; Yadav et.al., 2015)
Xantham gum	Xanthomonas campestris	Thickening agents, petroleum recovery, food additives, and cosmetic products.	(Jadav et.al., 2023; Lachke, 2004)
Scleroglucan	Epicoccum nigrum, Botrytis cinerea, Schizophyllum commune, S. glucanicum, and Sclerotium rolfsii	Cosmetics, immune system simulators, petroleum recovery, and pharmaceutical coatings.	(Jeong et al., 2022; Castillo et al., 2015)
Gellan	Sphingomonas species (mostly S. paucimobilis ATCC 31461), and Pseudomonas elodea	Tissue engineering, agar substitution, food additives, and cell immobilisation.	(Fialho et., 2008; Raghunandan et al., 2018; Bingül et al., 2022)
Poly(lactic acid) (PLA)	Polycondensation of D- or L-lactic acids or ROP (Ring-Opening Polymerisation) of lactide	Packaging materials, disposable products, medical implants, etc.	(Gunatillake et al., 2006)

Poli(trimetilen carbonat) (PTMC)	Trimethylene carbonate ROP	Soft tissue regeneration implant material	(Nair & Laurencin, 2007; Zhang et al., 2006)
Polysaccharides	The combination of monosaccharide groups forms it. It is found in bacteria, algae, fungi, plants, mammals, and other micro- and macro-life forms.	It functions as an essential component of the cell wall of most flora and moulds.	(Yu et al., 2018)
Polynucleotides	It is a chemical molecule consisting of three subunits: a nucleobase (purine or pyrimidine), a pentose (a five-carbon sugar), and a phosphate group.	In all living organisms, polynucleotides, especially DNA, are the primary carriers of genetic information.	(Wang & Seeman, 2002; Du et al., 1995)

Biocomposites

Composite materials are heterogeneous structural mixtures formed by combining two or more components with distinctly different physical and chemical properties on a macro scale (Christian, 2020). Biocomposites, on the other hand, are defined as biodegradable systems obtained by reinforcing natural fibres of animal or plant origin with natural or synthetic biopolymers that form the matrix phase (Azammi et.al., 2020). In biocomposite systems, the biopolymer matrix, which forms the continuous phase, acts as a binder that holds the components together; while the fibres, which are natural reinforcement elements in the discontinuous or constant phase, increase the rigidity and tensile strength of the structure, giving the system its fundamental mechanical strength (Şahan, 2010).

The basis of obtaining biocomposite materials is to combine the superior mechanical behaviour provided by the reinforcement element with the strength performance of the biopolymer matrix in the same structure. In the literature, the modulus of elasticity of such biocomposites has been reported to range from 1 to 4 GPa, and their tensile strength from 20 to 200 MPa (Christian, 2020).

Beyond mechanical strength, natural fibre reinforcements directly affect the thermal stability, electrical conductivity, morphological structure, crystallinity, biodegradation rate, and unit production cost of the material. Currently, the automotive, aerospace, and structural construction sectors stand out as priority application areas for natural fibre reinforced polymer composites (Hosseini, 2020). Advantages such as sustainability, cost-effectiveness, low density, high specific strength, and the use of renewable resources make biocomposites a strategic option both industrially and environmentally (Muhammed et al., 2018). In particular, integrating biologically based reinforcement components into the system significantly improves critical mechanical properties, such as tensile and impact resistance, of the final product (Halimatul et al., 2019; Sapuan et al., 2018).

Classification of Biocomposites

Biocomposites can be classified into three categories according to the structure of the reinforcing material: particle-reinforced composites, fibre-reinforced composites, and structural composites (Şahan, 2010). The classification is schematically illustrated in Figure 2.

Figure 2. Composite materials classification

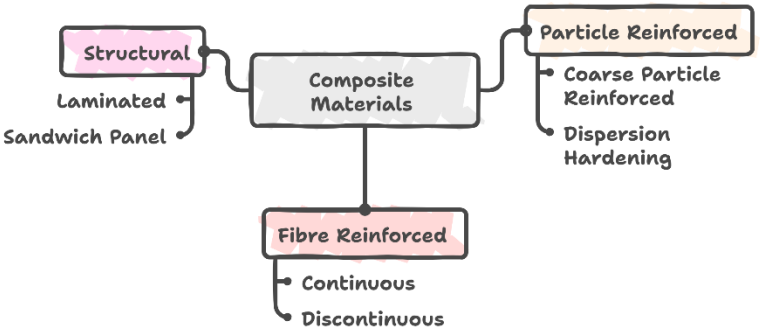

In these types of composite materials, the length of the fibres significantly affects the properties of the material. If the length of the fibres used is above a certain limit, they are called "continuous fibre reinforced composites," and if it is below a certain limit, they are called "short (discontinuous) fibre reinforced composites." The limiting value of fibre length varies with the diameter of the material used as the fibre, its tensile strength, and the fibre-matrix bond strength (Şahan, 2010; Topsakal & Özel, 2018). In biopolymer composites, natural fibres (reinforcement material) are added to the biopolymer matrix in the continuous phase to improve the stiffness and tensile strength of the prepared composite. The aim of preparing such composites is to obtain a product with good mechanical behaviour and durability performance provided by the natural fibre and biopolymer, respectively (Christian, 2020). The classification of fibres in composites according to their material origin is shown in Figure 3.

Figure 3. Fibre types according to the materials from which they are obtained.

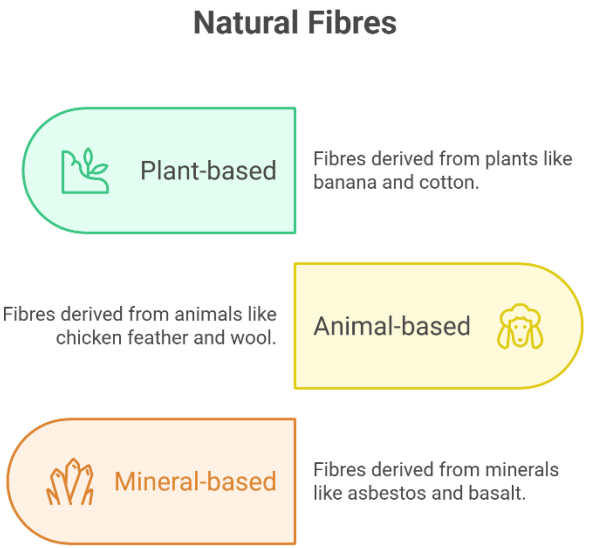

Applications of Biocomposites

Natural fibre reinforcements directly affect the thermal, morphological, and electrical properties of biopolymer composites, as well as their biodegradability rates and production costs. As a result of these advantages, natural fibre-reinforced composites find wide application in the medical, automotive, aerospace, and construction sectors (Hosseini, 2020). The use of these materials provides strategic benefits such as sustainability, low density, high specific strength, and biodegradability, and supports environmental compliance and user health standards (Muhammed et.al., 2018).

The final performance and mechanical characterisation of biocomposites depend on the type and ratio of the fibres used, their moisture absorption capacity, and the surface modification methods. In addition, the interfacial adhesion force between the matrix and the fibre, the composite design, the void ratio in the structure, and the

additives included in the matrix are fundamental parameters that determine the properties of the material (Sudamrao Getme & Patel, 2020; Kabir et al., 2012).

Table 2 provides examples of the properties and applications of various biopolymer composites prepared using different processing techniques.

Table 2. Properties and application areas of various biopolymer composites prepared with different processing techniques.

Matrix	Reinforcement	Processing Technique	Remarkable properties of biopolymer composites	Source
PLA	Silkworm silk fibre	Extrusion and injection moulding	The values of the elastic modulus, ductility, glass transition temperature, and thermal stability increased. It can be used to produce polymeric scaffolds in tissue engineering studies.	(Cheung et al., 2008)
PLA	Chicken feather fibre	Extrusion and injection moulding	Tensile modulus and thermal stability increased.	(Cheng et.al., 2009)
Maleic anhydride-inoculated PCL	Bamboo fibre	Hot press moulding	Tensile strength and elongation at break increased, while the rate of biological	(Su & Wu, 2010)

			degradation decreased.	
PLA	Rice straw fibre treated with poly(butyl acrylate)	It is produced by melting and mixing in a rheometer, then using a hot-press moulding method.	Hydrophobicity, tensile strength, and thermal stability have increased.	(Qin et.al., 2011)
PBS	Alkaline-treated coconut fibre	Hot press moulding	Tensile strength and modulus, as well as flexural strength and modulus, were increased.	(Nam et al., 2011)
PLA	starch mixture	Molten mix twin-screw extruder for poly(L-lactic acid)	Mechanical properties were improved compared to a mix of pure PLA and starch.	(Parvin et al., 2010)
Chitin	Thermoplastic starch	Melting and mixing method	After the addition of chitosan, the tensile strength increased by up to 85%.	(Oyeoka et al., 2021; Syafiq, 2020)
Chitin	Ostrich feather fibre	The mixture was dripped into an alkaline coagulant solution.	This composite material can be used as an absorbent for treating lead-containing industrial wastewater.	(Anantha & Kota, 2016)
PVOH	Cornstarch	Solution casting method	Biodegradable films are developed and easily composted with the help of enzymes.	(A et.al., 2025)

Mechanical Properties of Biopolymers and Biocomposites

The strength values for biopolymers and biocomposites vary depending on their intended use. These strength values are determined by performing appropriate tensile, compressive, and bending tests on the material (Soboyejo, 2002). Generally, these tests determine the value resulting from changes in the material after applying compressive, tensile, or bending forces.

In tensile tests, which are applied to determine the mechanical behaviour of materials, specimens are subjected to gradual stress under an axial load. During this process, ductile materials exhibit significant elongation and deformation before fracture, while brittle materials show sudden fracture before entering the plastic deformation phase. In the stress-strain diagram, the boundary point where the elastic region ends and permanent deformation begins is defined as the yield strength. The maximum load the material can carry in the plastic region is called the tensile strength (ultimate tensile strength). In addition to tensile tests, compressive and flexural tests are also critical for evaluating the structural performance of biocomposites. In compressive tests, the dimensional and structural changes under vertical compressive forces applied to the specimen are recorded, and in flexural tests, the dimensional and structural changes under bending loads applied at specific points are recorded, and the relevant strength values of the material are calculated (Raghavan, 2015). Through these mechanical tests, the mechanical properties of the specimens, such as the modulus of elasticity, tensile strength, and elongation at break, can be determined.

Mechanical Tests

There are many test methods to determine the mechanical properties of materials. Some of these are tensile tests, compression tests, flexural tests, shear tests, fatigue tests, and creep tests. The most used test methods are explained in detail below.

Tensile Test

Tensile testing, one of the most fundamental methods in the mechanical characterisation of materials, is applied to determine the strength limits, ductility potential, and general deformation behaviour of a material under static load. This test procedure involves controlled pulling of a standard-prepared specimen under an axial load until it reaches the fracture point (Azamni et.al., 2020; Ramamoorthy et al., 2019). The stress-strain curve created based on the data obtained during the test allows for the calculation of critical mechanical properties of the material, such as yield strength, ultimate tensile strength, modulus of elasticity (Young's modulus), and elongation at break (Netravali & Chabba, 2003; Macedo et al., 2010).

The basic parameters obtained from the tensile test and the calculation methods are detailed below:

Tensile stress (σ) is defined as the intensity of internal forces acting on a specific cross-sectional area of a material. This stress, occurring in the cross-sectional area perpendicular to the direction of load application, results from the force system that causes the material to deform. Even if the applied force remains constant, the stress varies with the cross-sectional area over which the force acts. Engineering stress (yield or tensile) is calculated by dividing the instantaneous load (F) by the initial cross-sectional area (A_0) of the material using the following equation (Equation 1):

$$\sigma = \frac{F}{A_0} \qquad \text{(MPa)} \tag{1}$$

Tensile strain (ε) is the ratio of the dimensional change in a material due to external forces to the original dimensions of the material. When a load is applied to a material, stress causes a change in shape (deformation). Strain is the mathematical expression of this change and represents the amount of elongation or shortening per unit length of the material. The dimensional change (ΔL) is found by taking the difference between the final length (L) and the initial length (L_0) of the specimen. Tensile strain is expressed using the following equations (Equation 2 and Equation 3) (Macedo et.al., 2010; Petinakis ., 2009):

$$\varepsilon = \frac{\Delta L}{L_0} = \frac{L - L_0}{L_0} \quad [mm/mm] \tag{2}$$

$$\Delta L = L - L_0 \qquad \text{[mm]} \tag{3}$$

The tensile testing device shown in Figure 4 measures the resistance of a material to an applied static or dynamic load. After the production of all tensile specimens with the necessary parameters, the tensile specimens conforming to the ISO 527 standard, as shown in Figure 5, were subjected to the testing device to analyze their mechanical properties. These tests are performed using a universal testing device equipped with a load cell and a video extensometer capable of measuring elongation. In this device, which enables the determination of the mechanical properties of the material, a unidirectional force is applied to the material at a determined tensile speed, and the elongation and force values of the

material are measured to obtain the tensile strength and tensile strain curve.

Figure 4. Tensile testing machine

Figure 5. Tensile specimen according to ISO 527 standard.

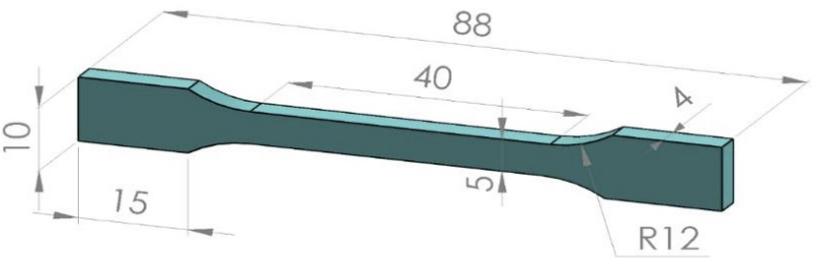

Bending Test

One of the most critical factors determining the deformation capability and rigidity of materials is flexural strength. Therefore, flexural tests are the most frequently used method after tensile tests in the mechanical characterisation of biopolymer composites. Theoretically, the flexural behaviour of a material is directly dependent on the Young's modulus (elasticity) and the moment of inertia, which is a function of the cross-sectional geometry (Faruk & Ain, 2013).

Studies show that the type of reinforcing fibres and their interaction with the matrix are decisive in flexural performance. For example, it has been reported that composites reinforced with natural fibres such as hemp and ramie exhibit a high fracture modulus, but increasing the amount of fibre does not always increase strength. Sawpan et al. stated that natural "kink" points in the fibre structure can cause stress concentrations, reducing flexural strength (Sawpan et al., 2012). In contrast, it has been observed that both flexural strength and modulus can be improved by using bonding agents or applying irradiation methods to increase matrix-fibre compatibility (Ibrahim et al., 2009).

In order to determine the flexural behaviour of biocomposites, a three-point bending test is generally used. In this test method, a rectangular cross-section specimen is placed on two supports with a specified span (ℓ), and deformation is measured by applying a controlled load at the exact midpoint of the specimen. Using the data obtained during the test process, the flexural stress, flexural strain, and flexural modulus of the material are calculated using the following formulations:

Flexural (Yield) Stress (σ_f): This represents the maximum stress occurring on the outer surface of the specimen during bending. The calculation is done with the following equation (Equation 4)

(Ramamoorthy et.al., 2019; Macedo et.al., 2010; Faruk & Ain, 2013):

$$\sigma_f = \frac{3F\ell}{2bh^2} \tag{4}$$

Flexural Strain (ε_f): Like tensile strain, this is a quantitative measure of the extent to which the top surface of the specimen is deflected from its original position during bending.

Flexural modulus (E_b): Represents the stiffness of the material in the elastic region and is calculated from data obtained from the linear portion of the force-displacement curve (Equation 5) (Ramamoorthy et al., 2019; Macedo et al., 2010; Faruk & Ain, 2013).

$$E_b = \frac{\ell^3 F}{4bh^3 Y} \tag{5}$$

For bending testing, a three-point bending test apparatus is attached to the tensile testing machine shown in Figure 6, and the bending test is performed on the ASTM D790 standard specimen shown in Figure 7, prepared at a specified test speed, like the tensile test specimens. The test apparatus used for bending testing is a structure supported by two supports that generates a stress with a single force F. The test setup is shown in Figure 8.

Figure 6. While performing the three-point bending test

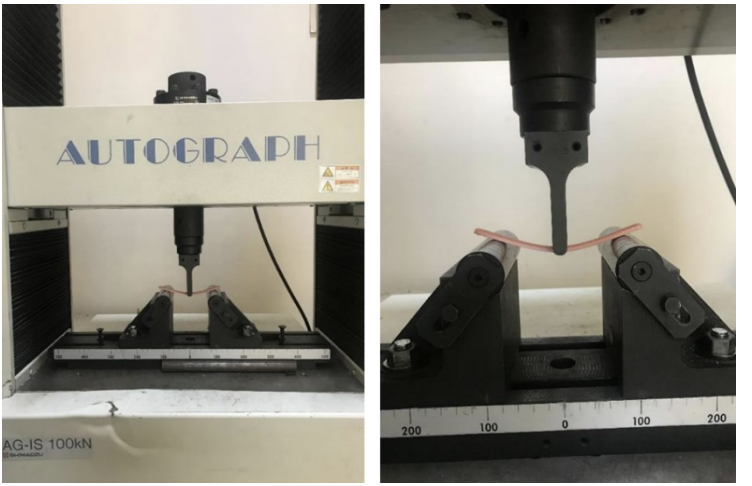

Figure 7. Bending specimen according to ASTM D790 standards.

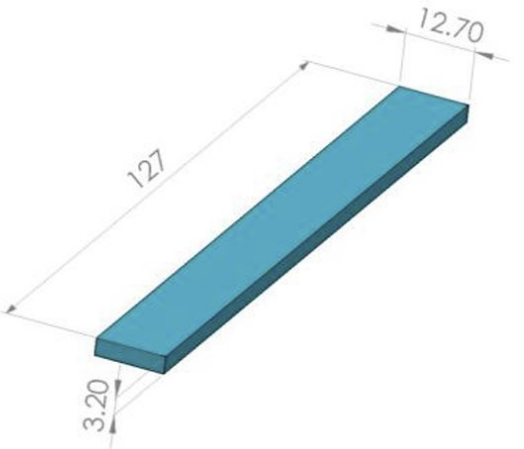

Figure 8. Three-point bending test setup.

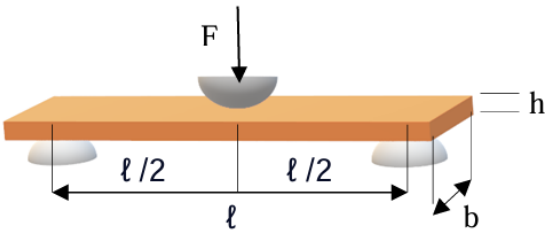

Hardness Test

Hardness can be expressed as the resistance of a material to deformation. It is calculated by applying a deformation to the material with a higher strength than itself. It is measured using the hardness measuring device shown in Figure 9 (Smith & Hashemi, 2006).

Several methods are used when measuring the hardness of biopolymers and biocomposites, as shown in Table 3. Brinell, Rockwell, Vickers and Shore hardness tests are used to measure the hardness of relatively soft materials such as elastomers and biopolymers (Jr & Rethwisch, 2020). These measurements are made by calculating the diameter or depth of the indentation left after an indenter penetrates. For Brinell (steel ball) and Vickers (diamond pyramid), the diameter of the indentation is measured. In contrast, for Rockwell (diamond cone or steel ball) and Shore (ball), the depth is measured to calculate the hardness value (Raghavan, 2015). The relationships among depth, diameter, and hardness are inversely proportional. For the material to be hard, the depth or diameter value must be small. The less deep or wide the indentation left on the surface of the material by the penetrating tip, the harder it is said to be.

Figure 9. Hardness testing device

Table 3. Hardness measurement methods (Smith & Hashemi, 2006; Jr & Rethwisch, 2020; Raghavan, 2015)

Measurement Type	The tip used	Method	Unit
Brinell (HB)	Steel or tungsten carbide ball	The end material used is pressed against the surface under a specific load.	Load / (π * D * (D - $\sqrt{(D^2 - d^2)}$)
Vickers (HV)	Pyramid diamond tip	The end material used is pressed against the surface under a specific load.	Vickers Hardness = 1.854 * Load / (A^2)
Rockwell (HRC, HRB, HRA)	Conical or round ball	The end material used is pressed against the surface under a specific load.	The amount of retraction is measured when the load is lifted.
Shore (HS)	Conical or round ball	The end material used is pressed against the surface under a specific load.	By measuring how much the material penetrates the surface under load.
Leeb (HLD)	Conical or round ball	A hammer falls onto the surface of the material.	By measuring the speed at which the hammer rises

Table 4 lists the mechanical properties of biopolymers and biocomposites that were studied in the articles and whose mechanical properties were determined.

Table 4. Mechanical properties of some biopolymers and biocomposites.

Material	Hardness (J/cm^3)	Modulus of Elasticity (MPa)	Tensile Strength (MPa)	Yield Strength (MPa)	Elongation (%)	Source
PLA (Poly(lactic acid)		3.5-3.8		48-110	2.5-100	(Carrasco et.al., 2010)
PLA-I (injectable)		3.7+-0.1		65.6±1.3	4.0±0.8	(Carrasco et.al., 2010)
PLA-EI (Extruded and injectable)		3.9±0.1		65.2±0.9	5.4±0.6	(Carrasco et.al., 2010)
PLA-IA (injected and annealed)		4.1±-0.1		75.4±0.9	2.5±0.2	(Carrasco et.al., 2010)
PLA-EAI (Extruded, injected, and annealed)		4.1±-0.1		77.0±1.1	3.3±0.3	(Carrasco et.al., 2010)
PS (Polystyrene)		2.9-3.5		34-46	3.0-4.0	(Carrasco et.al., 2010)
i-PP (polypropylene)		1.1-1.5		21-37	20-800	(Carrasco et.al., 2010)
TPS (Thermoplastic starch) winette 20 wt%			15-16		19	(Sadasivuni et.al., 2020)

TPS Cellulose NFs 15% by weight		224 ± 15.4	220	6.78±0.55		(Sadasivuni et.al., 2020)
TPS wheat straw NFs 10 wt%		271 ± 27.4		7.71±0.67		(Sadasivuni et.al., 2020)
TPS BC 22 wt%		361.4 ± 1.9	31.6±0.89		5.3±0.1	(Sadasivuni et.al., 2020)
PVA ChW			5.7±0.6			(Sadasivuni et.al., 2020)
TPS Chitosan NPs 6 wt%			10.8		22.7	(Sadasivuni et.al., 2020)
Chitosan CWs 20 wt%			120 (dry) 17.3 (wet)		6 (dry) 10 (wet)	(Sadasivuni et.al., 2020)
Chitosan SG 5 wt%		5100 ± 240	200±2.9			(Sadasivuni et.al., 2020)
PLA CNCs		2600 ± 300		31.9 ± 2.8	157 ±30	(Sadasivuni et.al., 2020)
HPMC BCNC and AgNPs 4 wt% BCNC and 1 wt% AgNPs		2280 ± 270	78 ± 6.9		44±4.5	(Sadasivuni et.al., 2020)
PLA (Polylactic Acid)		0.35-3.5	21-60		2.5-6	(Van de Velde & Kiekens, 2002)

L-PLA		2.7-4.14	15.5-150		3-10	(Van de Velde & Kiekens, 2002)
DL-PLA		1-3.45	27.6-50		2-10	(Van de Velde & Kiekens, 2002)
PGA (Polyglycolic acid)		6-7	60-99.7		1.5-20	(Van de Velde & Kiekens, 2002)
DL-PLA/PGA 50/50		1-4.34	41.4-55.2		2-10	(Van de Velde & Kiekens, 2002)
DL-PLA/PGA 75/25		1.38-4.13	41.4-55.2		2.5-10	(Van de Velde & Kiekens, 2002)
PCL (Polycaprolactone)		0.21-0.44	20.7-42		300-1000	(Van de Velde & Kiekens, 2002)
PHB (Polyhydroxybuty rate)		3.5-4	40		5-8	(Van de Velde & Kiekens, 2002)
Uncoated cardboard			40±3.1		3.9±0.4	(Rhim, Lee, & Hong, 2006)
Alginate (Alginate film-			33.6±1.4		4.1±0.2	(Rhim et.al., 2006)

coated paperboards)						
Alg/$CaCl_2$ (Alginate film-coated and $CaCl_2$-treated paperboards)			35.3±2.6		4.6±0.2	(Rhim et.al., 2006)
Alg/OMMT (Alginate and OMMT composite film-coated paperboards.)			34.2±2.9		4.7±0.2	(Rhim et.al., 2006)
SPI (Soy Protein Isolate) (SPI film-coated paperboards)			25±7.9		6±2.2	(Rhim et.al., 2006)
SPISPI/FA (SPI film-coated and formaldehyde-treated paperboards)			26±5.6		6.9±1.9	(Rhim et.al., 2006)
SPI/OMMT (SPI and OMMT composite film-coated paperboards)			27±5.9		6.6±2.6	(Rhim et.al., 2006)

1:1 wt chitosan-SP	19.9	1.86	95.9			(Meng, Xie, Zhang, Wang, & Yu, 2019)
SF fibre (Bombyx mori)		10-17	300-700			(Meng et.al., 2019)
Egg white 10%w/v		0.008±0.00051	0.077±0.00015		0.85±0.007	
Egg white 10%w/v + 6% MG (mastic gum) (90-125µm)		0.0107±0.00011	0.0082±0.00007		0.70±0.011	(Mavrakis & Kiosseoglou, 2008)
Egg white 10%w/v +6% MG (75-90µm)		0.123±0.00025	0.008.5±0.00006		0.71±0.026	(Mavrakis & Kiosseoglou, 2008)
Egg white 10%w/v +6% MG (45-75µm)		0.0143±0.00031	0.0118±0.00010		0.76±0.010	(Mavrakis & Kiosseoglou, 2008)
E-PHBV		233±3	7.5±0.4			(Gallo, Schartel, Acierno, Cimino, & Russo, 2013)
Kefiran Film			6.40±2.62		18.35±3.76	(Shahabi-Ghahfarrokhi et al., 2015)

Kefiran Film (3 kGy Irradiation)			11.40±0.85		16.80±2.77	(Shahabi-Ghahfarrokhi et al., 2015)
Kefiran Film (6 kGy Irradiation)			16.65±0.33		13.12±0.97	(Shahabi-Ghahfarrokhi et al., 2015)
Kefiran Film (9 kGy Irradiation)			19.04±2.01		10.38±1.10	(Shahabi-Ghahfarrokhi et al., 2015)
Tendon Chitosan			56.5-79.3		11.9-14.7	(Rebelo, Fernandes, & Fangueiro, 2017)
Bombyx Mori Silk			740		20	(Rebelo et.al., 2017)
Spider Silk			875-972		17-18	(Rebelo et.al., 2017)
PLLA			28-50		6	(Rebelo et.al., 2017)
DL-PLA			29-35		6	(Rebelo et.al., 2017)
PLA (1 wt% of EFB (empty fruit bunch) fibre) Addition of inorganic nanosilica		1.375	34			(Asyraf et.al., 2022)

PLA (1 wt% of EFB fibre) Addition of organic nanosilica		1.475	39			(Asyraf et.al., 2022)
TPS (20 wt% mesocarpal fibre) (Untreated)		0.25	0.8			(Asyraf et.al., 2022)
TPS (10% by weight of alkali-treated mesocarp fibre)		0.1	0.9			(Asyraf et.al., 2022)
PHA (20% mesocarpal fibre) (Untreated)		3.35	13			(Asyraf et.al., 2022)
PHA (Maleic and hydride fibres combine with 20% of mesocarpal fibre)		4.25	24			(Asyraf et.al., 2022)
PHB (Polihidroksi bütirat) Machine Direction (MD)	0.13	2700±200	24±2		1.2±0.1	(Zaccone et.al., 2022)
PHB Transfer Direction (TD)	60±100	1800±200	14		1.0±0.2	(Zaccone et.al., 2022)
PHB/1ChNC MD	180±0.1	2700±100	27±1		1.5±0.2	(Zaccone et.al., 2022)

PHB/1ChNC TD	130±0.1	2400±300	22		1.1±0.1	(Zaccone et.al., 2022)
PHB/5ChNC MD	220	2800±100	33±4		1.7±0.4	(Zaccone et.al., 2022)
PHB/5ChNC TD	120	2500±200	21		1.0±0.1	(Zaccone et.al., 2022)

Table 4 compares the mechanical properties of some biopolymers and biocomposites. The highest stiffness was observed in films prepared with 50% by weight of chitosan-silk peptide (19.9 J/cm³), while the lowest stiffness was found in PHB (0.06 J/cm³) in the transverse direction calculation. The highest yield strength was 77 MPa in extruded, injected, and annealed PLA (PLA-EAI), and the lowest was 6.78 MPa in TPS (thermoplastic starch) cellulose nanofibres (15% by weight). The maximum elongation value was 300% in PCL (polycaprolactone), while the minimum elongation value was 1% in PHB (polyhydroxybutyrate) containing 5% by weight of ChNC (chitin nanocrystals). In the research, various methods such as reprocessing, heat treatment, and doping were used to improve the mechanical properties of biopolymers and biocomposites.

Conclusion

This review systematically examined the mechanical behaviour of biopolymers and biocomposites by analysing the combined effects of material selection, reinforcement strategies, and processing conditions reported in the literature. The findings clearly demonstrate that the mechanical performance of biopolymer-based systems is not solely governed by the intrinsic properties of the polymer matrix, but is strongly influenced by reinforcement type, interfacial adhesion, and processing parameters such as heat treatment, cooling rate, and fabrication techniques.

The reviewed studies indicate that the incorporation of natural fibres, nanofillers, and bio-based reinforcements can significantly enhance tensile strength, stiffness, and toughness, provided that effective matrix–reinforcement compatibility is achieved. In particular, nanoscale reinforcements such as cellulose nanofibres, graphene derivatives, and chitin nanocrystals were shown to deliver notable mechanical improvements at relatively low

loading levels, highlighting their potential for lightweight and high-performance applications.

Future research should focus on establishing standardized testing protocols to improve the comparability of mechanical data, as well as on developing multifunctional biocomposites that integrate mechanical performance with biological activity and environmental sustainability. Such advancements will be essential for accelerating the transition of biopolymer-based materials from laboratory-scale research to industrial and biomedical applications.Based on the results presented here, the following comments and recommendations for the future can be made:

• Since biomaterials and biocomposites are actively used in many fields, different properties may be required for various needs.

• The desired change in mechanical properties can be achieved by adding additives to the materials in the appropriate proportion.

• In addition to the additive ratio, factors such as the production method of the material, the applied heat treatment, and the conditions under which the experiment is conducted can also cause changes in mechanical properties.

• Based on these given mechanical property values, the mechanical properties can be modified to the desired level by changing the additive ratio or the methods applied.

References

A, M. V., Ponnuchamy, M., Jacob, M. M., & Kapoor, A. (2025). A Discursive Review of Biopolymer Composites: Classification, Characterization, and Applications. *Asia-Pacific Journal of Chemical Engineering*, *20*(4), e70036. https://doi.org/10.1002/apj.70036

Alborzi, Z., Izadi-Vasafi, H., & Ghayoumi, F. (2021). Wound dressings based on chitosan and gelatin containing starch, sesame oil and banana peel powder for the treatment of skin burn. *Journal of Polymer Research*, *28*(61). Geliş tarihi gönderen https://link.springer.com/article/10.1007/s10965-021-02427-y

Anantha, R. K., & Kota, S. (2016). Removal of lead by adsorption with the renewable biopolymer composite of feather (*Dromaius novaehollandiae*) and chitosan (*Agaricus bisporus*). *Environmental Technology & Innovation*, *6*, 11-26. https://doi.org/10.1016/j.eti.2016.04.004

Asyraf, M. R. M., Ishak, M. R., Syamsir, A., Nurazzi, N. M., Sabaruddin, F. A., Shazleen, S. S., … Razman, M. R. (2022). Mechanical properties of oil palm fibre-reinforced polymer composites: A review. *Journal of Materials Research and Technology*, *17*, 33-65. https://doi.org/10.1016/j.jmrt.2021.12.122

Azamni, A. M. N., İlyas, R. A., Sapuan, S. M., Ibrahim, R., Atikah, M. S. N., Mochamad, A., & Atiqah, A. (2020). Characterization studies of biopolymeric matrix and cellulose fibres based composites related to functionalized fibre-matrix interface. İçinde *Interfaces in Particle and Fibre Reinforced Composites* (ss. 29-93). Woodhead Publishing. https://doi.org/10.1016/B978-0-08-102665-6.00003-0

Bingül, N. D., Öz, Y. E., Şendemir, A., & Hameş, E. E. (2022). Microbial biopolymers in articular cartilage tissue engineering. *Journal of Polymer Research*, *29*(8), 334. https://doi.org/10.1007/s10965-022-03178-0

Carrasco, F., Pagès, P., Gámez-Pérez, J., Santana, O. O., & Maspoch, M. L. (2010). Processing of poly (lactic acid): Characterization of chemical structure, thermal stability and mechanical properties. *Polymer Degradation and Stability*, *95*(2), 116-125. https://doi.org/10.1016/j.polymdegradstab.2009.11.045

Castillo, N. A., Valdez, A. L., & Fariña, J. I. (2015). Microbial production of scleroglucan and downstream processing. *Frontiers in Microbiology*, *6*. https://doi.org/10.3389/fmicb.2015.01106

Cheng, S., Lau, K., Liu, T., Zhao, Y., Lam, P.-M., & Yin, Y. (2009). Mechanical and thermal properties of chicken feather fiber/PLA green composites. *Composites Part B: Engineering*, *40*(7), 650-654. https://doi.org/10.1016/j.compositesb.2009.04.011

Cheung, H.-Y., Lau, K.-T., Tao, X.-M., & Hui, D. (2008). A potential material for tissue engineering: Silkworm silk/PLA

biocomposite. *Composites Part B: Engineering*, *39*(6), 1026-1033. https://doi.org/10.1016/j.compositesb.2007.11.009

Christian, S. J. (2020). Natural fibre-reinforced noncementitious composites (biocomposites). İçinde *Nonconventional and Vernacular Construction Materials* (ss. 169-187). Woodhead Publishing. https://doi.org/10.1016/B978-0-08-102704-2.00008-1

Du, S. M., Wang, H., Tse-Dinh, Y.-C., & Seeman, N. C. (1995). Topological Transformations of Synthetic DNA Knots | Biochemistry. *Biochemistry*, *34*(2), 673-682.

Faruk, O., & Ain, B. (2013). Biofiber reinforced polymer composites for structural applications. İçinde *Developments in Fiber-Reinforced Polymer (FRP) Composites for Civil Engineering* (ss. 18-53). Woodhead Publishing. https://doi.org/10.1533/9780857098955.1.18

Fialho, A. M., Moreira, L. M., Granja, A. T., Popescu, A. O., Hoffmann, K., & Sá-Correia, I. (2008). Occurrence, production, and applications of gellan: Current state and

perspectives. *Applied Microbiology and Biotechnology*, *79*. Geliş tarihi gönderen https://link.springer.com/article/10.1007/s00253-008-1496-0

Flaris, V., & Singh, G. (2009). Recent Developments in Biopolymers. *Journal of Vinyl and Additive Technology*, (15), 1-11. https://doi.org/10.1002/vnl.20171

Frent, O. D., Vicas, L. G., Duteanu, N., Morgovan, C. M., Jurca, T., Pallag, A., … Marian, E. (2022). Sodium Alginate—Natural Microencapsulation Material of Polymeric Microparticles. *International Journal of Molecular Sciences*, *23*(20). https://doi.org/10.3390/ijms232012108

Gallo, E., Schartel, B., Acierno, D., Cimino, F., & Russo, P. (2013). Tailoring the flame retardant and mechanical performances of natural fiber-reinforced biopolymer by multi-component laminate. *Composites Part B: Engineering*, *44*(1), 112-119. https://doi.org/10.1016/j.compositesb.2012.07.005

Grujic, R., Vukic, M., & Gojkovic, V. (2017). Application of Biopolymers in the Food Industry. Içinde E. Pellicer, D. Nikolic, J. Sort, M. Baró, F. Zivic, N. Grujovic, … S. Pelemis (Ed.), *Advances in Applications of Industrial Biomaterials* (ss. 103-119). Cham: Springer International Publishing. https://doi.org/10.1007/978-3-319-62767-0_6

Gunatillake, P., Mayadunne, R., & Adhikari, R. (2006). Recent developments in biodegradable synthetic polymers. İçinde *Biotechnology Annual Review* (C. 12, ss. 301-347). Elsevier. https://doi.org/10.1016/S1387-2656(06)12009-8

Halimatul, M. J., Sapuan, S. M., Jawaid, M., Ishak, M. R., & Ilyas, R. A. (2019). Effect of sago starch and plasticizer content on the properties of thermoplastic films: Mechanical testing and cyclic soaking-drying. *Polimery*, *T. 64, nr 6*. https://doi.org/10.14314/polimery.2019.6.5

Hazar Yoruç, A. B., & Uğraşkan, V. (2017). Green Polymers and Applications. *Afyon Kocatepe University Journal of Sciences*

and Engineering, *17*(1), 318-337. https://doi.org/10.5578/fmbd.53940

Hosseini. (2020). Natural fiber polymer nanocomposites. İçinde *Fiber-Reinforced Nanocomposites: Fundamentals and Applications* (ss. 279-299). Elsevier. https://doi.org/10.1016/B978-0-12-819904-6.00013-X

Ibrahim, N. A., Ahmad, S. N. A., Yunus, W. M. Z. W., & Dahlan, K. Z. M. (2009). Effect of electron beam irradiation and poly(vinylpyrrolidone) addition on mechanical properties of polycaprolactone with empty fruit bunch fibre (OPEFB) composite. *Express Polymer Letters*, *3*(4), 226-234. https://doi.org/10.3144/expresspolymlett.2009.29

Jadav, M., Pooja, D., Adams, D. J., Kulhari, H., Jadav, M., Pooja, D., … Kulhari, H. (2023). Advances in Xanthan Gum-Based Systems for the Delivery of Therapeutic Agents. *Pharmaceutics*, *15*(2). https://doi.org/10.3390/pharmaceutics15020402

Jeong, J., Kim, Y., Hu, Y., & Jung, S. (2022). Bacterial Succinoglycans: Structure, Physical Properties, and Applications. *Polymers*, *14*(2), 276.

John, M. J., & Thomas, S. (2008). Biofibres and biocomposites. *Carbohydrate Polymers*, *71*(3), 343-364. https://doi.org/10.1016/j.carbpol.2007.05.040

Jr, W. D. C., & Rethwisch, D. G. (2020). *Callister's Materials Science and Engineering, Global Edition*. John Wiley & Sons.

Kabir, M. M., Wang, H., Lau, K. T., & Cardona, F. (2012). Chemical treatments on plant-based natural fibre reinforced polymer composites: An overview. *Composites Part B: Engineering*, *43*(7), 2883-2892. https://doi.org/10.1016/j.compositesb.2012.04.053

Kim, S.-K. (2020). *Encyclopedia of Marine Biotechnology*. John Wiley & Sons.

Lachke, A. (2004). Xanthan—A versatile gum. *Resonance*, *9*(10), 25-33. https://doi.org/10.1007/BF02834866

Lim, L.-T., Auras, R., & Rubino, M. (2008). Processing technologies for poly(lactic acid). *Progress in Polymer Science*, *33*(8), 820-852. https://doi.org/10.1016/j.progpolymsci.2008.05.004

Macedo, J. de S., Costa, M. F., Tavares, M. I. B., & Thiré, R. M. S. M. (2010). Preparation and characterization of composites based on polyhydroxybutyrate and waste powder from coconut fibers processing. *Polymer Engineering and Science*, *50*(7), 1466-1475.

Mavrakis, C., & Kiosseoglou, V. (2008). The structural characteristics and mechanical properties of biopolymer/mastic gum microsized particles composites. *Food Hydrocolloids*, *22*(5), 854-861. https://doi.org/10.1016/j.foodhyd.2007.03.011

Meng, L., Xie, F., Zhang, B., Wang, D. K., & Yu, L. (2019). Natural Biopolymer Alloys with Superior Mechanical Properties. *ACS Sustainable Chemistry & Engineering*, *7*(2), 2792-2802. https://doi.org/10.1021/acssuschemeng.8b06009

Mohanty, A. K., Misra, M., & Drzal, L. T. (2002). Sustainable Bio-Composites from Renewable Resources: Opportunities and Challenges in the Green Materials World. *Journal of Polymers and the Environment*, *10*(1), 19-26. https://doi.org/10.1023/A:1021013921916

Muhammed, S. A. N., Zainudin, E. S., Sapuan, S. M., Azaman, M. D., & Arifin, A. M. D. (2018). Introduction to Natural Fiber Reinforced Vinyl Ester and Vinyl Polymer Composites. İçinde *Natural Fibre Reinforced Vinyl Ester and Vinyl Polymer Composites* (ss. 1-25). Woodhead Publishing. https://doi.org/10.1016/B978-0-08-102160-6.00001-9

Murariu, M., & Dubois, P. (2016). PLA composites: From production to properties. *Advanced Drug Delivery Reviews*, *107*, 17-46. https://doi.org/10.1016/j.addr.2016.04.003

Nair, L. S., & Laurencin, C. T. (2007). Biodegradable polymers as biomaterials. *Progress in Polymer Science*, *32*(8), 762-798. https://doi.org/10.1016/j.progpolymsci.2007.05.017

Nam, T. H., Ogihara, S., Tung, N. H., & Kobayashi, S. (2011). Effect of alkali treatment on interfacial and mechanical properties of coir fiber reinforced poly(butylene succinate) biodegradable composites. *Composites Part B: Engineering*, *42*(6), 1648-1656. https://doi.org/10.1016/j.compositesb.2011.04.001

Netravali, A. N., & Chabba. (2003). Composites get greener. *Materials Today*, *6*(4), 22-29. https://doi.org/10.1016/S1369-7021(03)00427-9

Noor, N. Q. I. M., Razali, R. S., Ismail, N. K., Ramli, R. A., Razali, U. H. M., Bahauddin, A. R., … Shaarani, S. M. (2021). Application of Green Technology in Gelatin Extraction: A Review. *Processes*, *9*(12). https://doi.org/10.3390/pr9122227

Oyeoka, H. C., Ewulonu, C. M., Nwuzor, I. C., Obele, C. M., & Nwabanne, J. T. (2021). Packaging and degradability properties of polyvinyl alcohol/gelatin nanocomposite films filled water hyacinth cellulose nanocrystals. *Journal of*

Bioresources and Bioproducts, *6*(2), 168-185. https://doi.org/10.1016/j.jobab.2021.02.009

Parvin, F., Rahman, M. A., Islam, J. M. M., Khan, M. A., & Saadat, A. H. M. (2010). Preparation and Characterization of Starch/PVA Blend for Biodegradable Packaging Material. *Advanced Materials Research*, *123-125*, 351-354. https://doi.org/10.4028/www.scientific.net/AMR.123-125.351

Pawde, S. M., & Deshmukh, K. (2008). Characterization of polyvinyl alcohol/gelatin blend hydrogel films for biomedical applications. *Journal of Applied Polymer Science*, *109*(5), 3431-3437. https://doi.org/10.1002/app.28454

Petinakis, E., Yu, L., Edward, G., Dean, K., Liu, H., & Scully, A. D. (2009). Effect of Matrix–Particle Interfacial Adhesion on the Mechanical Properties of Poly(lactic acid)/Wood-Flour Micro-Composites. *Journal of Polymers and the*

Environment, *17*(2), 83-94. https://doi.org/10.1007/s10924-009-0124-0

Potts, J. R., Dreyer, D. R., Bielawski, C. W., & Ruoff, R. S. (2011). Graphene-based polymer nanocomposites. *Polymer*, *52*(1), 5-25. https://doi.org/10.1016/j.polymer.2010.11.042

Qin, L., Qiu, J., Liu, M., Ding, S., Shao, L., Lü, S., … Fu, X. (2011). Mechanical and thermal properties of poly(lactic acid) composites with rice straw fiber modified by poly(butyl acrylate). *Chemical Engineering Journal*, *166*(2), 772-778. https://doi.org/10.1016/j.cej.2010.11.039

Raghavan, V. (2015). *MATERIALS SCIENCE AND ENGINEERING, SIXTH EDITION: A FIRST COURSE*. PHI Learning Pvt. Ltd.

Raghunandan, K., Kumar, A., Kumar, S., Permaul, K., & Singh, S. (2018). Production of gellan gum, an exopolysaccharide, from biodiesel-derived waste glycerol by Sphingomonas spp. *3 Biotech*, *8*(1), 71. https://doi.org/10.1007/s13205-018-1096-3

Ramamoorthy, S. K., Åkesson, D., Rajan, R., Periyasamy, A. P., & Skrifvars, M. (2019). Mechanical performance of biofibers and their corresponding composites. İçinde *Mechanical and Physical Testing of Biocomposites, Fibre-Reinforced Composites and Hybrid Composites* (ss. 259-292). Woodhead Publishing. https://doi.org/10.1016/B978-0-08-102292-4.00014-X

Rebelo, R., Fernandes, M., & Fangueiro, R. (2017). Biopolymers in Medical Implants: A Brief Review. *Procedia Engineering*, *200*, 236-243. https://doi.org/10.1016/j.proeng.2017.07.034

Rhim, J.-W., Lee, J.-H., & Hong, S.-I. (2006). Water resistance and mechanical properties of biopolymer (alginate and soy protein) coated paperboards. *LWT - Food Science and Technology*, *39*(7), 806-813. https://doi.org/10.1016/j.lwt.2005.05.008

Sadasivuni, K. K., Saha, P., Adhikari, J., Deshmukh, K., Ahamed, M. B., & Cabibihan, J.-J. (2020). Recent advances in mechanical

properties of biopolymer composites: A review. *Polymer Composites*, *41*(1), 32-59. https://doi.org/10.1002/pc.25356

Sapuan, S. M., Sahari, J., Ishak, M. R., & Sanyang, M. L. (2018). *Sugar Palm Biofibers, Biopolymers, and Biocomposites*. CRC Press.

Sawpan, M. A., Pickering, K. L., & Fernyhough, A. (2012). Flexural properties of hemp fibre reinforced polylactide and unsaturated polyester composites. *Composites Part A: Applied Science and Manufacturing*, *43*(3), 519-526. https://doi.org/10.1016/j.compositesa.2011.11.021

Shahabi-Ghahfarrokhi, I., Khodaiyan, F., Mousavi, M., & Yousefi, H. (2015). Effect of γ-irradiation on the physical and mechanical properties of kefiran biopolymer film. *International Journal of Biological Macromolecules*, *74*, 343-350. https://doi.org/10.1016/j.ijbiomac.2014.11.038

Sharma, S., & Gupta, A. (2016). Sustainable Management of Keratin Waste Biomass: Applications and Future Perspectives.

Brazilian Archives of Biology and Technology, *59*, e16150684. https://doi.org/10.1590/1678-4324-2016150684

Sin, L. T., Rahmat, A. R., & Rahman, W. A. W. A. (2012). *Polylactic Acid: PLA Biopolymer Technology and Applications*. William Andrew.

Smith, W. F., & Hashemi, J. (2006). Foundations of Materials Science and Engineering. *Foundations of Materials Science and Engineering*, *509*.

Soboyejo, W. (2002). *Mechanical Properties of Engineered Materials*. Boca Raton: CRC Press. https://doi.org/10.1201/9780203910399

Su, S.-K., & Wu, C.-S. (2010). The Processing and Characterization of Polyester/Natural Fiber Composites. *Polymer-Plastics Technology and Engineering*, *49*(10), 1022-1029. https://doi.org/10.1080/03602559.2010.482083

Sudamrao Getme, A., & Patel, B. (2020). A Review: Bio-fiber's as reinforcement in composites of polylactic acid (PLA).

Materials Today: Proceedings, *26*, 2116-2122. https://doi.org/10.1016/j.matpr.2020.02.457

Syafiq, R., Sapuan, S. M., Zuhri, M. Y. M., Ilyas, R. A., Nazrin, A., Sherwani, S. F. K., … Khalina, A. (2020). Antimicrobial Activities of Starch-Based Biopolymers and Biocomposites Incorporated with Plant Essential Oils: A Review. *Polymers*, *12*(10). https://doi.org/10.3390/polym12102403

Şahan, B. G. (2010). *Hidroksiapatit Katkılı Yapay Kemik Kompozitlerin Mekanik Özelliklerine Bağlayıcı Ajanları Etkileri* (PhD Thesis). Yüksek Lisans Tezi). İstanbul Üniversitesi Fen Bilimleri Enstitüsü. İstanbul.

Topsakal, A., & Özel, C. (2018). Lif Takviyeli Polimer Kompozit Malzemelerde Lif Türü ve Oranının Fiziksel ve Mekanik Özelliklere Etkisi. *El-Cezeri*, *5*(1), 107-116. https://doi.org/10.31202/ecjse.365820

Tripathy, S., & Das, M. K. (2013). GUAR GUM: PRESENT STATUS AND APPLICATIONS. *Journal of Pharmaceutical*

and Scientific Innovation, *4*(4), 24-28. https://doi.org/10.7897/2277-4572.02447

Upadhye, M. C., Kuchekar, M. C., Pujari, R. R., & Sable. (2022). Biopolymers: A comprehensive review. *Open Access Research Journal of Science and Technology*, *4*(1), 013-018. https://doi.org/10.53022/oarjst.2022.4.1.0070

Valado, A., Pereira, M., Amaral, M., Cotas, J., Pereira, L., Valado, A., … Pereira, L. (2022). Bioactivity of Carrageenans in Metabolic Syndrome and Cardiovascular Diseases. *Nutraceuticals*, *2*(4), 441-454. https://doi.org/10.3390/nutraceuticals2040032

Van de Velde, K., & Kiekens, P. (2002). Biopolymers: Overview of several properties and consequences on their applications. *Polymer Testing*, *21*(4), 433-442. https://doi.org/10.1016/S0142-9418(01)00107-6

Wang, H., & Seeman, N. C. (2002, Mayıs 1). Structural Domains of DNA Mesojunctions [Research-article]. https://doi.org/10.1021/bi00003a026

Yadav, P., Yadav, H., Shah, V. G., Shah, G., & Dhaka, G. (2015). Biomedical Biopolymers, their Origin and Evolution in Biomedical Sciences: A Systematic Review. *Journal of Clinical and Diagnostic Research : JCDR*, *9*(9), ZE21-ZE25. https://doi.org/10.7860/JCDR/2015/13907.6565

Yu, Y., Mingyue, S., Song, Q., & Jianhua, X. (2018). Biological activities and pharmaceutical applications of polysaccharide from natural resources: A review. *Carbohydrate Polymers*, *183*, 91-101. https://doi.org/10.1016/j.carbpol.2017.12.009

Zaccone, M., Patel, M. K., Brauwer, L. D., Nair, R., Montalbano, M. L., Monti, M., … Oksman, K. (2022). Influence of Chitin Nanocrystals on the Crystallinity and Mechanical Properties of Poly(hydroxybutyrate) Biopolymer. *Polymers*, *14*(3). https://doi.org/10.3390/polym14030562

Zaman, A., Huang, F., Jiang, M., Wei, W., & Zhou, Z. (2020). Preparation, Properties, and Applications of Natural Cellulosic Aerogels: A Review. *Energy and Built*

Environment, *1*(1), 60-76. https://doi.org/10.1016/j.enbenv.2019.09.002

Zhang, Z., Kuijer, R., Bulstra, S. K., Grijpma, D. W., & Feijen, J. (2006). The in vivo and in vitro degradation behavior of poly(trimethylene carbonate). *Biomaterials*, *27*(9), 1741-1748. https://doi.org/10.1016/j.biomaterials.2005.09.017

CHAPTER 5

POLYMER-BASED ADDITIVE MANUFACTURING TECHNOLOGIES: A COMPARATIVE REVIEW OF FUSED DEPOSITION MODELING (FDM) AND STEREOLITHOGRAPHY (SLA)

1. KUBİLAY HAN[1]
2. MÜCAHİT ABDULLAH SARI[2]

Introduction

Additive Manufacturing (AM) technologies have emerged over the past three decades as a strong alternative to conventional subtractive and forming-based manufacturing methods(Bahnini et al., 2018; Sathish et al., 2022; Yeshiwas et al., 2025). Based on a layer-by-layer fabrication principle, these technologies enable the direct transformation of digital designs into physical objects, thereby enhancing design freedom, reducing material waste, and significantly shortening the time between prototyping and final part production (B.A et al., 2022; Çerlek et al., 2025). Owing to these

[1] Dr., Sakarya University of Applied Science, Department of Mechanical Engineering, Orcid: 0000-0003-1472-2832
[2] Research Assistant, Sakarya University of Applied Science, Department of Metallurgical and Materials Engineering, Orcid: 0000-0003-4855-4195

advantages, additive manufacturing methods have been widely adopted across a broad range of sectors, including automotive, aerospace, biomedical, defense, and education (Kanishka & Acherjee, 2023).

Additive manufacturing technologies are classified into various categories based on the energy source employed, the type of material used, and the layer formation mechanism (Çerlek & Çobaner, 2025; Yeshiwas et al., 2025). Among these categories, polymer-based manufacturing methods stand out in both academic and industrial applications due to their relatively low cost and high accessibility (Shanmugam et al., 2021). Within polymer-based additive manufacturing technologies, Fused Deposition Modeling (FDM) and Stereolithography (SLA) have emerged as the two most widely used and prominent techniques today (Abbasi et al., 2025; Kafle et al., 2021).

The FDM method is based on the layer-by-layer deposition of thermoplastic filaments extruded through a heated nozzle and is widely preferred by both individual and industrial users due to its simple operating principle, broad material versatility, and low equipment cost (Han et al., 2025; Mazur et al., 2025). In contrast, the SLA method is an additive manufacturing technology that operates on the principle of selectively curing liquid photopolymer resins using a laser or light source, offering high resolution and superior surface quality (Akın et al., 2025). The fundamental differences between the working principles of these two methods directly influence a wide range of parameters, including the mechanical properties, surface quality, dimensional accuracy, and production costs of the fabricated parts (Sofu et al., 2023).

Although FDM and SLA methods have been extensively investigated individually in the literature, studies that address these two techniques from a comparative perspective—particularly in terms of application-oriented selection criteria—remain relatively

limited (Orzeł & Stecuła, 2022). However, from the standpoint of designers and engineers, determining the most suitable additive manufacturing method for a specific application requires the simultaneous evaluation of multidimensional criteria, including mechanical performance, surface quality, post-processing requirements, and cost-effectiveness, rather than relying solely on ease of fabrication (Ren et al., 2022).

In this context, a comparative analysis of FDM and SLA methods is of critical importance for applications such as prototyping, functional part production, and precision-oriented manufacturing (Equbal et al., 2022). Especially in cases involving the fabrication of mechanical test specimens, applications where surface quality is a determining factor, and designs with high geometric complexity, a clear identification of the advantages and limitations of these two methods is essential (Manoj Prabhakar et al., 2021). Moreover, with the rapid advancement of additive manufacturing technologies, the development of next-generation filaments and photopolymer resins has progressively expanded the traditional boundaries of both methods (Saleh Alghamdi et al., 2021).

Within this book chapter, FDM and SLA additive manufacturing methods are examined through a systematic and comparative approach in terms of their working principles, materials employed, processing parameters, mechanical behavior, surface quality, and application areas. The primary objective is to provide readers with a comprehensive perspective on the technical characteristics of these two methods and to contribute to informed method selection for diverse engineering and design applications.

2. FDM (Fused Deposition Modeling)

Working Principle

Fused Deposition Modeling (FDM) is one of the most widely used additive manufacturing technologies and is based on the layer-by-layer deposition of thermoplastic filaments that are melted in a controlled manner (Cano-Vicent et al., 2021; Seçgin et al., 2022). In this process, the polymer material in filament form is fed through a nozzle heated to a predetermined temperature, where it is brought into a semi-molten state and subsequently extruded onto the build platform following toolpaths generated from computer-aided design (CAD) data (Ligon et al., 2017). Upon exposure to ambient conditions, the extruded material rapidly solidifies, forming mechanical and partially thermal bonding with the previously deposited layer (Aniyambeth et al., 2022).

Figure 1 Basic schematic diagram of the operation of a 3D printer by FDM

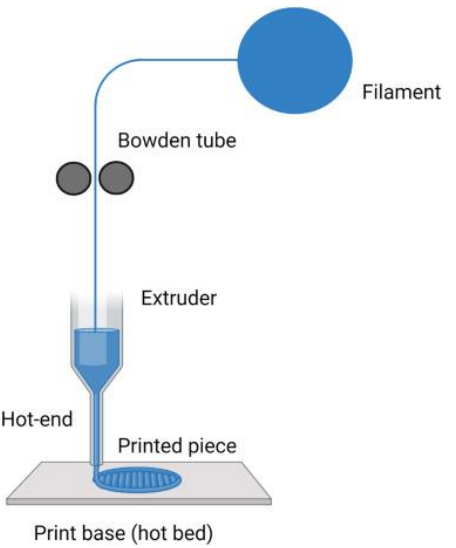

Source: (Cano-Vicent et al., 2021)

In the FDM process, layers are typically formed in the XY plane, while the structure is built up along the Z-axis according to the specified layer thickness (Dey & Yodo, 2019). This manufacturing approach inherently leads to an anisotropic structure, in which the interlayer bonding strength is generally lower than the intralayer strength. As a result, interlayer adhesion represents one of the primary factors directly influencing the mechanical performance of parts fabricated using the FDM method (Levenhagen & Dadmun, 2019).

Materials Used in FDM

The materials used in the FDM method consist predominantly of thermoplastic polymers and their reinforced derivatives (Periyasamy et al., 2023). Thermoplastic materials exhibit suitable processing behavior for the FDM process due to their ability to soften and become flowable when heated and to solidify again upon cooling. This characteristic enables the controlled melting of the material within the nozzle and its subsequent deposition onto the build platform in a layer-by-layer manner (Selvamani et al., 2019).

Among the most commonly used FDM filaments in the literature and industrial practice are polylactic acid (PLA), acrylonitrile butadiene styrene (ABS), polyethylene terephthalate glycol (PETG), and acrylonitrile styrene acrylate (ASA) (Erdaş et al., 2024; Wojnowski et al., 2022; Zisopol et al., 2025). PLA is frequently preferred in applications such as education, visual prototyping, and components with low mechanical requirements due to its biodegradable nature, low printing temperature, and relatively good surface quality. However, the low glass transition temperature of PLA limits its use in applications exposed to elevated operating temperatures (Çerlek, Cobaner, et al., 2024; Plamadiala et al., 2025).

Amorphous thermoplastics such as ABS and ASA offer higher temperature resistance and improved impact strength compared to PLA (Akin et al., 2025; Butt & Bhaskar, 2020). Owing to these properties, they are widely employed in the fabrication of functional parts and components subjected to mechanical loads. Nevertheless, the high thermal shrinkage tendency of these materials during printing may lead to manufacturing challenges such as warping and interlayer delamination. Therefore, the use of enclosed build chambers and controlled cooling conditions is of particular importance when printing with ABS and ASA (Sreejith et al., 2021).

PETG stands out as a material that provides a balanced combination of properties between PLA and ABS (Erdaş et al., 2024; Khan et al., 2023). Its relatively high impact resistance, low warping tendency, and good chemical resistance make it suitable for both prototyping and semi-functional applications. In addition, the more homogeneous material flow exhibited by PETG during printing positively influences interlayer adhesion (Baltić et al., 2024).

For applications requiring higher mechanical performance, nylon (PA), polycarbonate (PC), and fiber-reinforced composite filaments are commonly utilized (Dimitrellou et al., 2024; Yilmaz, 2024). Nylon-based filaments provide high toughness and wear resistance but are sensitive to moisture absorption (Banjo et al., 2022). Polycarbonate filaments offer high temperature resistance and stiffness; however, they require precise control of printing parameters. Carbon- or glass-fiber-reinforced filaments enhance stiffness and specific strength, thereby extending the applicability of FDM-fabricated parts in engineering applications (Kantaros et al., 2023).

In conclusion, material selection in the FDM process should be based not only on mechanical strength criteria but also on multiple parameters such as printing temperature, cooling behavior, dimensional stability, surface quality, and performance under

environmental conditions. Appropriate material selection represents a fundamental factor that directly determines both the process stability during fabrication and the final performance of parts produced using the FDM method. As summarized in Table 1, typical processing temperatures, mechanical strength levels, and surface quality characteristics of common FDM materials vary significantly depending on filament type

Table 1 Typical Properties and Processing Characteristics of Common FDM Materials

Material	Printing Temperature (°C)	Mechanical Strength	Thermal Resistance	Warping Tendency	Surface Quality
PLA	190–220	Moderate	Low	Very low	Good
ABS	220–260	High	Medium–high	High	Moderate
PETG	220–250	Moderate–high	Medium	Low	Moderate–good
ASA	240–260	High	High	Medium	Moderate
PA	240–280	High	Medium	Medium	Moderate
PC	260–300	Very high	Very high	High	Moderate
CF	250–300	Very high	High	Medium	Moderate

Source: (Porima | 3D Yazıcı Filamentleri, 2025)

Process Parameters and Manufacturing Characteristics

The geometric accuracy, surface quality, and mechanical performance of parts produced by the FDM method are directly dependent on a wide range of process parameters controlled throughout fabrication. These parameters govern the flow behavior of the molten thermoplastic material, the quality of interlayer bonding, and the resulting microstructure of the final part. Therefore, the FDM process should be regarded not merely as a fabrication technique but as a multivariable manufacturing system (Bakır et al., 2021; Dey & Yodo, 2019).

Layer thickness is one of the most critical parameters in FDM, as it determines the fundamental trade-off between surface

quality and production time (Figure 2). Reducing the layer thickness contributes to diminished layer lines and improved surface finish; however, it increases the total number of layers and consequently prolongs the printing time. Conversely, thicker layers shorten the production time but may lead to pronounced surface degradation, particularly on inclined surfaces (Bhosale et al., 2022; Nurhidayanti et al., 2025; Syrlybayev et al., 2021).

Figure 2 Schematic and real-view representation of the effect of layer thickness on part surface in the FDM process

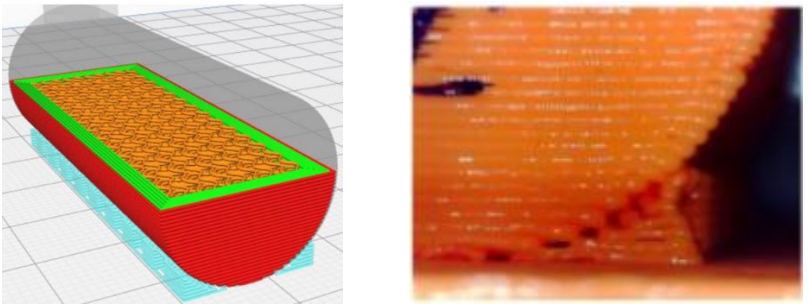

Source: (Kónya, 2024)

Nozzle temperature is a key parameter that governs adequate filament melting and effective interlayer bonding. Insufficient nozzle temperatures may result in poor interlayer adhesion and reduced mechanical strength, whereas excessively high temperatures can cause material degradation, stringing, and dimensional inaccuracies. Accordingly, the nozzle temperature should be selected within an optimal range specific to the filament material used (Gkertzos et al., 2024; Mosleh et al., 2024; Rivera-López et al., 2024; Ulkir et al., 2024).

Printing speed represents another important parameter influencing the balance between production efficiency and part quality. While higher printing speeds reduce manufacturing time, they may adversely affect extrusion stability and layer placement accuracy. Lower printing speeds, on the other hand, promote more

homogeneous material flow and stronger interlayer bonding but at the expense of increased production time (Agarwal et al., 2022; Rafique et al., 2024; Y. Zhao et al., 2022). As shown in Figure 3, lower printing speeds result in more homogeneous and smoother surface finishes, whereas higher printing speeds significantly reduce the total production time but lead to a deterioration in surface quality.

Figure 3 Visual comparison of the effect of printing speed on surface roughness and production time in the FDM process.

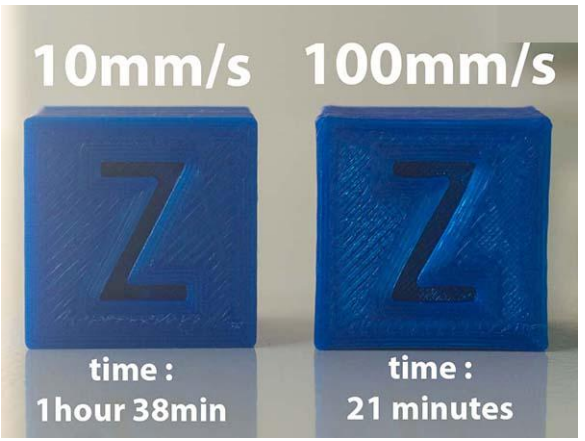

Infill density and infill geometry constitute fundamental structural parameters that determine the mechanical behavior of FDM-fabricated parts. Higher infill densities enhance part stiffness and strength while significantly increasing material consumption and printing time. The selection of infill geometry plays a decisive role in load transfer, energy absorption, and deformation mechanisms. In particular, lattice and periodic infill structures enable the optimization of mechanical performance (Daly et al., 2024; Hozdić & Hozdić, 2024; Qamar Tanveer et al., 2022; B. Yang, 2025). As shown in Figure 4 , both infill pattern and infill density play a critical role in defining the internal structure of FDM-printed components, directly influencing their mechanical behavior, weight, and material consumption.

Figure 4 Visual comparison of different infill patterns and infill densities used in the FDM process

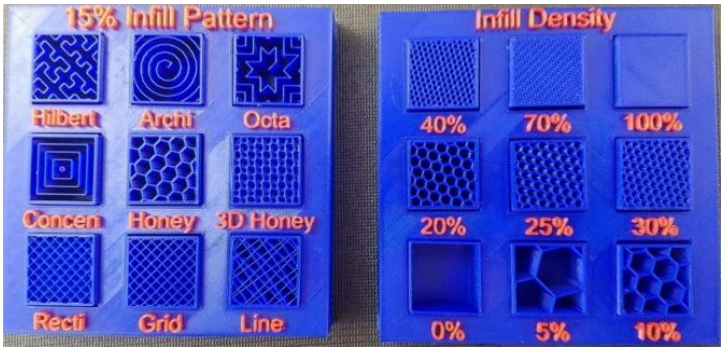

Source: (Qamar Tanveer et al., 2022)

Build orientation and layer arrangement are among the most influential factors responsible for the directional dependence of mechanical properties in FDM-produced components. Higher strength values are generally achieved when loads are applied parallel to the deposited layers, whereas loading perpendicular to the layers typically results in lower mechanical performance due to limited interlayer bonding. This anisotropic behavior leads to pronounced differences in tensile, compressive, and flexural test results depending on the build orientation (Doshi et al., 2022; Lalegani Dezaki & Mohd Ariffin, 2020; Lokesh et al., 2022). Figure 5 demonstrates that both build orientation (flat vs. on-edge) and printing angle play a critical role in determining surface quality and dimensional stability in FDM-manufactured parts.

Figure 5 Effect of build orientation and inclination angle on the geometry and surface characteristics of FDM-printed specimens, produced in flat and on-edge configurations at different angles (0°–90°)

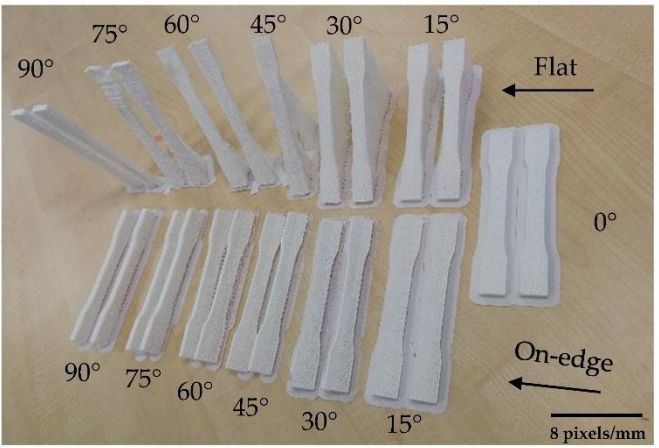

Source: (Lalegani Dezaki & Mohd Ariffin, 2020)

Consequently, when evaluating the mechanical properties of parts fabricated using the FDM method, it is essential to consider process parameters such as build orientation, layer thickness, and nozzle temperature in conjunction with material type and infill density. Optimization of these process parameters enables the FDM method to deliver more reliable and reproducible results for engineering applications.

Advantages of the FDM Method

One of the most significant advantages of the FDM method is its low equipment and material cost. Compared to other additive manufacturing technologies, the installation and operation of FDM systems require relatively modest investment, while the widespread availability of thermoplastic materials in filament form substantially reduces overall production costs. This characteristic enables the extensive use of FDM not only in industrial environments but also

in educational institutions, research laboratories, and small- and medium-sized enterprises (Cano-Vicent et al., 2021; Rahim et al., 2019).

Another major advantage of the FDM method is the wide range of materials it offers. In addition to commonly used thermoplastics such as PLA, ABS, PETG, and ASA, the availability of nylon, polycarbonate, and fiber-reinforced composite filaments allows the method to be adapted to applications with diverse mechanical and environmental requirements. This material versatility supports the use of FDM in both visual prototyping and functional part production (Nekin Joshua & Sakthivel, 2025).

Furthermore, FDM stands out for its suitability in manufacturing large-scale components. Printer systems with relatively simple mechanical architectures allow large build volumes to be achieved at comparatively low cost, which is particularly advantageous for the production of industrial prototypes, enclosures, and structural components. While increasing build volume in many additive manufacturing methods leads to significant rises in cost and process complexity, such increases remain more limited in the case of FDM (Ali et al., 2023).

The ease of use and maintenance associated with FDM represents another key factor contributing to its widespread adoption (Akin et al., 2024). The process is highly observable and controllable, enabling users to make rapid adjustments to printing parameters during fabrication. In addition, the limited need for post-processing operations shortens overall production time and facilitates rapid prototyping cycles (Ahmad et al., 2022; Cano-Vicent et al., 2021).

From a mechanical performance perspective, parts produced using the FDM method can exhibit satisfactory and application-appropriate strength when suitable materials are selected and process

parameters are properly optimized. In particular, informed selection of parameters such as infill density, infill geometry, and build orientation enables FDM-fabricated components to be used not only as visual prototypes but also as load-bearing and functional elements. Consequently, the FDM method can be regarded as a flexible and cost-effective manufacturing alternative for a wide range of engineering applications. Table 2 outlines the key advantages of the FDM method and their practical implications, highlighting its suitability for cost-effective manufacturing, large-scale parts, and mechanically functional applications.

Table 2 Key Advantages of the FDM Method and Their Practical Implications

Advantage Category	Description	Application / Outcome
Low equipment cost	Installation and maintenance costs of FDM printer systems are relatively low	Accessibility for educational institutions and SMEs
Low material cost	Thermoplastics in filament form are more economical compared to photopolymer resins	Cost-effective production and rapid prototyping
Wide material diversity	Availability of PLA, ABS, PETG, ASA, PA, PC, and composite filaments	Adaptability to diverse mechanical and environmental conditions
Suitability for large-scale parts	Large build volumes can be achieved at relatively low cost	Industrial enclosures and structural components
Ease of use	The process is observable and parameters are user-friendly	Rapid learning curve and experimental studies
Limited post-processing requirements	Post-processing operations are generally minimal	Time savings and accelerated prototyping cycles
Mechanical strength potential	Satisfactory strength can be achieved through parameter optimization	Functional and load-bearing components

Design–manufacturing flexibility	Process parameters can be rapidly modified	Iterative design and engineering optimization

Limitations of the FDM Method

Despite its cost-effectiveness and manufacturing flexibility, the FDM method exhibits several inherent limitations arising from its fabrication principle and the physical properties of the materials employed. These limitations may restrict its applicability, particularly in applications requiring high precision, superior surface quality, and isotropic mechanical behavior (Çevik & Kam, 2020; Dey & Yodo, 2019).

One of the most pronounced limitations of FDM is the adverse effect of its layer-by-layer fabrication nature on surface quality. Layer lines formed as a function of nozzle diameter and layer thickness become especially noticeable on inclined surfaces and complex geometries. In regions where support structures are required, surface degradation and support marks are more prominent. Consequently, applications with high aesthetic demands or critical fluid–surface interactions often necessitate additional post-processing operations such as sanding, chemical smoothing, or coating, thereby increasing both production time and cost (Abdulridha et al., 2024; Carta et al., 2025).

Another significant limitation is the restricted interlayer bonding strength, which leads to mechanical anisotropy. Although FDM-fabricated parts generally exhibit high strength within individual layers, the interlayer adhesion strength remains comparatively lower. As a result, mechanical performance decreases markedly under tensile, compressive, or flexural loading applied perpendicular to the layer orientation. This directional dependency represents a critical design constraint, particularly for components subjected to dynamic loads and impact conditions (Uddin et al., 2017; Yu et al., 2022).

Thermal shrinkage and dimensional instability constitute additional limiting factors in the FDM process. In high-temperature thermoplastics such as ABS, ASA, and PC, thermal stresses generated during printing and cooling can induce manufacturing defects including warping, interlayer separation, and geometric deviations. These issues are especially pronounced in large-scale and thin-walled parts, adversely affecting production repeatability and dimensional accuracy (Dilberoglu et al., 2019; Ramian et al., 2021; Sreejith et al., 2021).

Furthermore, the FDM method offers limited resolution for the fabrication of micro-scale features and fine geometrical details. The physical constraints imposed by nozzle diameter and molten material flow restrict the achievable resolution, rendering the method less suitable for applications demanding high detail fidelity. This limitation is particularly relevant in the production of medical, dental, and micro-mechanical components (Dey & Yodo, 2019; Kouassi et al., 2024).

Finally, the strong sensitivity of the FDM process to a wide range of process parameters increases its dependence on user expertise. Inadequate adjustment of parameters such as nozzle temperature, printing speed, cooling conditions, and infill settings can lead to significant variations in part quality. This sensitivity necessitates additional optimization and control efforts, especially in applications requiring standardized and repeatable production.

In summary, while the FDM method offers substantial advantages in terms of rapid prototyping and cost-effective manufacturing, it should not be regarded as a universally sufficient solution for all applications due to its limitations in surface quality, mechanical anisotropy, dimensional stability, and resolution. Therefore, careful consideration of these constraints during the design phase is essential when defining the appropriate application domain for FDM-based manufacturing. The limitations associated

with the FDM process, as outlined in Table 3, play a critical role in determining its suitability for applications requiring high surface quality, isotropic mechanical behavior, and tight dimensional tolerances.

Table 3 Key Limitations of the FDM Method and Their Effects on Part Quality and Applications

Limitation	Source	Effect on Part / Process	Implications for Applications
Low surface quality	Layered manufacturing nature, nozzle diameter	Pronounced layer lines	Additional post-processing required for aesthetic and fluid-contact surfaces
Support marks	Geometries requiring support structures	Surface degradation and roughness	Loss of quality in tight-tolerance regions
Mechanical anisotropy	Limited interlayer bonding	Strength variations depending on load direction	Constraints in applications requiring isotropic behavior
Weak interlayer strength	Insufficient thermal bonding	Risk of fracture under loads perpendicular to layers	Limited use under dynamic and impact loading
Thermal shrinkage (warping)	High-temperature processing filaments	Dimensional deviations and warping	Manufacturing difficulties in large and thin-walled parts
Dimensional instability	Cooling-induced internal stresses	Deviation from geometric tolerances	Increased risk in precision assembly applications
Limited geometric resolution	Nozzle and extrusion constraints	Inability to fabricate micro-scale features	Unsuitability for medical and micro-mechanical applications
Sensitivity to process parameters	Multivariable process nature	Quality fluctuations	Increased need for user experience and parameter optimization

3. SLA (Stereolithography)

Working Principle of the SLA Method

Stereolithography (SLA) is regarded as one of the additive manufacturing technologies capable of delivering the highest surface quality and dimensional accuracy (Mhmood & Al-Karkhi, 2023; Mukhangaliyeva et al., 2023). This method is based on the selective curing of liquid photopolymer resins through exposure to light energy at a specific wavelength. In the SLA process, cross-sectional layers derived from computer-aided design (CAD) data are successively solidified within a resin vat using either a laser beam or a mask-based light source (Çerlek, Kesercioğlu, et al., 2024; Pagac et al., 2021).

In conventional SLA systems, an ultraviolet (UV) laser beam scans the predefined contours on the resin surface, initiating a photopolymerization reaction (Armentia et al., 2022; Huang et al., 2020; Pagac et al., 2021). Figure 6 demonstrates the fundamental working principle of the SLA method, where a focused laser beam selectively cures a photopolymer resin layer by layer. In more recent systems, LCD- or DLP-based light sources are employed to cure an entire layer simultaneously in a single exposure. After each layer is cured, the build platform moves by a predetermined distance to allow the formation of the subsequent layer. This layer-by-layer curing process enables the fabrication of parts with high resolution and smooth surface finish (Chaudhary et al., 2023; Quan et al., 2020; Wu & Song, 2025).

Figure 6 Schematic representation of the laser-based stereolithography (SLA) manufacturing process

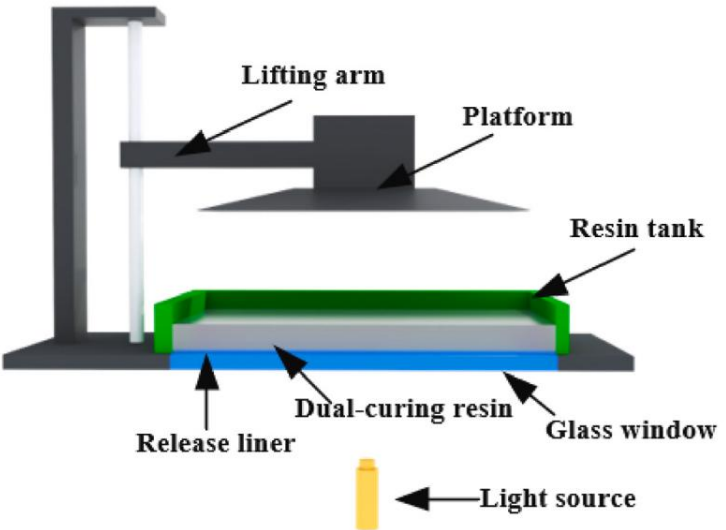

Source: (Wang et al., 2023)

Materials Used in the SLA Method

The materials employed in the SLA method consist primarily of light-sensitive photopolymer resins. These resins undergo polymerization through a photochemical reaction when exposed to light energy at a specific wavelength, transitioning from a liquid to a solid state (Choi et al., 2022; Shi et al., 2021). Unlike the thermoplastic-based FDM method, the curing mechanism in SLA relies on chemical bonding, which directly influences the surface quality and dimensional accuracy of the fabricated parts (Pagac et al., 2021).

SLA resins are classified into different categories based on criteria such as mechanical properties, elastic behavior, thermal resistance, and biocompatibility (Grygier et al., 2024). Standard resins, characterized by low viscosity and high printing stability, are

widely used in applications where visual prototyping, design verification, and geometric accuracy are of primary importance. Although these resins provide excellent surface finish and high detail resolution, they typically exhibit limited mechanical strength and low impact resistance (Pongwisuthiruchte et al., 2022).

ABS-like and tough resins developed for functional applications aim to offer higher toughness and improved impact resistance compared to standard resins. These materials have expanded the applicability of SLA to engineering prototypes and components subjected to low to moderate mechanical loads. Nevertheless, even these reinforced resin types may exhibit a tendency toward brittle fracture under long-term mechanical loading and cyclic stresses (Dias Gonçalves et al., 2024; Golubović et al., 2023; Hozdić, 2024).

Another important class of materials in SLA technology includes flexible and elastomeric resins. These resins exhibit rubber-like behavior with limited deformation capability and are commonly used in applications such as seals, flexible connectors, and ergonomic prototypes. However, their elastic performance is generally more restricted than that of thermoplastic elastomers, and their mechanical stability is highly sensitive to post-curing conditions (Martín-Montal et al., 2021; Rodriguez et al., 2021).

High-temperature-resistant resins constitute another material group that enhances the potential of SLA for engineering applications. Owing to their elevated glass transition temperatures, these resins are suitable for mold masters, casting applications, and prototypes requiring thermal stability. However, increased thermal resistance is often accompanied by higher brittleness and reduced impact strength (Cingesar et al., 2022; Susanto et al., 2025).

In medical and dental applications, biocompatible and certified resins play a prominent role. These resins are formulated to

comply with specific biological standards and are utilized in applications such as surgical planning models, dental molds, and temporary medical devices. The availability of biocompatible resins has significantly increased the relevance of SLA technology in clinical and semi-clinical applications (Guttridge et al., 2022; Melchels et al., 2010; Prakash et al., 2024; Yüceer et al., 2025).

Overall, while SLA resins provide superior surface quality, precision, and detail resolution, their predominantly brittle mechanical behavior represents one of the primary limiting factors defining the application scope of this method. In addition, the mechanical properties of photopolymer resins are highly sensitive to build orientation, exposure parameters, and especially post-print UV curing conditions. Therefore, material selection in SLA should be evaluated holistically, considering not only resin type but also intended service conditions and post-processing requirements. As presented in Table 4, SLA resin types exhibit significantly different mechanical behavior, elasticity, and thermal resistance, which directly influence their suitability for specific applications.

Table 4 Typical Properties and Application Areas of SLA Resin Types

Resin Type	Mechanical Behavior	Elasticity / Toughness	Thermal Resistance	Surface Quality	Typical Applications
Standard resin	Low–moderate strength	Low, brittle	Low	Very high	Visual prototypes, design validation
ABS-like resin	Moderate strength	Moderate	Moderate	High	Engineering prototypes, enclosure parts
Tough (reinforced) resin	Moderate–high strength	Relatively high	Moderate	High	Functional prototypes, impact-loaded parts
Flexible resin	Low strength	High elasticity	Low	High	Flexible joints, seals, ergonomic components

Elastomeric resin	Low–moderate strength	Very high elasticity	Low	High	Rubber-like components, flexible models
High-temperature resin	Moderate strength	Low	High	High	Mold masters, thermally tested parts
Biocompatible resin	Moderate strength	Low–moderate	Moderate	Very high	Medical and dental applications

Process Parameters and Manufacturing Characteristics

In the SLA method, the surface quality, dimensional accuracy, and mechanical performance of fabricated parts are directly dependent on the precise control of process parameters throughout production (Badanova et al., 2022). Unlike the FDM method, SLA relies on a photochemical curing mechanism rather than thermal processing; therefore, the influence of process parameters is primarily manifested through curing depth, polymerization uniformity, and detail resolution (Abbasi et al., 2025).

Layer thickness is one of the most critical parameters governing surface quality and detail resolution in the SLA process. Reduced layer thickness minimizes interlayer boundaries, enabling the production of smooth surfaces and high geometric accuracy. This characteristic makes SLA particularly advantageous for manufacturing components with micro-scale details, thin-walled structures, and geometries requiring tight tolerances. However, decreasing layer thickness significantly increases build time, thereby reducing overall printing efficiency (Badanova et al., 2022; Cotabarren et al., 2019; Sabbah et al., 2021). Figure 7 demonstrates how layer thickness in the SLA process is governed by laser scanning and controlled photopolymerization.

Figure 7 Layer thickness in SLA

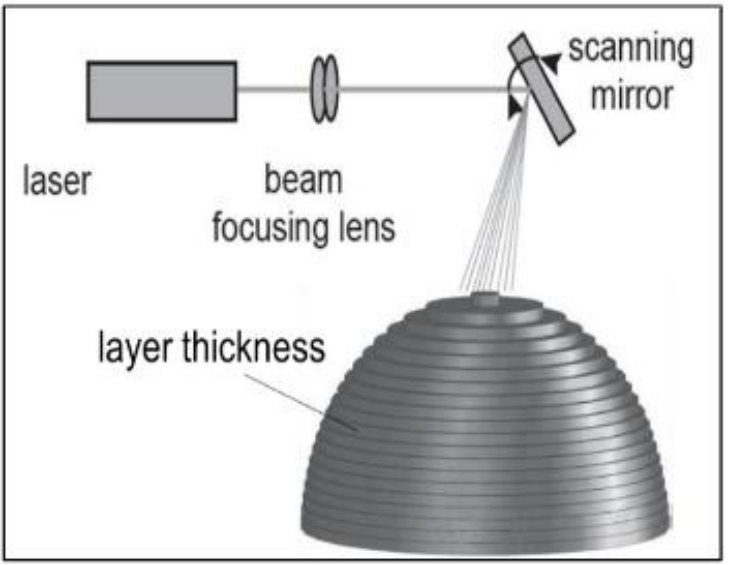

Source: (Mhmood & Al-Karkhi, 2023)

Exposure time and light intensity are key parameters that directly determine curing depth and interlayer bonding quality in SLA. Insufficient exposure may result in incomplete polymerization of the photopolymer resin, leading to weak interlayer adhesion, deformation during printing, or reduced mechanical strength after fabrication. Conversely, excessive exposure can cause over-curing beyond the intended boundaries, resulting in dimensional inaccuracies, corner rounding, and loss of fine details. Consequently, exposure parameters must be carefully optimized according to the specific resin formulation used (Pszczółkowski & Zaborowska, 2025; Valizadeh & Weeger, 2022). The SEM images presented in Figure 8 reveal that finer layer thickness leads to improved surface continuity and reduced micro-scale surface irregularities in SLA-fabricated components.

Figure 8 Micrography opto-SEM mode of SLA-LCD printed samples cured under different exposure times: (a) T2-2 s, (b) T4-4 s, (c) T6-6 s, (d) T8-8 s. All images were acquired at 500× magnification using the same scale bar.

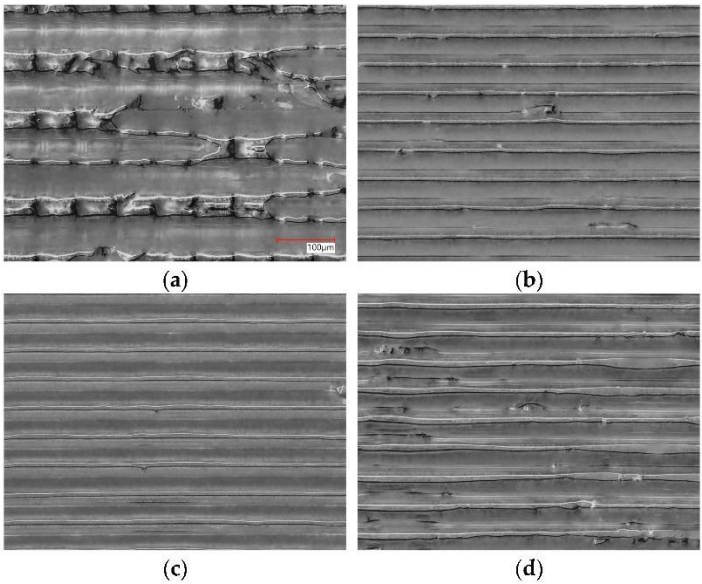

Source: (Pszczółkowski & Zaborowska, 2025)

Build orientation represents another important parameter influencing both surface quality and mechanical behavior of SLA-fabricated parts. Build orientation determines the placement of support structures and the locations of potential surface marks. Although SLA generally yields a more isotropic structure compared to FDM, a limited degree of directional dependence in mechanical properties may still arise due to the layer-by-layer nature of the process. Therefore, build orientation should be selected judiciously to preserve critical surface aesthetics and to optimize load-bearing regions (Li & Teng, 2024; N.-N. Yang et al., 2021). As illustrated in Figure 9, build orientation determines the layer arrangement and the direction of applied loads in SLA-fabricated components.

Figure 9 Build orientation in SLA

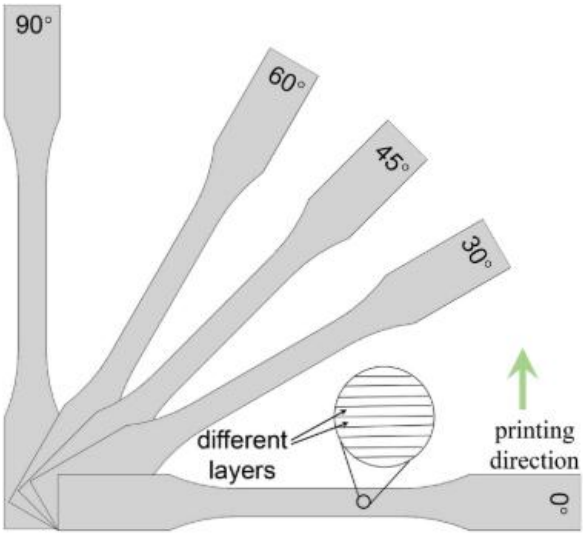

Source: (Li & Teng, 2024)

The configuration of support structures in SLA is a critical design factor that directly affects production success and surface integrity. Insufficient or improperly positioned supports may lead to deformation or print failure, whereas excessive support usage can cause surface damage at contact points and increase post-processing requirements. Accordingly, the number, placement, and contact areas of supports must be optimized in accordance with part geometry (G. Zhao et al., 2015).

A defining characteristic of the SLA method is that post-processing operations constitute an integral part of the manufacturing workflow. After printing, parts are typically washed in isopropyl alcohol to remove uncured resin residues from the surface. Subsequent UV post-curing enables the parts to achieve their final mechanical properties. The duration and intensity of UV exposure play a decisive role in determining hardness, strength, and

long-term mechanical stability. Insufficient post-curing results in reduced mechanical performance, whereas excessive post-curing may increase brittleness (Nowacki et al., 2021).

In conclusion, the SLA process is characterized as a high-precision manufacturing method that requires the simultaneous optimization of layer thickness, exposure parameters, build orientation, support design, and post-processing conditions. Conscious control of these parameters enables the maximization of surface quality, dimensional accuracy, and mechanical performance of parts produced using the SLA technique.

Advantages of the SLA Method

The most prominent and distinguishing advantage of the SLA method is its superior surface quality and high dimensional accuracy. The selective curing of photopolymer resins using light energy minimizes the formation of interlayer boundaries, enabling the production of smooth surfaces and well-defined geometric features. Particularly for components with tight tolerances, SLA offers a significant advantage over conventional additive manufacturing technologies (Mukhtarkhanov et al., 2020).

Another important advantage of SLA is its ability to fabricate complex geometries and micro-scale details with high accuracy. Thin-walled structures, internal cavities, and intricate surface topologies can be produced without deformation due to the high resolution inherent to the SLA process. This capability makes SLA a preferred manufacturing technology, especially in medical, dental, micro-mechanical, and precision engineering applications(Huang et al., 2020).

The surface smoothness of SLA-fabricated parts is often sufficient for direct use without the need for additional surface finishing operations. This characteristic significantly reduces post-processing time and cost, thereby enhancing process efficiency in

applications such as mold masters, visual prototypes, and systems requiring precise assembly. Moreover, the high surface quality renders SLA particularly advantageous for fluid-contact surfaces and optical applications (Golhin et al., 2023).

From a dimensional accuracy standpoint, the SLA method provides high repeatability owing to its fine layer thicknesses and homogeneous curing mechanism. This feature enables the reliable production of series prototypes and comparative test specimens. In addition, laser- and digital mask-based systems employed in SLA ensure high fidelity in transferring CAD data to physical models (Yankov & Nikolova, 2017).

Another notable advantage of SLA is the steadily increasing potential for functional prototyping. With the development of ABS-like, toughened, and high-temperature-resistant resins, SLA has extended beyond purely aesthetic and visual applications and can now be utilized, to a limited extent, for the fabrication of components subjected to mechanical loads. These advancements have broadened the applicability of SLA within engineering design processes (Drechslerová et al., 2023).

In conclusion, owing to its advantages in surface quality, dimensional accuracy, detail resolution, and geometric fidelity, the SLA method represents a powerful additive manufacturing solution for applications requiring high precision. These strengths constitute the primary reasons for the widespread adoption of SLA in aesthetic, medical, and precision engineering domains. Table 5 provides an overview of the key advantages of the SLA method and their practical implications across engineering, medical, and prototyping applications.

Table 5 Key Advantages of the SLA Method and Their Practical Implications

Advantage Category	Description	Application / Outcome
High surface quality	Minimal formation of interlayer boundaries	Direct use without the need for additional surface finishing
High dimensional accuracy	Homogeneous photopolymer curing	Components requiring tight tolerances and precise assembly
Micro-detail fabrication capability	Fine layer thickness and high resolution	Micro-scale and highly complex geometries
Complex geometry fabrication	Stable printing of thin walls and internal cavities	Medical, dental, and precision engineering applications
High repeatability	Digital masking and controlled exposure	Experimental studies and serial prototyping
Low surface roughness	Smooth surface topography	Fluid-contact and aesthetic components
Advanced resin options	ABS-like, tough, and high-temperature resins	Enhanced functional prototyping capability
Superior visual quality	Sharp edges and smooth surfaces	Presentation models and pre-mold components

Limitations of the SLA Method

Despite offering high surface quality and dimensional accuracy, the SLA method exhibits several important limitations arising from both the production process and the intrinsic characteristics of photopolymer materials. These limitations represent key factors that define the applicability of SLA, particularly in functional and long-term engineering applications (Cotabarren et al., 2019; Robles Martinez et al., 2018).

One of the most prominent limitations of SLA is the relatively high cost of photopolymer resins. The unit volume cost of resin-based materials is considerably higher than that of thermoplastic filaments used in FDM. In addition, the limited shelf life of resins and their sensitivity to environmental conditions such

as light, temperature, and humidity increase the risk of material waste, thereby negatively affecting overall production costs. This issue restricts the economic feasibility of SLA, especially in applications requiring large-scale or serial production (Abbasi et al., 2025).

Another significant limitation is the predominantly brittle mechanical behavior of photopolymer resins. Although SLA-fabricated parts may exhibit sufficient strength under short-term static loading, they tend to show brittle failure under long-term mechanical loads, cyclic stresses, or impact conditions. This characteristic substantially limits the use of SLA components in continuously load-bearing, dynamically operating, or impact-resistant applications (Jirků et al., 2023; Riccio et al., 2021).

The mandatory post-processing steps associated with the SLA method constitute another constraint of the production workflow. Washing with isopropyl alcohol and subsequent UV post-curing, which are required after printing, extend production time and demand additional equipment, time, and operator attention. Insufficient post-curing can result in reduced mechanical performance, whereas excessive post-curing may increase brittleness and induce dimensional deviations. Consequently, these post-processing requirements complicate process repeatability and standardization (Harmatys et al., 2025; Nowacki et al., 2021).

The liquid nature of photopolymer resins introduces additional concerns related to occupational safety and environmental conditions. Photopolymer resins may pose potential risks through skin contact or inhalation, necessitating the use of personal protective equipment and controlled working environments. Furthermore, the proper disposal of cleaning solvents and waste resins is essential to ensure environmental sustainability (Abbasi et al., 2025).

Another limitation of the SLA method is the relatively restricted build volume and part size. Systems that provide high precision and resolution typically feature smaller build volumes, which constrains the fabrication of large components and limits the use of SLA primarily to small, detailed, and high-precision parts (Cotabarren et al., 2019).

Finally, the high sensitivity of the SLA process to parameter variations increases its dependence on user expertise. Even minor deviations in exposure time, light intensity, support configuration, or post-processing conditions can lead to significant variations in part quality. This sensitivity necessitates additional monitoring and optimization efforts, particularly in industrial applications requiring standardized and repeatable production processes.

In summary, although the SLA method offers outstanding precision, superior surface quality, and excellent detail resolution, it cannot be considered a universal solution for all applications due to limitations related to cost, mechanical brittleness, post-processing requirements, and occupational safety. Therefore, SLA is most suitable for applications demanding high accuracy and surface quality but not subjected to continuous or high mechanical loading. The key limitations of the SLA method and their implications for manufacturing and applications are summarized in Table 6.

Table 6 Key Limitations of the SLA Method and Their Implications for Manufacturing and Applications

Limitation	Source	Effect on Part / Process	Implications for Applications
High material cost	Unit volume cost of photopolymer resins	Increased production cost	Economic limitations for serial and large-volume production
Limited resin shelf life	Sensitivity of resins to light and environmental conditions	Risk of material waste	Increased inventory management complexity and cost
Mechanical brittleness	Chemical nature of photopolymer structure	Tendency toward fracture under impact and fatigue	Unsuitability for continuous and dynamic loading
Instability under long-term loading	Polymer chain structure	Degradation of mechanical performance over time	Limited use in structural and load-bearing components
Mandatory post-processing	Requirement for washing and UV curing	Extended production time	Increased time and operational costs
Post-processing sensitivity	Dependence on curing duration and conditions	Excessive brittleness or insufficient strength	Repeatability and consistency issues
Occupational safety requirements	Liquid resins and cleaning solvents	Necessity for personal protective equipment	Need for controlled working environments
Environmental concerns	Use of waste resin and solvents	Waste management requirements	Limitations in environmental sustainability
Limited build volume	Design of high-resolution systems	Constraints on large-part fabrication	Use restricted to small and high-precision parts
Sensitivity to process parameters	Exposure and support settings	Quality fluctuations	Increased need for experience and process optimization

4. Comparative Evaluation of FDM and SLA Methods

Among the additive manufacturing techniques widely used today, FDM and SLA exhibit distinct differences in terms of mechanical behavior, surface quality, dimensional accuracy, production workflow, and cost structure, primarily due to their fundamentally different manufacturing principles. While the FDM method is based on the mechanical deposition of molten thermoplastic materials, the SLA method operates through the chemical curing of photopolymer resins using light energy. This fundamental distinction constitutes the underlying source of the respective advantages and limitations associated with each method (Abbasi et al., 2025; Subramani et al., 2025).

A comparative evaluation of FDM and SLA methods should be regarded not merely as a technical comparison but also as an application-oriented decision-making process. In additive manufacturing, it is often impractical to define a single “best” method. Instead, method selection requires the simultaneous consideration of multiple criteria, including the intended function of the part, mechanical loading conditions, surface finish and tolerance requirements, production volume, and cost constraints (Abbasi et al., 2025; Ren et al., 2022; Subramani et al., 2025).

From the perspective of surface quality and dimensional accuracy, the SLA method generally demonstrates superior performance compared to FDM. Owing to its fine layer thicknesses and homogeneous curing mechanism, SLA-fabricated parts exhibit smooth surfaces and high geometric fidelity. In contrast, the FDM method inherently produces more pronounced layer lines as a result of its layer-by-layer deposition nature, which may necessitate additional surface finishing operations, particularly in applications requiring high aesthetic quality or tight tolerances (Mou & Koc, 2019; ÖzdiLli, 2021).

In terms of mechanical performance, the comparison between FDM and SLA is more balanced and context-dependent. Parts produced via FDM can achieve high mechanical strength when appropriate filament materials are selected and process parameters are properly optimized. However, these parts typically exhibit pronounced mechanical anisotropy due to limited interlayer bonding. SLA-fabricated components, on the other hand, generally present a more homogeneous internal structure, yet the inherent brittleness of photopolymer resins often results in limited performance under long-term or dynamic loading conditions (Hozdić, 2024; O'Connor, 2025).

With respect to production workflow and cost, the FDM method is generally characterized as a more economical and user-friendly solution. Lower equipment and material costs, limited post-processing requirements, and relatively large build volumes make FDM particularly attractive for rapid prototyping and functional part fabrication. Conversely, the SLA method involves higher material costs and mandatory post-processing steps, leading to increased production time and operational complexity. Nevertheless, the superior surface quality and dimensional precision achieved with SLA often justify these additional costs in many applications (Abbasi et al., 2025; Subramani et al., 2025).

The comparative assessment presented in this section indicates that FDM and SLA methods should be regarded as complementary rather than competing technologies, each addressing different application requirements. FDM emerges as a more suitable option in applications where mechanical strength, production volume, and cost-effectiveness are prioritized, whereas SLA is preferred in applications demanding high surface quality, fine detail resolution, and superior dimensional accuracy. Consequently, method selection in additive manufacturing necessitates a holistic evaluation of application-specific requirements alongside the

technical characteristics of the available processes. Table 7 provides a synthesis comparison of FDM and SLA methods, highlighting their respective advantages and limitations to support application-oriented method selection.

Table 7 Synthesis Comparison of FDM and SLA Methods in Terms of Advantages and Limitations

Evaluation Criterion	FDM	SLA
Surface quality	Moderate	Very high
Dimensional accuracy	Moderate	High
Micro-detail fabrication	Limited	Excellent
Mechanical strength potential	High (with appropriate materials)	Moderate
Mechanical behavior	Anisotropic	More isotropic but brittle
Large-part fabrication	Suitable	Limited
Material cost	Low	High
Equipment cost	Low–moderate	Moderate–high
Post-processing requirements	Low	Mandatory and time-consuming
Production speed (same build volume)	Relatively fast	Relatively slow
Occupational safety requirements	Low	High (resins and solvents)
Process stability	Moderate	High but parameter-sensitive
Ease of use	High	Moderate
Primary limiting factor	Surface quality and anisotropy	Cost and mechanical brittleness

Table 8 summarizes a decision matrix that links common application requirements with the most appropriate additive manufacturing method. The comparison demonstrates that FDM is generally preferred for cost-sensitive, large-scale, and mechanically functional applications due to its material versatility and production efficiency. In contrast, SLA is better suited for applications demanding high surface quality, fine geometric detail, and dimensional accuracy, such as aesthetic prototypes, medical models,

and precision assemblies. Overall, the table provides a clear, application-oriented guideline to facilitate informed method selection in design, prototyping, and manufacturing processes.

Table 8 "Which Method for Which Application?" Decision Matrix

Application / Requirement	Preferred Method	Rationale
Rapid prototyping	FDM	Low cost and short production time
Functional part manufacturing	FDM	Higher potential mechanical strength
Large-volume parts	FDM	Large build volume and cost-effective production
Aesthetic prototypes	SLA	Superior surface quality
Micro-detailed components	SLA	High resolution and dimensional accuracy
Medical / dental models	SLA	Biocompatible resins and geometric precision
Pre-mold (tooling) models	SLA	Smooth surfaces and dimensional accuracy
Educational use	FDM	Safe, economical, and user-friendly
Parts requiring precise assembly	SLA	Suitability for tight tolerances
Components under continuous mechanical load	FDM	More suitable compared to the brittle nature of SLA
Low-budget projects	FDM	Lower material and operating costs
Presentation models requiring high visual quality	SLA	Superior visual appearance and surface finish

Table 9 summarizes the fundamental differences between FDM and SLA in terms of their working principles and structural characteristics. As shown, FDM exhibits an anisotropic internal structure due to its mechanically deposited material buildup, whereas SLA provides a more homogeneous structure as a result of its chemical photopolymerization mechanism. These structural differences play a decisive role in explaining the variations in

mechanical behavior, surface quality, and application domains of the two methods.

Table 9 Comparison of FDM and SLA Methods in Terms of Working Principles and Structural Characteristics

Comparison Criterion	FDM	SLA
Material used	Thermoplastic filament	Liquid photopolymer resin
Layer formation mechanism	Mechanical deposition of molten material	Chemical curing induced by light energy
Interlayer bonding	Thermal fusion and mechanical interlocking	Chemical bonding via photopolymerization
Internal structure characteristic	Relatively heterogeneous	More homogeneous
Mechanical structure	Pronounced anisotropy	Relatively isotropic but brittle
Layer boundaries	Clearly distinguishable	Minimal
Microstructural continuity	Limited	High
Structural design flexibility	High (control of infill and internal architecture)	Limited

Table 10 provides a direct comparison of FDM and SLA with respect to surface quality, dimensional accuracy, and mechanical performance. While SLA offers superior surface finish and geometric precision, FDM demonstrates a higher potential for mechanical strength when appropriate materials and process parameters are employed. Consequently, method selection should be guided by the relative importance of surface quality, tolerance requirements, mechanical performance, and cost constraints of the intended application.

Table 10 Comparison of FDM and SLA Methods in Terms of Surface Quality, Dimensional Accuracy, and Mechanical Performance

Evaluation Criterion	FDM	SLA
Surface quality	Moderate; visible layer lines, especially on inclined and curved surfaces	Very high; smooth surfaces with sharp edge definition
Visibility of layer boundaries	Clearly visible	Minimal
Micro-detail fabrication capability	Limited; constrained by nozzle diameter and material flow	Excellent; fine features and thin walls can be produced accurately
Dimensional accuracy	Moderate; sensitive to thermal shrinkage and flow instability	High; homogeneous curing and digital control
Repeatability	Moderate	High
Thermal effects	Cooling and residual stresses may cause dimensional deviations	Thermal effects are limited; photochemical curing dominates
Mechanical strength potential	High (with appropriate material and parameter optimization)	Moderate
Mechanical behavior	Strongly anisotropic	More isotropic but generally brittle
Performance under long-term / dynamic loading	More suitable	Limited
Post-processing requirements	Limited; mainly support removal and optional surface finishing	Mandatory; washing and UV post-curing are required

Table 11 presents a concise synthesis of the fundamental differences between FDM and SLA methods. The comparison highlights the inherent trade-offs between material extrusion–based and photopolymerization-based additive manufacturing processes in terms of surface quality, dimensional accuracy, mechanical behavior, cost structure, and post-processing requirements. While FDM offers advantages in mechanical strength potential, material cost, and production of functional components, SLA stands out for its superior

surface quality and high dimensional precision. Accordingly, this table serves as a practical reference to support application-oriented method selection in engineering design and manufacturing.

Table 11 General Comparison of FDM and SLA Additive Manufacturing Methods

Criterion	FDM	SLA
Working principle	Thermoplastic extrusion	Photopolymer curing
Surface quality	Moderate	Very high
Dimensional accuracy	Moderate	High
Mechanical strength	High (with appropriate material selection)	Moderate
Mechanical behavior	Anisotropic	Relatively isotropic but brittle
Material cost	Low	High
Post-processing	Limited	Mandatory
Typical application domain	Functional parts	Precision and aesthetic parts

5. Conclusion and Future Perspectives

This chapter has presented a comprehensive and comparative evaluation of Fused Deposition Modeling (FDM) and Stereolithography (SLA), two of the most widely adopted polymer-based additive manufacturing technologies. By systematically examining their working principles, material characteristics, process parameters, mechanical behavior, surface quality, dimensional accuracy, and application domains, the chapter has aimed to provide

an application-oriented framework for informed method selection in engineering design and manufacturing.

The analysis clearly demonstrates that the fundamental differences between FDM and SLA originate from their distinct material deposition and solidification mechanisms. FDM relies on the mechanical extrusion and solidification of thermoplastic filaments, resulting in pronounced anisotropy, relatively lower surface quality, and high flexibility in internal structural design. In contrast, SLA is based on the photochemical curing of liquid resins, enabling superior surface finish, high dimensional accuracy, and improved microstructural continuity, albeit at the expense of higher material cost, mandatory post-processing, and limited long-term mechanical robustness.

From a performance perspective, neither method can be universally regarded as superior. Instead, their suitability is highly dependent on application-specific requirements. FDM emerges as a more favorable option for cost-sensitive applications, functional prototyping, and components subjected to continuous or moderate mechanical loading, where material versatility and mechanical strength potential are prioritized. Conversely, SLA is particularly advantageous for applications demanding high surface quality, fine geometric detail, and tight dimensional tolerances, such as aesthetic prototypes, medical and dental models, and precision assemblies.

The comparative tables and decision matrices presented in this chapter reinforce the notion that additive manufacturing method selection should not be driven solely by fabrication convenience or surface quality considerations. Rather, it requires a holistic evaluation of mechanical performance expectations, surface and tolerance requirements, production volume, post-processing constraints, and economic factors. In this regard, FDM and SLA should be viewed as complementary technologies that can be

strategically combined within hybrid manufacturing workflows to exploit their respective strengths.

Looking toward future developments, several emerging trends are expected to further reshape the capabilities and application boundaries of both methods. In the context of FDM, ongoing advancements in high-performance thermoplastics, fiber-reinforced filaments, and controlled thermal environments are likely to reduce mechanical anisotropy and improve dimensional stability. The integration of lattice optimization, functionally graded infill structures, and data-driven process optimization techniques is expected to significantly enhance the structural efficiency of FDM-fabricated components.

For SLA, future progress is anticipated primarily in material innovation. The development of tougher, more fatigue-resistant, and less brittle photopolymer resins has the potential to expand the use of SLA into more demanding functional applications. Additionally, improvements in post-curing strategies, resin recyclability, and occupational safety practices are expected to mitigate some of the current limitations associated with cost, brittleness, and environmental concerns. Larger build volumes and faster exposure systems may also increase the scalability of SLA for industrial applications.

From a broader perspective, the convergence of additive manufacturing with digital design tools, simulation-based optimization, and artificial intelligence–driven process control is expected to transform both FDM and SLA into more predictable, repeatable, and performance-oriented manufacturing solutions. In this evolving landscape, the role of engineers and designers will increasingly shift from simple method selection toward the strategic integration of multiple additive manufacturing technologies within a single product development cycle.

In conclusion, FDM and SLA represent two fundamentally different yet complementary approaches within polymer-based additive manufacturing. A clear understanding of their respective advantages, limitations, and future trajectories is essential for achieving optimal design, performance, and cost efficiency. The comparative framework presented in this chapter is intended to support such informed decision-making and to serve as a reference for both current applications and future research in additive manufacturing technologies.

References

Abbasi, M., Váz, P., Silva, J., & Martins, P. (2025). Head-to-Head Evaluation of FDM and SLA in Additive Manufacturing: Performance, Cost, and Environmental Perspectives. *Applied Sciences*, *15*(4), 2245. https://doi.org/10.3390/app15042245

Abdulridha, H. H., Abbas, T. F., & Bedan, A. S. (2024). Investigate the Effect of Chemical Post Processing on the Surface Roughness of Fused Deposition Modeling Printed Parts. *Advances in Science and Technology Research Journal*, *18*(2), 47–60. https://doi.org/10.12913/22998624/183528

Agarwal, K. M., Shubham, P., Bhatia, D., Sharma, P., Vaid, H., & Vajpeyi, R. (2022). Analyzing the Impact of Print Parameters on Dimensional Variation of ABS specimens printed using Fused Deposition Modelling (FDM). *Sensors International*, *3*, 100149. https://doi.org/10.1016/j.sintl.2021.100149

Ahmad, N. N., Wong, Y. H., & Ghazali, N. N. N. (2022). A systematic review of fused deposition modeling process parameters. *Soft Science*, *2*(3), 11. https://doi.org/10.20517/ss.2022.08

Akin, Y., Han, K., Çerlek, Ö., & Seçgin, Ö. (2025). Impact of Epoxy Infill on the Mechanical Strength of ABS Specimens Produced by Fused Filament Fabrication. *Arabian Journal*

for Science and Engineering. https://doi.org/10.1007/s13369-025-10341-4

Akin, Y., Han, K., & Kılıç, R. (2024). *Impact of Parameters on Final Products in Fused Filament Fabrication (FFF) Technology: An Overview*.

Akın, Y., Han, K., Tüylü, A., Aktaş, N. F., Çobaner, S., Çerlek, Ö., Kesercioğlu, M. A., Kılıç, R., & Seçgin, Ö. (2025). Compressive strength and performance of horizontally and vertically oriented hybrid lattice structures manufactured by stereolithography. *Proceedings of the Institution of Mechanical Engineers, Part E: Journal of Process Mechanical Engineering*, 09544089251400793. https://doi.org/10.1177/09544089251400793

Ali, Md. H., Kurokawa, S., Shehab, E., & Mukhtarkhanov, M. (2023). Development of a large-scale multi-extrusion FDM printer, and its challenges. *International Journal of Lightweight Materials and Manufacture*, *6*(2), 198–213. https://doi.org/10.1016/j.ijlmm.2022.10.001

Aniyambeth, S., Malekar, D., & Özel, T. (2022). Physics-Based Filament Adhesion Modeling in Fused Filament Fabrication. *Volume 2A: Advanced Manufacturing*, V02AT02A027. https://doi.org/10.1115/IMECE2022-96486

Armentia, S. L. D., Fernández-Villamarín, S., Ballesteros, Y., C. Del Real, J., Dunne, N., & Paz, E. (2022). 3D Printing of a Graphene-Modified Photopolymer Using Stereolithography for Biomedical Applications: A Study of the Polymerization Reaction. *International Journal of Bioprinting*, *8*(1), 503. https://doi.org/10.18063/ijb.v8i1.503

B.A, P., N, L., Buradi, A., N, S., B L, P., & R, V. (2022). A comprehensive review of emerging additive manufacturing (3D printing technology): Methods, materials, applications, challenges, trends and future potential. *Materials Today: Proceedings*, *52*, 1309–1313. https://doi.org/10.1016/j.matpr.2021.11.059

Badanova, N., Perveen, A., & Talamona, D. (2022). Study of SLA Printing Parameters Affecting the Dimensional Accuracy of the Pattern and Casting in Rapid Investment Casting. *Journal of Manufacturing and Materials Processing*, *6*(5), 109. https://doi.org/10.3390/jmmp6050109

Bahnini, I., Rivette, M., Rechia, A., Siadat, A., & Elmesbahi, A. (2018). Additive manufacturing technology: The status, applications, and prospects. *The International Journal of Advanced Manufacturing Technology*, *97*(1–4), 147–161. https://doi.org/10.1007/s00170-018-1932-y

Bakır, A. A., Atik, R., & Özerinç, S. (2021). Mechanical properties of thermoplastic parts produced by fused deposition modeling:a review. *Rapid Prototyping Journal*, *27*(3), 537–561. https://doi.org/10.1108/RPJ-03-2020-0061

Baltić, M. Z., Vasić, M. R., Vorkapić, M. D., Bajić, D. M., Piteľ, J., Svoboda, P., & Vencl, A. (2024). PETG as an Alternative Material for the Production of Drone Spare Parts. *Polymers*, *16*(21), 2976. https://doi.org/10.3390/polym16212976

Banjo, A. D., Agrawal, V., Auad, M. L., & Celestine, A.-D. N. (2022). Moisture-induced changes in the mechanical behavior of 3D printed polymers. *Composites Part C: Open Access*, *7*, 100243. https://doi.org/10.1016/j.jcomc.2022.100243

Bhosale, V., Gaikwad, P., Dhere, S., Sutar, C., & Raykar, S. J. (2022). Analysis of process parameters of 3D printing for surface finish, printing time and tensile strength. *Materials Today: Proceedings*, *59*, 841–846. https://doi.org/10.1016/j.matpr.2022.01.210

Butt, J., & Bhaskar, R. (2020). Investigating the Effects of Annealing on the Mechanical Properties of FFF-Printed Thermoplastics. *Journal of Manufacturing and Materials Processing*, *4*(2), 38. https://doi.org/10.3390/jmmp4020038

Cano-Vicent, A., Tambuwala, M. M., Hassan, Sk. S., Barh, D., Aljabali, A. A. A., Birkett, M., Arjunan, A., & Serrano-Aroca, Á. (2021). Fused deposition modelling: Current status, methodology, applications and future prospects. *Additive Manufacturing*, *47*, 102378. https://doi.org/10.1016/j.addma.2021.102378

Carta, M., Loi, G., El Mehtedi, M., Buonadonna, P., & Aymerich, F. (2025). Improving Surface Roughness of FDM-Printed Parts Through CNC Machining: A Brief Review. *Journal of Composites Science*, *9*(6), 296. https://doi.org/10.3390/jcs9060296

Çerlek, Ö., & Çobaner, S. (2025). Selective Laser Sintering (SLS): A High Precision Additive Manufacturing Process. *All Science Academy*.

Çerlek, Ö., Cobaner, S., & Akin, Y. (2024). *AN EXPERIMENTAL ANALYSIS OF THE FACTORS INFLUENCING THE TENSILE STRENGTH OF PLA PARTS MANUFACTURED WITH 3D PRINTING USING FDM TECHNIQUE*.

Çerlek, Ö., Han, K., Akin, Y., & Seçgin, Ö. (2025). Experimental Investigation of Parameters Affecting the Tensile Strength of Silicone-Filled 3D Printed ABS Products. *Journal of Materials Engineering and Performance*, *34*(11), 9627–9636. https://doi.org/10.1007/s11665-024-10498-3

Çerlek, Ö., Kesercioğlu, M. A., & Han, K. (2024). *Stereolithography(SLA): An Innovative Additive Manufacturing Process* (pp. 399–413). New trends and frontiers in engineering.

Çevik, Ü., & Kam, M. (2020). A Review Study on Mechanical Properties of Obtained Products by FDM Method and Metal/Polymer Composite Filament Production. *Journal of Nanomaterials*, *2020*, 1–9. https://doi.org/10.1155/2020/6187149

Chaudhary, R., Fabbri, P., Leoni, E., Mazzanti, F., Akbari, R., & Antonini, C. (2023). Additive manufacturing by digital light processing: A review. *Progress in Additive Manufacturing*, *8*(2), 331–351. https://doi.org/10.1007/s40964-022-00336-0

Choi, Y., Yoon, J., Kim, J., Lee, C., Oh, J., & Cho, N. (2022). Development of Bisphenol-A-Glycidyl-Methacrylate- and Trimethylolpropane-Triacrylate-Based Stereolithography 3D Printing Materials. *Polymers*, *14*(23), 5198. https://doi.org/10.3390/polym14235198

Cingesar, I. K., Marković, M.-P., & Vrsaljko, D. (2022). Effect of post-processing conditions on polyacrylate materials used in stereolithography. *Additive Manufacturing*, *55*, 102813. https://doi.org/10.1016/j.addma.2022.102813

Cotabarren, I., Palla, C. A., McCue, C. T., & Hart, A. J. (2019). An assessment of the dimensional accuracy and geometry-resolution limit of desktop stereolithography using response surface methodology. *Rapid Prototyping Journal*, *25*(7), 1169–1186. https://doi.org/10.1108/RPJ-03-2019-0060

Daly, M., Tarfaoui, M., Bouali, M., & Bendarma, A. (2024). Effects of Infill Density and Pattern on the Tensile Mechanical Behavior of 3D-Printed Glycolyzed Polyethylene Terephthalate Reinforced with Carbon-Fiber Composites by the FDM Process. *Journal of Composites Science*, *8*(4), 115. https://doi.org/10.3390/jcs8040115

Dey, A., & Yodo, N. (2019). A Systematic Survey of FDM Process Parameter Optimization and Their Influence on Part Characteristics. *Journal of Manufacturing and Materials Processing*, *3*(3), 64. https://doi.org/10.3390/jmmp3030064

Dias Gonçalves, V. P., Vieira, C. M. F., Simonassi, N. T., Perissé Duarte Lopes, F., Youssef, G., & Colorado, H. A. (2024). Evaluation of Mechanical Properties of ABS-like Resin for Stereolithography Versus ABS for Fused Deposition Modeling in Three-Dimensional Printing Applications for

Odontology. *Polymers*, *16*(20), 2921. https://doi.org/10.3390/polym16202921

Dilberoglu, U. M., Simsek, S., & Yaman, U. (2019). Shrinkage compensation approach proposed for ABS material in FDM process. *Materials and Manufacturing Processes*, *34*(9), 993–998. https://doi.org/10.1080/10426914.2019.1594252

Dimitrellou, S., Iakovidis, I., & Psarianos, D.-R. (2024). Mechanical Characterization of Polylactic Acid, Polycarbonate, and Carbon Fiber-Reinforced Polyamide Specimens Fabricated by Fused Deposition Modeling. *Journal of Materials Engineering and Performance*, *33*(7), 3613–3626. https://doi.org/10.1007/s11665-024-09144-9

Doshi, M., Mahale, A., Kumar Singh, S., & Deshmukh, S. (2022). Printing parameters and materials affecting mechanical properties of FDM-3D printed Parts: Perspective and prospects. *Materials Today: Proceedings*, *50*, 2269–2275. https://doi.org/10.1016/j.matpr.2021.10.003

Drechslerová, V., Neuhäuserová, M., Falta, J., Šleichrt, J., & Kytýř, D. (2023). Stereolithography for manufacturing of advanced porous solids. *Acta Polytechnica CTU Proceedings*, *41*, 1–7. https://doi.org/10.14311/APP.2023.41.0001

Equbal, A., Israr Equbal, Md., Badruddin, I. A., & Algahtani, A. (2022). A critical insight into the use of FDM for production of EDM electrode. *Alexandria Engineering Journal*, *61*(5), 4057–4066. https://doi.org/10.1016/j.aej.2021.09.033

Erdaş, M. U., Yıldız, B. S., & Yıldız, A. R. (2024). Experimental analysis of the effects of different production directions on the mechanical characteristics of ABS, PLA, and PETG materials produced by FDM. *Materials Testing*, *66*(2), 198–206. https://doi.org/10.1515/mt-2023-0206

Gkertzos, P., Kotzakolios, A., Mantzouranis, G., & Kostopoulos, V. (2024). Nozzle temperature calibration in 3D printing. *International Journal on Interactive Design and*

Manufacturing (IJIDeM), *18*(2), 879–899. https://doi.org/10.1007/s12008-023-01681-2

Golhin, A. P., Tonello, R., Frisvad, J. R., Grammatikos, S., & Strandlie, A. (2023). Surface roughness of as-printed polymers: A comprehensive review. *The International Journal of Advanced Manufacturing Technology*, *127*(3–4), 987–1043. https://doi.org/10.1007/s00170-023-11566-z

Golubović, Z., Danilov, I., Bojović, B., Petrov, L., Sedmak, A., Mišković, Ž., & Mitrović, N. (2023). A Comprehensive Mechanical Examination of ABS and ABS-like Polymers Additively Manufactured by Material Extrusion and Vat Photopolymerization Processes. *Polymers*, *15*(21), 4197. https://doi.org/10.3390/polym15214197

Grygier, D., Kurzawa, A., Stachowicz, M., Krawiec, K., Stępczak, M., Roszak, M., Kazimierczak, M., Aniszewska, D., & Pyka, D. (2024). Investigations into the Material Characteristics of Selected Plastics Manufactured Using SLA-Type Additive Methods. *Polymers*, *16*(11), 1607. https://doi.org/10.3390/polym16111607

Guttridge, C., Shannon, A., O'Sullivan, A., O'Sullivan, K. J., & O'Sullivan, L. W. (2022). Biocompatible 3D printing resins for medical applications: A review of marketed intended use, biocompatibility certification, and post-processing guidance. *Annals of 3D Printed Medicine*, *5*, 100044. https://doi.org/10.1016/j.stlm.2021.100044

Han, K., Kesercioğlu, M. A., Akın, Y., Çay, Y., & Tanyeri, B. (2025). Effect of Elastomer Filling on the Tensile, Compressive, and Flexural Strength of Cross-Lattice Structured Acrylonitrile Styrene Acrylate Specimens Fabricated via Fused Filament Fabrication. *Journal of Materials Engineering and Performance*, *34*(24), 30499–30509. https://doi.org/10.1007/s11665-025-11562-2

Harmatys, W., Gąska, A., Gąska, P., & Gruza, M. (2025). Identification of the Influence of IPA Rinsing Times on

Surface Roughness of SLA-Printed Parts Made of Different Materials. *Materials*, *18*(9), 2082. https://doi.org/10.3390/ma18092082

Hozdić, E. (2024). Characterization and Comparative Analysis of Mechanical Parameters of FDM- and SLA-Printed ABS Materials. *Applied Sciences*, *14*(2), 649. https://doi.org/10.3390/app14020649

Hozdić, E., & Hozdić, E. (2024). Influence of Infill Structure Shape and Density on theMechanical Properties of FDM 3D-Printed PETG andPETG+CF Materials. *Advanced Technologies & Materials*, *49*(2), 15–27. https://doi.org/10.24867/ATM-2024-2-002

Huang, J., Qin, Q., & Wang, J. (2020). A Review of Stereolithography: Processes and Systems. *Processes*, *8*(9), 1138. https://doi.org/10.3390/pr8091138

Jirků, P., Urban, J., Müller, M., Kolář, V., Chandan, V., Svobodová, J., Mishra, R. K., & Jamshaid, H. (2023). Evaluation of Mechanical Properties and Filler Interaction in the Field of SLA Polymeric Additive Manufacturing. *Materials*, *16*(14), 4955. https://doi.org/10.3390/ma16144955

Kafle, A., Luis, E., Silwal, R., Pan, H. M., Shrestha, P. L., & Bastola, A. K. (2021). 3D/4D Printing of Polymers: Fused Deposition Modelling (FDM), Selective Laser Sintering (SLS), and Stereolithography (SLA). *Polymers*, *13*(18), 3101. https://doi.org/10.3390/polym13183101

Kanishka, K., & Acherjee, B. (2023). Revolutionizing manufacturing: A comprehensive overview of additive manufacturing processes, materials, developments, and challenges. *Journal of Manufacturing Processes*, *107*, 574–619. https://doi.org/10.1016/j.jmapro.2023.10.024

Kantaros, A., Soulis, E., Petrescu, F. I. T., & Ganetsos, T. (2023). Advanced Composite Materials Utilized in FDM/FFF 3D Printing Manufacturing Processes: The Case of Filled

Filaments. *Materials*, *16*(18), 6210. https://doi.org/10.3390/ma16186210

Khan, I., Tariq, M., Abas, M., Shakeel, M., Hira, F., Al Rashid, A., & Koç, M. (2023). Parametric investigation and optimisation of mechanical properties of thick tri-material based composite of PLA-PETG-ABS 3D-printed using fused filament fabrication. *Composites Part C: Open Access*, *12*, 100392. https://doi.org/10.1016/j.jcomc.2023.100392

Kónya, G. (2024). Investigating the Impact of Productivity on Surface Roughness and Dimensional Accuracy in FDM 3D Printing. *Periodica Polytechnica Transportation Engineering*, *52*(2), 128–133. https://doi.org/10.3311/PPtr.22952

Kouassi, M., Kallel, A., Abdallah, A. B., Nouira, S., Ballut, S., Fitoussi, J., & Shirinbayan, M. (2024). Assessment of fused deposition modeling (FDM) parameters for fabrication of solid and hollow microneedles using polylactic acid (PLA). *Polymers for Advanced Technologies*, *35*(8), e6548. https://doi.org/10.1002/pat.6548

Lalegani Dezaki, M., & Mohd Ariffin, M. K. A. (2020). The Effects of Combined Infill Patterns on Mechanical Properties in FDM Process. *Polymers*, *12*(12), 2792. https://doi.org/10.3390/polym12122792

Levenhagen, N. P., & Dadmun, M. D. (2019). Improving Interlayer Adhesion in 3D Printing with Surface Segregating Additives: Improving the Isotropy of Acrylonitrile–Butadiene–Styrene Parts. *ACS Applied Polymer Materials*, *1*(4), 876–884. https://doi.org/10.1021/acsapm.9b00051

Li, Y., & Teng, Z. (2024). Effect of printing orientation on mechanical properties of SLA 3D-printed photopolymer. *Fatigue & Fracture of Engineering Materials & Structures*, *47*(5), 1531–1545. https://doi.org/10.1111/ffe.14265

Ligon, S. C., Liska, R., Stampfl, J., Gurr, M., & Mülhaupt, R. (2017). Polymers for 3D Printing and Customized Additive Manufacturing. *Chemical Reviews*, *117*(15), 10212–10290. https://doi.org/10.1021/acs.chemrev.7b00074

Lokesh, N., Praveena, B. A., Sudheer Reddy, J., Vasu, V. K., & Vijaykumar, S. (2022). Evaluation on effect of printing process parameter through Taguchi approach on mechanical properties of 3D printed PLA specimens using FDM at constant printing temperature. *Materials Today: Proceedings*, *52*, 1288–1293. https://doi.org/10.1016/j.matpr.2021.11.054

Manoj Prabhakar, M., Saravanan, A. K., Haiter Lenin, A., Jerin Leno, I., Mayandi, K., & Sethu Ramalingam, P. (2021). A short review on 3D printing methods, process parameters and materials. *Materials Today: Proceedings*, *45*, 6108–6114. https://doi.org/10.1016/j.matpr.2020.10.225

Martín-Montal, J., Pernas-Sánchez, J., & Varas, D. (2021). Experimental Characterization Framework for SLA Additive Manufacturing Materials. *Polymers*, *13*(7), 1147. https://doi.org/10.3390/polym13071147

Mazur, J., Sobczak, P., Panasiewicz, M., Łusiak, P., Krajewska, M., Findura, P., Obidziński, S., & Żukiewicz-Sobczak, W. (2025). Mechanical properties and biodegradability of samples obtained by 3D printing using FDM technology from PLA filament with by-products. *Scientific Reports*, *15*(1), 5847. https://doi.org/10.1038/s41598-025-89984-0

Melchels, F. P. W., Feijen, J., & Grijpma, D. W. (2010). A review on stereolithography and its applications in biomedical engineering. *Biomaterials*, *31*(24), 6121–6130. https://doi.org/10.1016/j.biomaterials.2010.04.050

Mhmood, T. R., & Al-Karkhi, N. K. (2023). A Review of the Stereo lithography 3D Printing Process and the Effect of Parameters on Quality. *Al-Khwarizmi Engineering Journal*, *19*(2), 82–94. https://doi.org/10.22153/kej.2023.04.003

Mosleh, N., Esfandeh, M., & Dariushi, S. (2024). Simulation of temperature profile in fused filament fabrication 3D printing method. *Rapid Prototyping Journal*, *30*(1), 134–144. https://doi.org/10.1108/RPJ-02-2023-0067

Mou, Y. A., & Koc, M. (2019). Dimensional capability of selected 3DP technologies. *Rapid Prototyping Journal*, *25*(5), 915–924. https://doi.org/10.1108/RPJ-03-2019-0061

Mukhangaliyeva, A., Dairabayeva, D., Perveen, A., & Talamona, D. (2023). Optimization of Dimensional Accuracy and Surface Roughness of SLA Patterns and SLA-Based IC Components. *Polymers*, *15*(20), 4038. https://doi.org/10.3390/polym15204038

Mukhtarkhanov, M., Perveen, A., & Talamona, D. (2020). Application of Stereolithography Based 3D Printing Technology in Investment Casting. *Micromachines*, *11*(10), 946. https://doi.org/10.3390/mi11100946

Nekin Joshua, R., & Sakthivel, A. R. (2025). Reinforced Polymer Composite Filaments in Fused Deposition Modeling of 3D Printing Technology: A Review. *Advanced Engineering Materials*, *27*(9), 2402509. https://doi.org/10.1002/adem.202402509

Nowacki, B., Kowol, P., Kozioł, M., Olesik, P., Wieczorek, J., & Wacławiak, K. (2021). Effect of Post-Process Curing and Washing Time on Mechanical Properties of mSLA Printouts. *Materials*, *14*(17), 4856. https://doi.org/10.3390/ma14174856

Nurhidayanti, Lukmanul Hakim Arma, & Rusdi Nur. (2025). ANALYSIS OF THE EFFECT OF LAYER THICKNESS ON SURFACE ROUGHNESS OF PLA PRINTED PRODUCTS USING FDM TECHNOLOGY FOR THE MANUFACTURING INDUSTRY. *Scientific Journal of Mechanical Engineering Kinematika*, *10*(1), 125–135. https://doi.org/10.20527/sjmekinematika.v10i1.737

O'Connor, L. (2025). Comparative analysis of the mechanical properties of FDM and SLA 3D printed components. *Journal of Micromanufacturing*, 25165984251364689. https://doi.org/10.1177/25165984251364689

Orzeł, B., & Stecuła, K. (2022). Comparison of 3D Printout Quality from FDM and MSLA Technology in Unit Production. *Symmetry*, *14*(5), 910. https://doi.org/10.3390/sym14050910

ÖzdiLli, Ö. (2021). Comparison of the Surface Quality of the Products Manufactured by the Plastic Injection Molding and SLA and FDM Method. *Uluslararası Muhendislik Arastirma ve Gelistirme Dergisi*, 428–437. https://doi.org/10.29137/umagd.762942

Pagac, M., Hajnys, J., Ma, Q.-P., Jancar, L., Jansa, J., Stefek, P., & Mesicek, J. (2021). A Review of Vat Photopolymerization Technology: Materials, Applications, Challenges, and Future Trends of 3D Printing. *Polymers*, *13*(4), 598. https://doi.org/10.3390/polym13040598

Periyasamy, R., Hemanth Kumar, M., Rangappa, S. M., & Siengchin, S. (2023). A comprehensive review on natural fillers reinforced polymer composites using fused deposition modeling. *Polymer Composites*, *44*(7), 3715–3747. https://doi.org/10.1002/pc.27369

Plamadiala, I., Croitoru, C., Pop, M. A., & Roata, I. C. (2025). Enhancing Polylactic Acid (PLA) Performance: A Review of Additives in Fused Deposition Modelling (FDM) Filaments. *Polymers*, *17*(2), 191. https://doi.org/10.3390/polym17020191

Pongwisuthiruchte, A., Dubas, S. T., Aumnate, C., & Potiyaraj, P. (2022). Mechanically tunable resins based on acrylate-based resin for digital light processing (DLP) 3D printing. *Scientific Reports*, *12*(1), 20025. https://doi.org/10.1038/s41598-022-24667-8

Porima | 3D Yazıcı Filamentleri. (2025, December 23). Porima. https://porima3d.com/

Prakash, J., Shenoy, M., Alhasmi, A., Al Saleh, A. A., C, S. G., & Shivakumar, S. (2024). Biocompatibility of 3D-Printed Dental Resins: A Systematic Review. *Cureus*. https://doi.org/10.7759/cureus.51721

Pszczółkowski, B., & Zaborowska, M. (2025). Effect of Layer Exposure Time in SLA-LCD Printing on Surface Topography, Hardness and Chemical Structure of UV-Cured Photopolymer. *Lubricants*, *13*(9), 406. https://doi.org/10.3390/lubricants13090406

Qamar Tanveer, Md., Mishra, G., Mishra, S., & Sharma, R. (2022). Effect of infill pattern and infill density on mechanical behaviour of FDM 3D printed Parts- a current review. *Materials Today: Proceedings*, *62*, 100–108. https://doi.org/10.1016/j.matpr.2022.02.310

Quan, H., Zhang, T., Xu, H., Luo, S., Nie, J., & Zhu, X. (2020). Photo-curing 3D printing technique and its challenges. *Bioactive Materials*, *5*(1), 110–115. https://doi.org/10.1016/j.bioactmat.2019.12.003

Rafique, A. S., Munir, A., Ghazali, N., Ahsan, M. N., & Khurram, A. A. (2024). Correlation between the part quality, strength and surface roughness of material extrusion process. *Rapid Prototyping Journal*, *30*(3), 513–528. https://doi.org/10.1108/RPJ-10-2023-0347

Rahim, T. N. A. T., Abdullah, A. M., & Md Akil, H. (2019). Recent Developments in Fused Deposition Modeling-Based 3D Printing of Polymers and Their Composites. *Polymer Reviews*, *59*(4), 589–624. https://doi.org/10.1080/15583724.2019.1597883

Ramian, J., Ramian, J., & Dziob, D. (2021). Thermal Deformations of Thermoplast during 3D Printing: Warping in the Case of

ABS. *Materials*, *14*(22), 7070. https://doi.org/10.3390/ma14227070

Ren, D., Choi, J.-K., & Schneider, K. (2022). A multicriteria decision-making method for additive manufacturing process selection. *Rapid Prototyping Journal*, *28*(11), 77–91. https://doi.org/10.1108/RPJ-11-2021-0302

Riccio, C., Civera, M., Grimaldo Ruiz, O., Pedullà, P., Rodriguez Reinoso, M., Tommasi, G., Vollaro, M., Burgio, V., & Surace, C. (2021). Effects of Curing on Photosensitive Resins in SLA Additive Manufacturing. *Applied Mechanics*, *2*(4), 942–955. https://doi.org/10.3390/applmech2040055

Rivera-López, F., Pavón, M. M. L., Correa, E. C., & Molina, M. H. (2024). Effects of Nozzle Temperature on Mechanical Properties of Polylactic Acid Specimens Fabricated by Fused Deposition Modeling. *Polymers*, *16*(13), 1867. https://doi.org/10.3390/polym16131867

Robles Martinez, P., Basit, A. W., & Gaisford, S. (2018). The History, Developments and Opportunities of Stereolithography. In A. W. Basit & S. Gaisford (Eds.), *3D Printing of Pharmaceuticals* (Vol. 31, pp. 55–79). Springer International Publishing. https://doi.org/10.1007/978-3-319-90755-0_4

Rodriguez, N., Ruelas, S., Forien, J.-B., Dudukovic, N., DeOtte, J., Rodriguez, J., Moran, B., Lewicki, J. P., Duoss, E. B., & Oakdale, J. S. (2021). 3D Printing of High Viscosity Reinforced Silicone Elastomers. *Polymers*, *13*(14), 2239. https://doi.org/10.3390/polym13142239

Sabbah, A., Romanos, G., & Delgado-Ruiz, R. (2021). Impact of Layer Thickness and Storage Time on the Properties of 3D-Printed Dental Dies. *Materials*, *14*(3), 509. https://doi.org/10.3390/ma14030509

Saleh Alghamdi, S., John, S., Roy Choudhury, N., & Dutta, N. K. (2021). Additive Manufacturing of Polymer Materials:

Progress, Promise and Challenges. *Polymers*, *13*(5), 753. https://doi.org/10.3390/polym13050753

Sathish, K., Kumar, S. S., Magal, R. T., Selvaraj, V., Narasimharaj, V., Karthikeyan, R., Sabarinathan, G., Tiwari, M., & Kassa, A. E. (2022). A Comparative Study on Subtractive Manufacturing and Additive Manufacturing. *Advances in Materials Science and Engineering*, *2022*, 1–8. https://doi.org/10.1155/2022/6892641

Seçgin, Ö., Arda, E., Ata, E., & Çelik, H. A. (2022). Dimensional Optimization of Additive Manufacturing Process. *Journal of the Chinese Society of Mechanical Engineers*, *Vol.43*(No.1), 75~78.

Selvamani, S. K., Samykano, M., Subramaniam, S. R., Ngui, W. K., Kadirgama, K., Kanagaraj, G., & Idris, M. S. (2019). *3D printing: Overview of ABS evolvement*. 020041. https://doi.org/10.1063/1.5085984

Shanmugam, R., Ramoni, M. O., Chandran, J., Mohanavel, V., & Pugazhendhi, L. (2021). A Review on the significant classification of Additive Manufacturing. *Journal of Physics: Conference Series*, *2027*(1), 012026. https://doi.org/10.1088/1742-6596/2027/1/012026

Shi, Y., Yan, C., Zhou, Y., Wu, J., Wang, Y., Yu, S., & Chen, Y. (2021). Polymer materials for additive manufacturing: Liquid materials. In *Materials for Additive Manufacturing* (pp. 191–359). Elsevier. https://doi.org/10.1016/B978-0-12-819302-0.00003-1

Sofu, M. M., Varol Özkavak, H., Bacak, S., & Fenkli, M. (2023). Comparison of Strength, Surface Quality and Cost of Different Additive Manufacturing Methods. *İmalat Teknolojileri ve Uygulamaları*, *4*(1), 25–36. https://doi.org/10.52795/mateca.1265509

Sreejith, P., Kannan, K., & Rajagopal, K. (2021). A thermodynamic framework for additive manufacturing, using amorphous

polymers, capable of predicting residual stress, warpage and shrinkage. *International Journal of Engineering Science*, *159*, 103412. https://doi.org/10.1016/j.ijengsci.2020.103412

Subramani, R., Leon, R. R., Nageswaren, R., Rusho, M. A., & Shankar, K. V. (2025). Tribological Performance Enhancement in FDM and SLA Additive Manufacturing: Materials, Mechanisms, Surface Engineering, and Hybrid Strategies—A Holistic Review. *Lubricants*, *13*(7), 298. https://doi.org/10.3390/lubricants13070298

Susanto, B., Putro, A. J. N., Ristyawan, M. R., Kumar, V. V., Nugraha, A. D., Kusumawanto, A., Prawara, B., Junianto, E., Hikmawan, M. F., & Muflikhun, M. A. (2025). Enhanced Mechanical Properties of the Additively Manufactured Modified Hybrid Stereolithography (SLA)–Glass Powder. *Journal of Composites Science*, *9*(5), 205. https://doi.org/10.3390/jcs9050205

Syrlybayev, D., Zharylkassyn, B., Seisekulova, A., Akhmetov, M., Perveen, A., & Talamona, D. (2021). Optimisation of Strength Properties of FDM Printed Parts—A Critical Review. *Polymers*, *13*(10), 1587. https://doi.org/10.3390/polym13101587

Uddin, M. S., Sidek, M. F. R., Faizal, M. A., Ghomashchi, R., & Pramanik, A. (2017). Evaluating Mechanical Properties and Failure Mechanisms of Fused Deposition Modeling Acrylonitrile Butadiene Styrene Parts. *Journal of Manufacturing Science and Engineering*, *139*(8), 081018. https://doi.org/10.1115/1.4036713

Ulkir, O., Ertugrul, I., Ersoy, S., & Yağımlı, B. (2024). The Effects of Printing Temperature on the Mechanical Properties of 3D-Printed Acrylonitrile Butadiene Styrene. *Applied Sciences*, *14*(8), 3376. https://doi.org/10.3390/app14083376

Valizadeh, I., & Weeger, O. (2022). Parametric visco-hyperelastic constitutive modeling of functionally graded 3D printed

polymers. *International Journal of Mechanical Sciences*, *226*, 107335. https://doi.org/10.1016/j.ijmecsci.2022.107335

Wang, H., Huang, Z., Zhang, Y., Li, L., & Li, J. (2023). Design of enhanced mechanical properties by interpenetrating network of 3D printing dual-curing resins. *Polymer*, *282*, 126153. https://doi.org/10.1016/j.polymer.2023.126153

Wojnowski, W., Marć, M., Kalinowska, K., Kosmela, P., & Zabiegała, B. (2022). Emission Profiles of Volatiles during 3D Printing with ABS, ASA, Nylon, and PETG Polymer Filaments. *Molecules*, *27*(12), 3814. https://doi.org/10.3390/molecules27123814

Wu, L., & Song, Y. (2025). Recent innovations in interfacial strategies for DLP 3D printing process optimization. *Materials Horizons*, *12*(2), 401–417. https://doi.org/10.1039/D4MH01160K

Yang, B. (2025). The influence of infill density on the mechanical properties of PLA samples in FDM 3D printing. *Journal of Physics: Conference Series*, *3019*(1), 012046. https://doi.org/10.1088/1742-6596/3019/1/012046

Yang, N.-N., Liu, H.-R., Mi, N., Zhou, Q., He, L.-Q., Liu, X., Zhao, L., & Yang, L.-D. (2021). Anisotropic Mechanical Properties of Rapid Prototyping Parts Fabricated by Stereolithography. *Science of Advanced Materials*, *13*(9), 1812–1819. https://doi.org/10.1166/sam.2021.4071

Yankov, E., & Nikolova, M. P. (2017). Comparison of the Accuracy of 3D Printed Prototypes Using the Stereolithography (SLA) Method with the Digital CAD Models. *MATEC Web of Conferences*, *137*, 02014. https://doi.org/10.1051/matecconf/201713702014

Yeshiwas, T. A., Tiruneh, A. B., & Sisay, M. A. (2025). A review article on the assessment of additive manufacturing. *Journal of Materials Science: Materials in Engineering*, *20*(1), 85. https://doi.org/10.1186/s40712-025-00306-8

Yilmaz, S. (2024). Comprehensive analysis of 3D printed PA6 .6 and fiber-reinforced variants: Revealing mechanical properties and adhesive wear behavior. *Polymer Composites*, *45*(2), 1446–1460. https://doi.org/10.1002/pc.27865

Yu, N., Zhang, Q., Wang, Z., Zhang, D., & Li, J. (2022). Effects of a rotary shear field on the interlayer bond and mechanical properties of carbon-fiber-reinforced plastic composites fabricated using fused deposition modeling. *Journal of Manufacturing Processes*, *83*, 172–179. https://doi.org/10.1016/j.jmapro.2022.08.060

Yüceer, Ö. M., Kaynak Öztürk, E., Çiçek, E. S., Aktaş, N., & Bankoğlu Güngör, M. (2025). Three-Dimensional-Printed Photopolymer Resin Materials: A Narrative Review on Their Production Techniques and Applications in Dentistry. *Polymers*, *17*(3), 316. https://doi.org/10.3390/polym17030316

Zhao, G., Zhou, C., & Das, S. (2015). Solid Mechanics Based Design and Optimization for Support Structure Generation in Stereolithography Based Additive Manufacturing. *Volume 1A: 35th Computers and Information in Engineering Conference*, V01AT02A035. https://doi.org/10.1115/DETC2015-47902

Zhao, Y., Yang, G., Zhu, L., Ding, Y., Guan, X., Wu, X., & Yang, Z. (2022). Effects of rheological properties and printing speed on molding accuracy of 3D printing basalt fiber cementitious materials. *Journal of Materials Research and Technology*, *21*, 3462–3475. https://doi.org/10.1016/j.jmrt.2022.10.124

Zisopol, D. G., Minescu, M., & Iacob, D. V. (2025). A Technical–Economic Study on Optimizing FDM Parameters to Manufacture Pieces Using Recycled PETG and ASA Materials in the Context of the Circular Economy Transition. *Polymers*, *17*(1), 122. https://doi.org/10.3390/polym17010122

CHAPTER 6

THE EFFECT OF RECESSED SINGLE-LAP JOINT DESIGN ON FREE VIBRATION BEHAVIOR

AHMET ÇALIK[1]

Introduction

Adhesively bonded joints offer significant advantages over mechanical fastening, including weight reduction, more uniform stress distribution, and inherent sealing capability (Hülagü et al., 2024; Melro & Liu, 2020). Nevertheless, in single-lap joints (SLJs) the overlap region is often characterized by local stress concentrations and complex deformation fields (Patil, 2019). This condition can govern not only the static strength but also the dynamic response and the evolution of damage under vibration. In particular, vibration-induced delamination represents a critical threat to the integrity of SLJs; therefore, investigating their modal characteristics is essential for reliable structural design (Hülagü et al., 2024).

Within this context, the influence of adhesive properties on vibrational behaviour has been addressed since early studies. He and Oyadiji (2001) demonstrated that adhesive material parameters—such as elastic modulus and Poisson's ratio—can noticeably affect

[1] Prof. Dr, Burdur Mehmet Akif Ersoy Üniversitesi, Mühendislik-Mimarlık Fakültesi, Makine Mühendisliği Bölümü, Orcid: 0000-0001-7425-4546

the natural frequencies and mode shapes of cantilevered beams incorporating SLJs. Subsequently, He (2012) combined numerical and experimental methods to examine the forced vibration response and the frequency response functions (FRFs) of adhesively bonded SLJs. Similarly, for tubular joints, Rao and Zhou investigated how structural parameters and material properties influence modal loss factors and resonant frequencies, while Ko and co-workers developed finite element formulations capable of capturing the coupled responses of the adherends and the adhesive layer (Zeaiter et al., 2019).

More recently, geometric modifications within the bonded region (e.g., recesses/slots, joggles, and wavy interfaces) have been reported to alter both the stress field and the dynamic response. Such approaches have attracted attention due to their potential to mitigate stress concentrations, tailor stiffness distribution, and consequently improve modal characteristics (Marchione, 2020; Rajesh et al., 2024).

Building on these insights, this chapter investigates the dynamic behaviour of a recessed SLJ configuration through a finite-element-based modal analysis. A conventional (classical) SLJ is considered as the baseline for comparison. By varying the recess diameter (D) and the recess-length parameter (L), the study quantitatively evaluates their effects on the first six natural frequencies. In this way, the fundamental trends governing the vibration response of the modified joint geometry are identified, providing design-relevant conclusions for adhesively bonded structures.

Materials and Methods

Geometry and Boundary Conditions

The analysed configurations include (i) a classical single-lap joint and (ii) a recessed single-lap joint, where a recess is introduced

in the overlap region. The recess is parameterised by diameter D and by a length-related parameter L as defined in the CAD model. The overall joint geometry and the applied boundary conditions used in the modal analysis are shown in Figure 1.

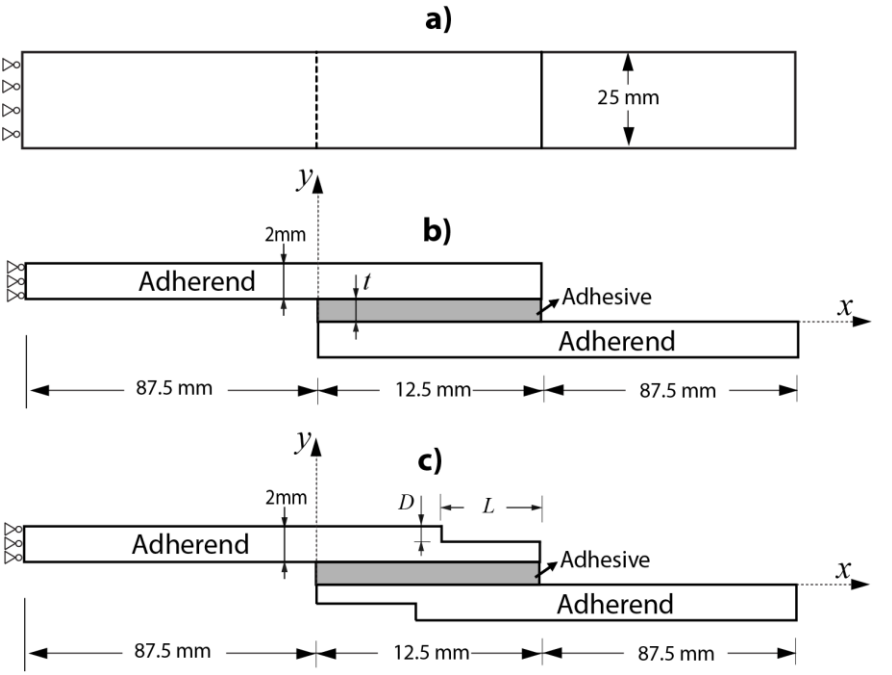

Figure 1 Geometry, key dimensions, and boundary conditions used in the FE model.

Material Properties

Material properties for the adherends and the adhesive layer are summarised in Table 1. The adhesive is DP460, while the adherends are AA2024-T3 aluminium alloy. Linear elastic isotropic behaviour is assumed for the modal analysis.

Table 1 Material properties used in the study.

Material	Properties	Value
Adhesive (DP460)	Elasticity Modulus	2.07 GPa
	Poission ratio	0.38
	Density	2,7e-06 kg/mm³
Adherend (AA2024-T3)	Elasticity Modulus	72.4 GPa
	Poission ratio	0.33
	Density	2,7e-06 kg/mm³

Finite-Element Model and Modal Extraction

The FE model is created in ANSYS Workbench Mechanical. The adhesive layer is explicitly modelled between the adherends. A suitable mesh refinement is applied in the overlap region to capture local deformation. Figure 2 shows a representative mesh. The first six natural frequencies (Modes 1–6) are extracted for each configuration. The analysis is repeated for three values of the recess diameter (D = 8, 10, 12 mm) and three values of the length parameter (L = 40, 60, 80 mm), in addition to the classical SLJ baseline.

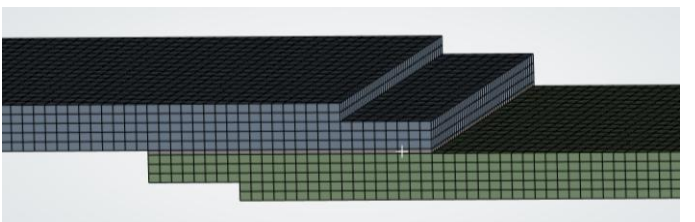

Figure 2. Representative FE mesh for the adhesively bonded joint model.

3. Results and Discussion

Tables 2–4 report the first six natural frequencies for the baseline classical SLJ and for recessed SLJs with different (D, L)

combinations. For compactness, each table corresponds to a fixed L and compares D = 8–12 mm against the classical case. Percentage changes are discussed to highlight the sensitivity of each mode to recess parameters.

L = 40 mm

At L = 40 mm, the recessed designs show small increases in the first three modes (≤ about +1.12%), while Mode 4 exhibits a nearly unchanged response with a slight decrease for the largest recess (D = 12 mm). The largest increase at this L is observed in Mode 2 for D = 12 mm (+1.12%), whereas the most negative change is about −0.11% (Mode 4, D = 12 mm).

Table 2. Natural frequencies for L = 40 mm (classical vs recessed SLJ).

Mode	Classic	D8	D10	D12
1	47.855	48.000	48.025	48.051
2	298.870	301.500	301.890	302.220
3	557.400	559.540	559.910	560.200
4	707.140	707.420	706.970	706.380
5	838.950	839.380	839.420	839.520
6	1660.800	1668.600	1668.900	1668.900

Note: Natural frequencies are reported in Hz.

L = 60 mm

At L = 60 mm, the sensitivity becomes more pronounced in higher modes. Modes 1–3 still increase slightly relative to the classical SLJ. In contrast, Mode 4 decreases as D increases, reaching approximately −0.79% for D = 12 mm. The largest increase across all examined cases occurs at this L in Mode 2 for D = 10 mm (+1.16%).

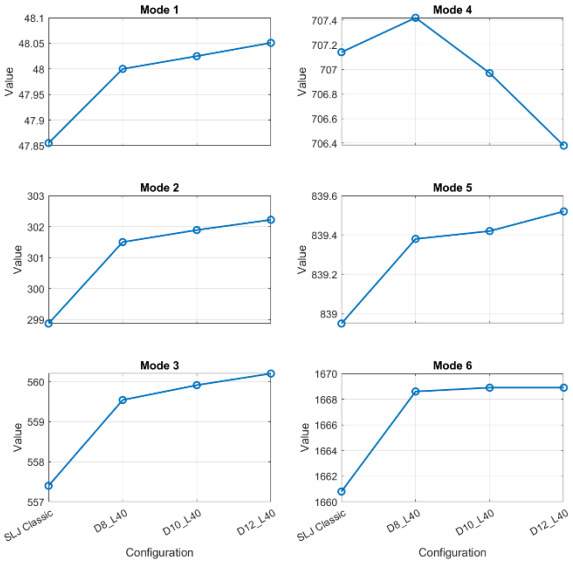

Figure 3. Modal results comparison for L = 40 mm (natural frequencies of the first six modes).

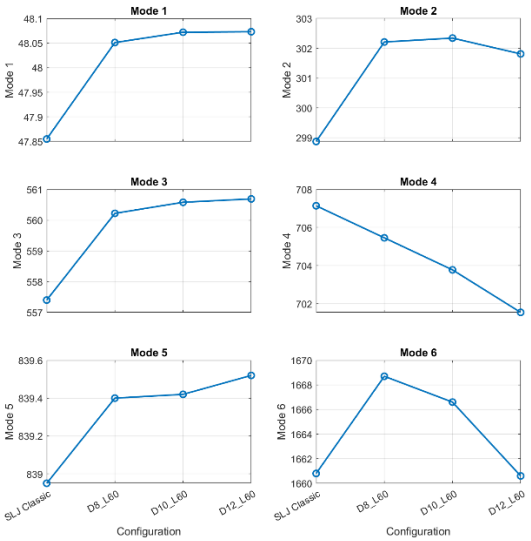

Figure 3. Modal results comparison for L = 60 mm (natural frequencies of the first six modes).

Table 3. Natural frequencies for L = 60 mm (classical vs recessed SLJ).

Mode	Classic	D8	D10	D12
1	47.855	48.051	48.072	48.073
2	298.870	302.210	302.340	301.810
3	557.400	560.220	560.580	560.690
4	707.140	705.460	703.780	701.550
5	838.950	839.400	839.420	839.520
6	1660.800	1668.700	1666.600	1660.600

Note: Natural frequencies are reported in Hz.

L = 80 mm

For L = 80 mm, the effect of recessing is strongly mode-dependent. While Mode 2 increases for D = 8 mm (+0.99%), the largest recess (D = 12 mm) reduces higher-mode frequencies, with the most notable reduction in Mode 6 (−2.17%). This behaviour aligns with the general observation that geometric discontinuities may have limited influence on the lowest modes but can affect the dynamic response more noticeably at higher frequencies (Marchione, 2020).

Table 4. Natural frequencies for L = 80 mm (classical vs recessed SLJ).

Mode	Classic	D12	D10	D8
1	47.855	47.888	48.029	48.064
2	298.870	295.970	300.310	301.840
3	557.400	560.920	561.070	560.790
4	707.140	693.580	698.430	702.170
5	838.950	839.280	839.310	839.350
6	1660.800	1624.700	1650.600	1662.700

Note: Natural frequencies are reported in Hz.

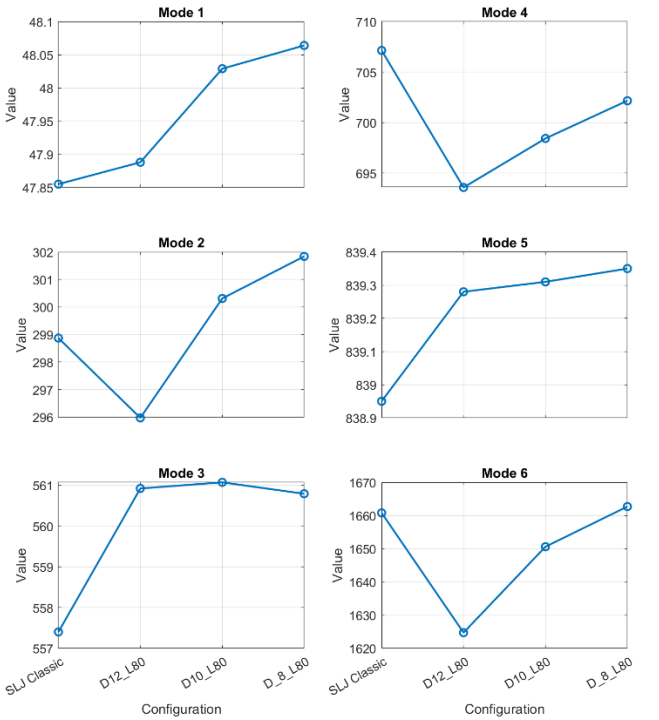

Figure 3. Modal results comparison for L = 80 mm (natural frequencies of the first six modes).

Overall Trends and Interpretation

Across the parameter space, recessed SLJs tend to slightly increase the lowest modes (particularly Modes 1–3), suggesting a small change in effective stiffness–mass distribution near the overlap. Conversely, for larger L and D, reductions emerge in higher modes (Modes 4–6), indicating that the recess can introduce local flexibility that becomes more influential for higher mode shapes.

From a design perspective, these results imply a trade-off: recessing may offer benefits such as stress redistribution or weight reduction, but it can also reduce certain higher-mode frequencies, potentially shifting resonance conditions. Similar trade-offs have been discussed for other overlap modifications, including slots (Marchione, 2020) and additively manufactured joggle/wavy profiles (Rajesh et al., 2024). Finally, the adhesive elastic properties are known to affect SLJ modal response (He & Oyadiji, 2001), and future work may therefore combine geometric optimisation with adhesive material tailoring.

Conclusions

This chapter presented an FE-based modal comparison between classical and recessed single-lap adhesive joints. Based on the first six natural frequencies obtained from ANSYS Workbench for D = 8–12 mm and L = 40–80 mm, the following conclusions are drawn:

• Recessing produces modest increases in the first modes (typically < 1.2%), with the maximum increase of about +1.16% observed in Mode 2 (L = 60 mm, D = 10 mm).

• For larger recess parameters, reductions occur in higher modes; the maximum reduction is about −2.17% in Mode 6 (L = 80 mm, D = 12 mm).

• The effect is strongly mode-dependent, consistent with literature indicating that geometric discontinuities may affect higher-frequency behaviour more than the lowest modes.

Future studies can extend the present work by including experimental modal testing, damping identification, and strength–dynamics multi-objective optimisation for recessed SLJ designs.

References

He, X., & Oyadiji, S. O. (2001). Influence of adhesive characteristics on the transverse free vibration of single lap-jointed cantilevered beams. Journal of Materials Processing Technology, 119, 366–373.

He, X. (2012). Forced vibration behavior of adhesively bonded single-lap joint. Applied Mechanics and Materials, 110–116, 3611–3616. https://doi.org/10.4028/www.scientific.net/AMM.110-116.3611

Hülagü, B., Acar, V., Çakır, F., & Akbulut, H. (2024). Numerical Analysis of Modal and Flexural Behavior of Nanocomposite Adhesively Bonded Joints. Research Square (Research Square). https://doi.org/10.21203/rs.3.rs-5245609/v1

Marchione, F. (2020). Investigation of vibration modes of double-lap adhesive joints: Effect of slot. International Journal of Engineering, IJE Transactions A: Basics, 33(10), 1917–1923. https://doi.org/10.5829/ije.2020.33.10a.10

Melro, A., & Liu, K. (2020). Determination of the modal parameters of a single lap adhesively bonded joint using the transfer matrix method plus model updating. International Journal of Adhesion and Adhesives, 101, 102628. https://doi.org/10.1016/j.ijadhadh.2020.102628

Patil, Mr. K. P. (2019). Experimental and Finite Element Analysis of Adhesively Bonded Riveted Joint. International Journal for Research in Applied Science and Engineering Technology, 7(11), 258. https://doi.org/10.22214/ijraset.2019.11042

Rajesh, M., Venkatesan, R., Kesavan, S., Murali, A. P., Sasikumar, R., Kim, S.-C., Dhilipkumar, T., & Al-Asbahi, B. A. (2024). Influence of 3D printed adherend design on structural performance and vibrational behaviour of adhesively bonded joints.

Journal of the Brazilian Society of Mechanical Sciences and Engineering, 46, 402. https://doi.org/10.1007/s40430-024-04995-8

Zeaiter, A., Challita, G., & Khalil, K. (2019). Investigation of vibration modes of a double-lap bonded joint. SN Applied Sciences, 1(5). https://doi.org/10.1007/s42452-019-0340-8

CHAPTER 7

FORMABILITY, BUCKLING AND STABILITY OF THIN-WALLED SECTIONS IN SEVERE PLASTIC DEFORMATION (SPD) PROCESSING

ÖMER KARABEY[1]
HÜSEYİN BEYTÜT[2]

Introduction

Lightweighting in transportation and energy systems has pushed designers toward thin-walled load-bearing structures extruded tubes, hydroformed shells, stamped sheets and open-section beams because they provide high stiffness-to-mass ratios and excellent crash/energy-absorption potential (Olabi, Morris, & Hashmi, 2007; Wierzbicki & Abramowicz, 1983). At the same time, a persistent limitation of many lightweight alloys is the trade-off between strength and ductility: microstructural strengthening often reduces the safe strain window in forming (Ashby, 2011). SPD offers a microstructure-based pathway to break part of this trade-off by creating UFG or nanostructured states

[1] Dr., Bitlis Eren University, Mechanical Engineering, Orcid: 0000-0002-5726-9284
[2] Dr., Bitlis Eren University, Mechanical Engineering, Orcid: 0000-0001-8751-2225

through imposing very large plastic strains without significant change in external dimensions (or with controlled shape change) (Bagherpour, Pardis, Reihanian, & Ebrahimi, 2019; Beytüt, Özbeyaz, & Temiz, 2025; Karabey, 2023; Özbeyaz, Kaya, & Kentli, 2022; Segal, 1995; Ruslan Z. Valiev & Langdon, 2006). In conventional (bulk) SPD, the billet is typically compact and supported by surrounding material and tooling (Ruslan Z. Valiev et al., 2006). In thin-walled SPD, the geometry itself becomes a dominant "material parameter": the same constitutive law can lead to stable flow in bulk but to buckling, wrinkling or localization in shells and plates (Karabey, 2025). This chapter therefore frames thin-walled SPD as a coupled microstructure stability problem in which processing windows must be designed with both microstructural evolution and geometric instabilities in mind.

Two complementary viewpoints are useful. The first is microstructural: grain refinement via dislocation subdivision, shear banding and dynamic recovery/recrystallization can enhance strength and sometimes enable low-temperature superplasticity or improved fatigue performance (Bagherpour et al., 2019; Iwahashi, Wang, Horita, Nemoto, & Langdon, 1996; Ruslan Z. Valiev & Langdon, 2006). The second is structural: thin-walled members have reduced bending stiffness and can undergo bifurcation at stresses far below the material's flow stress, especially under compressive or shear-dominated loading. Therefore, a process that increases flow stress (e.g., through strong work hardening) may raise forming forces and simultaneously lower the margin against buckling. The central aim of this chapter is to clarify this balance and provide a roadmap for designing thin-walled SPD operations that achieve microstructural benefits while maintaining process stability.

Engineering Importance of Thin-Walled Structures (Automotive and Aerospace)

Thin-walled components are pervasive in automotive body-in-white structures, battery enclosures, crash boxes, subframes and suspension arms, as well as in aerospace fuselage skins, stringers, stiffened panels and hydraulic tubing (Altan & Tekkaya, 2012; Megson, n.d.; Özel, Beytüt, & Karagöz, 2019; Pan, Xiong, Wu, Diao, & Guo, 2021). For many of these components, the design driver is stiffness and buckling resistance per unit mass rather than absolute strength. Consequently, material innovations are valuable when they improve strength and fatigue life without sacrificing forming robustness. Magnesium alloys, Al-Li alloys and high-strength aluminum series exemplify this need; they offer low density but require careful processing to achieve acceptable ductility and damage tolerance (Kulekci, 2008; Zhan, Li, & Chen, 2008).

SPD Fundamentals and Challenges for Thin-Walled Materials

SPD refers to processing routes that impose very high equivalent plastic strains, often via simple-shear-dominated deformation paths, while aiming to retain overall geometry and avoid fracture. Canonical methods include ECAP/ECAE, HPT, accumulative roll bonding, twist extrusion and multi-directional forging (Edalati & Horita, 2016; Karabey & Özbeyaz, 2023; Langdon, 2013; Segal, 1995; Ruslan Z. Valiev & Langdon, 2006). The grain refinement mechanisms are well studied for bulk billets, but applying the same strain paths to tubes or sheets introduces additional constraints:

1. limited through-thickness support leads to local plate-like buckling (wrinkling),
2. contact/friction conditions dominate because the surface-to-volume ratio is large, and

3. thickness variations or eccentricities can trigger early bifurcation.

Practical thin-walled SPD therefore relies on auxiliary supports (mandrels/canning), pressure assistance (back-pressure, hydrostatic confinement) and carefully tailored die geometries.

Mechanical Behavior and Stability Theory in Thin-Walled Structures

In bulk SPD, the deformation field is constrained by surrounding material and the tool cavity, and instability typically appears as shear localization or fracture. In thin-walled sections, the deformation field interacts with the structure's bending and membrane stiffness. As a result, the apparent formability is controlled by a hierarchy of instabilities: diffuse necking or shear localization (material-driven), local wrinkling of walls (geometry-driven), and global Euler-type buckling of the entire member (structure-driven). Classical stability theory provides the first-order scaling for these phenomena and guides which mitigation strategy is most effective (Estrin & Vinogradov, 2013; Stephen P. Timoshenko & Gere, 2012; R. Z Valiev, Islamgaliev, & Alexandrov, 2000).

Stability Criteria During Plastic Deformation (Drucker Postulate and Bifurcation)

Drucker's stability postulate is a cornerstone concept in incremental plasticity, establishing the criteria for a stable material system. In its most general form, Drucker proposed that for a stable material, the work done by an external agency on the system during a complete cycle of loading and unloading must be non-negative. For incremental plasticity, this implies that the scalar product of the stress increment tensor $d\sigma_{ij}$ and the associated strain increment tensor $d\varepsilon_{ij}$ must be positive (*Theory of Plasticity*, 2006):

$$d\sigma_{ij}, d\varepsilon_{ij} > 0 \text{ (Stability Condition)}$$

This inequality, often referred to as "stability in the small," ensures two fundamental properties of the yield surface: convexity and the normality rule (the plastic strain increment vector is normal to the yield surface) (Drucker, 1952).

However, in the context of large deformations and thin-walled forming, violation of this condition marks the onset of instability. Mathematically, the constitutive behavior is described by the tangent modulus tensor C_{ijkl}^{ep} :

$$d\sigma_{ij} = C_{ijkl}^{ep} d\varepsilon_{kl}$$

Instability or loss of uniqueness occurs when the determinant of the stiffness matrix vanishes or becomes negative ($\det(C^{ep}) \leq 0$), a condition rigorously analyzed by Hill for bifurcation problems. In thin-walled structures, this material instability is coupled with geometric non-linearities. Therefore, the governing bifurcation analysis requires the assembly of the total tangent stiffness matrix K_T, which is the superposition of the material stiffness K_M (derived from constitutive laws) and the geometric stiffness K_σ (stress-dependent):

$$K_T = K_M(C^{ep}) + K_\sigma(\sigma)$$

The critical state for localization or buckling is defined by the singularity of this total stiffness matrix (Hill, 1958):

$$\det(K_T) = 0$$

Thus, predicting failure in thin-walled sections requires a coupled analysis where Drucker's material stability and Euler's structural stability are evaluated simultaneously.

Buckling Modes

Buckling in thin-walled SPD can be broadly categorized as global or local. Global buckling resembles the Euler instability of slender columns: the entire tube or billet bends as a whole when compressive forces exceed a critical load. In contrast, local buckling (wrinkling) involves short-wavelength undulations of individual walls, typical of plates and shells under compression or shear. Both are strongly influenced by boundary conditions and the presence of internal/external supports. The difference between buckling and wrinkling can be illustrated by Figure 1.

Figure 1 Global buckling and local wrinkling in thin-walled materials.

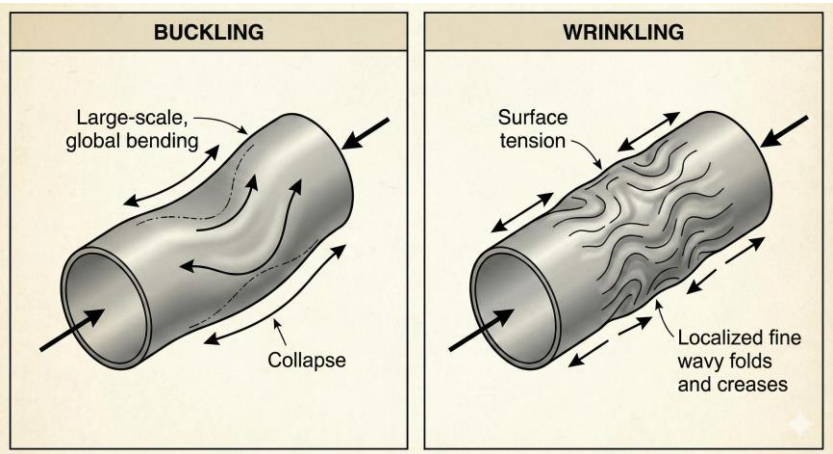

For global buckling, a classical estimate for the critical load of a prismatic member is

$$P_{cr} = \frac{\pi^2 EI}{(KL)^2}$$

where E is Young's modulus, I is the second moment of area, L is the effective length and K is the end-condition factor (Stephen P. Timoshenko & Gere, 2012). While plasticity reduces the effective

stiffness relative to E, the Euler formula remains a useful scaling law: increasing strength by SPD increases required forming forces, which may raise compressive loads toward P_{cr} if the tool does not provide sufficient lateral support.

Local buckling of plate-like walls can be estimated by the classical plate buckling stress

$$\sigma_{cr} = \frac{k\pi^2 E}{12(1-v^2)}\left(\frac{t}{b}\right)^2$$

where t is wall thickness, b is the plate width between supports/stiffeners, ν is Poisson's ratio and k depends on edge constraints and loading mode (S. P. Timoshenko & Woinowsky-Krieger, 1959). This equation highlights a critical geometric sensitivity: σ_{cr} scales with $(t/b)^2$, so even modest thickness reductions or wider unsupported spans sharply reduce wrinkling resistance.

Role of Hydrostatic Pressure: Preventing Cracks vs. Triggering Buckling

Hydrostatic pressure increases the apparent ductility of metals by suppressing void growth and delaying ductile fracture, as shown in classic high-pressure experiments by Bridgman and later analyses by Pugh (Bridgman, 1953; Pugh & Green, 1964). In SPD, back-pressure and confinement are often used to improve bonding or prevent cracking. However, hydrostatic pressure can also alter instability tendencies. For thin-walled members, increased contact pressure elevates frictional shear stresses at interfaces and can generate compressive membrane stresses in the wall, potentially promoting wrinkling if the wall is not adequately supported. The practical implication is that "more pressure" is not always better: pressure assistance must be coupled with support strategies (mandrels, canning, die constraint) to avoid shifting failure from fracture to buckling.

Formability Constraints

In thin-walled SPD, it is useful to separate;

a. intrinsic formability limits tied to the evolving microstructure and constitutive response and

b. geometric formability limits tied to instability and constraint.

This separation clarifies why some SPD routes produce high-strength thin parts that nevertheless have poor forming robustness: the part may fail by wrinkling or global buckling before the material reaches a ductile fracture criterion.

Reduced Ductility and Work-Hardening Capacity

A common outcome of SPD is a sharp increase in flow stress accompanied by a reduction in uniform elongation because the strain-hardening capacity decreases once the microstructure saturates at ultrafine grain sizes (Bagherpour et al., 2019; R. Z. Valiev, Alexandrov, Zhu, & Lowe, 2002; Ruslan Z. Valiev & Langdon, 2006). In sheet or tube forming, strain hardening delays diffuse necking and stabilizes deformation. If work hardening is diminished, deformation localizes earlier, narrowing the stable processing window. Nevertheless, some SPD states exhibit improved post-uniform ductility (e.g., via enhanced strain-rate sensitivity or activation of multiple deformation mechanisms), especially at elevated temperatures. Therefore, the influence of SPD on formability must be evaluated under the exact thermomechanical conditions of the thin-walled process, not inferred solely from room-temperature tensile ductility (Ivanov & Ovcharenko, 2020; Langdon, 2013).

Surface-to-Volume Ratio and Friction Effects

Thin-walled geometries amplify surface effects. The fraction of material in direct contact with tools is higher, and friction can become a first-order driver of strain heterogeneity. In ECAP-type processes, friction affects the location and intensity of the shear zone and can promote dead-metal zones near corners; these effects are widely studied in bulk ECAP simulations and remain even more pronounced in thin-walled variants (Djavanroodi & Ebrahimi, 2010b; Kim, 2001; Nagasekhar, Tick-Hon, & Seow, 2007). From a stability perspective, friction can be beneficial (providing lateral constraint) or detrimental (introducing non-uniform compressive membrane stresses and shear tractions that seed wrinkling). Therefore, thin-walled SPD tooling often aims for controlled friction: high enough to avoid slip-induced inhomogeneity, but not so high that wall compression becomes unstable (Segal, 1995).

Critical Damage Criteria and Their Use in Thin Sections

Ductile fracture in metals is commonly modeled through criteria based on stress triaxiality, equivalent plastic strain and sometimes the Lode parameter. Comparative assessments of multiple fracture models emphasize that calibration must cover the stress state space relevant to the process (Drucker, 1952). In thin-walled SPD, the local stress state may vary rapidly across thickness due to bending, contact pressure and friction. Consequently, damage criteria should be embedded within coupled contact-plasticity simulations and evaluated alongside instability indicators (eigenvalue-type buckling checks or bifurcation measures). A practical engineering rule is to treat damage and buckling as competing failure modes: mitigation strategies that reduce triaxiality (via pressure) should be checked for their impact on wall compression and wrinkling (Bao & Wierzbicki, 2004).

SPD Methods Adapted for Thin-Walled Sections

This section surveys SPD methods that have been adapted specifically for thin-walled tubes, sheets and open-section profiles. The central idea in most adaptations is to re-introduce confinement and support that is naturally present in bulk billets. Methods may be grouped by geometry:

- tube-based methods using mandrels or internal pressure, and
- sheet-based methods using rolling-bonding or corrugation-straightening cycles.

Methods for Tubes and Tubular Parts

Tube geometries are attractive because they already provide a closed section and can carry loads efficiently, yet their walls are vulnerable to ovalization and wrinkling under compressive/shear loading. A schematic representation of a thin-walled tube containing an inner mandrel used to prevent buckling/wrinkling during the SPD process is shown in Figure 2. Several SPD routes have been proposed for tubes:

Figure 2 Tubular channel angular pressing (TCAP) method with an internal mandrel used to prevent wrinkling/creasing during the SPD process

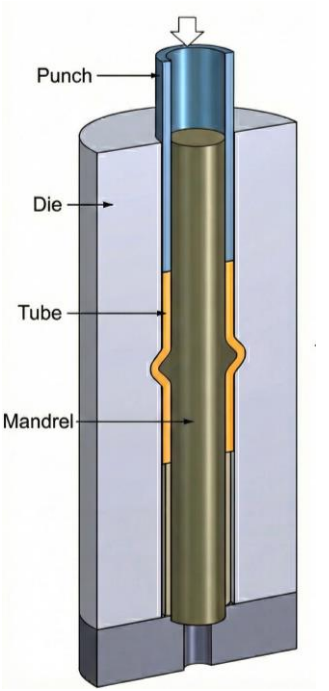

Reference: (Mesbah, Faraji, & Bushroa, 2014)

Tube Channel Pressing (TCP)

Zangiabadi and Kazeminezhad introduced TCP as a pipe-specific SPD method, where the pipe is pressed through a pipe-shaped channel with a constricted/necked region (Figure 3). The mandrel is used to form the pipe-shaped channel and prevent the pipe from wrinkling. In this way, the pipe is passed through the necked region while maintaining a constant pipe thickness. After one pass is applied, the ram is withdrawn and the entire die is rotated vertically by 180◦, and the second pass is applied in the same manner (Figures 3b and 3c). Because the deformation is imposed through the die geometry rather than through torsional friction, TCP can produce

comparatively homogeneous strains along tube length while remaining scalable (Zangiabadi & Kazeminezhad, 2011).

Figure 3 Schematic and procedure of TCP; (a) beginning of the first pass, (b) the end of the first pass and (c) beginning of the second pass

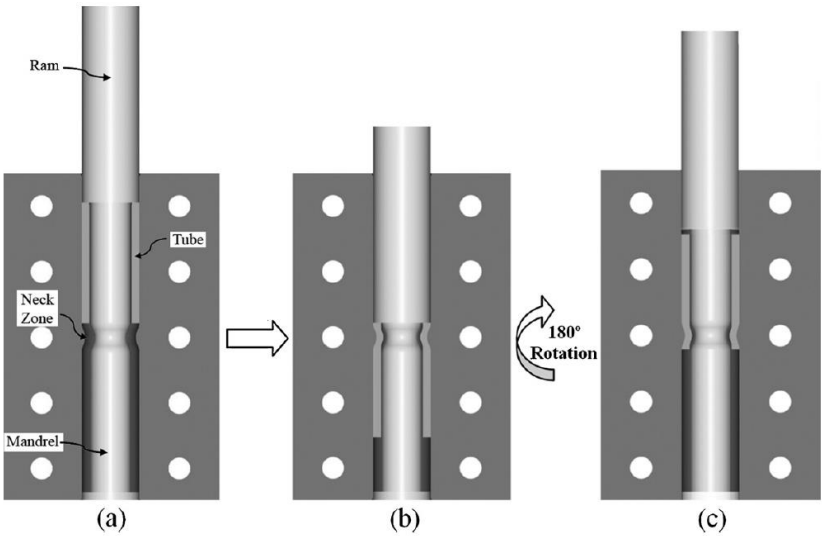

Reference: (Zangiabadi & Kazeminezhad, 2011)

Equal-Channel Angular Pressing of Tubes with Mandrels

Al-Mufadi and Djavanroodi presented a customized Equal Channel Angular Pressing (ECAP) application in their study, which involved placing a supporting "mandrel" inside the pipe to ensure that thin-walled copper pipes undergo extreme plastic deformation while maintaining their shape. For the dies used in the process, a traditional ECAP die with cylindrical channels perfectly matching the outer diameter of the tube was used; however, to prevent the punch from buckling when transferring the pressing force, multiple "short-piece punches" placed one after the other were preferred instead of a single long punch. Figure 4a-b is shown. In the mandrel selection, which forms the basis of the method, three different filling

materials (sand, grease, and flexible polyurethane rubber) were tested to prevent the pipe walls from collapsing. During the application phase, pipes filled with these mandrels and sealed at both ends were passed through the mold with the aid of friction-reducing lubricants; after each pass, the samples were rotated along specific paths and the process was repeated. The experiments revealed that the grease filling failed to withstand the pressure and collapsed the pipe, the sand filling was successful but the filling-emptying process took too long, and the flexible polyurethane rubber was the most successful mandrel choice in terms of both ease of application and maintaining the pipe's shape (Al-Mufadi & Djavanroodi, 2015). The approach generalizes to aluminum and magnesium tubes, but the stability margin depends strongly on thickness, corner radii and lubrication.

Figure 4 (a) Illustration of ECAP die and (b) related parameters of the die

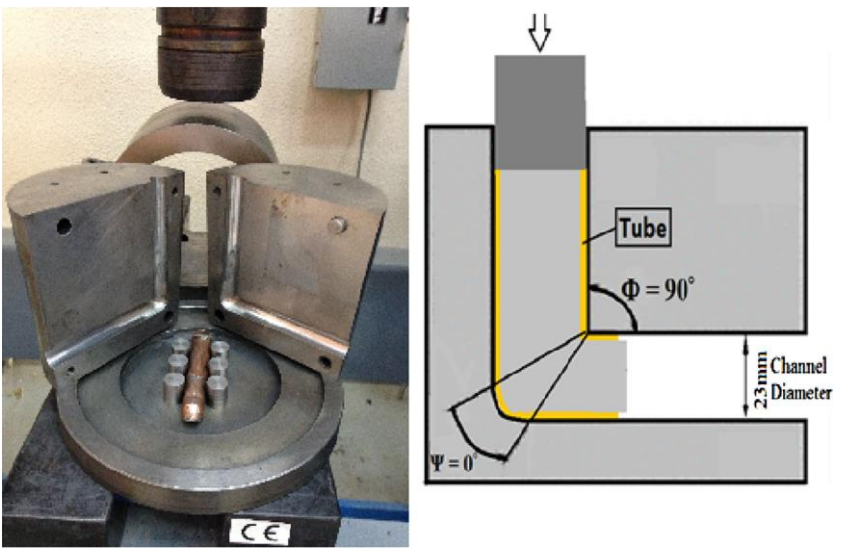

Reference: (Al-Mufadi & Djavanroodi, 2015)

High-Pressure Tube Twisting (HPTT)

The High Pressure Tube Twisting (HPTT) method proposed by Tóth and colleagues is based on the principle of subjecting thin-walled pipes to a very high degree of plastic deformation without changing their dimensions. As shown in Figure 5, in this process, the pipe sample is placed inside a rigid disk, and a compressible mandrel is placed inside the pipe. The pressure generation mechanism, which is the most distinctive feature of the method, works both through the elastic expansion of the mandrel and through a geometric constraint: The pipe, deliberately selected to be slightly longer than the disk thickness, is axially compressed prior to processing, and the excess material forms structures called “ears” at the top and bottom of the disk, trapping the volume. in addition, when an axial load is applied to the inner mandrel, the mandrel is forced to expand radially, creating a very high hydrostatic pressure in the pipe walls. During the deformation stage, taking advantage of the friction force created by this high pressure, the inner mandrel is held stationary while the outer disk is rotated with an external torque, and the pipe material is deformed by a simple shear mechanism. However, since the success of the method is entirely dependent on the friction at the interface, an operational difficulty has also been reported; while complete deformation was achieved in aluminum samples, unwanted slippage occurred between the mandrel and the pipe in copper experiments, preventing the deformation from spreading homogeneously throughout the entire wall thickness (Tóth et al., 2009). In thin walls, the high pressure is beneficial for fracture suppression, but tooling must still avoid wrinkling and ovalization.

Figure 5 Schematic vertical section of the experimental tube twisting setup under high hydrostatic pressure

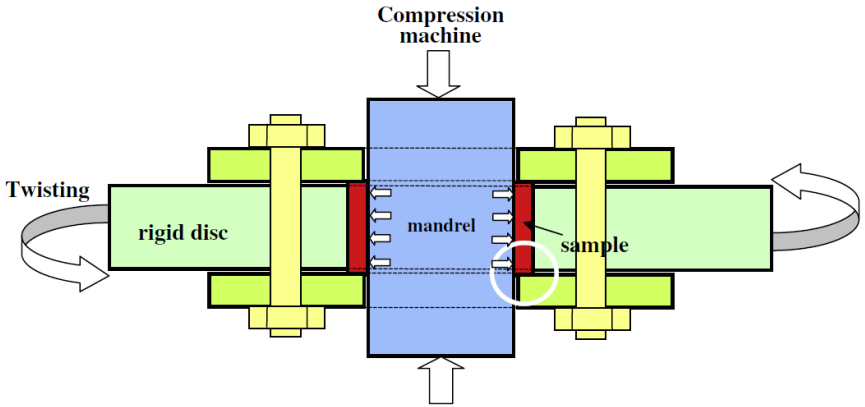

Reference: (Tóth et al., 2009)

Tubular Channel Angular Pressing and Parallel Variants (TCAP/PTCAP)

The Parallel Tubular Channel Angular Pressing (PTCAP) method presented in the work of G. Faraji and colleagues has a unique physical design consisting of two half-cycles based on the principle of sequentially expanding and contracting the pipe material, as shown in Figure 6. In the first half-cycle, the pipe placed between the mandrel and the die is pushed by the first punch through two cutting zones and expanded to its maximum diameter. Immediately afterwards, in the second half-cycle, the pipe is pressed from the other end with a second punch, passing the material back through the same cutting zones and returning the pipe diameter to its initial dimensions. This specific "expansion and recovery" mechanism provides a distinct advantage over the TCAP (Tubular Channel Angular Pressing) method, both mechanically and structurally. Physical experiments show that while strain differences occur between the inner and outer regions in the TCAP method, the PTCAP method provides excellent strain homogeneity throughout

the pipe wall thickness and length. The greatest operational advantage is that this new design reduces the required pressing load by approximately 57.5% compared to the TCAP method, enabling the process to be performed with much lower forces. These methods are often combined with mandrels/back-pressure to enhance stability (Faraji, Babaei, Mashhadi, & Abrinia, 2012; Faraji, Mashhadi, & Kim, 2011).

Figure 6 Schematic of PTCAP

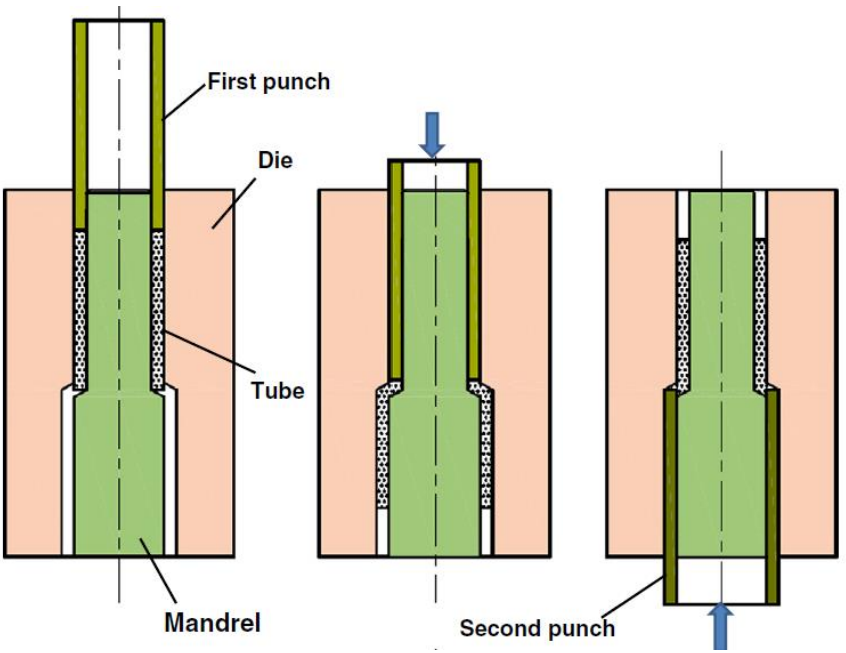

Reference: (Faraji et al., 2012)

Methods for Sheets and Plates

For thin sheets, the most industrially relevant SPD methods are those that can be implemented using rolling or continuous processing. Key routes include:

Accumulative Roll Bonding (ARB)

The Accumulative Roll Bonding (ARB) method proposed in the article is a cyclic process that enables sheet-form materials to be joined using the solid-state bonding principle, subjecting them to extreme plastic deformation. The method was originally introduced by Saito, Utsunomiya, Tsuji and Sakai (Saito, Utsunomiya, Tsuji, & Sakai, 1999) and has since been reviewed extensively (Ghalehbandi, Malaki, & Gupta, 2019; Tsuji, Saito, Lee, & Minamino, 2003). The graphical representation of the ARB method is shown in Figure 7. The most critical first step determining the success of the process is surface preparation; to ensure the layers adhere perfectly to each other, the contact surfaces are first degreased with acetone, then cleaned of oxide layers and roughened by wire brushing with stainless steel wire brushes. After the two prepared strips are stacked on top of each other, they undergo a rolling process that reduces the thickness by exactly 50%; this ratio is the fundamental geometric rule that ensures both the fusion of the materials and the preservation of the total thickness. The rolled material is then cut in half, re-surfaced, re-stacked, and rolled again; this “cut-stack-roll” cycle allows for theoretically infinite amounts of plastic strain to be accumulated without changing the material's dimensions. Unlike methods such as ECAP or HPT, the ARB process does not require complex and expensive mold designs; it differs from other SPD techniques in that it enables the industrial-scale and highly efficient production of large-sized sheets (bulk materials) using existing rolling infrastructure. ARB is well suited to thin geometries but faces characteristic defects: edge cracking due to strain localization at free edges, non-uniform bonding quality, and waviness arising from through-thickness shear and residual stresses (Ebrahimi, Dehghani, Aghazadeh, Ghasemian, & Zangeneh, 2018; Eizadjou, Kazemi Talachi, Danesh Manesh, Shakur Shahabi, & Janghorban, 2008).

Figure 7 Accumulative Roll Bonding

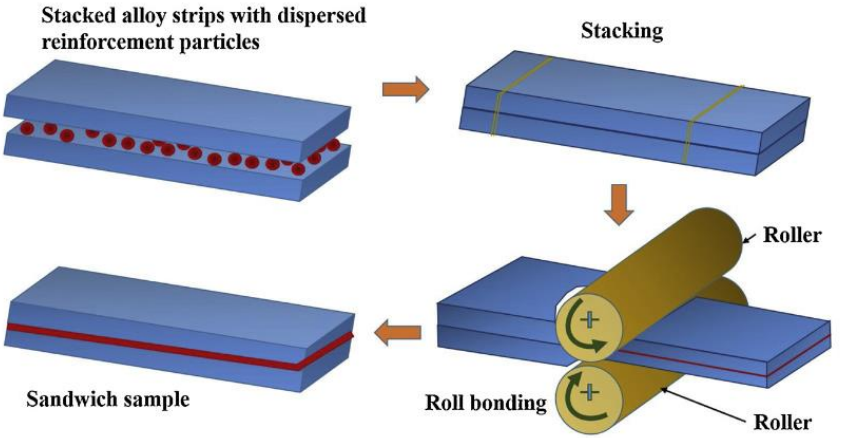

Reference: (Ramanathan, Krishnan, & Muraliraja, 2019)

Repetitive Corrugation and Straightening (RCS)

The Repeated Corrugation and Straightening (RCS) method is based on a cycle in which metallic sheets or bars are first passed through toothed dies or rollers to give them a curved (corrugated) form, and then immediately returned to their original flat form using flat dies or rollers (Figure 8). In the second-generation continuous system first tested by J Huang and colleagues, the process was performed using a rolling mechanism; however, it was observed that this design only applied "bending" stress to the material, causing fatigue cracks without sufficiently refining the grain structure (J. Y. Huang, Zhu, Jiang, & Lowe, 2001; J. Huang et al., 2004). To overcome this problem, the third-generation design (RSCS - Repetitive Shear Corrugation and Straightening) was developed, using special dies with 45-degree inclined teeth that could apply not only bending stress but also "shear" stress, which is critical for severe plastic deformation. In this new process, after the material is corrugated and straightened, the process is repeated by rotating it around its own axis (e.g., 90 degrees) to ensure the homogeneity of the deformation; thus, unlike the previous method, the material

accumulates much higher plastic strain without reaching its fracture limit, and more effective grain refinement is achieved. However, it has been reported that deformation is not completely homogeneous throughout the material thickness in this method either, with a more intense strain forming at the center compared to the surface.

Figure 8 Repetitive Corrugation and Straightening (RCS)

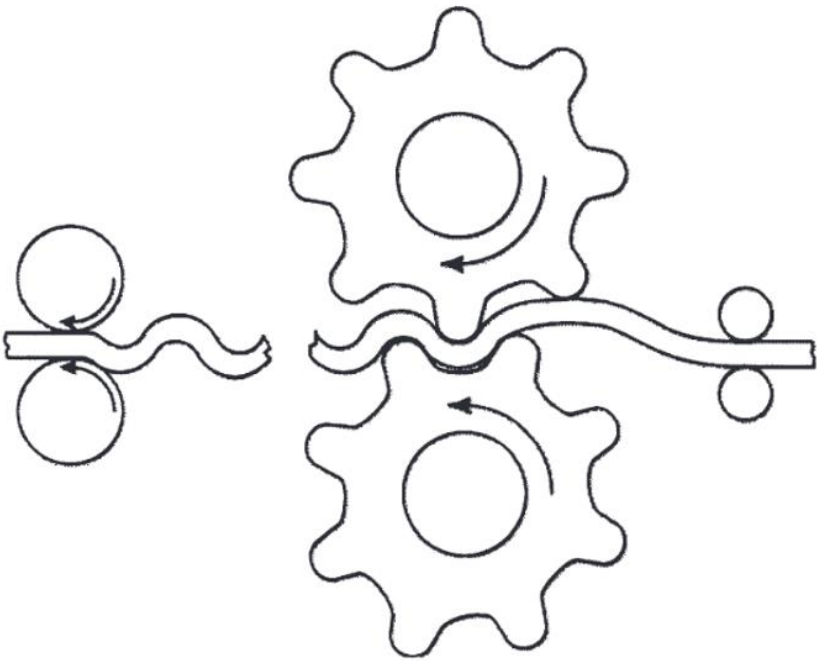

Reference: (J. Y. Huang et al., 2001)

ECAP-based Methods for Sheets (Parallel Channels and Plate ECAP)

Various plate-ECAP concepts apply ECAP-like shear to sheets using parallel channels or constrained shear zones. The dominant challenge is maintaining flatness and preventing out-of-plane buckling of the sheet during the shear step. Controlled back-pressure and guide plates are often used to stabilize the sheet during passage through corners.

For ECAP-type methods, the imposed equivalent strain per pass is commonly estimated from die geometry. A widely used expression relates the strain to channel angle Φ and outer corner curvature angle Ψ (Aida, Matsuki, Horita, & Langdon, 2001; Iwahashi et al., 1996):

$$\varepsilon_{eq} = \frac{2\cot\left(\frac{\Phi}{2}+\frac{\Psi}{2}\right)+\Psi\,\mathrm{cosec}\left(\frac{\Phi}{2}+\frac{\Psi}{2}\right)}{\sqrt{3}}$$

This relation emphasizes why die design is especially critical in thin-walled SPD: decreasing Φ increases strain per pass but also increases the severity of the corner region, where local buckling and strain concentration tend to initiate.

Buckling Prevention and Process Stabilization Strategies

The practical question in thin-walled SPD is not whether instability can occur, but how to engineer tooling and processing conditions so that stable plastic flow is maintained throughout the target strain path. Stabilization strategies can be grouped into die/tool design, supporting elements, pressure assistance, and thermal control.

Die and Tool Design

Die geometry controls both the imposed strain and the stability margin. In ECAP-type tools, the channel angle Φ and the outer corner angle Ψ set the strain per pass and the spatial extent of the shear zone (Aida et al., 2001; Iwahashi et al., 1996). For thin-walled members, a larger Ψ (smoother outer corner) generally reduces local strain gradients and lowers the risk of wrinkling at the inner wall, but it may reduce effective strain per pass. Similarly, increasing the corner radius reduces contact pressure peaks and improves stability, but may enlarge dead-metal zones if friction is high. Finite element studies of ECAP die parameters show that friction factor, corner radii and channel angle strongly influence

strain homogeneity and required load (Djavanroodi & Ebrahimi, 2010b).

Supporting Elements

Internal or external supports are often the most effective buckling suppression measure. Mandrels (rigid or compliant) provide internal support for tubes, raising local buckling stress by reducing the effective unsupported width b and preventing ovalization. Mandrels may be fixed, floating or pressure-assisted, depending on whether axial motion is needed. TCP explicitly uses a fitted mandrel to prevent crumpling while enabling large strain accumulation (Zangiabadi & Kazeminezhad, 2011). Canning or sacrificial cladding involves enclosing a thin-walled workpiece within a thicker outer shell that carries compressive loads and provides lateral constraint. After processing, the can may be removed chemically or mechanically. This strategy is widely used in powder metallurgy and diffusion bonding and is directly transferable to thin-walled SPD when surface protection and constraint are needed.

Sandwich architectures where the thin workpiece is bonded to support sheets during rolling-based SPD can also mitigate edge cracking and waviness in ARB-type processing (Ghalehbandi et al., 2019; Saito et al., 1999).

Back-Pressure Application

Back-pressure is a hallmark stabilization tool in SPD, typically applied through a secondary ram or a pressure-generating element at the die exit (Figure 9). By increasing the mean stress, back-pressure suppresses void growth and helps maintain contact, thereby reducing internal cracking (Bridgman, 1953; Edalati & Horita, 2016). For thin-walled geometries, back-pressure can also stabilize material flow by reducing slip and preventing sudden accelerations through the shear zone. However, because increased

pressure can raise friction and wall compression, the combined use of back-pressure with mandrels or canning is often necessary to avoid shifting the dominant failure mode to wrinkling (Faraji, Kim, & Kashi, 2018; Özbeyaz et al., 2022).

Figure 9 Back-pressure concept in an ECAP-type

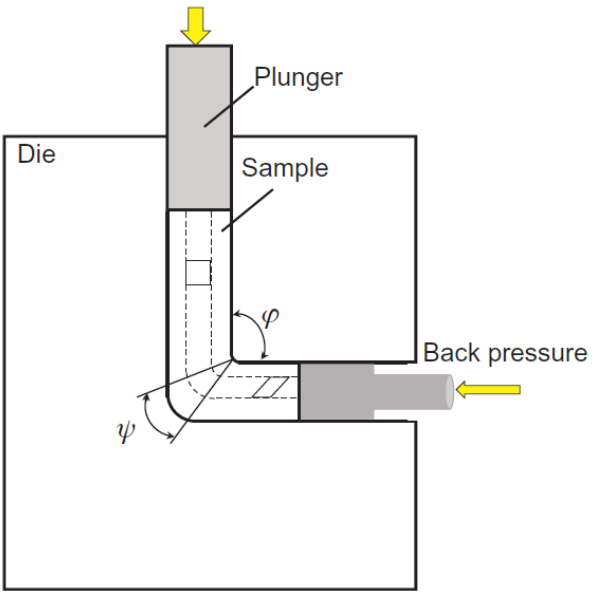

Reference: (Faraji et al., 2018)

Temperature Control

Temperature modifies both constitutive response and instability. Raising temperature reduces flow stress and therefore reduces the compressive loads that drive global buckling. It also increases strain-rate sensitivity in many alloys, which can stabilize plastic flow and delay localization. For magnesium alloys in particular, elevated temperatures activate additional slip systems and can substantially improve formability; nevertheless, high temperature may promote dynamic recrystallization and grain growth, potentially eroding UFG benefits if thermal exposure is prolonged. Therefore, temperature control in thin-walled SPD is best

treated as a coupled design variable: it should be optimized together with processing speed, cooling strategy and pass schedule (Al-Mufadi & Djavanroodi, 2015; Koike et al., 2003; Saito et al., 1999; Ruslan Z. Valiev & Langdon, 2006; Wei, Cheng, Ramesh, & Ma, 2004).

Numerical Modeling (FEM) and Prediction Methods

Simulation is indispensable for thin-walled SPD because experimental trial-and-error is costly and instability windows can be narrow. FEM enables prediction of strain distribution, contact pressures, load–stroke response, and critical instability indicators (wrinkling onset, global buckling modes, localization). However, thin-walled SPD poses special modeling challenges because large strain, severe contact and geometric nonlinearity interact with element distortion and remeshing (Belytschko, Liu, Moran, & Elkhodary, 2014).

Meshing and Remeshing Issues

High gradients near die corners and at contact interfaces require fine meshes, but thin walls demand multiple elements through thickness to capture bending and wrinkling. Consequently, element aspect ratios can become extreme during deformation, and explicit remeshing or adaptive mesh refinement may be required. In practice, one should validate mesh adequacy not only by load–stroke convergence but also by sensitivity of predicted instability onset (e.g., wrinkling wavelength and critical strain) (Belytschko, Liu, Moran, & Elkhodary, 2013; Djavanroodi & Ebrahimi, 2010a).

Buckling Analysis: Explicit vs. Implicit Solvers

Implicit solvers are efficient for quasi-static problems and can incorporate eigenvalue-type buckling analyses on tangent stiffness matrices. Explicit solvers are robust for complex contact and severe nonlinearity but may require careful mass-scaling and

damping control to represent quasi-static conditions. A common workflow is to use explicit simulation to obtain a realistic deformed configuration and stress state, then perform a linearized buckling analysis (or a perturbation analysis) to identify the most dangerous modes. For local wrinkling, geometric imperfections must be introduced (measured or assumed) because perfect models may delay instability unrealistically (Faraji et al., 2012; Harewood & McHugh, 2007).

Integration of Damage Models

Damage models based on stress triaxiality and equivalent strain can be integrated to predict fracture and to quantify the benefit of back-pressure or hydrostatic confinement. Comparative work on fracture model calibration highlights that model selection must match the stress state path (Drucker, 1952). For thin-walled SPD, calibration ideally includes shear-dominated states (near simple shear) as well as bending-dominated states, and it should be validated against observed failure locations (inner corner cracking vs. edge cracking vs. wall wrinkling) (Bao & Wierzbicki, 2004).

Case Studies from the Literature

The following cases illustrate the interplay between microstructural refinement and geometric stability, and how tooling choices determine whether processing succeeds.

Case 1: ECAP-Type Processing of Thin-Walled Tubes Mandrel Effects

Al-Mufadi and Djavanroodi processed thin-walled copper tubes using an ECAP approach with internal support, showing that multi-pass processing can produce substantial strengthening while preserving tube integrity (Al-Mufadi & Djavanroodi, 2015). Although the material is copper, the stability lessons translate directly to aluminum tubes: the mandrel effectively prevents inward

collapse and delays local wrinkling by constraining the wall against radial displacement. The study highlights two practical design takeaways: (i) the mandrel diameter tolerance should be chosen to provide support without excessive friction, and (ii) lubrication strategy must be re-optimized relative to bulk ECAP because contact area is larger and heat generation can be significant in thin walls.

Case 2: Magnesium Sheet/Profiles at Elevated Temperature Fracture vs. Instability

Magnesium alloys benefit strongly from elevated-temperature processing because additional slip systems become active. Nevertheless, processing routes may still fail by fracture if strain localization occurs. Gzyl and co-workers studied fracture during I-ECAP of AZ31B magnesium alloy and emphasized that a fine-grained and homogeneous initial microstructure is required to avoid fracture at low temperatures (Gzyl, Rosochowski, Boczkal, & Qarni, 2015). In rolling-based SPD for magnesium sheets, ARB has been shown to improve mechanical properties when conducted at elevated temperatures compatible with bonding and ductility; for example, Zhan, Li and Chen reported property improvements in Mg-Al-Zn alloy sheets processed by ARB (Zhan et al., 2008). For thin magnesium profiles (e.g., U-sections), newly developed methods such as TWO-CAP demonstrate that thin-walled SPD can be feasible when tooling provides adequate lateral support and deformation is controlled (Şahbaz, Kaya, & Kentli, 2020). Overall, these cases demonstrate that stability and damage mitigation must be tailored to alloy-specific deformation mechanisms.

Comparative Summary

The processing of thin-walled structures (tubes, plates, and open sections) using Severe Plastic Deformation (SPD) requires much more complex boundary conditions and process control

compared to bulk materials. While the primary objective in bulk materials is internal grain refinement, the main challenge in thin-walled structures is to achieve this objective while preserving the macroscopic form and integrity of the specimen. Low wall thickness/diameter ratios or the presence of free edges expose the material to geometric instabilities such as buckling, wrinkling, ovalization, or edge cracking under the applied high hydrostatic pressure and shear forces.

In this context, the literature has developed various mitigation methods to ensure geometric integrity, such as mandrel use, counterpressure application, die constraints, and multi-pass strategies. Table 1 summarizes the main SPD methods customized for thin-walled materials, the geometries targeted by these methods, the predominant instability risks encountered during the process, and the typical solution strategies developed in the literature to address these issues.

Table 1 Representative thin-walled SPD methods, typical instability risks and common mitigation strategies

Method	**Target geometry**	**Dominant instability risk**	**Typical mitigation**	**Representative refs.**
ECAP of tubes with mandrel	Thin-walled tubes	Local wrinkling; ovalization	Internal mandrel; controlled lubrication; back-pressure	(Al-Mufadi & Djavanroodi, 2015)
TCP	Tubes	Crumpling at neck/entry; non-uniform strain	Fitted mandrel; optimized die neck; multi-pass routes	(Zangiabadi & Kazeminezhad, 2011)
HPTT	Tubes	Ovalization; wall shear instability	High confinement pressure; rigid supports; process control	(Tóth et al., 2009)
ARB	Sheets	Edge cracking; waviness; imperfect bonding	Edge trimming; surface prep; sandwich/canning; temperature control	(Ghalehbandi et al., 2019; Saito et al., 1999)
RCS / corrugation-based	Sheets	Folding; thickness non-uniformity	Optimized groove geometry; intermediate anneals; guide constraint	(Sunil, 2015)
TWO-CAP (open sections)	U-profiles, thin beams	Local wall buckling in webs/flanges	Die constraints; supportive tooling; route optimization	(Şahbaz et al., 2020)
PTCAP/TCAP variants	Tubes	Thickness non-uniformity; wrinkling	Parallel channels; mandrels; back-pressure	(Faraji et al., 2012)

Conclusions

Thin-walled SPD processing sits at the intersection of microstructural engineering and structural stability. The main barrier to industrial adoption is not the ability of SPD to refine grains this is well established but the ability to impose large strains in geometries that are intrinsically vulnerable to buckling and wrinkling. The chapter has shown that a successful thin-walled SPD design typically combines:

- geometric support (mandrels, canning, guide plates),
- pressure assistance (back-pressure or hydrostatic confinement) to suppress fracture, and
- die/process parameter optimization to reduce strain gradients and compressive wall stresses.

FEM is essential to predict not only loads and strain distributions but also instability onset.

Future progress is expected from hybrid processing routes that integrate SPD with conventional forming e.g., pre-SPD sheet conditioning followed by stamping, or tube-SPD followed by hydroforming so that UFG microstructures are placed where they provide the most benefit. Equally important are scalable, continuous variants (rolling-based, incremental shear-based) and robust process monitoring/control to manage imperfections that trigger buckling. These developments can enable thin-walled lightweight structures with improved strength, fatigue life and damage tolerance while maintaining manufacturability.

References

Aida, T., Matsuki, K., Horita, Z., & Langdon, T. G. (2001). Estimating the equivalent strain in equal-channel angular pressing. *Scripta Materialia*, *44*(4), 575–579. https://doi.org/10.1016/S1359-6462(00)00640-0

Al-Mufadi, F., & Djavanroodi, F. (2015). Equal-Channel Angular Pressing of Thin-Walled Copper Tube. *Arabian Journal for Science and Engineering*, *40*(9), 2785–2794. https://doi.org/10.1007/s13369-015-1750-6

Altan, T., & Tekkaya, A. E. (2012). *Sheet Metal Forming: Processes and Applications*. ASM International.

Ashby, M. F. (2011). *Materials Selection in Mechanical Design* (Fourth). Burlington, USA: Elsevier.

Bagherpour, E., Pardis, N., Reihanian, M., & Ebrahimi, R. (2019). An overview on severe plastic deformation: Research status, techniques classification, microstructure evolution, and applications. *The International Journal of Advanced Manufacturing Technology*, *100*(5), 1647–1694. https://doi.org/10.1007/s00170-018-2652-z

Bao, Y., & Wierzbicki, T. (2004). On fracture locus in the equivalent strain and stress triaxiality space. *International Journal of Mechanical Sciences*, *46*(1), 81–98. https://doi.org/10.1016/j.ijmecsci.2004.02.006

Belytschko, T., Liu, W. K., Moran, B., & Elkhodary, K. (2013). *Nonlinear Finite Elements for Continua and Structures*. John Wiley & Sons.

Belytschko, T., Liu, W. K., Moran, B., & Elkhodary, K. (2014). *Nonlinear Finite Elements for Continua and Structures*. John Wiley & Sons.

Beytüt, H., Özbeyaz, K., & Temiz, Ş. (2025). A Novel Hybrid Die Design for Enhanced Grain Refinement: Vortex Extrusion–Equal-Channel Angular Pressing (Vo-CAP). *Applied Sciences*, *15*(1), 359. https://doi.org/10.3390/app15010359

Bridgman, P. W. (1953). The Effect of Pressure on the Tensile Properties of Several Metals and Other Materials. *Journal of Applied Physics*, *24*(5), 560–570. https://doi.org/10.1063/1.1721329

Djavanroodi, F., & Ebrahimi, M. (2010a). Effect of die channel angle, friction and back pressure in the equal channel angular pressing using 3D finite element simulation. *Materials Science and Engineering: A*, *527*(4), 1230–1235. https://doi.org/10.1016/j.msea.2009.09.052

Djavanroodi, F., & Ebrahimi, M. (2010b). Effect of die parameters and material properties in ECAP with parallel channels. *Materials Science and Engineering: A*, *527*(29), 7593–7599. https://doi.org/10.1016/j.msea.2010.08.022

Drucker, D. C. (1952). *A more fundamental approach to plastic stress-strain relations*. *II*, 487–491. Chicago: USA.

Ebrahimi, S. H. S., Dehghani, K., Aghazadeh, J., Ghasemian, M. B., & Zangeneh, Sh. (2018). Investigation on microstructure and mechanical properties of Al/Al-Zn-Mg–Cu laminated composite fabricated by accumulative roll bonding (ARB) process. *Materials Science and Engineering: A*, *718*, 311–320. https://doi.org/10.1016/j.msea.2018.01.130

Edalati, K., & Horita, Z. (2016). A review on high-pressure torsion (HPT) from 1935 to 1988. *Materials Science and Engineering: A*, *652*, 325–352. https://doi.org/10.1016/j.msea.2015.11.074

Eizadjou, M., Kazemi Talachi, A., Danesh Manesh, H., Shakur Shahabi, H., & Janghorban, K. (2008). Investigation of structure and

mechanical properties of multi-layered Al/Cu composite produced by accumulative roll bonding (ARB) process. *Composites Science and Technology*, *68*(9), 2003–2009. https://doi.org/10.1016/j.compscitech.2008.02.029

Estrin, Y., & Vinogradov, A. (2013). Extreme grain refinement by severe plastic deformation: A wealth of challenging science. *Acta Materialia*, *61*(3), 782–817. https://doi.org/10.1016/j.actamat.2012.10.038

Faraji, G., Babaei, A., Mashhadi, M. M., & Abrinia, K. (2012). Parallel tubular channel angular pressing (PTCAP) as a new severe plastic deformation method for cylindrical tubes. *Materials Letters*, *77*, 82–85. https://doi.org/10.1016/j.matlet.2012.03.007

Faraji, G., Kim, H. S., & Kashi, H. T. (2018). Severe Plastic Deformation Methods for Bulk Samples. In *Severe Plastic Deformation*. Elsevier. https://doi.org/10.1016/B978-0-12-813518-1.00002-3

Faraji, G., Mashhadi, M. M., & Kim, H. S. (2011). Tubular channel angular pressing (TCAP) as a novel severe plastic deformation method for cylindrical tubes. *Materials Letters*, *65*(19), 3009–3012. https://doi.org/10.1016/j.matlet.2011.06.039

Ghalehbandi, S. M., Malaki, M., & Gupta, M. (2019). Accumulative Roll Bonding—A Review. *Applied Sciences*, *9*(17), 3627. https://doi.org/10.3390/app9173627

Gzyl, M., Rosochowski, A., Boczkal, S., & Qarni, M. J. (2015). The Origin of Fracture in the I-ECAP of AZ31B Magnesium Alloy. *Metallurgical and Materials Transactions A*, *46*(11), 5275–5284. https://doi.org/10.1007/s11661-015-3069-z

Harewood, F. J., & McHugh, P. E. (2007). Comparison of the implicit and explicit finite element methods using crystal plasticity.

Computational Materials Science, *39*(2), 481–494. https://doi.org/10.1016/j.commatsci.2006.08.002

Hill, R. (1958). A general theory of uniqueness and stability in elastic-plastic solids. *Journal of the Mechanics and Physics of Solids*, *6*(3), 236–249. https://doi.org/10.1016/0022-5096(58)90029-2

Huang, J. Y., Zhu, Y. T., Jiang, H., & Lowe, T. C. (2001). Microstructures and dislocation configurations in nanostructured Cu processed by repetitive corrugation and straightening. *Acta Materialia*, *49*(9), 1497–1505. https://doi.org/10.1016/S1359-6454(01)00069-6

Huang, J., Zhu, Y. T., Alexander, D. J., Liao, X., Lowe, T. C., & Asaro, R. J. (2004). Development of repetitive corrugation and straightening. *Materials Science and Engineering: A*, *371*(1), 35–39. https://doi.org/10.1016/S0921-5093(03)00114-X

Ivanov, K. V., & Ovcharenko, V. E. (2020). Structural features of ultrafine-grained aluminum processed through accumulative roll bonding providing improved mechanical properties and thermal stability. *Materials Science and Engineering: A*, *775*, 138988. https://doi.org/10.1016/j.msea.2020.138988

Iwahashi, Y., Wang, J., Horita, Z., Nemoto, M., & Langdon, T. G. (1996). Principle of equal-channel angular pressing for the processing of ultra-fine grained materials. *Scripta Materialia*, *35*(2), 143–146. https://doi.org/10.1016/1359-6462(96)00107-8

Karabey, Ö. (2023). Design, Finite Element Analysis and Optimization of Helical Angular Pressing (HAP) Method as a Novel SPD Technique. *Bitlis Eren Üniversitesi Fen Bilimleri Dergisi*, *12*(4), 959–968. https://doi.org/10.17798/bitlisfen.1295905

Karabey, Ö. (2025, July 11). *Finite Element Analysis of The Effect of Different Cross-Section Geometries on The Plastic Deformation Behavior of Aa5083 Alloy in The Two-Cap Method*. 62–73. Italy: Liberty Publishing House. Retrieved from https://www.eucongress.org/books

Karabey, Ö., & Özbeyaz, K. (2023). Investigating the Effect of Cross-Sectional Geometries in Equal Channel Angular Pressing (ECAP) Method. *3rd INTERNATIONAL RAHVA TECHNICAL AND SOCIAL RESEARCHES CONGRESS*, 181–183. Ankara, Türkiye: Sonçağ Akademi. Retrieved from http://rahva.beu.edu.tr/images/Dergi/Belgeler/3_Rahva_Congress_Book.pdf

Kim, H. S. (2001). Finite element analysis of equal channel angular pressing using a round corner die. *Materials Science and Engineering: A*, *315*(1), 122–128. https://doi.org/10.1016/S0921-5093(01)01188-1

Koike, J., Kobayashi, T., Mukai, T., Watanabe, H., Suzuki, M., Maruyama, K., & Higashi, K. (2003). The activity of non-basal slip systems and dynamic recovery at room temperature in fine-grained AZ31B magnesium alloys. *Acta Materialia*, *51*(7), 2055–2065. https://doi.org/10.1016/S1359-6454(03)00005-3

Kulekci, M. K. (2008). Magnesium and its alloys applications in automotive industry. *The International Journal of Advanced Manufacturing Technology*, *39*(9), 851–865. https://doi.org/10.1007/s00170-007-1279-2

Langdon, T. G. (2013). Twenty-five years of ultrafine-grained materials: Achieving exceptional properties through grain refinement. *Acta Materialia*, *61*(19), 7035–7059. https://doi.org/10.1016/j.actamat.2013.08.018

Megson, T. H. G. (n.d.). *Aircraft Structures for Engineering Students*. Butterworth-Heinemann.

Mesbah, M., Faraji, G., & Bushroa, A. R. (2014). Characterization of nanostructured pure aluminum tubes produced by tubular channel angular pressing (TCAP). *Materials Science and Engineering: A*, *590*, 289–294. https://doi.org/10.1016/j.msea.2013.10.036

Nagasekhar, A. V., Tick-Hon, Y., & Seow, H. P. (2007). Deformation behavior and strain homogeneity in equal channel angular extrusion/pressing. *Journal of Materials Processing Technology*, *192–193*, 449–452. https://doi.org/10.1016/j.jmatprotec.2007.04.093

Olabi, A. G., Morris, E., & Hashmi, M. S. J. (2007). Metallic tube type energy absorbers: A synopsis. *Thin-Walled Structures*, *45*(7), 706–726. https://doi.org/10.1016/j.tws.2007.05.003

Özbeyaz, K., Kaya, H., & Kentli, A. (2022). Novel SPD Method: Twisted Variable Channel Angular Extrusion. *Metals and Materials International*, *28*(5), 1290–1305. https://doi.org/10.1007/s12540-021-01086-4

Özel, S., Beytüt, H., & Karagöz, S. (2019). EFFECT OF FORMING HISTORY ON CRASHWORTHINESS OF A SPOT-WELDED AND DOUBLE-HAT ELLIPTICAL THIN-WALLED TUBE. *European Journal of Technique (EJT)*, *9*(2), 275–285. https://doi.org/10.36222/ejt.621147

Pan, Y., Xiong, Y., Wu, L., Diao, K., & Guo, W. (2021). Lightweight Design of an Automotive Battery-Pack Enclosure via Advanced High-Strength Steels and Size Optimization. *International Journal of Automotive Technology*, *22*(5), 1279–1290. https://doi.org/10.1007/s12239-021-0112-5

Pugh, H. Ll. D., & Green, D. (1964). The Effect of Hydrostatic Pressure on the Plastic Flow and Fracture of Metals. *Proceedings of the Institution of Mechanical Engineers*, *179*(1), 415–437. https://doi.org/10.1243/PIME_PROC_1964_179_030_02

Ramanathan, A., Krishnan, P. K., & Muraliraja, R. (2019). A review on the production of metal matrix composites through stir casting – Furnace design, properties, challenges, and research opportunities. *Journal of Manufacturing Processes*, *42*, 213–245. https://doi.org/10.1016/j.jmapro.2019.04.017

Şahbaz, M., Kaya, H., & Kentli, A. (2020). A new severe plastic deformation method: Thin-walled open channel angular pressing (TWO-CAP). *The International Journal of Advanced Manufacturing Technology*, *106*(3), 1487–1496. https://doi.org/10.1007/s00170-019-04748-1

Saito, Y., Utsunomiya, H., Tsuji, N., & Sakai, T. (1999). Novel ultra-high straining process for bulk materials—Development of the accumulative roll-bonding (ARB) process. *Acta Materialia*, *47*(2), 579–583. https://doi.org/10.1016/S1359-6454(98)00365-6

Segal, V. M. (1995). Materials processing by simple shear. *Materials Science and Engineering: A*, *197*(2), 157–164. https://doi.org/10.1016/0921-5093(95)09705-8

Sunil, B. R. (2015). Repetitive Corrugation and Straightening of Sheet Metals. *Materials and Manufacturing Processes*, *30*(10), 1262–1271. https://doi.org/10.1080/10426914.2014.973600

Theory of Plasticity. (2006). Retrieved from https://shop.elsevier.com/books/theory-of-plasticity/chakrabarty/978-0-7506-6638-1

Timoshenko, S. P., & Woinowsky-Krieger, S. (1959). *Theory of Plates and Shells* (2nd ed.). New York, USA: McGraw-Hill.

Timoshenko, Stephen P., & Gere, J. M. (2012). *Theory of Elastic Stability*. Courier Corporation.

Tóth, L. S., Arzaghi, M., Fundenberger, J. J., Beausir, B., Bouaziz, O., & Arruffat-Massion, R. (2009). Severe plastic deformation of metals by high-pressure tube twisting. *Scripta Materialia*, *60*(3), 175–177. https://doi.org/10.1016/j.scriptamat.2008.09.029

Tsuji, N., Saito, Y., Lee, S.-H., & Minamino, Y. (2003). ARB (Accumulative Roll-Bonding) and other new Techniques to Produce Bulk Ultrafine Grained Materials. *Advanced Engineering Materials*, *5*(5), 338–344. https://doi.org/10.1002/adem.200310077

Valiev, R. Z., Alexandrov, I. V., Zhu, Y. T., & Lowe, T. C. (2002). Paradox of Strength and Ductility in Metals Processed Bysevere Plastic Deformation. *Journal of Materials Research*, *17*(1), 5–8. https://doi.org/10.1557/JMR.2002.0002

Valiev, R. Z, Islamgaliev, R. K., & Alexandrov, I. V. (2000). Bulk nanostructured materials from severe plastic deformation. *Progress in Materials Science*, *45*(2), 103–189. https://doi.org/10.1016/S0079-6425(99)00007-9

Valiev, Ruslan Z., Estrin, Y., Horita, Z., Langdon, T. G., Zechetbauer, M. J., & Zhu, Y. T. (2006). Producing bulk ultrafine-grained materials by severe plastic deformation. *JOM*, *58*(4), 33–39. https://doi.org/10.1007/s11837-006-0213-7

Valiev, Ruslan Z., & Langdon, T. G. (2006). Principles of equal-channel angular pressing as a processing tool for grain refinement. *Progress in Materials Science*, *51*(7), 881–981. https://doi.org/10.1016/j.pmatsci.2006.02.003

Wei, Q., Cheng, S., Ramesh, K. T., & Ma, E. (2004). Effect of nanocrystalline and ultrafine grain sizes on the strain rate sensitivity and activation volume: Fcc versus bcc metals. *Materials Science and*

Engineering: A, *381*(1), 71–79. https://doi.org/10.1016/j.msea.2004.03.064

Wierzbicki, T., & Abramowicz, W. (1983). On the Crushing Mechanics of Thin-Walled Structures. *Journal of Applied Mechanics*, *50*(4a), 727–734. https://doi.org/10.1115/1.3167137

Zangiabadi, A., & Kazeminezhad, M. (2011). Development of a novel severe plastic deformation method for tubular materials: Tube Channel Pressing (TCP). *Materials Science and Engineering: A*, *528*(15), 5066–5072. https://doi.org/10.1016/j.msea.2011.03.012

Zhan, M., Li, Y., & Chen, W. (2008). Improving mechanical properties of Mg-Al-Zn alloy sheets through accumulative roll-bonding. *Transactions of Nonferrous Metals Society of China*, *18*(2), 309–314. https://doi.org/10.1016/S1003-6326(08)60054-0

CHAPTER 8

SELECTIVE LASER MELTING (SLM): A PRECISION-BASED METAL ADDITIVE MANUFACTURING PROCESS

Yasin AKIN[1]
Ömer ÇERLEK[2]

1. Introduction

Additive Manufacturing (AM) is recognized as one of the fundamental pillars of the industry 4.0 vision and, unlike subtractive manufacturing methods such as machining and shaping techniques such as casting and forging, is based on the layer-by-layer addition of material to produce three-dimensional objects (Akın et al., 2025). This approach has led to significant paradigm shifts in manufacturing. First, AM substantially enhances design freedom by enabling the direct fabrication of internal channels, complex lattice structures, and topologically optimized organic geometries that are impossible to manufacture using conventional methods (Akin et al., 2025; Çerlek & Çobaner, 2025; Tüylü et al., 2024). Moreover, particularly in the aerospace and automotive sectors, it has become

[1]Dr, Sakarya University of Applied Sciences, Mechanical Engineering, Orcid: 0000-0003-3201-379X
[2]Asst. Prof. Dr., Sakarya University of Applied Sciences, Mechanical Engineering, Orcid: 0000-0003-2490-5915

possible to reduce component weight by up to 50% without compromising mechanical performance, thereby promoting lightweight and performance-oriented designs (Çerlek et al., 2024; Prathyusha & Raghu Babu, 2022; Çobaner et al., 2024). In addition, AM supports the concept of on-demand production by reducing the need for inventory, while also enabling the economical and rapid manufacture of highly customized products such as patient-specific medical implants (Cui et al., 2021; Kubilay & Aktaş, 2024).

The profound transformation introduced by AM in manufacturing has led to the emergence of different technological approaches depending on the type of feedstock used and the mechanisms by which layers are bonded. Accordingly, additive manufacturing technologies are classified into seven main categories within the framework of ASTM/ISO standards (Dubey et al., 2024). Among the methods prominent in metallic part production is Direct Energy Deposition (DED), in which metal powder or wire feedstock is delivered through a nozzle and simultaneously melted by a laser or electron beam and deposited onto a substrate; this method is particularly suitable for the production of large-scale components and the repair of damaged parts (S.-H. Li et al., 2023). Another important method, Binder Jetting, is based on selectively spraying a liquid binder onto a powder bed to form a “green” part, followed by sintering or furnace treatment to impart the final mechanical properties (M. Li et al., 2020). In Powder Bed Fusion (PBF) processes, intense thermal energy sources such as lasers or electron beams are used to selectively melt specific regions of the powder bed, creating strong metallurgical bonds between layers; within this category, Selective Laser Melting (SLM) stands out as one of the most widely used and advanced techniques in metal additive manufacturing due to its high dimensional accuracy and the superior mechanical properties of the produced parts (Dejene & Lemu, 2023).

Selective Laser Melting (SLM) is an advanced additive manufacturing technique based on the complete melting of metallic powders and their subsequent solidification from the liquid phase. Through this approach, produced parts can achieve relative density values exceeding 99.9%, enabling the fabrication of components with extremely low porosity and high structural integrity. Owing to the fine-grained microstructures formed as a result of rapid melting and solidification cycles, the mechanical properties of SLM-fabricated parts can compete with those of conventionally cast components and, in many cases, even surpass the mechanical performance of forged parts (Pekok et al., 2021).

The process mechanism underlying these superior properties begins with a high-energy laser source, typically a fiber laser, selectively scanning the powder bed by following cross-sectional data derived from a digital CAD model. The SLM process has a cyclic structure consisting of sequential and repetitive steps, each of which directly affects the dimensional accuracy and mechanical properties of the final part (Figure 1). In the first stage of the process, a recoater mechanism spreads a homogeneous layer of metal powder, typically 20–50 μm thick, over the build platform. The uniformity and thickness of this layer are critical to the stability of the subsequent melting process (Nandhakumar & Venkatesan, 2023).

Following the powder spreading step, the process proceeds to the laser scanning stage. At this stage, the laser beam is directed with high speed and precision through galvanometer mirrors, selectively melting the powder particles only in the regions defined by the CAD data. The molten pool formed as a result of the interaction between the laser and the powder bed remains in direct contact with the previously solidified layer and advances in a controlled manner throughout the process. In this way, the melted powder particles establish strong metallurgical bonds with the

underlying layer, forming an integrated and fully consolidated structure (Kaplan et al., 2025).

Figure 1. The working principle of SLM

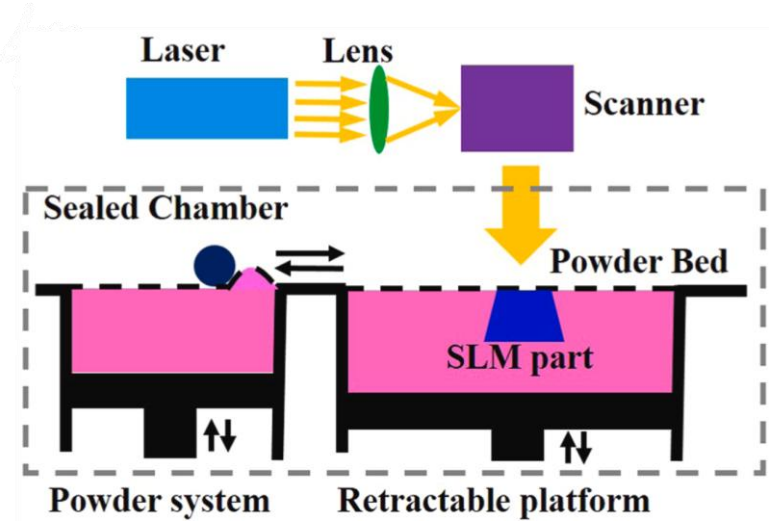

Source:(Wu et al., 2021)

After the completion of laser scanning and melting, the build platform is lowered by one layer thickness, and the system returns to the powder spreading stage for the next layer. This cycle is repeated consecutively until the entire part geometry is fully formed, with each new layer being built in complete conformity with the previous one. Consequently, the SLM process enables the production of metallic components with high precision, high density, and superior mechanical properties through micrometer-scale layer deposition (Abd-Elaziem et al., 2022).

The density, microstructure, and mechanical performance of parts produced by the SLM method are directly dependent on the delicate balance among process parameters. This balance, referred to in the literature as the “process window,” defines the range of parameters within which stable laser–material interaction can be maintained. In this context, laser power (P) provides the thermal

energy required to fully melt the metal powder, while scanning speed (v) determines the laser travel rate across the powder bed and controls the lifetime and cooling rate of the molten pool. The hatch spacing (h), defined as the distance between adjacent laser scan tracks, influences the quality of intra-layer bonding, whereas the layer thickness (t) is a key parameter governing both vertical resolution and production rate. Rather than evaluating these parameters individually, the concept of volumetric energy density (VED) is employed to assess their combined effect. VED represents the amount of energy delivered per unit volume and is defined by the following expression (Pechlivani et al., 2023):

$$VED = \frac{P}{v \cdot h \cdot t} \tag{1}$$

Maintaining the VED value within the process window is critical for achieving a dense and defect-free structure. Very low VED values lead to incomplete melting of the powder, resulting in lack-of-fusion defects and irregular porosity (Figure 2a). In contrast, excessively high VED values cause localized metal vaporization, which promotes the formation of deep and spherical keyhole-type pores (Figure 2b). Therefore, in SLM process design, VED is regarded as a central parameter for process optimization.

Figure 2. Optical images obtained at (a) high VED (1400 J/mm³) and (b) low VED (117 J/mm³) values.

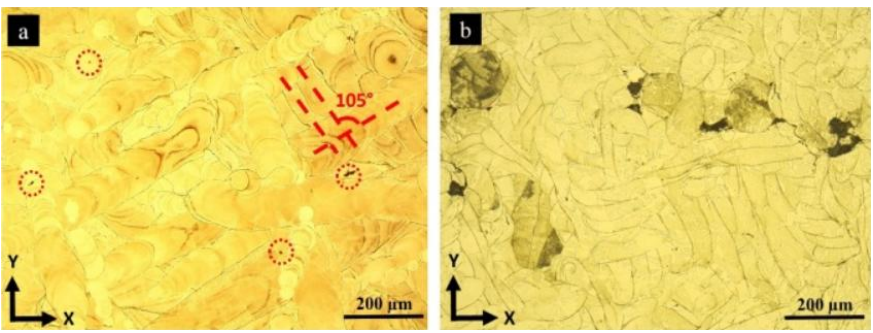

Source: (Ghayoor et al., 2020)

Another fundamental aspect directly related to process parameters is the heat transfer and solidification mechanisms occurring during the SLM process. Due to the extremely high energy density of the laser and its short interaction time, very high cooling rates on the order of 10^4-10^6 K/s are achieved in SLM. These rapid cooling conditions promote the formation of fine-grained, and even cellular or columnar, microstructures that are not typically observed in conventional manufacturing methods, thereby significantly influencing the mechanical properties of the material (Chen et al., 2020).

Within the molten pool, Marangoni convection plays a decisive role in governing fluid flow behavior. Temperature gradients induce variations in surface tension, causing rapid circulation of the liquid metal and the development of complex flow patterns within the melt pool. This flow enhances the homogeneous distribution of alloying elements and contributes to the reduction of chemical segregation. However, instability in the flow regime may also lead to fluctuations in melt pool geometry and promote pore formation (Song et al., 2020).

Moreover, the rapid and repetitive heating–cooling cycles inherent to the SLM process result in the accumulation of high residual stresses in the fabricated parts. If these thermal stresses are not adequately controlled, severe structural defects such as warpage, dimensional inaccuracies, and even interlayer delamination may occur. Therefore, the use of preheated build platforms, the selection of appropriate scanning strategies, and the application of post-process stress-relief heat treatments are considered critical complementary measures for ensuring structural integrity in SLM processes (Cheng et al., 2016).

The primary objective of this book chapter is to comprehensively analyze the metallurgical fundamentals of Selective Laser Melting (SLM), the effects of process parameters on

material performance, and the design flexibility offered by this innovative manufacturing technique in light of current literature. By integrating theoretical concepts with practical industrial insights, the study aims to provide a valuable reference for researchers and engineers. Accordingly, the subsequent sections will address the unique microstructural characteristics arising during the SLM process and the theory of rapid solidification (Chapter 2), followed by an in-depth examination of metallurgical defects encountered during processing and strategies for their mitigation (Chapter 3). Chapter 4 will then present material-based performance analyses across a broad range of systems, from steels and titanium composites to magnesium alloys and the hydrogen embrittlement resistance of austenitic stainless steels. The book concludes with future technological perspectives and a final conclusions section.

2. Microstructural Characteristics and Solidification Theory

The Selective Laser Melting (SLM) process is thermodynamically defined as a distinctly non-equilibrium solidification mechanism. While cooling rates in conventional casting processes are typically in the range of 1–100 K/s, SLM achieves cooling rates as high as 10^4-10^6 K/s. These extremely rapid solidification conditions lead to profound changes in atomic arrangements, phase formation mechanisms, and microstructural evolution. As a result, fine-scale microstructures, metastable phases, and unconventional elemental distributions can be formed (Takata et al., 2019).

2.1. Solidification Morphology and the G/R Ratio

The solidification morphology developed during SLM—whether equiaxed, dendritic, or cellular—is primarily governed by the relationship between the thermal gradient (G) and the solidification rate (R). The G/R ratio is widely accepted as a key parameter that determines the stability of the solid–liquid interface

and the resulting growth mode (Figure 3). In the SLM process, the thermal gradient (G) reaches very high values due to the intense laser energy input, while the solidification rate (R) varies predominantly with the laser scanning speed. High G/R ratios promote the formation of cellular solidification morphologies, which are commonly observed in SLM-fabricated components (Dong et al., 2020).

Figure 3. a) Evolution of the thermal gradient (G) and solidification rate (R) within the melt pool, and b) evolution of the solidification mode in the melt pool.

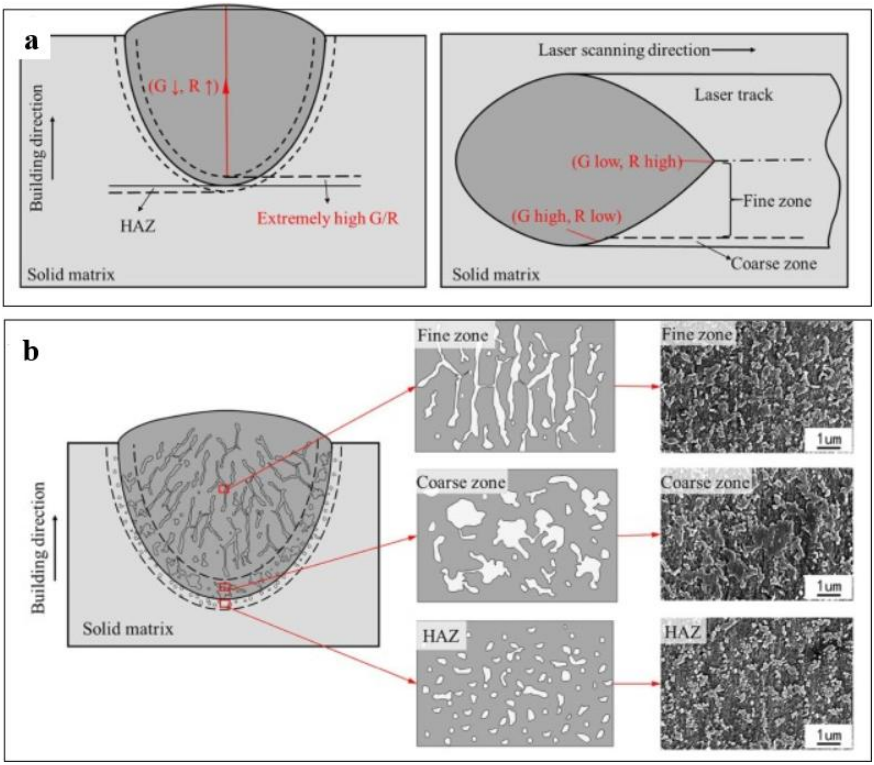

Source: (X. Wang et al., 2024)

Another important indicator of solidification kinetics is the product G×R, which represents the cooling rate. As the cooling rate increases, the spacing between adjacent cells decreases significantly,

leading to a progressively finer microstructure. According to results reported in the literature, cellular feature sizes in AlSi10Mg alloys produced by SLM can be reduced to approximately 0.5–1.0 μm (Aboulkhair et al., 2014).

2.2. Cellular Substructures and Elemental Distribution

One of the distinctive microstructural features of SLM-fabricated materials is the presence of numerous sub micrometer-scale cellular substructures within each grain. During solidification, the primary matrix element (e.g., Al or Fe) solidifies preferentially, while alloying elements such as Si, Cr, and Ni are rejected at the solid–liquid interface and segregate along the cell boundaries. This phenomenon, commonly referred to in the literature as solute segregation, leads to the formation of an element-rich network along the cellular boundaries (Park et al., 2021).

Figure 4. a) Hydrogen micro-printing of the SLM-fabricated material, and b) schematic illustration of the microstructures and hydrogen distributions.

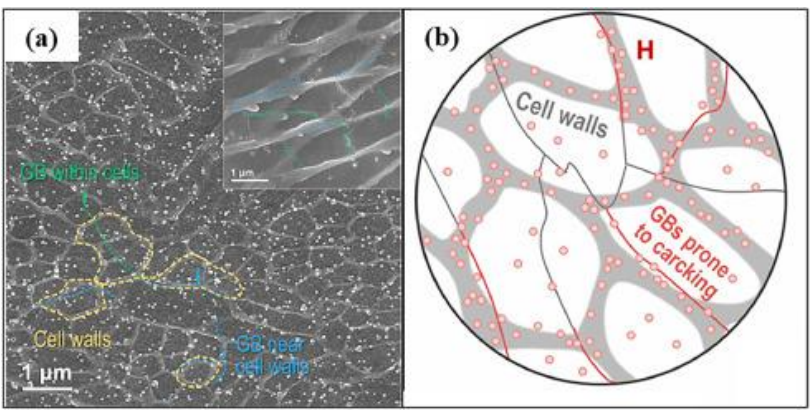

Source:(Zhou et al., 2025)

This cellular network has particularly important functional implications in austenitic stainless steels. For instance, in SLM-produced 316L stainless steel, the dense networks formed at the cell boundaries hinder the free diffusion of hydrogen atoms within the

material, causing the cell boundaries to act as effective “hydrogen traps” (Figure 4). As a result, such SLM-fabricated steels have been reported to exhibit enhanced resistance to hydrogen embrittlement compared to their conventionally manufactured counterparts (Mei et al., 2024).

2.3. Crystallographic Texture and Epitaxial Growth

Metallic parts produced by SLM often exhibit pronounced crystallographic textures. In Figure 5, the crystallographic texture in Area I was analyzed using inverse pole figures (IPFs) of the YZ plane. A dominant ⟨111⟩ ∥ Z orientation was observed in Area I, which can be attributed to the directional heat flow and epitaxial grain growth inherent to the SLM process (Kolomy et al., 2024). The energy density applied during laser melting governs the melt pool geometry and solidification conditions, thereby directly influencing the intensity of the crystallographic texture. Consequently, variations in texture observed across different regions can be correlated with local differences in energy input throughout the process.

Figure 5. (a) EBSD orientation map and grain boundaries, (b) areal distribution of the maximum Feret diameter, and (c) inverse pole figures (IPFs) obtained for the YZ plane.

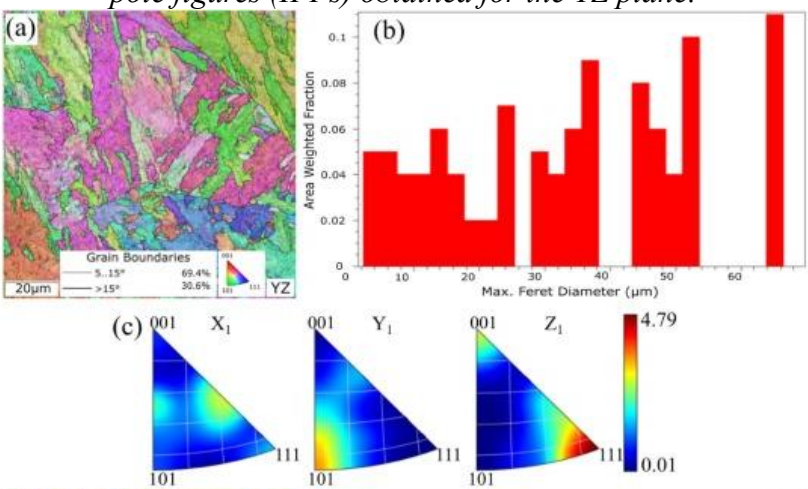

Source: (Kolomy et al., 2024).

This columnar grain structure formed as a result of epitaxial growth gives rise to pronounced anisotropy in the material. Mechanical properties may differ significantly between the build direction (Z-axis) and the horizontal plane (XY-plane). For instance, Taylor Anvil tests conducted on M300 maraging steel have shown that the dynamic deformation behavior varies depending on grain orientation, leading to directional differences in yielding behavior (Kolomy et al., 2024).

2.4. Thermal Cycles and In-situ Heat Treatment Effects

During the SLM process, the fabrication of each new layer not only reheats the top surface but also subjects multiple underlying layers to repeated thermal exposure. As a result, the material experiences numerous thermal cycles throughout the build process. This phenomenon is commonly referred to in the literature as intrinsic heat treatment. Repeated heating and cooling cycles can activate tempering or precipitation-hardening mechanisms in certain alloys during fabrication (Deirmina et al., 2019).

As illustrated in Figure 6, the intrinsic heat treatment effect occurring during the SLM process leads to the formation of both needle-like (indicated by yellow arrows) and globular-type (indicated by red arrows) precipitates within the microstructure. The presence of these precipitates indicates that the repeated heating–cooling cycles inherent to layer-by-layer fabrication trigger precipitation mechanisms, resulting in precipitation behavior that is consistent with findings reported in the literature (Tan et al., 2017).

Figure 6. TEM image of nanoscale precipitates formed as a result of the intrinsic heat treatment effect during the SLM process; needle-like precipitates are indicated by yellow arrows, while globular-type precipitates are indicated by red arrows.

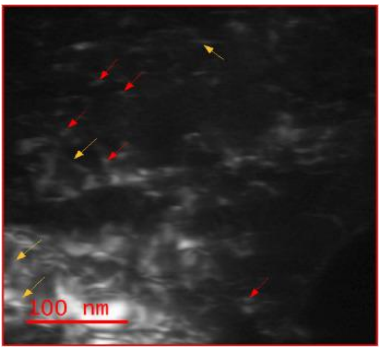

Source: (Vishwakarma et al., 2020)

2.5. Origin of Microstructural Defects

Although the microstructure obtained by SLM is generally composed of fine and well-organized cellular features, process instabilities may give rise to various microstructural defects. One of the most common defects is gas porosity, which originates from gases trapped within powder particles or from turbulence in the protective gas atmosphere that becomes entrained in the molten pool. This type of defect typically appears as spherical pores within the material. Another critical defect is hot tearing, which occurs when thin liquid films remaining along grain boundaries during the final stages of solidification rupture under tensile stresses. This phenomenon is particularly prevalent in the SLM processing of magnesium alloys, where the narrow process window significantly increases susceptibility to hot tearing (Snow et al., 2020).

3. Metallurgical Defects and Mitigation Strategies

The stable operation of the Selective Laser Melting (SLM) process relies on the precise balance of the complex and dynamic energy transfer between the laser source and the powder bed. Disruption of this balance can destabilize the molten pool and lead to the formation of various metallurgical

defects that directly compromise the mechanical integrity of the final component (T. Yang et al., 2020). This section discusses the most frequently reported defect types in the SLM literature, along with mitigation strategies developed based on experimental observations and numerical simulations.

Figure 7 schematically illustrates the relationship between the laser–powder interaction (LPMP system) and the internal defects formed during the SLM process. Phenomena such as balling, spatter, and keyhole formation occurring within the molten pool as a result of laser–powder bed interaction are identified as the primary micro-mechanisms responsible for defects including lack of fusion, gas porosity, and microcracking. These mechanisms directly influence molten pool stability and promote oxidation, residual stress accumulation, and bonding deficiencies during processing. Consequently, they are regarded as critical factors governing the internal structural integrity of SLM-fabricated components (G. Yang et al., 2022).

Figure 7. Schematic diagram illustrating the relationship between laser–powder interaction (LPMP system) and internal defects during the Selective Laser Melting (SLM) process.

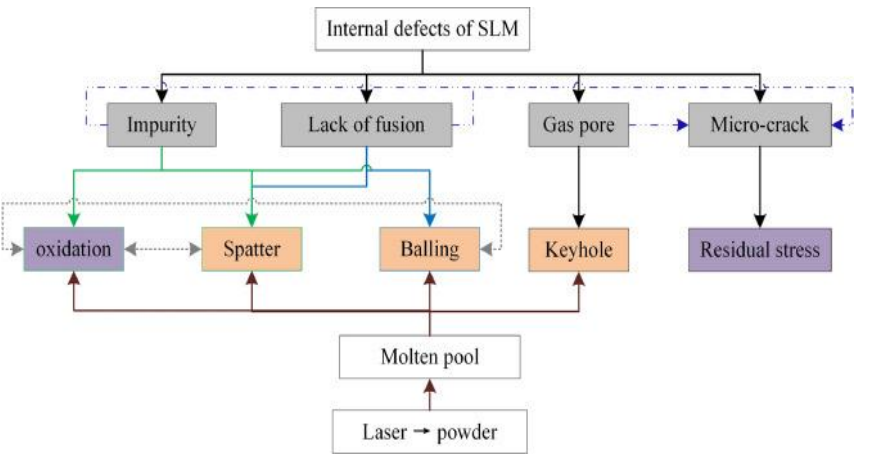

Source: (G. Yang et al., 2022)

3.1. Porosity Mechanisms

Porosity is one of the most common and critical defect types observed in SLM-fabricated parts and generally arises through two primary mechanisms.

3.1.1. Lack of Fusion (LoF)

Lack of fusion occurs when the volumetric energy density (VED) is insufficient to fully melt the metal powder, resulting in discontinuous regions between adjacent tracks or layers. Pores formed by this mechanism are typically irregular in shape and angular in morphology, often containing unmelted or partially melted powder particles (Figure 8). This type of defect is particularly detrimental from a mechanical standpoint, as it leads to significant reductions in tensile strength and fatigue performance (G. Yang et al., 2022). The literature reports that optimizing the energy input—most commonly by increasing laser power or reducing scanning speed—can substantially mitigate lack-of-fusion defects (Guo et al., 2019).

Figure 8. Defects arising from mismatches between laser and powder parameters during the SLM process (G. Yang et al., 2022).

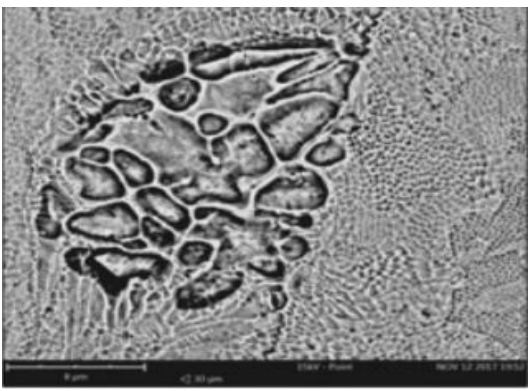

Source: (G. Yang et al., 2022)

3.1.2. Gas Porosity

Gas porosity originates from gases trapped during the powder production process or from voids formed as a result of partial metal

vaporization at high temperatures during SLM. These pores are typically small, spherical in shape, and characterized by smooth internal surfaces (Hojjatzadeh et al., 2020). Gas porosity is considered a critical defect, particularly in applications requiring high density and structural integrity. To mitigate this defect, drying the metal powders prior to processing to remove moisture and optimizing the protective gas flow rate during fabrication are commonly recommended strategies (Ge et al., 2021).

3.2. Keyhole Effect

At high laser power combined with low scanning speed, the laser energy can reach the boiling point of the metal, leading to intense vaporization. Under these conditions, the generated metal vapor forms a narrow and deep cavity within the molten pool, commonly referred to as a "keyhole" (Ge et al., 2021). The instability and subsequent collapse of the keyhole can trap large and deep spherical pores inside the part (Figure 9).

Figure 9. Keyhole-shaped pore surrounding unmelted powder particles (Aboulkhair et al., 2014).

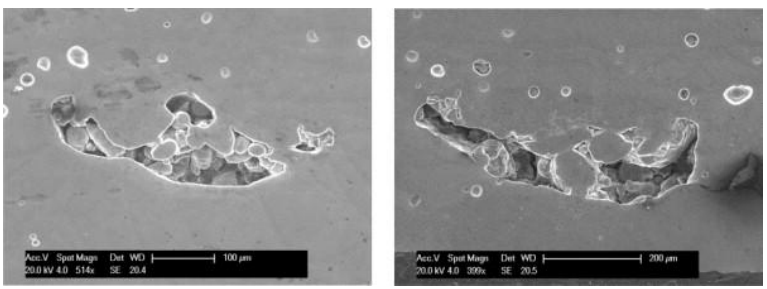

Source: (Aboulkhair et al., 2014)

Such pores pose a significant risk, particularly in aerospace applications, as they act as critical initiation sites for fatigue cracks (Aboulkhair et al., 2014). Therefore, careful balancing of laser power and scanning speed is of critical importance to prevent keyhole formation.

3.3. Balling Phenomenon

The balling phenomenon occurs when the molten metal fails to adequately wet the underlying layer and surface tension becomes dominant, causing the liquid metal to agglomerate into spherical droplets. This defect is typically associated with excessively high scanning speeds or elevated oxygen content in the powder bed, both of which increase surface tension (Gong et al., 2014). Balling leads to surface discontinuities that hinder uniform spreading of subsequent powder layers and severely deteriorate surface quality, resulting in a pronounced increase in surface roughness (Ra).

Figure 10. Formation mechanism of the balling effect.

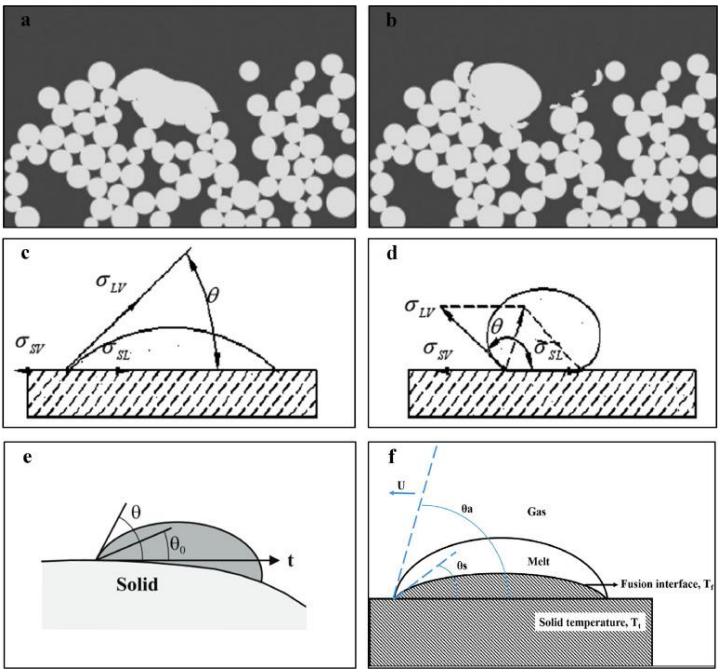

Source: (G. Yang et al., 2022)

Figure 10 illustrates the wetting behavior of the melt pool on a solid surface during the SLM process. Under good wetting conditions ($0°<\theta<90°$), the molten metal spreads effectively over the solid surface, resulting in a stable melt pool. In contrast, when $\theta>90°$,

wetting becomes ineffective, and due to the resultant effect of surface tension forces and Marangoni convection, the liquid phase contracts into a spherical shape, exhibiting a tendency toward balling (G. Yang et al., 2022).

3.4. Spatter Behavior

During the Selective Laser Melting (SLM) process, spatter behavior is a fundamental phenomenon arising from melt pool instability and the entrainment effect of metal vapor during laser–powder interaction (Yin et al., 2020). Spatter mainly originates from two sources: droplet spatter, which consists of molten metal ejected from the melt pool, and powder spatter, which occurs when powder particles are dragged by metal vapor through the Bernoulli effect. The literature reports that powder spatter constitutes the majority of total spatter, with the metal vapor plume playing a dominant role in this process (Gunenthiram et al., 2018).

Droplet spatter forms when molten metal detaches from the melt pool under the combined effects of recoil pressure, Marangoni convection, and surface tension, whereas powder spatter occurs when metal vapor entrains the surrounding gas and draws powder particles toward the laser interaction zone. Increases in laser power and scanning speed significantly raise the amount, ejection velocity, and directionality of spatter. Moreover, powder morphology and protective gas pressure exert critical influences on spatter behavior (Ly et al., 2017).

Spattered particles may fall back onto the powder bed during fabrication, leading to internal defects such as satellite clusters, porosity, lack of fusion, and surface irregularities. Therefore, understanding spatter formation mechanisms and effectively controlling energy input, scanning parameters, and the gas environment are essential for ensuring the internal structural integrity of SLM-fabricated components (Liu et al., 2021).

4. Application Areas and Performance Analyses of SLM Technology

Selective Laser Melting (SLM) has increasingly replaced conventional manufacturing techniques in many industries due to its high design flexibility, superior density levels, and the ability to achieve mechanical properties that are difficult to obtain using traditional methods. The capability to fabricate complex geometries as monolithic components, precisely control material performance through process parameters, and design functional properties at the microstructural level has positioned SLM as a strategic manufacturing method for advanced engineering applications. This section provides a comprehensive evaluation of the key application areas of SLM technology and the performance characteristics of materials used in these domains.

4.1. Biomedical and Dental Applications

SLM technology has driven a significant transformation in biomedical and dental applications, where personalized production is essential. Titanium, cobalt–chromium (Co–Cr), and magnesium alloys are among the most commonly used materials in this field due to their biocompatibility and mechanical properties. In particular, for the fabrication of fixed dental prostheses (FDPs), SLM offers significantly higher dimensional accuracy and repeatability compared to conventional casting methods. Systematic studies have demonstrated that Co–Cr prostheses produced by SLM exhibit marginal and internal fit values within clinically acceptable limits; however, build orientation and support structure geometry directly affect the final fit (Dzhendov & Dikova, 2016).

Biodegradable magnesium alloys have also attracted attention for bone fixation devices such as screws and plates due to their elastic modulus close to that of human bone and their ability to degrade controllably in the body. The SLM process enables precise

design of porous scaffold structures in such implants, thereby promoting cell adhesion and osteointegration (Zhang et al., 2020).

4.2. Aerospace and Defense Industry: Metal Matrix Composites

The aerospace and defense industries require materials capable of operating under extreme temperatures, pressures, and dynamic loads while maintaining a low weight-to-strength ratio. In this context, metal matrix composites (MMCs) produced via SLM—particularly titanium- and aluminum-based systems—offer substantial advantages. In titanium matrix composites (TMCs), the combination of titanium's low density with the high hardness of ceramic reinforcements such as TiC or TiB_2 significantly enhances wear resistance and specific strength. SLM enables the direct fabrication of these composites into complex engine components and structural elements, delivering superior performance compared to conventional titanium alloys (Fereiduni et al., 2020).

Similarly, particulate-reinforced aluminum matrix composites (PAMCs) produced by SLM exhibit extremely fine and homogeneous reinforcement distributions due to rapid solidification conditions. This microstructural refinement contributes notably to improved fatigue resistance, which is critical for aircraft structural components (P. Wang et al., 2020).

4.3. Advanced Engineering Structures: Auxetic Metamaterials

The design freedom offered by SLM enables the fabrication of auxetic structures possessing a negative Poisson's ratio—materials that are rarely found in nature. Auxetic structures contract laterally under compressive loading instead of expanding, providing exceptional energy absorption capabilities. This unique behavior offers significant advantages in applications such as automotive bumpers, ballistic armor, and advanced helmet systems (Bronder et al., 2022). Furthermore, re-entrant or chiral auxetic lattice structures produced by SLM can serve as sandwich panel cores, delivering high

buckling resistance and energy absorption at low weight (Mercer et al., 2022).

4.4. Energy and Chemical Industry: Hydrogen Storage and Resistance

In the transition toward green energy, the safe storage and transportation of hydrogen have become critical research topics in the energy and chemical industries. Austenitic stainless steels—particularly 316L—are widely used in high-pressure hydrogen storage tanks. SLM-fabricated 316L stainless steels have been reported to exhibit enhanced resistance to hydrogen embrittlement due to their fine cellular microstructures and dense dislocation networks, which slow hydrogen diffusion along grain boundaries compared to conventionally manufactured steels (Lin et al., 2020; Zheng et al., 2023).

4.5. Applications under Dynamic Loading: M300 Maraging Steel

M300 maraging steel is widely used in defense applications requiring high impact and collision resistance due to its excellent strength–ductility balance. Taylor Anvil tests conducted on SLM-fabricated M300 steel have demonstrated that the material maintains superior deformation capability and hardness balance even at impact velocities of approximately 185 m/s. These findings confirm the reliability and performance-oriented nature of SLM technology for critical applications such as ammunition components and armor-piercing systems (Kolomy et al., 2024).

The success of SLM across various industries stems not only from its ability to fabricate components but also from its potential to enhance material efficiency and functional integration. While traditional manufacturing adheres to the principle that “complexity increases cost,” SLM transforms complexity into a performance-enhancing advantage. Weight reduction in aerospace applications leads to fuel savings, while patient-specific anatomical compatibility

in biomedical applications shortens recovery times—both representing tangible value propositions of SLM. Nevertheless, literature case studies indicate that sustaining this success requires material-specific optimization of process-related defect mechanisms and microstructural anisotropy. Consequently, SLM has evolved beyond a prototyping tool to become a mature industrial standard for producing high-value, mission-critical components across sectors ranging from defense and healthcare to energy and automotive industries (Sefene, 2022).

5. Conclusions and Future Perspectives

Over the past decade, Selective Laser Melting (SLM) technology has evolved from a rapid prototyping tool into a mature and reliable manufacturing method for producing high-value and mission-critical engineering components. The solidification physics, microstructural evolution, metallurgical defects, failure mechanisms, and multidisciplinary application examples discussed in this chapter clearly demonstrate the current scientific and industrial maturity of SLM. At the same time, the technology's future development potential is both broad and profound. In this context, the key directions along which SLM is expected to evolve are outlined below.

5.1. Artificial Intelligence and Machine Learning–Based Process Control

One of the primary challenges in SLM is the nonlinear and complex interaction among numerous process parameters, including laser power, scanning speed, layer thickness, and scanning strategies. These interactions can lead to unpredictable defects such as porosity, microcracking, and geometric deviations. Artificial intelligence (AI) and machine learning–based approaches are expected to offer transformative solutions to these challenges.

Through real-time in-situ monitoring systems, data acquired from high-speed cameras, photodiodes, and thermal sensors can be analyzed instantaneously. Deviations in melt pool geometry or energy density can thus be detected during fabrication, enabling automatic parameter adjustment and paving the way for closed-loop SLM systems.

5.2. Hybrid Manufacturing Approaches

Although SLM offers unparalleled design freedom, conventional manufacturing methods remain advantageous in terms of surface quality, production speed, and economic fabrication of large-scale components. As a result, hybrid manufacturing systems that integrate SLM with CNC machining or forging are expected to gain prominence. Such approaches enable complex internal geometries to be produced by SLM, followed by post-processing to improve surface finish and dimensional tolerances. In large aerospace and energy components, producing the main body via casting and functional regions via SLM represents a strategically promising manufacturing model.

5.3. Next-Generation Alloy Design: "Additive-First" Materials

Most alloys currently used in SLM were originally developed for conventional casting or forging. However, the extreme cooling rates, repeated thermal cycles, and localized energy inputs characteristic of SLM limit the full exploitation of these alloys. This has driven the emergence of "additive-first" alloys—materials specifically designed for additive manufacturing processes.

5.4. Sustainability and Circular Economy Perspective

One of the core advantages of additive manufacturing is its near-zero-waste principle, which aligns closely with global sustainability and carbon reduction goals. In SLM, improvements in powder recycling, control of powder aging, and optimization of energy consumption will further reduce environmental impact. In the

future, SLM facilities integrated with renewable energy sources, low-carbon production lines, and circular-economy-oriented powder management systems will strengthen the strategic position of SLM, particularly in aerospace, energy, and defense industries.

5.5. General Assessment and Conclusions

Overall, Selective Laser Melting is not merely a manufacturing technique but an interdisciplinary research domain situated at the intersection of materials science, mechanical engineering, and digital technologies. The theoretical and applied insights presented in this chapter highlight the decisive roles of microstructure control, precise process parameter optimization, and Design for Additive Manufacturing (DfAM) approaches in ensuring the reliability of SLM-fabricated components. With the integration of AI-based process control, next-generation alloy development, and sustainable manufacturing strategies, SLM is expected to transform the concept of "mass customization" into an industrial reality in the coming years—positioning it as a central pillar of the future manufacturing ecosystem.

Reference

Abd-Elaziem, W., Elkatatny, S., Abd-Elaziem, A.-E., Khedr, M., Abd El-baky, M. A., Hassan, M. A., Abu-Okail, M., Mohammed, M., Järvenpää, A., Allam, T., & Hamada, A. (2022). On the current research progress of metallic materials fabricated by laser powder bed fusion process: A review. *Journal of Materials Research and Technology*, *20*, 681–707. https://doi.org/10.1016/j.jmrt.2022.07.085

Aboulkhair, N. T., Everitt, N. M., Ashcroft, I., & Tuck, C. (2014). Reducing porosity in AlSi10Mg parts processed by selective laser melting. *Additive Manufacturing*, *1–4*, 77–86. https://doi.org/10.1016/j.addma.2014.08.001

Akin, Y., Han, K., Çerlek, Ö., & Seçgin, Ö. (2025). Impact of Epoxy Infill on the Mechanical Strength of ABS Specimens Produced by Fused Filament Fabrication. *Arabian Journal*

for Science and Engineering. https://doi.org/10.1007/s13369-025-10341-4

Akın, Y., Han, K., Tüylü, A., Aktaş, N. F., Çobaner, S., Çerlek, Ö., Kesercioğlu, M. A., Kılıç, R., & Seçgin, Ö. (2025). Compressive strength and performance of horizontally and vertically oriented hybrid lattice structures manufactured by stereolithography. *Proceedings of the Institution of Mechanical Engineers, Part E: Journal of Process Mechanical Engineering*, 09544089251400793. https://doi.org/10.1177/09544089251400793

Bronder, S., Herter, F., Röhrig, A., Bähre, D., & Jung, A. (2022). Design Study for Multifunctional 3D Re-entrant Auxetics. *Advanced Engineering Materials*, *24*(1), 2100816. https://doi.org/10.1002/adem.202100816

Çerlek, Ö., & Çobaner, S. (2025). Selective laser sintering (SLS): A high precision additive manufacturing process. Allsciences Academy.

Çerlek, Ö., Kesercioğlu, M. A., & Han, K. (2024). Stereolithography (SLA): An Innovative Additive Manufacturing Process. *New Trends and Frontiers in Engineering*, 399–412.

Çobaner, S., Kesercioğlu, M. A., & Aktaş, N. F. (2024). Eklemeli İmalat Parametrelerinin Eğilme Dayanıklılığına Etkisinin İncelenmesi. Presented at the 4. Bilsel Internatıonal Harput Scıentıfıc Researches Congress 09-10 November Elazığ/Türkiye.

Chen, Y., Chen, H., Chen, J., Xiong, J., Wu, Y., & Dong, S. (2020). Numerical and experimental investigation on thermal behavior and microstructure during selective laser melting of high strength steel. *Journal of Manufacturing Processes*, *57*, 533–542. https://doi.org/10.1016/j.jmapro.2020.06.041

Cheng, B., Shrestha, S., & Chou, Y. K. (2016). Stress and Deformation Evaluations of Scanning Strategy Effect in Selective Laser Melting. *Volume 3: Joint MSEC-NAMRC Symposia*, V003T08A009. https://doi.org/10.1115/MSEC2016-8819

Cui, W., Yang, Y., Di, L., & Dababneh, F. (2021). Additive manufacturing-enabled supply chain: Modeling and case studies on local, integrated production-inventory-

transportation structure. *Additive Manufacturing*, *48*, 102471. https://doi.org/10.1016/j.addma.2021.102471

Deirmina, F., Peghini, N., AlMangour, B., Grzesiak, D., & Pellizzari, M. (2019). Heat treatment and properties of a hot work tool steel fabricated by additive manufacturing. *Materials Science and Engineering: A*, *753*, 109–121. https://doi.org/10.1016/j.msea.2019.03.027

Dejene, N. D., & Lemu, H. G. (2023). Current Status and Challenges of Powder Bed Fusion-Based Metal Additive Manufacturing: Literature Review. *Metals*, *13*(2), 424. https://doi.org/10.3390/met13020424

Dong, S., Zhang, X., Ma, F., Jiang, J., & Yang, W. (2020). Research on deposited tracks and microstructures of AlSi10Mg alloy produced by selective laser melting. *Applied Physics A*, *126*(8), 643. https://doi.org/10.1007/s00339-020-03826-6

Dubey, D., Singh, S. P., & Behera, B. K. (2024). A review on recent advancements in additive manufacturing techniques. *Proceedings of the Institution of Mechanical Engineers, Part E: Journal of Process Mechanical Engineering*, 09544089241275860. https://doi.org/10.1177/09544089241275860

Dzhendov, D., & Dikova, T. (2016). Application of Selective Laser Melting in Manufacturing of Fixed Dental Prostheses. *Journal of IMAB – Annual Proceeding Scientific Papers*, *22*(4), 1414–1417. https://doi.org/10.5272/jimab.2016224.1414

Fereiduni, E., Ghasemi, A., & Elbestawi, M. (2020). Selective Laser Melting of Aluminum and Titanium Matrix Composites: Recent Progress and Potential Applications in the Aerospace Industry. *Aerospace*, *7*(6), 77. https://doi.org/10.3390/aerospace7060077

Ge, W., Fuh, J. Y. H., & Na, S. J. (2021). Numerical modelling of keyhole formation in selective laser melting of Ti6Al4V. *Journal of Manufacturing Processes*, *62*, 646–654. https://doi.org/10.1016/j.jmapro.2021.01.005

Ghayoor, M., Lee, K., He, Y., Chang, C., Paul, B. K., & Pasebani, S. (2020). Selective laser melting of 304L stainless steel: Role of volumetric energy density on the microstructure, texture

and mechanical properties. *Additive Manufacturing*, *32*, 101011. https://doi.org/10.1016/j.addma.2019.101011

Gong, H., Rafi, K., Gu, H., Starr, T., & Stucker, B. (2014). Analysis of defect generation in Ti–6Al–4V parts made using powder bed fusion additive manufacturing processes. *Additive Manufacturing*, *1–4*, 87–98. https://doi.org/10.1016/j.addma.2014.08.002

Gunenthiram, V., Peyre, P., Schneider, M., Dal, M., Coste, F., Koutiri, I., & Fabbro, R. (2018). Experimental analysis of spatter generation and melt-pool behavior during the powder bed laser beam melting process. *Journal of Materials Processing Technology*, *251*, 376–386. https://doi.org/10.1016/j.jmatprotec.2017.08.012

Guo, Q., Zhao, C., Qu, M., Xiong, L., Escano, L. I., Hojjatzadeh, S. M. H., Parab, N. D., Fezzaa, K., Everhart, W., Sun, T., & Chen, L. (2019). In-situ characterization and quantification of melt pool variation under constant input energy density in laser powder bed fusion additive manufacturing process. *Additive Manufacturing*, *28*, 600–609. https://doi.org/10.1016/j.addma.2019.04.021

Hojjatzadeh, S. M. H., Parab, N. D., Guo, Q., Qu, M., Xiong, L., Zhao, C., Escano, L. I., Fezzaa, K., Everhart, W., Sun, T., & Chen, L. (2020). Direct observation of pore formation mechanisms during LPBF additive manufacturing process and high energy density laser welding. *International Journal of Machine Tools and Manufacture*, *153*, 103555. https://doi.org/10.1016/j.ijmachtools.2020.103555

Kaplan, A. F. H., Mouzon, J., Guo, P., Volpp, J., Casati, R., Marola, S., Lupoi, R., & Zhang, W. (2025). AM by scanned laser melting of binder-based metal powder sheets. *IOP Conference Series: Materials Science and Engineering*, *1332*(1), 012004. https://doi.org/10.1088/1757-899X/1332/1/012004

Kolomy, S., Jopek, M., Sedlak, J., Benc, M., & Zouhar, J. (2024). Study of dynamic behaviour via Taylor anvil test and structure observation of M300 maraging steel fabricated by the selective laser melting method. *Journal of Manufacturing*

Processes, *125*, 283–294. https://doi.org/10.1016/j.jmapro.2024.07.057

Han, K., & Aktaş, N. F. (2024). Properties and applications of resin types used in SLA 3D printers. In Pioneer and innovative studies in engineering (Vol. 1, pp. 552–575). All Sciences Academy.

Li, M., Du, W., Elwany, A., Pei, Z., & Ma, C. (2020). Metal Binder Jetting Additive Manufacturing: A Literature Review. *Journal of Manufacturing Science and Engineering*, *142*(9), 090801. https://doi.org/10.1115/1.4047430

Li, S.-H., Kumar, P., Chandra, S., & Ramamurty, U. (2023). Directed energy deposition of metals: Processing, microstructures, and mechanical properties. *International Materials Reviews*, *68*(6), 605–647. https://doi.org/10.1080/09506608.2022.2097411

Lin, J., Chen, F., Liu, F., Xu, D., Gao, J., & Tang, X. (2020). Hydrogen permeation behavior and hydrogen-induced defects in 316L stainless steels manufactured by additive manufacturing. *Materials Chemistry and Physics*, *250*, 123038. https://doi.org/10.1016/j.matchemphys.2020.123038

Liu, Y., Zhang, M., Shi, W., Ma, Y., & Yang, J. (2021). Study on performance optimization of 316L stainless steel parts by High-Efficiency Selective Laser Melting. *Optics & Laser Technology*, *138*, 106872. https://doi.org/10.1016/j.optlastec.2020.106872

Ly, S., Rubenchik, A. M., Khairallah, S. A., Guss, G., & Matthews, M. J. (2017). Metal vapor micro-jet controls material redistribution in laser powder bed fusion additive manufacturing. *Scientific Reports*, *7*(1), 4085. https://doi.org/10.1038/s41598-017-04237-z

Mei, X., Qiao, L., Su, Y., & Yan, Y. (2024). The role of cell structures in hydrogen embrittlement of L-PBF 18Ni(300) maraging steel. *Corrosion Science*, *236*, 112276. https://doi.org/10.1016/j.corsci.2024.112276

Mercer, C., Speck, T., Lee, J., Balint, D. S., & Thielen, M. (2022). Effects of geometry and boundary constraint on the stiffness and negative Poisson's ratio behaviour of auxetic

metamaterials under quasi-static and impact loading. *International Journal of Impact Engineering*, *169*, 104315. https://doi.org/10.1016/j.ijimpeng.2022.104315

Nandhakumar, R., & Venkatesan, K. (2023). A process parameters review on selective laser melting-based additive manufacturing of single and multi-material: Microstructure, physical properties, tribological, and surface roughness. *Materials Today Communications*, *35*, 105538. https://doi.org/10.1016/j.mtcomm.2023.105538

Park, J. M., Asghari-Rad, P., Zargaran, A., Bae, J. W., Moon, J., Kwon, H., Choe, J., Yang, S., Yu, J.-H., & Kim, H. S. (2021). Nano-scale heterogeneity-driven metastability engineering in ferrous medium-entropy alloy induced by additive manufacturing. *Acta Materialia*, *221*, 117426. https://doi.org/10.1016/j.actamat.2021.117426

Pechlivani, E. M., Melidis, L., Pemas, S., Katakalos, K., Tzovaras, D., & Konstantinidis, A. A. (2023). On the Effect of Volumetric Energy Density on the Characteristics of 3D-Printed Metals and Alloys. *Metals*, *13*(10), 1776. https://doi.org/10.3390/met13101776

Pekok, M. A., Setchi, R., Ryan, M., Han, Q., & Gu, D. (2021). Effect of process parameters on the microstructure and mechanical properties of AA2024 fabricated using selective laser melting. *The International Journal of Advanced Manufacturing Technology*, *112*(1–2), 175–192. https://doi.org/10.1007/s00170-020-06346-y

Prathyusha, A. L. R., & Raghu Babu, G. (2022). A review on additive manufacturing and topology optimization process for weight reduction studies in various industrial applications. *Materials Today: Proceedings*, *62*, 109–117. https://doi.org/10.1016/j.matpr.2022.02.604

Sefene, E. M. (2022). State-of-the-art of selective laser melting process: A comprehensive review. *Journal of Manufacturing Systems*, *63*, 250–274. https://doi.org/10.1016/j.jmsy.2022.04.002

Snow, Z., Nassar, A. R., & Reutzel, E. W. (2020). Invited Review Article: Review of the formation and impact of flaws in powder bed fusion additive manufacturing. *Additive*

Manufacturing, *36*, 101457. https://doi.org/10.1016/j.addma.2020.101457

Song, B., Yu, T., Jiang, X., Xi, W., & Lin, X. (2020). The relationship between convection mechanism and solidification structure of the iron-based molten pool in metal laser direct deposition. *International Journal of Mechanical Sciences*, *165*, 105207. https://doi.org/10.1016/j.ijmecsci.2019.105207

Takata, N., Oide, K., Kobayashi, T., Suzuki, A., & Kobashi, M. (2019). Toward Understanding the Mechanism behind Microstructure Development of Aluminum Alloy Powders Additively Manufactured by Selective Laser Melting. *Journal of the Japan Society of Powder and Powder Metallurgy*, *66*(12), 573–580. https://doi.org/10.2497/jjspm.66.573

Tan, C., Zhou, K., Ma, W., Zhang, P., Liu, M., & Kuang, T. (2017). Microstructural evolution, nanoprecipitation behavior and mechanical properties of selective laser melted high-performance grade 300 maraging steel. *Materials & Design*, *134*, 23–34. https://doi.org/10.1016/j.matdes.2017.08.026

Tüylü, A., Çobaner, S., & Çerlek, Ö. (2024). Eklemeli imalat parametrelerinin gyroıd kafes yapılı parçaların mekanik özelliklerine etkisi. Presented at the 4. Bilsel Internatıonal Harput Scıentıfic Researches Congress, Elazığ.

Vishwakarma, J., Chattopadhyay, K., & Santhi Srinivas, N. C. (2020). Effect of build orientation on microstructure and tensile behaviour of selectively laser melted M300 maraging steel. *Materials Science and Engineering: A*, *798*, 140130. https://doi.org/10.1016/j.msea.2020.140130

Wang, P., Eckert, J., Prashanth, K., Wu, M., Kaban, I., Xi, L., & Scudino, S. (2020). A review of particulate-reinforced aluminum matrix composites fabricated by selective laser melting. *Transactions of Nonferrous Metals Society of China*, *30*(8), 2001–2034. https://doi.org/10.1016/S1003-6326(20)65357-2

Wang, X., Lu, Q., Zhang, P., Yan, H., Shi, H., Sun, T., Zhou, K., & Chen, K. (2024). A review on the simulation of selective laser melting AlSi10Mg. *Optics & Laser Technology*, *174*, 110500. https://doi.org/10.1016/j.optlastec.2023.110500

Wu, Y., Sun, K., Yu, S., & Zuo, L. (2021). Modeling the selective laser melting-based additive manufacturing of thermoelectric powders. *Additive Manufacturing*, *37*, 101666. https://doi.org/10.1016/j.addma.2020.101666

Yang, G., Xie, Y., Zhao, S., Qin, L., Wang, X., & Wu, B. (2022). Quality Control: Internal Defects Formation Mechanism of Selective Laser Melting Based on Laser-powder-melt Pool Interaction: A Review. *Chinese Journal of Mechanical Engineering: Additive Manufacturing Frontiers*, *1*(3), 100037. https://doi.org/10.1016/j.cjmeam.2022.100037

Yang, T., Liu, T., Liao, W., MacDonald, E., Wei, H., Zhang, C., Chen, X., & Zhang, K. (2020). Laser powder bed fusion of AlSi10Mg: Influence of energy intensities on spatter and porosity evolution, microstructure and mechanical properties. *Journal of Alloys and Compounds*, *849*, 156300. https://doi.org/10.1016/j.jallcom.2020.156300

Yin, J., Wang, D., Yang, L., Wei, H., Dong, P., Ke, L., Wang, G., Zhu, H., & Zeng, X. (2020). Correlation between forming quality and spatter dynamics in laser powder bed fusion. *Additive Manufacturing*, *31*, 100958. https://doi.org/10.1016/j.addma.2019.100958

Zhang, W., Wang, L., Feng, Z., & Chen, Y. (2020). Research progress on selective laser melting (SLM) of magnesium alloys: A review. *Optik*, *207*, 163842. https://doi.org/10.1016/j.ijleo.2019.163842

Zheng, L., Zhang, H., Shi, Q., Ma, J., Liang, W., & Hu, J. (2023). The high strength and hydrogen embrittlement resistance of selective laser melted 304 austenitic stainless steel. *Materials Letters*, *338*, 134013. https://doi.org/10.1016/j.matlet.2023.134013

Zhou, C., Yan, X., Wang, H., Huang, Y., Xue, J., Li, J., Li, X., & Han, W. (2025). Advancements in hydrogen embrittlement of selective laser melting austenitic stainless steel: Mechanisms, microstructures, and future directions. *Journal of Materials Science & Technology*, *230*, 219–235. https://doi.org/10.1016/j.jmst.2025.01.019

CHAPTER 9

LATTICE STRUCTURES FOR CRASHWORTHINESS APPLICATIONS: DESIGN, MANUFACTURING, AND PERFORMANCE

1. Hüseyin BEYTÜT[1]
2. Ömer KARABEY[2]

Abstract

Lattice structures have emerged as promising candidates for crashworthiness applications due to their exceptional specific energy absorption (SEA) characteristics and controlled deformation behavior. These three-dimensional periodic cellular architectures, enabled by advances in additive manufacturing technologies such as selective laser melting (SLM) and electron beam melting (EBM), offer superior performance compared to traditional energy-absorbing components. This chapter provides a comprehensive review of lattice structures for crashworthiness, covering fundamental design principles, unit cell topologies, and mechanical behavior under impact loading. Key performance metrics including SEA, peak crushing force (PCF), and crushing force efficiency (CFE) are critically examined. The influence of geometric parameters such as relative density, strut diameter, and unit cell topology on energy absorption mechanisms is systematically analyzed. Manufacturing considerations, including process-induced

[1] Dr, Hüseyin BEYTÜT, Bitlis Eren University, Department of Mechanical Engineering, Orcid: 0000-0001-8751-2225

[2] Dr, Ömer KARABEY, Bitlis Eren University, Department of Mechanical Engineering, Orcid: 0000-0002-5726-9284

defects and surface roughness effects, are discussed in relation to mechanical performance. Functionally graded lattice structures, where density and topology vary spatially, demonstrate enhanced crashworthiness through progressive collapse and improved force distribution. Material selection strategies encompassing metallic alloys, polymers, and composite systems are evaluated for specific applications in automotive and aerospace sectors. Topology optimization methods, including SIMP and BESO approaches, are presented for maximizing energy absorption while maintaining structural integrity. Finite element modeling techniques for predicting lattice behavior under crash scenarios are reviewed. Practical applications in crash boxes, battery protection systems, and aerospace components demonstrate the transformative potential of lattice structures in next-generation safety systems.

Keywords: Lattice structures; Crashworthiness; Energy absorption; Additive manufacturing

Introduction

Crashworthiness is defined as the ability of a structure to protect its occupants during a collision by managing energy absorption and maintaining structural integrity. In transportation systems, particularly in automotive and aerospace industries, crashworthiness design is a critical aspect of safety engineering. The primary objective is to maximize energy absorption while minimizing the peak forces transmitted to passengers, thereby reducing the risk of injury or fatality during impact events. Lu and Yu [1] comprehensively reviewed energy absorption mechanisms in structures and materials, establishing fundamental principles that guide modern crashworthiness design. Jones [2] further developed the theoretical framework for structural impact, emphasizing the importance of controlled progressive collapse and energy dissipation mechanisms.

Traditional crashworthiness structures, such as thin-walled tubes and foam-filled components, have been extensively studied and implemented over the past several decades. Abramowicz and Jones [3] investigated the dynamic progressive buckling behavior of circular and

square tubes, demonstrating that geometric design significantly influences collapse modes and energy absorption capacity. However, recent advances in additive manufacturing have enabled the fabrication of complex geometries, particularly lattice structures, which offer superior energy absorption characteristics compared to conventional designs.

Cellular structures, including foams, honeycombs, and lattice structures, have emerged as promising candidates for crashworthiness applications due to their high specific energy absorption (SEA) and controlled deformation behavior. The seminal work by Gibson and Ashby [4] on cellular solids established the theoretical foundation for understanding how cellular architecture influences mechanical behavior. Unlike solid materials, cellular structures can be designed to exhibit a plateau stress region during compression, which is ideal for energy absorption as it maintains relatively constant force over large deformation ranges. Ashby et al. [5] developed comprehensive design guidelines for metal foams, demonstrating that cellular materials can achieve specific energy absorption values comparable to or exceeding traditional energy absorbers while offering significant weight savings. The key advantage lies in the ability to engineer the stress-strain response through careful control of cell topology and relative density.

Lattice structures consist of periodic arrangements of struts or walls forming three-dimensional unit cells, creating a highly porous architecture with tailorable mechanical properties. Wadley [6] explored the multifunctional capabilities of periodic cellular metals, highlighting their potential for simultaneous structural support and energy management. Ashby [7] characterized the fundamental properties of foams and lattices, establishing scaling laws that relate relative density to mechanical properties, which have become cornerstone principles in cellular material design. Lattice structures, in particular, offer several advantages over traditional cellular materials. Their periodic architecture allows for precise control over mechanical properties through geometric design parameters such as strut diameter, unit cell size, and topology. Deshpande et al. [8] analyzed the effective properties of octet-truss lattice materials, demonstrating that stretching-dominated topologies exhibit superior stiffness-to-weight ratios

compared to bending-dominated configurations. Furthermore, the advent of additive manufacturing technologies, including selective laser melting (SLM) and electron beam melting (EBM), has made it possible to fabricate these complex geometries with high precision and material efficiency. Murr [9] reviewed the frontiers of 3D printing and additive manufacturing, illustrating how these technologies enable the production of components ranging from biomedical implants to aerospace structures.

Cellular structures, including foams, honeycombs, and lattice structures, have emerged as promising candidates for crashworthiness applications due to their high specific energy absorption (SEA) and controlled deformation behavior. The seminal work by Gibson and Ashby on cellular solids established the theoretical foundation for understanding how cellular architecture influences mechanical behavior. Unlike solid materials, cellular structures can be designed to exhibit a plateau stress region during compression, which is ideal for energy absorption as it maintains relatively constant force over large deformation ranges. Tancogne-Dejean et al. [10] investigated additively-manufactured metallic micro-lattice materials under both static and dynamic loading conditions, demonstrating that optimized octet-truss lattice topologies can achieve substantial specific energy absorption while maintaining structural integrity and exhibiting superior performance compared to conventional energy absorbers in multi-directional loading scenarios. Zheng et al. [11] demonstrated ultralight, ultrastiff mechanical metamaterials with unprecedented mechanical properties, opening new possibilities for lightweight structural applications.

The ability to functionally grade lattice structures varying density and topology throughout the structure provides additional design freedom for tailoring crash performance to specific loading conditions. Maskery et al. [12] investigated reinforced and functionally graded lattice structures, demonstrating that spatial density gradients can significantly enhance energy absorption performance. Their study on BCCz (reinforced body-centered-cubic) lattices revealed that functionally graded structures absorbed approximately 114% more energy per unit volume compared to uniform designs (1371 kJ/m³

versus 640 kJ/m³), highlighting the substantial potential of density gradation for crashworthiness applications.

This chapter provides a comprehensive review of lattice structures for crashworthiness applications, covering fundamental concepts, design methodologies, manufacturing considerations, and practical implementations. The primary aim is to introduce the fundamental principles of lattice structure design and their mechanical behavior under impact loading, establishing a foundation for understanding how these advanced cellular architectures respond to crash scenarios. Building upon this foundation, the chapter reviews energy absorption mechanisms and performance metrics relevant to crashworthiness, enabling readers to quantitatively assess and compare different lattice configurations.

A significant portion of the discussion is devoted to manufacturing technologies and their influence on mechanical performance, recognizing that the theoretical potential of lattice structures can only be realized through appropriate fabrication methods. The chapter presents optimization strategies for enhancing crash performance, demonstrating how computational tools and multi-objective algorithms can be leveraged to design superior energy-absorbing structures. Furthermore, the review examines numerical modeling approaches for predicting lattice structure behavior, providing guidance on simulation techniques that enable virtual prototyping and reduce development costs.

Energy Absorption Metrics

The performance of energy-absorbing structures in crashworthiness applications is evaluated through a set of standardized metrics that quantify their load-bearing capacity, deformation stability, and mass efficiency. These parameters enable systematic comparison of different structural configurations and material systems, facilitating informed design decisions for lightweight protective components. The following subsections define the key metrics employed in characterizing the energy absorption behavior of lattice structures under quasi-static and dynamic loading conditions.

Specific Energy Absorption (SEA): Higher SEA values indicate better energy absorption efficiency per unit mass, which is critical for lightweight design in transportation applications.

Peak Crushing Force (PCF): Typically occurring at the initial elastic peak before the plateau begins. Minimizing PCF is crucial for crashworthiness to reduce peak accelerations transmitted to occupants. High PCF values can result in injury to occupants even if total energy absorption is adequate, making this metric critical for safety-critical applications.

Crushing Force Efficiency (CFE): Can define as the ratio of mean crushing force to peak crushing force: An ideal energy absorber should have CFE close to 1 indicating stable and uniform energy absorption with minimal force fluctuations. Values of CFE > 0.7 are generally considered excellent for crashworthiness applications. Structures with low CFE values exhibit large force oscillations, which can be detrimental to occupant safety.

Definition and Classification of Lattice Structures

Lattice structures are topologically ordered, three-dimensional open-celled structures composed of one or more repeating unit cells. Schaedler and Carter [13] provided a comprehensive overview of architected cellular materials, noting that these structures differ from large-scale structures for example trusses or frames in terms of their unit cells of a lattice structure have a millimeter or micrometer scale. They explained that while the unit cells can be analyzed as space frames using classical mechanics, a lattice structure can be considered a material with its own mechanical properties. The cellular architecture determines the mechanical properties and density of these materials and can influence a wide range of other properties, including acoustic, thermal, and biological properties [13]. Maconachie et al. [14] conducted a comprehensive review of SLM (Selective Laser Melting) lattice structures, systematically analyzing their design, fabrication, and mechanical performance. They categorized lattice structures into three main types based on their geometric features. First, strut-based lattice structures represent the most common topologies investigated,

including body-centred cubic (BCC) and face-centred-cubic (FCC), or variations such as BCCZ and FCCZ (with z-struts), named after analogous crystalline structures as shown in figure 1. These structures can be characterized by their Maxwell number, which determines whether they exhibit bending-dominated or stretch-dominated behavior. Second, triply periodic minimal surface (TPMS) lattice structures have unit cells based on mathematical formulae such as Schoen gyroid, Schwartz diamond, and Neovius as shown in figure 2. These topologies offer potential advantages in terms of manufacturability and biological applications due to their continuously varying surface curvature. Third, shell lattice structures are cellular structures whose unit cells are composed of plates rather than struts, and these have been shown to exhibit superior strength and stiffness at very low densities compared to strut-based structures [14]. Maconachie et al. also provided extensive meta-analysis of reported mechanical performance data and discussed the applicability of the Gibson-Ashby model to SLM lattice structures, demonstrating that most experimental data fell within the predicted range for bending-dominated structures. Dong et al. [15] conducted a comprehensive survey on the modeling of lattice structures fabricated by additive manufacturing. They introduced various aspects of modeling and the correlations between design, simulation, and fabrication, while summarizing existing modeling approaches for simulation. The review discussed the strengths and weaknesses of different simulation methods and examined how the characteristics of additive manufacturing processes influence the modeling of lattice structures.

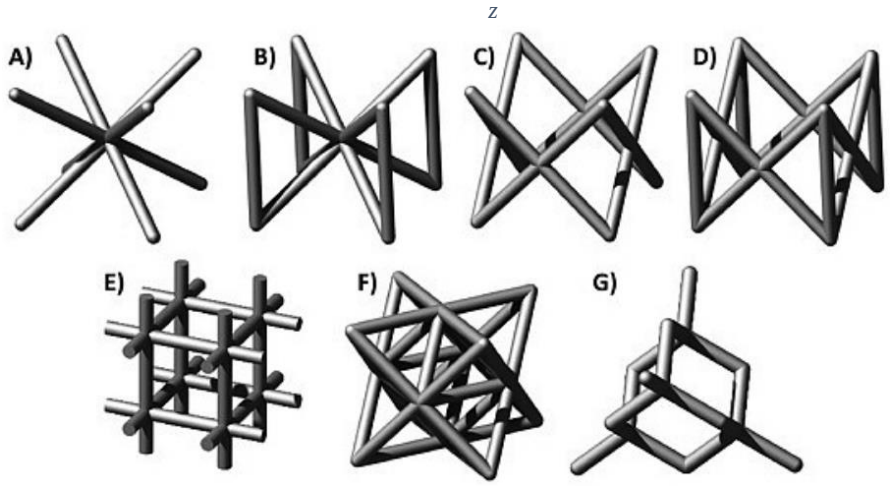

Figure 1: . Strut-based lattice structures: BCC (A), BCCZ (B), FCC (C), FCCZ (D), cubic (F), Octet-truss (G), and diamond (H) [14]

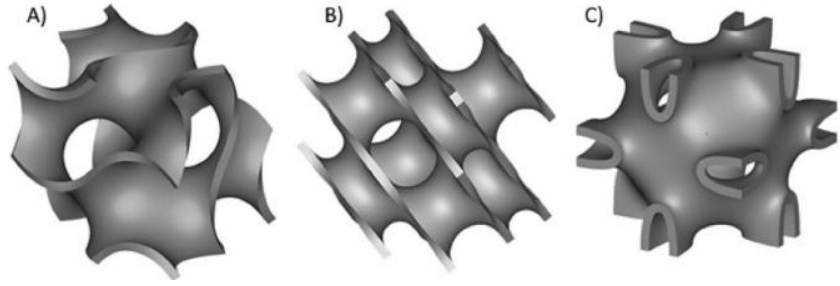

Figure 2: surface based lattice structure: Schoen gyroid (A), Schwarz diamond (B) and Neovius (C) [14].

The classification of lattice structures can also be based on their mechanical behavior under loading. Deshpande et al. [16] established the topological criteria that dictate whether cellular solids deform by bending or stretching of cell walls, demonstrating that stretching-dominated lattices require a minimum node connectivity of Z=12 in 3D, while structures with lower connectivity (such as BCC with Z=8) are bending-dominated. Deshpande et al. [8] further investigated the octet-truss lattice material, showing that stretching-dominated structures, where struts deform primarily through axial loading, exhibit significantly higher stiffness and strength compared to bending-dominated structures at the same relative density. While stretching-dominated foams are more weight-efficient for structural applications,

bending-dominated foams offer advantages for energy absorption applications due to their extended plateau regions during compression, albeit at lower absolute stiffness and strength values. Lattice structure types and general mechanical behavior of them are given figure 3.

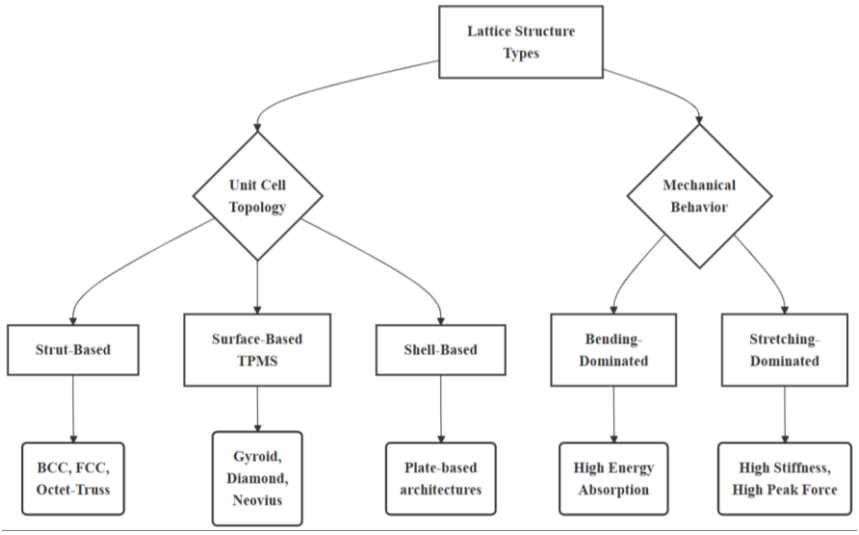

Figure 3: Lattice structure types and general mechanical behavior.

Unit Cell Topologies

The unit cell is the fundamental building block of lattice structures, and its topology significantly influences the mechanical properties and energy absorption behavior of the entire structure. Helou and Kara [17] provided a comprehensive overview of lattice structure design, analysis, and manufacturing, emphasizing that unit cell selection is the most critical decision in the design process. Unit cell architectures can be fundamentally classified based on their primary deformation mechanism: bending-dominated or stretching-dominated behavior. Deshpande et al. [16] established that this classification is governed by node connectivity, with stretching-dominated structures requiring a minimum connectivity of Z=12 in three dimensions, where Z represents the number of struts at each node. This topological distinction has profound implications for crashworthiness design: stretching-dominated lattices offer superior stiffness and load-bearing capacity but often exhibit brittle collapse with high peak forces, while

bending-dominated structures provide lower absolute stiffness but demonstrate more favorable energy absorption characteristics through progressive, stable collapse mechanisms.

The selection of unit cell topology for crashworthiness applications therefore involves balancing competing performance metrics: initial stiffness and strength versus specific energy absorption (SEA), peak crushing force (PCF) versus crushing force efficiency (CFE), and manufacturing complexity versus functional performance. Recent advances in additive manufacturing have enabled the fabrication of increasingly complex topologies, including triply periodic minimal surface (TPMS) structures that offer smooth, continuous geometries with potentially superior combinations of stiffness, strength, and energy absorption. The following subsections examine the most prevalent unit cell topologies, analyzing their geometric characteristics, deformation mechanisms, and crashworthiness performance. Gümrük and Mines [18] investigated the compressive behavior of stainless steel micro-lattice structures, finding that BCC (figure 3) topologies exhibited excellent energy absorption due to progressive layer-by-layer collapse. This topology is bending-dominated and exhibits relatively low stiffness but excellent energy absorption due to progressive buckling of struts. The BCC structure typically has 8 struts per unit cell and demonstrates isotropic mechanical behavior. Leary et al. [19] studied selective laser melting of AlSi12Mg lattice structures, reporting that BCC configurations achieved specific energy absorption values of 18-25 kJ/kg depending on relative density.

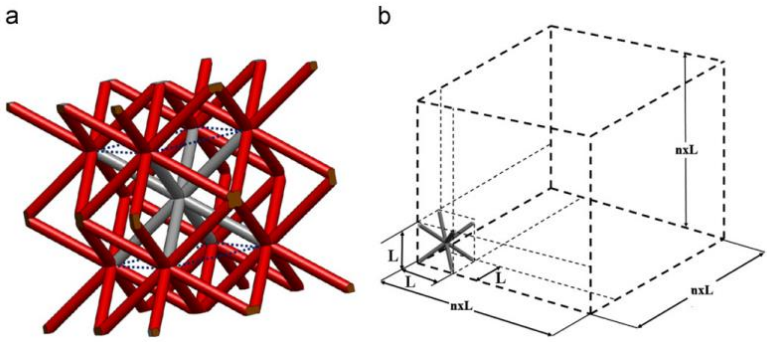

Figure 4: Body centred cubic; (a) unit-cell in light grey and (b) lattice block [18].

Deshpande et al. [8] analytically determined the effective properties of octet-truss lattices, showing that these structures achieve near-optimal stiffness for their weight. However, their high initial stiffness often results in higher peak forces during impact, which can be disadvantageous for crashworthiness applications. Abueidda et al. [20] studied the mechanical properties of 3D printed polymeric cellular materials with TPMS architectures. Al-Ketan et al. [21] investigated the topology-mechanical property relationship of various TPMS structures. Maskery et al. [22] examined several TPMS lattice structures made by polymer additive manufacturing as shown figüre 4, reporting that the diamond structure typically exhibits higher stiffness due to its more stretching-dominated behavior, while the primitive structure shows better energy absorption characteristics. These TPMS structures offer similar advantages to gyroid but with different surface curvatures and mechanical characteristics, allowing designers to select the most appropriate topology for specific applications.

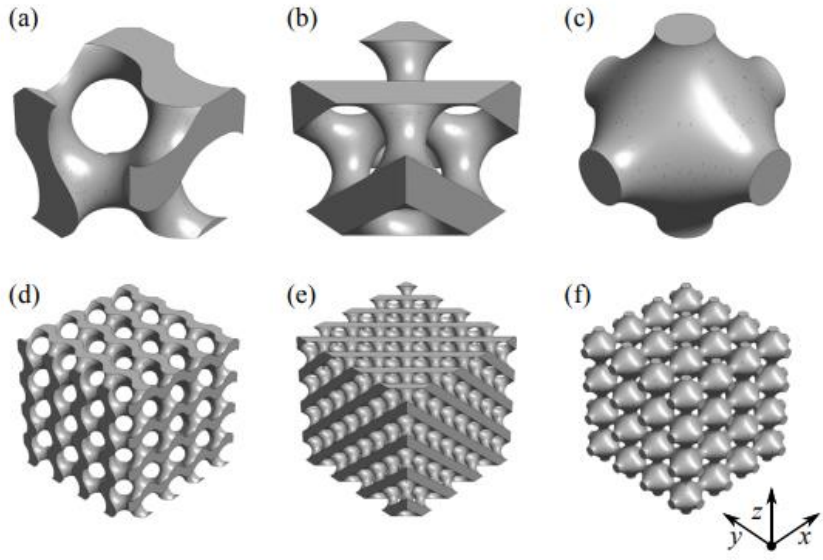

Figure 5: a) gyroid b) diamond c) primitive, while lattice structures comprising 4 x 4 x 4 cells are shown in d,e and f [22].

Table 1: Summary of Studies on Metallic Lattice Structures

Ref.	Author(s)	Year	Material	Lattice Type	Key Findings
[8]	Deshpande et al.	2001	316L Stainless Steel	Octet-truss	Stretching-dominated structure characterization - Analytical and FEM modeling - 3× stronger than metallic foams
[18]	Gümrük & Mines	2013	316L Stainless Steel	BCC, BCCZ, FCC, FCCZ, FBCCZ	Material overlap effect at nodes investigated - Timoshenko beam theory used - Work hardening considered - Aspect ratio effect is critical
[19]	Leary et al.	2016	AlSi12Mg	BCC, BCCZ, FCC, FCCZ, FBCCZ	Process parameter optimization completed - 99.86% density achieved - Manufacturability limits defined - Surface roughness characterized
[23]	Queheillalt & Wadley	2005	316L Stainless Steel	Hollow truss (Square, Diamond)	Hollow trusses increase buckling resistance - Strength for hollow vs ρ^3 for solid - Node rotation constraint observed - Highest specific peak strength reported
[20]	Abueidda et al.	2017	PA 2200 (Polyamide 12)	TPMS: Primitive, IWP, Neovius	IWP & Neovius similar performance - Primitive lower modulus/strength - Buckling at low ρ, yielding at high ρ - Specimen size effects significant - Strain rate dependent
[21]	Al-Ketan et al.	2018	Maraging Steel	Strut-based, Skeletal-TPMS, Sheet-TPMS:	Sheet-TPMS based structures showed superior mechanical properties among all tested structures. Sheet-Diamond showed nearly independent behavior from relative density Cubic and Diamond lattices most effective for temporal load spreading. Geometry effect more pronounced at lower relative densities. Skeletal structures showed bending-dominated behavior
[24]	Ozdemir et al.	2016	Ti6Al4V Titanium Alloy	Sheet-TPMS: Cubic, Diamond, Re-entrant cube	Cubic and Diamond lattices most effective for impact load temporal spreading by small margin. Significant rate dependency identified. Low velocity: random layer collapse. High velocity: sequential layer collapse (shock-like behavior). Peak stress reduced to ~20-35% of bare impact. Load duration increased by 250-2000%

					depending on impact velocity. First published experimental dynamic load-deformation studies of AM lattice structures
[25]	Rashed et al.	2016	Stainless Steel 316L, Ti-6Al-4V	BCC, BCC-Z, Octet-truss, Pyramidal, Kagome	Relative density achievable: 0.01-23%; SLM structures show bending-dominated behavior; manufacturing process significantly affects mechanical properties; periodicity provides better properties than stochastic foams
[26]	Xiao et al.	2017	Ti-6Al-4V	Rhombicdodecahedron	Strain rate effects observed - peak stress increases with loading rate for smaller unit cells; deformation mode unchanged at quasi-static and dynamic rates; shear bands form along 45° plane
[27]	Ullah et al.	2014	Ti-6Al-4V	Kagome	Bio-inspired Kagome structures show superior compressive and shear strength compared to honeycomb cores; minimum truss diameter 0.6mm; internal angle limit 60°; failure validated using ductile fracture model with stress triaxiality dependence

Geometric Parameters and Design Variables

The mechanical behavior and energy absorption characteristics of lattice structures are governed by several key geometric parameters. Mines et al. [28] investigated drop weight impact behavior of sandwich panels with metallic micro lattice cores, demonstrating that geometric parameters have first-order effects on crashworthiness performance. Yan et al. [29] studied advanced lightweight 316L stainless steel cellular lattice structures, showing that systematic variation of design parameters enables tailoring of mechanical response.

Relative Density (ρ): The relative density is defined as the ratio of lattice density to the density of the parent solid material, typically ranging from 0.05 to 0.50 for crashworthiness applications. This parameter has a dominant effect on mechanical properties, with stiffness and strength generally scaling with relative density according to power-law relationships. Gibson [30] reviewed the biomechanics of cellular solids, establishing that relative density fundamentally governs the mechanical behavior of cellular materials through well-defined

scaling relationships. For beam-based lattices, the strut slenderness ratio (l/d) is a critical parameter that determines whether the structure will fail by yielding or buckling. Smith et al. [31] performed finite element modeling of lattice structures manufactured using selective laser melting, demonstrating that unit cell size affects the number of cells in a given volume and influences the deformation pattern. Smaller unit cells generally result in more uniform stress distribution and smoother stress-strain curves, while larger cells may exhibit more localized deformation and potential for stress concentrations. For surface-based lattices, wall thickness is the primary design variable. Ahmadi et al. [32] investigated the mechanical behavior of regular open-cell porous biomaterials made of diamond lattice unit cells, showing that wall thickness controls the relative density and mechanical properties in a manner analogous to strut diameter in beam-based lattices.

These scaling laws provide fundamental guidance for lattice structure design, although actual behavior may deviate due to manufacturing defects, material properties, and geometric imperfections. Lei et al. [33] evaluated compressive properties of SLM-fabricated multi-layer lattice structures by experimental test and μ-CT-based finite element analysis, finding that manufacturing-induced geometric deviations can reduce mechanical properties by 15-30% compared to ideal designs. Liu et al. [34] studied the elastic and failure response of imperfect three-dimensional metallic lattices, demonstrating that geometric defects induced by selective laser melting significantly influence both stiffness and strength, with defect sensitivity varying by topology.

Functionally graded lattice structures also represent an advanced design approach where material distribution, topology, or geometric parameters vary continuously or discretely throughout the structure to achieve optimized performance. This spatial variation enables tailoring of mechanical properties to match local loading conditions and stress distributions, offering superior crashworthiness compared to uniform lattice structures [35-40]. Density gradient implementation constitutes the most straightforward approach to functional grading. By systematically varying the relative density from

one region to another, designers can create structures with progressive stiffness and strength characteristics. In crashworthiness applications, increasing density gradients in the direction of impact loading promotes sequential layer collapse and more stable energy absorption behavior. The gradient profile—whether linear, exponential, or stepwise—significantly influences the crushing force efficiency and deformation mode stability.

Mechanical Behavior and Energy Absorption Mechanisms

The compression behavior of lattice structures is characterized by three distinct regions in the stress-strain curve: an initial linear elastic region, a plateau region, and a densification region. Maskery et al. [41] evaluated graded density Al-Si10-Mg lattice structures manufactured by selective laser melting, demonstrating that this three-stage behavior is consistently observed across various topologies and materials. Understanding these regions is crucial for designing effective energy absorbers for crashworthiness applications.

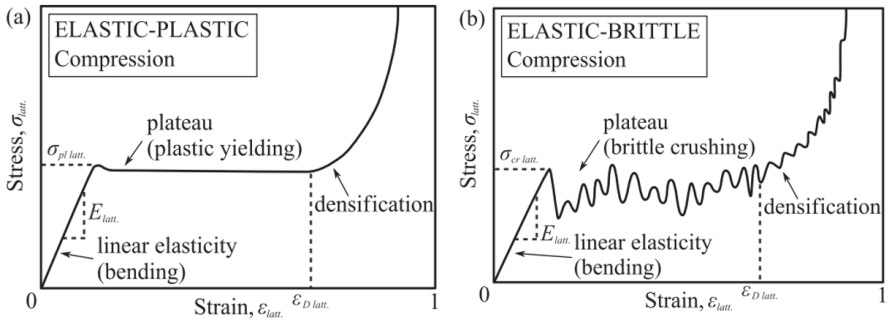

Figure 5:Schematic compressive stress-strain curves for lattices of (a) elastic-plastic and (b) elastic-brittle materials [41].

In the linear elastic region, the structure deforms elastically with minimal permanent deformation. The slope of this region corresponds to the effective elastic modulus of the lattice, which depends on the unit cell topology, relative density, and parent material properties. Zheng et al. [42] studied the dynamic crushing of 2D cellular structures using finite element analysis, showing that the elastic region typically extends to strains of 1-5% depending on the lattice configuration and material properties. The failure mechanisms of structurs give figure 6.

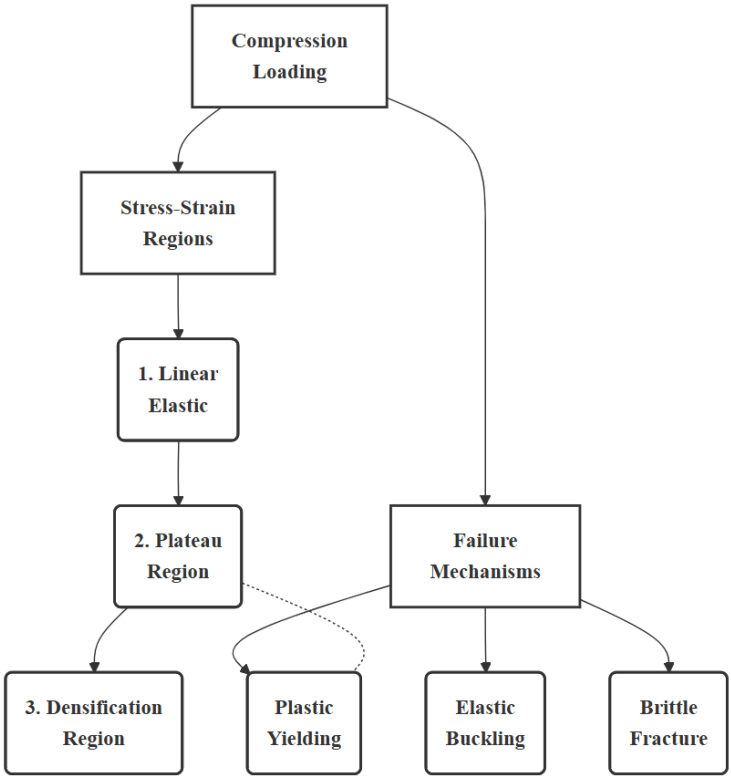

Figure 6: failure mechanisms.

The plateau region is the most critical for energy absorption applications. In this region, the structure undergoes progressive collapse at relatively constant stress levels, absorbing significant amounts of energy through various deformation mechanisms including elastic buckling, plastic yielding, brittle fracture, or combinations thereof. McKown et al. [43] examined the quasi-static and blast loading response of lattice structures, finding that the length of the plateau region (typically 40-70% strain for metallic lattices) and the plateau stress level determine the total energy absorption capacity of the structure.

The densification region occurs when the collapsed material compacts and the opposing walls come into contact, causing a rapid increase in stress. Habib et al. [44] fabricated polymeric lattice structures for optimum energy absorption using Multi Jet Fusion

technology, reporting that the onset of densification typically occurs at strains of 50-80% depending on the relative density and cell topology.

The failure modes of lattice structures under compression are highly dependent on the unit cell topology and relative density. Common failure modes include:

Elastic Buckling: Christensen [45] analyzed the mechanics of cellular and other low-density materials, demonstrating that elastic buckling occurs in slender struts under compression, leading to sudden lateral deflection. This is common in bending-dominated lattices with low relative densities. The critical buckling stress can be predicted using Euler buckling theory for individual struts, though node constraints and strut connectivity significantly influence actual buckling behavior.

Plastic Yielding: Ahmadi et al. [32] investigated additively manufactured open-cell porous biomaterials made from six different space-filling unit cells, finding that thick struts or high relative density structures typically fail through plastic yielding and formation of plastic hinges at nodes or mid-spans. This mechanism is prevalent in stretching-dominated lattices and provides excellent energy absorption through plastic deformation work.

Brittle Fracture: Ling et al. [46] studied the mechanical behavior of additively-manufactured polymeric octet-truss lattice structures under quasi-static and dynamic compressive loading, observing that brittle fracture occurs in brittle materials such as ceramics or some additively manufactured metals with manufacturing defects. Fracture typically initiates at stress concentrations near nodes or at defect sites and propagates through the structure. Gümrük et al. [47] examined static mechanical behaviors of stainless steel micro-lattice structures under different loading conditions, demonstrating that fracture significantly reduces energy absorption capacity and should be avoided in crashworthiness design through proper material selection and quality control.

Layer-by-Layer Collapse: Ozdemir et al. [24] conducted extensive experiments on energy absorption in lattice structures under dynamic loading, identifying that progressive layer-by-layer collapse

represents a highly desirable failure mode where horizontal layers of the lattice structure collapse sequentially from top to bottom or from areas of initial defects. This mode provides stable and predictable energy absorption. Mines et al. [28] studied drop weight impact behavior of sandwich panels with metallic micro lattice cores, confirming that layer-by-layer collapse results in extended plateau regions and high crushing force efficiency, making it ideal for crashworthiness applications.

Additive Manufacturing Techniques of lattice structures

Additive manufacturing (AM) has revolutionized the fabrication of lattice structures by enabling the production of complex geometries that are impossible or economically impractical to manufacture using conventional methods. Herzog et al. [48] provided a comprehensive review of additive manufacturing of metals, demonstrating how these technologies have evolved from rapid prototyping tools to production-capable manufacturing systems. DebRoy et al. [49] examined additive manufacturing of metallic components, analyzing the intricate relationships between process, structure, and properties.

The most commonly used AM techniques for metallic and polymeric lattice structures include Selective Laser Melting (SLM), Electron Beam Melting (EBM), and Fused Deposition Modeling (FDM).

Selective Laser Melting (SLM): SLM, also known as Laser Powder Bed Fusion (L-PBF), uses a high-power laser beam to selectively melt and fuse metallic powder particles layer by layer. Sing et al. [50] reviewed laser and electron-beam powder-bed additive manufacturing of metallic implants, establishing that this technique offers excellent dimensional accuracy (±50-100 μm), fine feature resolution (minimum strut diameter ~200 μm), and is suitable for a wide range of alloys including AlSi10Mg, Ti-6Al-4V, 316L stainless steel, and Inconel 718. Yap et al. [51] provided a comprehensive review of selective laser melting materials and applications, documenting the expanding material portfolio available for this technology.

The typical layer thickness ranges from 20 to 60 μm, allowing for the fabrication of intricate lattice structures with high fidelity. However, Kasperovich and Hausmann [52] studied the improvement of fatigue resistance and ductility of TiAl6V4 processed by selective laser melting, finding that SLM-fabricated lattices often contain manufacturing defects such as partially melted powder particles adhered to surfaces, internal porosity (0.1-5% depending on process parameters), and residual stresses that can affect mechanical properties. Greitemeier et al. [53] investigated the effect of surface roughness on fatigue performance of additive manufactured Ti-6Al-4V, reporting that surface roughness is typically in the range of Ra = 10-20 μm for as-built parts, which can significantly influence fatigue behavior and create stress concentrations.

Electron Beam Melting (EBM): Murr et al. [54] examined metal fabrication by additive manufacturing using laser and electron beam melting technologies, noting that EBM uses a focused electron beam in a vacuum environment with helium bleed to preheat the powder bed to approximately 0.8 Tm (where Tm is the melting temperature), resulting in significantly higher build temperatures compared to SLM.. Gong et al. [55] investigated the influence of defects on mechanical properties of Ti-6Al-4V components produced by SLM and EBM, finding that defects from insufficient energy input (unmelted powder) are more detrimental to mechanical properties than defects from excessive energy input (small pores), even at similar porosity levelsEBM is particularly suitable for reactive metals such as titanium alloys, which benefit from the vacuum environment and elevated process temperatures.

Fused Deposition Modeling (FDM): For polymeric lattice structures, FDM is the most widely used technique due to its low cost, ease of use, and wide material availability. Turner et al. [56] provided a comprehensive review of melt extrusion additive manufacturing processes, including FDM, which works by extruding thermoplastic filaments through a heated nozzle to deposit material layer-by-layer. The review primarily focused on ABS as the most common material, while also noting the use of engineering thermoplastics including polycarbonate, polyphenylsulfone, and Ultem polyimide in industrial

systems, as well as PLA in low-cost personal fabrication systems. Ahn et al. [57] characterized anisotropic material properties of FDM ABS parts, finding that raster orientation and air gap are the most significant parameters affecting mechanical properties. Parts with criss-cross raster pattern ([±45°]) achieved 65-72% of injection-molded ABS tensile strength, while compressive strength reached 80-90% of injection-molded values.

Material Selection for Crashworthiness

Material selection is a critical factor in designing lattice structures for energy absorption applications. The choice of material fundamentally influences not only the mechanical response during impact but also the manufacturing feasibility, overall weight, cost, and operational environment limitations of the final structure.[58, 59].

Composite lattice structures represent an emerging class of materials that combine the geometric advantages of cellular architectures with the superior specific properties of fiber-reinforced composites [60-62]. These structures offer unique opportunities for achieving exceptional strength-to-weight ratios and tailored energy absorption characteristics that exceed the capabilities of monolithic metallic or polymeric lattices.

Continuous fiber-reinforced polymer lattices can be fabricated through advanced additive manufacturing techniques that enable controlled fiber placement along the strut directions [63]. This approach allows optimization of fiber orientation to maximize load-bearing capacity in primary loading directions. Carbon fiber and glass fiber reinforced lattices have demonstrated significantly higher specific stiffness and strength compared to unreinforced polymer lattices, making them attractive for weight-critical applications [64-66].

Hybrid metal-composite lattice structures [67] integrate metallic and polymeric components to leverage the complementary properties of different materials. For example, metallic core lattices can be over-molded with polymer matrices or enclosed in composite face sheets to create sandwich structures with exceptional energy absorption capabilities. These hybrid configurations enable progressive failure

modes where different materials activate at various stages of crushing, resulting in more controlled energy dissipation profiles.

Manufacturing of composite lattice structures presents unique challenges compared to their metallic counterparts. Fiber orientation control, void content management, and interface bonding between layers require careful process parameter optimization. However, recent advances in continuous fiber 3D printing and automated fiber placement technologies are expanding the feasible design space for complex composite lattice geometries [68, 69].

The anisotropic nature of composite materials introduces additional design considerations for lattice structures. Unlike isotropic metallic lattices, composite variants exhibit directionally dependent mechanical properties that must be carefully aligned with expected loading conditions. This anisotropy can be exploited beneficially to create structures with enhanced performance in specific directions while maintaining overall lightweight construction.

Aluminum Alloys: Aluminum alloys are extensively used in automotive and aerospace crashworthiness applications due to their excellent strength-to-weight ratio. The low density of aluminum makes it particularly attractive for applications where weight reduction is paramount, such as in vehicle body structures and aircraft components. During impact, aluminum lattices can effectively absorb energy through progressive plastic deformation while maintaining relatively predictable failure modes [35, 70]. The material's good weldability and compatibility with various manufacturing processes, combined with its recyclability, make it a preferred choice for mass-produced crash components. However, the susceptibility to temperature-related property degradation limits its use in high-temperature crash scenarios such as engine compartments or aerospace re-entry applications.

Titanium Alloys: Titanium alloys find their primary application in crashworthiness components where both high strength and lightweight construction are critical, particularly in aerospace and high-performance automotive applications. The exceptional corrosion resistance makes titanium lattices suitable for marine and offshore energy absorption systems where long-term durability in harsh

environments is essential. In biomedical applications, titanium's biocompatibility enables its use in implantable energy-absorbing devices such as spinal cages and bone scaffolds that must withstand impact loads while promoting tissue integration. The main limitation for widespread crashworthiness application is the high material and processing costs, which typically restrict its use to high-value applications where performance justifies the expense.

Stainless Steel: Stainless steel lattice structures are commonly employed in crashworthiness applications requiring a balance between performance and cost-effectiveness [71-73]. The material's excellent ductility allows for large plastic deformation before failure, resulting in extended energy absorption during progressive crushing. This characteristic makes stainless steel lattices particularly suitable for protective structures in industrial equipment, railway components, and architectural safety systems. The superior corrosion resistance compared to carbon steel enables deployment in outdoor and marine environments without significant protective coatings. In automotive applications, stainless steel crash components can provide consistent performance across a wide range of service temperatures, from arctic conditions to high-temperature engine bay applications.

Polymers: Polymeric lattice structures are increasingly utilized in crashworthiness applications [74, 75] where moderate impact energies are expected and weight minimization is crucial. These materials are particularly advantageous in consumer electronics protection, sports equipment, and packaging applications where the lower cost enables widespread implementation. The inherent damping properties of polymers provide additional benefits in applications requiring vibration attenuation alongside energy absorption, such as in helmet liners and protective padding. The ability to process polymers at lower temperatures compared to metals enables rapid prototyping and cost-effective small-batch production, making them ideal for customized protective equipment. Additionally, polymeric lattices can be designed with specific failure modes that prioritize occupant safety, such as in automotive interior components where gradual deformation is preferred over sudden catastrophic failure.

Topology Optimization Methods

Topology optimization is a powerful mathematical method in structural design that aims to achieve the best performance by optimizing material distribution. For crashworthiness applications in lattice structures, topology optimization is critically important in terms of maximizing energy absorption while maintaining structural integrity.

The historical development of topology optimization began with the homogenization method proposed by Bendsøe and Kikuchi in 1988 [76]. This pioneering work introduced the idea of optimizing material distribution at the microstructure level. Currently, widely used methods for crashworthiness optimization in lattice structures include SIMP (Solid Isotropic Material with Penalization), BESO (Bi-directional Evolutionary Structural Optimization), and level-set methods. The SIMP method treats material density as a continuous design variable varying between 0 and 1, and aims to obtain a clear 0-1 solution by penalizing intermediate density values. In crashworthiness applications, the SIMP method has provided effective results, particularly in optimizing multiple objectives such as energy absorption and peak force. Due to the nonlinear nature of structural collapse behavior, adapting the SIMP method to crashworthiness problems involves significant computational challenges.

The BESO method, developed by Xie and Steven [77], performs element addition and removal operations through an evolutionary process. This method offers an intuitive approach in crashworthiness optimization of lattice structures by gradually removing elements in low-stress regions and increasing material density in high-stress regions. The advantage of BESO is that it produces clear black-and-white designs and creates geometries suitable for manufacturing. Level-set methods represent structural boundaries using implicit functions and determine the optimum topology through the solution of the Hamilton-Jacobi equation. This method is particularly preferred for obtaining sharp boundaries and clean geometries in complex lattice structures. However, in problems involving severe geometric changes and contact, such as crashworthiness, the computational cost can be high.

Crashworthiness optimization of lattice structures deals with problems involving dynamic, large deformation, and material nonlinearity, unlike traditional static loading. Therefore, adapting topology optimization to crashworthiness applications requires special approaches. The equivalent static load (ESL) method significantly reduces computational cost by converting dynamic crashworthiness problems into a series of static problems. In this approach, load conditions at critical time steps obtained from crash simulation are extracted and applied as static loads. The ESL method has been successfully applied particularly in multi-cell lattice structures and hybrid material systems.

Multi-objective optimization techniques are widely used in crashworthiness design [78]. Conflicting objectives such as energy absorption maximization, peak force minimization, and crush force efficiency optimization can be balanced using Pareto optimal solutions. Evolutionary algorithms such as NSGA-II, MOPSO, and MOEA/D are effectively used in multi-objective topology optimization for crashworthiness in lattice structures.

Topology optimization for crashworthiness in lattice structures requires high computational cost due to large-scale finite element analyses and iterative optimization loops. Sensitivity analysis forms the basis of gradient-based optimization algorithms and can be efficiently calculated using adjoint methods. However, the presence of nonlinear events such as contact and plastic deformation complicates sensitivity calculations. Surrogate modeling techniques use kriging, artificial neural networks, and radial basis functions to replace high-fidelity simulations with approximate models to reduce computational burden. This approach accelerates the optimization process, especially in multi-parameter lattice structure designs.

Manufacturing constraints are critically important in practical applications of topology optimization. With the development of additive manufacturing technologies, the production of complex lattice structures has become possible, and AM constraints such as minimum element size, overhang angles, and support structures should be incorporated into the optimization problem. In crashworthiness optimization of lattice structures, manufacturing parameters such as

layer thickness, node connections, and cell wall thickness should also be considered as design variables.

Topology optimization provides a powerful tool for enhancing crashworthiness performance in lattice structures. Increases in computational power and the integration of machine learning techniques will enable the optimization of more complex and realistic crash scenarios in the future. In particular, hybrid approaches with deep learning-based surrogate models and genetic algorithms offer new possibilities in lattice structure design. Crashworthiness design typically involves multiple conflicting objectives that must be balanced. Fang et al. [79] comprehensively reviewed design optimization for structural crashworthiness and its state of the art, establishing the fundamental framework for multi-objective crashworthiness optimization. Sun et al. [80] developed a two-stage multi-fidelity optimization procedure for honeycomb-type cellular materials, demonstrating efficient strategies for balancing competing objectives.

Objective Functions:

- Maximize specific energy absorption (SEA)
- Minimize peak crushing force (PCF)
- Maximize crushing force efficiency (CFE)
- Minimize mass
- Maximize densification strain

Design Variables:

- Unit cell type (topology selection)
- Relative density distribution
- Strut diameter or wall thickness
- Unit cell size
- Gradient parameters (for functionally graded designs)
- Hybrid topology arrangements

Duddeck et al. [78] applied topology optimization for crashworthiness of thin-walled structures under axial impact using hybrid cellular automata, showing that multi-objective optimization methods such as Non-dominated Sorting Genetic Algorithm II (NSGA-II) and Multi-Objective Particle Swarm Optimization (MOPSO) are

commonly employed to generate Pareto-optimal solutions. Deb et al. [81] introduced the fast and elitist multiobjective genetic algorithm NSGA-II, which has become the standard benchmark for multi-objective optimization in crashworthiness applications. The Pareto front represents a set of non-dominated solutions where improving one objective requires compromising another, providing designers with a range of optimal trade-off solutions.

Finite Element Analysis of Lattice Structures

Finite element analysis (FEA) is the primary computational tool for predicting the mechanical behavior and crashworthiness performance of lattice structures. Rashed et al. [25] provided a comprehensive review on metallic microlattice materials covering manufacturing, mechanical properties, and applications, emphasizing the critical role of computational modeling. Two main modeling approaches are employed: detailed micro-scale modeling and homogenized macro-scale modeling. Smith et al. [31] performed finite element modeling of the compressive response of lattice structures manufactured using the SLM, establishing that this approach explicitly represents the geometry of individual struts or walls using beam, shell, or solid elements. Luxner et al. [82] developed finite element modeling concepts and linear analyses of 3D regular open cell structures, showing that beam elements (Timoshenko or Euler-Bernoulli) are computationally efficient for slender struts and can capture bending and buckling behavior with reasonable accuracy when the length-to-diameter ratio exceeds 10. Campoli et al. [83] investigated the mechanical properties of open-cell metallic biomaterials manufactured using additive manufacturing techniques (selective laser melting and selective electron beam melting). In their study, Timoshenko beam elements were employed to model the strut-based lattice structures, which were capable of capturing shear strains in thicker struts. Four different unit cell types were analyzed: cube, diamond, rhombic dodecahedron, and truncated octahedron. The study demonstrated that FE models including manufacturing irregularities provided significantly more accurate predictions compared to analytical models, particularly for structures with higher apparent densities. While

analytical models (based on slender beam theories) overestimated stiffness values, FE simulations incorporating structural variations showed good agreement with experimental measurements. The convergence study indicated that 6-10 unit cells were sufficient for accurate homogenized property predictions when periodic boundary conditions were applied.

For crashworthiness simulations involving large deformations and contact, explicit time integration schemes are typically used. Key modeling considerations include:

Material Models: Elastic-plastic constitutive models with isotropic or kinematic hardening are essential. Johnson and Cook [84] developed fracture characteristics of three metals subjected to various strains, strain rates, temperatures, and pressures, introducing the Johnson-Cook plasticity model that is commonly used for high strain-rate loading, which accounts for strain hardening, strain rate sensitivity, and thermal softening.

Element Formulation: Belytschko and Bindeman [85] developed assumed strain stabilization of the eight node hexahedral element, showing that reduced integration elements with hourglass control prevent volumetric locking and improve computational efficiency while maintaining accuracy in large deformation analyses.

Contact Algorithms: Wriggers [86] comprehensively covered computational contact mechanics, establishing that self-contact must be defined to capture strut-to-strut contact during collapse. Penalty-based or augmented Lagrangian contact algorithms are typically employed, with contact stiffness parameters carefully selected to balance accuracy and computational stability.

Mesh Sensitivity: Ullah et al. [87] İnvestigated the failure and energy absorption characteristics of advanced 3D truss core structures manufactured using selective laser melting (SLM). The study focused on Ti-6Al-4V Kagome and atomic lattice truss configurations (bcc, f2cc, and f2bcc) under both compression and shear loading conditions. The FE predictions showed very good agreement with experimental results for both deformation patterns and failure locations. The study demonstrated that Kagome structures exhibited superior performance,

with 60-100% higher specific strength and energy absorption compared to atomic lattice structures under compression. The validated numerical approach successfully predicted both progressive failure (compression) and catastrophic failure (shear) events across a wide range of lattice configurations and slenderness ratios.

Latiice structures for crashworthiness applications

Lattice structures have shown significant promise for automotive crashworthiness applications, particularly in energy-absorbing components such as bumper beams, crash boxes, and side-impact protection systems. Zarei and Kröger [88] optimized foam-filled aluminum tubes for crash box applications, while Fang et al. [89] developed a multiobjective robust design optimization (MORDO) methodology for foam-filled bitubal thin-walled structures considering uncertainties in manufacturing parameters (foam density and wall thickness). The study employed adaptive Kriging metamodels with sequential sampling strategies (AASO-AAMO) combined with Monte Carlo simulation and MOPSO algorithm. The results demonstrated that robust optimization significantly improved the stability of Pareto solutions by reducing performance fluctuations while maintaining crashworthiness criteria (maximizing SEA and minimizing peak force).

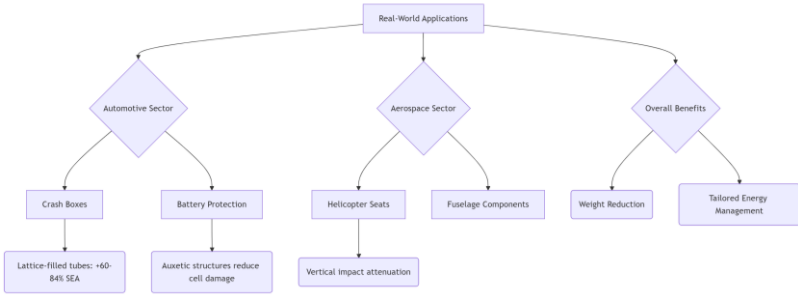

Figure 7: Lattice structures applications.

Traditional crash boxes made from thin-walled tubes are being replaced or supplemented with lattice-filled designs The pursuit of enhanced crashworthiness in vehicular structures has catalyzed a paradigm shift from traditional thin-walled tubes towards advanced, lattice-filled designs, a trend substantiated by extensive research into their superior energy absorption mechanisms and synergistic effects. [90-93]. Liu et al. [94] conducted a study on the energy absorption performance of multi-cell tubes filled with lattice structures (LS),

fabricated using Fused Deposition Modelling (FDM) from chopped carbon-fiber-reinforced polyamide. Their research highlighted the critical role of the lattice and its integration method. They found that the internal lattice significantly modified the deformation mode of the tube, leading to a more regular folding pattern and an increase in the number of folds. A key finding was the pronounced synergistic effect between the lattice and the tube walls, where the total energy absorption of the lattice-filled structures was 55.6% higher (for assembled tubes) and 83.8% higher (for integrally printed tubes) than the sum of the empty tube and the pure lattice. The study concluded that integrally manufacturing the tube and the lattice as a single piece was the most effective strategy, as it forced a change from an asymmetric to a symmetric folding mode, resulting in superior and more uniform energy absorption. Gunaydin [95] conducted a study investigating the energy absorption performance of aluminum crush boxes filled with various lattice structures, including both strut-based (BCC, FCC) and Triply Periodic Minimal Surface (TPMS) types (Gyroid, Diamond, Primitive). The lattice structures were fabricated using PolyJet technology and tested under quasi-static axial compression. The results demonstrated that all lattice fillers significantly enhanced the crashworthiness compared to empty tubes, with the Gyroid structure exhibiting the most superior performance. Specifically, the Gyroid-filled tubes achieved a 63.9% higher Crush Force Efficiency (CFE) and a 67.6% higher Specific Energy Absorption (SEA) than the empty tubes. The study concluded that TPMS-type lattice fillers, particularly the Gyroid, outperformed strut-based lattices and are recommended for optimal energy absorption in crush box applications.

Gültekin and Yahşi [96] investigated the crashworthiness performance of multi-cell tubes filled with composite lattice structures fabricated via additive manufacturing. Their research demonstrated a significant synergistic effect, where the total energy absorption of the integrally manufactured lattice-filled tubes substantially exceeded the sum of their individual components. The internal lattice structure was found to effectively modify the global deformation mode, transitioning it from an asymmetric to a more stable and symmetric folding pattern, thereby increasing the number of folds and distributing the crushing

force more uniformly. This led to a remarkable enhancement in key performance indicators, including Specific Energy Absorption (SEA) and Crush Force Efficiency (CFE). Scurtu et al. [97] conducted a numerical analysis to enhance the crashworthiness of an electric vehicle's battery case by integrating re-entrant auxetic structures as energy absorbers. Their study focused on mitigating impact forces during a low-velocity (10 m/s) pole collision to reduce the risk of battery cell damage and thermal runaway. Through finite element simulations, they compared the performance of battery cases surrounded by traditional cylindrical absorbers against those with cylindrical absorbers featuring auxetic cutouts. The results demonstrated that the auxetic structures were highly effective in distributing impact energy more evenly around the battery case, leading to a significant reduction in damaged cells. The optimal auxetic design (AUX3, 31 mm in length) reduced the number of critically deformed cells by 35.2% compared to the least effective auxetic configuration. Furthermore, the auxetic absorbers achieved this superior protection with a lower mass than their conventional counterparts, highlighting their potential for creating lighter and safer battery protection systems.

Aerospace applications of lattice structures for crashworthiness represent a natural extension of their automotive implementation, driven by even more stringent weight constraints and performance requirements [98]. The exceptional specific energy absorption characteristics of optimized lattice structures make them attractive candidates for various aircraft and spacecraft impact protection systems.

Helicopter crash-resistant seats [99, 100] incorporate lattice structures as primary energy absorbers to protect occupants during emergency landings or crash events. These seats must meet rigorous crashworthiness standards requiring controlled vertical deceleration within survivable limits while maintaining structural integrity. Metallic lattice structures, particularly those fabricated from aluminum or titanium alloys, provide the necessary energy absorption capacity within the limited packaging space available beneath the seat. The progressive collapse behavior of properly designed lattices ensures

relatively constant deceleration forces, avoiding dangerous force spikes that could cause spinal injuries.

Conclusion

Lattice structures represent a paradigm shift in crashworthiness design, offering unprecedented opportunities for lightweight energy absorption through their tailorable mechanical properties and complex three-dimensional architectures. The advancement of additive manufacturing technologies, particularly selective laser melting and electron beam melting, has transformed these structures from theoretical concepts into practical engineering solutions capable of outperforming traditional energy absorbers in terms of specific energy absorption and crushing force efficiency. This comprehensive review has demonstrated that the crashworthiness performance of lattice structures is governed by multiple interrelated factors, including unit cell topology, relative density, geometric parameters, and material selection. Stretching-dominated topologies such as octet-truss provide superior stiffness and strength, while bending-dominated configurations like BCC offer extended plateau regions ideal for progressive energy absorption. Triply periodic minimal surface (TPMS) structures, including gyroid and diamond configurations, have emerged as particularly promising candidates, combining favorable manufacturing characteristics with excellent mechanical performance.

Functionally graded lattice structures represent a significant advancement, enabling spatial variation of density and topology to achieve optimized crash performance. Research has demonstrated that density gradients can enhance energy absorption by 50-114% compared to uniform designs, while promoting sequential layer collapse and more stable deformation modes. This spatial tailoring capability allows designers to match structural response to specific loading conditions and impact scenarios. The integration of topology optimization methods with crashworthiness objectives has proven essential for achieving optimal designs. Multi-objective optimization approaches, particularly NSGA-II and MOPSO algorithms, enable systematic exploration of design trade-offs between conflicting objectives such as maximizing energy absorption while minimizing peak crushing force.

The development of surrogate modeling techniques and machine learning approaches continues to reduce computational costs, making optimization feasible for increasingly complex lattice configurations.

Material selection remains a critical consideration, with aluminum alloys dominating automotive applications due to their excellent strength-to-weight ratio, while titanium alloys find use in aerospace and biomedical applications where performance justifies higher costs. Stainless steel provides a cost-effective balance for industrial applications, and polymeric lattices offer advantages in consumer products and protective equipment. Emerging composite lattice structures, combining fiber reinforcement with cellular architectures, promise further improvements in specific mechanical properties. Manufacturing considerations significantly influence the practical implementation of lattice structures. Process-induced defects, including partially melted powder particles, internal porosity, and surface roughness, can reduce mechanical properties by 15-30% compared to ideal designs. Understanding these manufacturing limitations and incorporating appropriate safety factors in design is essential for reliable crashworthiness performance. The development of quality control methods and post-processing techniques continues to improve the consistency and reliability of additively manufactured lattice structures.

Finite element analysis has proven indispensable for predicting lattice structure behavior under crash loading, with detailed micro-scale models providing accurate representation of progressive collapse mechanisms and failure modes. The validation of simulation approaches through experimental testing remains critical, particularly for capturing strain rate effects and dynamic loading conditions. The continued refinement of material models and contact algorithms enhances the predictive capability of numerical simulations. Practical implementations in automotive crash boxes, battery protection systems, and aerospace structures demonstrate the real-world viability of lattice structures for crashworthiness applications. Studies have shown that lattice-filled crash boxes can achieve 60-84% higher specific energy absorption compared to empty tubes, with synergistic effects between the lattice filler and tube walls contributing to superior performance. In

electric vehicle battery protection, auxetic lattice structures have demonstrated 35% reductions in critically deformed cells during pole impact scenarios.

Despite these advances, several challenges remain. The high computational cost of crashworthiness optimization, particularly for problems involving large deformations and contact, necessitates continued development of efficient solution strategies. The integration of manufacturing constraints into topology optimization formulations requires further research to ensure that optimized designs are practically manufacturable. Long-term durability and fatigue behavior of lattice structures under cyclic loading conditions require additional investigation to establish design guidelines for structures experiencing multiple impact events.

Future research directions should focus on multi-material lattice structures that combine different materials within a single component to leverage complementary properties. The development of hybrid lattice-conventional structures, integrating lattice architectures with traditional structural elements, offers opportunities for enhanced crashworthiness in complex assemblies. Machine learning and artificial intelligence approaches show promise for accelerating the design process, enabling real-time optimization and adaptive structures that respond to varying impact conditions. The continued evolution of additive manufacturing technologies, including improvements in build rates, material quality, and process repeatability, will expand the practical applications of lattice structures. The development of new materials specifically designed for additive manufacturing and crashworthiness applications will further enhance performance capabilities. As manufacturing costs decrease and design tools become more accessible, lattice structures are poised to become standard components in next-generation safety systems across automotive, aerospace, and protective equipment industries.

In conclusion, lattice structures for crashworthiness applications represent a mature technology with demonstrated benefits and clear pathways for continued improvement. The combination of advanced design methodologies, sophisticated manufacturing capabilities, and comprehensive analytical tools provides engineers with powerful

means to develop lightweight, high-performance energy-absorbing structures. As the field continues to evolve, lattice structures will play an increasingly important role in achieving the competing objectives of enhanced safety, reduced weight, and improved sustainability in engineering systems.

References

[1] G. Lu and T. Yu, *Energy absorption of structures and materials*. Elsevier, 2003.

[2] N. Jones, *Structural impact*. Cambridge university press, 2011.

[3] W. Abramowicz and N. Jones, "Dynamic progressive buckling of circular and square tubes," International Journal of Impact Engineering, vol. 4, no. 4, 1986) pp. 243-270.

[4] L. J. Gibson, "Cellular solids," Mrs Bulletin, vol. 28, no. 4, 2003) pp. 270-274.

[5] M. Ashby, A. Evans, N. Fleck, L. Gibson, J. Hutchinson, and H. Wadley, "Metal foams a design guide, Butter worth Heinemann," United States of America, vol. 1, no. 23, 2000) p. 119.

[6] H. N. G. Wadley, "Multifunctional periodic cellular metals," Philos T R Soc A, vol. 364, no. 1838, (Jan 15 2006) pp. 31-68.10.1098/rsta.2005.1697.

[7] M. F. Ashby, "The properties of foams and lattices," Philos T R Soc A, vol. 364, no. 1838, (Jan 15 2006) pp. 15-30.10.1098/rsta.2005.1678.

[8] V. S. Deshpande, N. A. Fleck, and M. F. Ashby, "Effective properties of the octet-truss lattice material," J Mech Phys Solids, vol. 49, no. 8, (Aug 2001) pp. 1747-1769.Doi 10.1016/S0022-5096(01)00010-2.

[9] L. E. Murr, "Frontiers of 3D Printing/Additive Manufacturing: from Human Organs to Aircraft Fabrication," J Mater Sci Technol, vol. 32, no. 10, (Oct 2016) pp. 987-995.10.1016/j.jmst.2016.08.011.

[10] T. Tancogne-Dejean, A. B. Spierings, and D. Mohr, "Additively-manufactured metallic micro-lattice materials for high specific energy absorption under static and dynamic loading," Acta Mater, vol. 116, (Sep 1 2016) pp. 14-28.10.1016/j.actamat.2016.05.054.

[11] X. Y. Zheng *et al.*, "Ultralight, Ultrastiff Mechanical Metamaterials," Science, vol. 344, no. 6190, (Jun 20 2014) pp. 1373-1377.10.1126/science.1252291.

[12] I. Maskery *et al.*, "An investigation into reinforced and functionally graded lattice structures," J Cell Plast, vol. 53, no. 2, (Mar 2017) pp. 151-165.10.1177/0021955x16639035.

[13] T. A. Schaedler and W. B. Carter, "Architected Cellular Materials," Annu Rev Mater Res, vol. 46, 2016) pp. 187-210.10.1146/annurev-matsci-070115-031624.

[14] T. Maconachie *et al.*, "SLM lattice structures: Properties, performance, applications and challenges," Mater Design, vol. 183, (Dec 5 2019).ARTN 10813710.1016/j.matdes.2019.108137.

[15] G. Dong, Y. Tang, and Y. F. Zhao, "A Survey of Modeling of Lattice Structures Fabricated by Additive Manufacturing (vol 139, 100906, 20)," J Mech Design, vol. 140, no. 1, (Jan 2018).Artn 017001Doi 10.1115/1.4038265.

[16] V. S. Deshpande, M. F. Ashby, and N. A. Fleck, "Foam topology bending versus stretching dominated architectures," Acta Mater, vol. 49, no. 6, (Apr 2 2001) pp. 1035-1040.Doi 10.1016/S1359-6454(00)00379-7.

[17] M. Helou and S. Kara, "Design, analysis and manufacturing of lattice structures: an overview," Int J Comput Integ M, vol. 31, no. 3, 2018) pp. 243-261.10.1080/0951192x.2017.1407456.

[18] R. Gümrük and R. A. W. Mines, "Compressive behaviour of stainless steel micro-lattice structures," Int J Mech Sci, vol. 68, (Mar 2013) pp. 125-139.10.1016/j.ijmecsci.2013.01.006.

[19] M. Leary *et al.*, "Selective laser melting (SLM) of AlSi12Mg lattice structures," Mater Design, vol. 98, (May 15 2016) pp. 344-357.10.1016/j.matdes.2016.02.127.

[20] D. W. Abueidda, M. Bakir, R. K. Abu Al-Rub, J. S. Bergström, N. A. Sobh, and I. Jasiuk, "Mechanical properties of 3D printed polymeric cellular materials with triply periodic minimal surface architectures," Mater Design, vol. 122, (May 15 2017) pp. 255-267.10.1016/j.matdes.2017.03.018.

[21] O. Al-Ketan, R. Rowshan, and R. K. Abu Al-Rub, "Topology-mechanical property relationship of 3D printed strut, skeletal, and sheet based periodic metallic cellular materials," Addit Manuf, vol. 19, (Jan 2018) pp. 167-183.10.1016/j.addma.2017.12.006.

[22] I. Maskery *et al.*, "Insights into the mechanical properties of several triply periodic minimal surface lattice structures made by polymer additive manufacturing," Polymer, vol. 152, (Sep 12 2018) pp. 62-71.10.1016/j.polymer.2017.11.049.

[23] D. T. Queheillalt and H. N. G. Wadley, "Cellular metal lattices with hollow trusses," Acta Mater, vol. 53, no. 2, (Jan 2005) pp. 303-313.10.1016/j.actamat.2004.09.024.

[24] Z. Ozdemir *et al.*, "Energy absorption in lattice structures in dynamics: Experiments," International Journal of Impact Engineering, vol. 89, (Mar 2016) pp. 49-61.10.1016/j.ijimpeng.2015.10.007.

[25] M. G. Rashed, M. Ashraf, R. A. W. Mines, and P. J. Hazell, "Metallic microlattice materials: A current state of the art on manufacturing, mechanical

properties and applications," Mater Design, vol. 95, (Apr 5 2016) pp. 518-533.10.1016/j.matdes.2016.01.146.

[26] L. J. Xiao *et al.*, "Mechanical properties of open-cell rhombic dodecahedron titanium alloy lattice structure manufactured using electron beam melting under dynamic loading," International Journal of Impact Engineering, vol. 100, (Feb 2017) pp. 75-89.10.1016/j.ijimpeng.2016.10.006.

[27] I. Ullah, J. Elambasseril, M. Brandt, and S. Feih, "Performance of bio-inspired Kagome truss core structures under compression and shear loading," Compos Struct, vol. 118, (Dec 2014) pp. 294-302.10.1016/j.compstruct.2014.07.036.

[28] R. A. W. Mines, S. Tsopanos, Y. Shen, R. Hasan, and S. T. McKown, "Drop weight impact behaviour of sandwich panels with metallic micro lattice cores," International Journal of Impact Engineering, vol. 60, (Oct 2013) pp. 120-132.10.1016/j.ijimpeng.2013.04.007.

[29] C. Z. Yan, L. Hao, A. Hussein, P. Young, and D. Raymont, "Advanced lightweight 316L stainless steel cellular lattice structures fabricated via selective laser melting," Mater Design, vol. 55, (Mar 2014) pp. 533-541.10.1016/j.matdes.2013.10.027.

[30] L. J. Gibson, "Biomechanics of cellular solids," J Biomech, vol. 38, no. 3, (Mar 2005) pp. 377-399.10.1016/j.jbiomech.2004.09.027.

[31] M. Smith, Z. Guan, and W. J. Cantwell, "Finite element modelling of the compressive response of lattice structures manufactured using the selective laser melting technique," Int J Mech Sci, vol. 67, (Feb 2013) pp. 28-41.10.1016/j.ijmecsci.2012.12.004.

[32] S. M. Ahmadi *et al.*, "Mechanical behavior of regular open-cell porous biomaterials made of diamond lattice unit cells," J Mech Behav Biomed, vol. 34, (Jun 2014) pp. 106-115.10.1016/j.jmbbm.2014.02.003.

[33] H. S. Lei *et al.*, "Evaluation of compressive properties of SLM-fabricated multi-layer lattice structures by experimental test and μ-CT-based finite element analysis," Mater Design, vol. 169, (May 5 2019).ARTN 10768510.1016/j.matdes.2019.107685.

[34] L. Liu, P. Kamm, F. García-Moreno, J. Banhart, and D. Pasini, "Elastic and failure response of imperfect three-dimensional metallic lattices: the role of geometric defects induced by Selective Laser Melting," J Mech Phys Solids, vol. 107, (Oct 2017) pp. 160-184.10.1016/j.jmps.2017.07.003.

[35] C. Baykasoglu, A. Baykasoglu, and E. Cetin, "Multi-objective crashworthiness optimization of square aluminum tubes with functionally graded BCC lattice structure filler," Int J Crashworthines, vol. 29, no. 1, (Jan 2 2024) pp. 80-94.10.1080/13588265.2023.2183801.

[36] J. P. M. Cheloni, B. Zluhan, M. E. Silveira, E. B. Fonseca, D. B. Valim, and E. S. N. Lopes, "Mechanical behavior and failure mode of body-centered cubic, gyroid, diamond, and Voronoi functionally graded additively manufactured biomedical lattice structures," J Mech Behav Biomed, vol. 163, (Mar 2025).ARTN 10679610.1016/j.jmbbm.2024.106796.

[37] A. Coluccia, G. Meyer, S. Liseni, C. Mittelstedt, and G. De Pasquale, "Functionally graded lattice structures for energy absorption: Numerical analysis and experimental validation," Compos Struct, vol. 360, (Apr 2025).ARTN 11901310.1016/j.compstruct.2025.119013.

[38] A. Dadashi, A. Farrokhabadi, and D. Chronopoulos, "A Comprehensive Investigation of the Geometric Functionally Graded Auxetic Double Arrowhead Composite Lattice Structures: Exploring Tailored Longitudinal and Lateral Young's Modulus," Int J Appl Mech, vol. 16, no. 09, (Nov 2024).Artn 245010510.1142/S1758825124501059.

[39] S. Daynes and S. Feih, "Functionally graded lattice structures with tailored stiffness and energy absorption," Int J Mech Sci, vol. 285, (Jan 1 2025).ARTN 10986110.1016/j.ijmecsci.2024.109861.

[40] T. Decker and S. Kedziora, "Local Thickness Optimization of Functionally Graded Lattice Structures in Compression," Appl Sci-Basel, vol. 13, no. 23, (Dec 2023).ARTN 1296910.3390/app132312969.

[41] I. Maskery *et al.*, "A mechanical property evaluation of graded density Al-Si10-Mg lattice structures manufactured by selective laser melting," Mat Sci Eng a-Struct, vol. 670, (Jul 18 2016) pp. 264-274.10.1016/j.msea.2016.06.013.

[42] Z. J. Zheng, J. L. Yu, and J. R. Li, "Dynamic crushing of 2D cellular structures: A finite element study," International Journal of Impact Engineering, vol. 32, no. 1-4, (Dec 2005) pp. 650-664.10.1016/j.ijimpeng.2005.05.007.

[43] S. McKown *et al.*, "The quasi-static and blast loading response of lattice structures," International Journal of Impact Engineering, vol. 35, no. 8, (Aug 2008) pp. 795-810.10.1016/j.ijimpeng.2007.10.005.

[44] F. N. Habib, P. Iovenitti, S. H. Masood, and M. Nikzad, "Fabrication of polymeric lattice structures for optimum energy absorption using Multi Jet Fusion technology," Mater Design, vol. 155, (Oct 5 2018) pp. 86-98.10.1016/j.matdes.2018.05.059.

[45] R. M. Christensen, "Mechanics of cellular and other low-density materials," Int J Solids Struct, vol. 37, no. 1-2, (Jan 2000) pp. 93-104.Doi 10.1016/S0020-7683(99)00080-3.

[46] C. Ling, A. Cernicchi, M. D. Gilchrist, and P. Cardiff, "Mechanical behaviour of additively-manufactured polymeric octet-truss lattice structures under quasi-static and dynamic compressive loading," Mater Design, vol. 162, (Jan 15 2019) pp. 106-118.10.1016/j.matdes.2018.11.035.

[47] R. Gümrük, R. A. W. Mines, and S. Karadeniz, "Static mechanical behaviours of stainless steel micro-lattice structures under different loading conditions," Mat Sci Eng a-Struct, vol. 586, (Dec 1 2013) pp. 392-406.10.1016/j.msea.2013.07.070.

[48] D. Herzog, V. Seyda, E. Wycisk, and C. Emmelmann, "Additive manufacturing of metals," Acta Mater, vol. 117, 2016) pp. 371-392.

[49] T. DebRoy *et al.*, "Additive manufacturing of metallic components - Process, structure and properties," Prog Mater Sci, vol. 92, (Mar 2018) pp. 112-224.10.1016/j.pmatsci.2017.10.001.

[50] S. L. Sing, J. An, W. Y. Yeong, and F. E. Wiria, "Laser and electron-beam powder-bed additive manufacturing of metallic implants: A review on processes, materials and designs," J Orthop Res, vol. 34, no. 3, (Mar 2016) pp. 369-385.10.1002/jor.23075.

[51] C. Y. Yap *et al.*, "Review of selective laser melting: Materials and applications," Appl Phys Rev, vol. 2, no. 4, (Dec 2015).Artn 04110110.1063/1.4935926.

[52] G. Kasperovich and J. Hausmann, "Improvement of fatigue resistance and ductility of TiAl6V4 processed by selective laser melting," J Mater Process Tech, vol. 220, (Jun 2015) pp. 202-214.10.1016/j.jmatprotec.2015.01.025.

[53] D. Greitemeier, C. D. Donne, F. Syassen, J. Eufinger, and T. Melz, "Effect of surface roughness on fatigue performance of additive manufactured Ti-6Al-4V," Mater Sci Tech-Lond, vol. 32, no. 7, 2016) pp. 629-634.10.1179/1743284715y.0000000053.

[54] L. E. Murr *et al.*, "Metal Fabrication by Additive Manufacturing Using Laser and Electron Beam Melting Technologies," J Mater Sci Technol, vol. 28, no. 1, (Jan 2012) pp. 1-14.Doi 10.1016/S1005-0302(12)60016-4.

[55] H. J. Gong, K. Rafi, H. F. Gu, G. D. J. Ram, T. Starr, and B. Stucker, "Influence of defects on mechanical properties of Ti-6Al-4 V components produced by selective laser melting and electron beam melting," Mater Design, vol. 86, (Dec 5 2015) pp. 545-554.10.1016/j.matdes.2015.07.147.

[56] B. N. Turner, R. Strong, and S. A. Gold, "A review of melt extrusion additive manufacturing processes: I. Process design and modeling," Rapid Prototyping J, vol. 20, no. 3, 2014) pp. 192-204.10.1108/Rpj-01-2013-0012.

[57] S. H. Ahn, M. Montero, D. Odell, S. Roundy, and P. K. Wright, "Anisotropic material properties of fused deposition modeling ABS," Rapid Prototyping J, vol. 8, no. 4, 2002) pp. 248-257.10.1108/13552540210441166.

[58] M. F. Ashby and D. Cebon, "Materials selection in mechanical design," Le Journal de Physique IV, vol. 3, no. C7, 1993) pp. C7-1-C7-9.

[59] C. Du, S. Kong, C. Xie, D. Wang, and F. Zhao, "An efficient material selection method driven by structural crashworthiness for lightweight design of vehicle parts," International Journal of Crashworthiness, vol. 30, no. 5, 2025) pp. 503-518.

[60] Y. L. Su, X. G. Ji, and G. F. Niu, "Shear performance of flexible and elastic composite lattice structures for application scenarios," P I Mech Eng L-J Mat, (Sep 25 2025).10.1177/14644207251379741.

[61] Y. H. Wang *et al.*, "Failure Evolution and Interface Strengthening Mechanisms of Bio-Inspired Gradient Composite Lattice Sandwich Structures," Polym Composite, (Nov 5 2025).10.1002/pc.70621.

[62] X. Xue, J. Gao, C. Zheng, Z. Y. Li, J. Liao, and M. G. Zhang, "Energy absorption and vibration characteristics of metal/polymer composited pyramidal lattice cylinder structure," Structures, vol. 76, (Jun 2025).ARTN 10887810.1016/j.istruc.2025.108878.

[63] K. Dong, T. N. Hou, P. Zheng, and Y. Xiong, "Continuous fiber-reinforced 2.5D hybrid lattice structures with superior compression performance via self-supporting suspension printing," Compos Sci Technol, vol. 257, (Oct 20 2024).ARTN 11084510.1016/j.compscitech.2024.110845.

[64] A. R. Bernard, M. M. Yalcin, and M. S. A. Elsayed, "Crashworthiness investigations for 3D printed multi-layer multi-topology carbon fiber nylon lattice materials," J Reinf Plast Comp, vol. 44, no. 11-12, (Jun 2025) pp. 634-649.10.1177/07316844241226834.

[65] H. Norouzi and M. Mahmoodi, "Experimental and Numerical Assessment of Flatwise Compression Behaviors of Sandwich Panels: Comparison Between Aluminum, Innegra Fiber and Glass/Epoxy New Symmetric Lattice Cores," Exp Techniques, vol. 48, no. 4, (Aug 2024) pp. 721-734.10.1007/s40799-023-00694-6.

[66] B. B. Vanani, M. Abbasi, and M. Givi, "Compressive behavior of octet lattice made by carbon fiber reinforced polymer composite hollow struts: molecular dynamic simulation," Multiscale Multi Mod, vol. 8, no. 1, (Jan 2025).ARTN 210.1007/s41939-024-00607-z.

[67] F. Di Caprio, V. Acanfora, S. Franchitti, A. Sellitto, and A. Riccio, "Hybrid Metal/Composite Lattice Structures: Design for Additive Manufacturing," Aerospace-Basel, vol. 6, no. 6, (Jun 2019).ARTN 7110.3390/aerospace6060071.

[68] A. Banas, R. Wojtuszewski, M. Olejarczyk, W. Krauze, T. Galaczynski, and T. Kurzynowski, "Selection of optimal test methods for developing process parameters in automated fiber placement technology," Adv Sci Technol-Res, vol. 19, no. 11, 2025) pp. 243-257.10.12913/22998624/208480.

[69] S. Carosella, S. Hügle, F. Helber, and P. Middendorf, "A short review on recent advances in automated fiber placement and filament winding technologies,"

Compos Part B-Eng, vol. 287, (Dec 2024).ARTN 11184310.1016/j.compositesb.2024.111843.

[70] L. Wan, D. Y. Hu, and H. B. Zhang, "Crashworthiness study of aluminum foam-filled tubular lattice structures based on triply periodic minimal surface metamaterials under lateral crushing," Thin Wall Struct, vol. 197, (Apr 2024).ARTN 11161610.1016/j.tws.2024.111616.

[71] A. Mandal, F. Li, X. Jia, and Y. T. Pei, "Compressive deformation behavior of functionally graded lattice structures of stainless steel 316L," J Mater Res Technol, vol. 35, (Mar-Apr 2025) pp. 4599-4613.10.1016/j.jmrt.2025.02.077.

[72] W. T. Shi, Y. X. Lin, J. Li, S. Liu, Y. F. Han, and B. Liu, "Mechanical Response and Energy Absorption of 316L Stainless Steel Body-Centered-Cubic Functionally Graded Lattice Structures under Quasistatic Compressive Test," Adv Eng Mater, vol. 25, no. 17, (Sep 2023).10.1002/adem.202300451.

[73] J. S. Weeks, V. Gandhi, and G. Ravichandran, "Shock compression behavior of stainless steel 316L octet-truss lattice structures," Int J Impact Eng, vol. 169, (Nov 2022).ARTN 10432410.1016/j.ijimpeng.2022.104324.

[74] M. Kopar and M. Sömer, "Energy absorption characteristics of 3D printed polymeric hybrid lattice structures fabricated by additive manufacturing," J Braz Soc Mech Sci, vol. 47, no. 12, (Oct 3 2025).ARTN 61910.1007/s40430-025-05912-3.

[75] Z. P. Sun, J. J. Zhang, T. Hua, and Y. Y. Ding, "Experimental investigation on anisotropy of additively manufactured polymeric lattices subjected to multi-directional compression," Eng Struct, vol. 340, (Oct 1 2025).ARTN 12069510.1016/j.engstruct.2025.120695.

[76] M. P. Bendsoe and N. Kikuchi, "Generating Optimal Topologies in Structural Design Using a Homogenization Method," Comput Method Appl M, vol. 71, no. 2, (Nov 1988) pp. 197-224.Doi 10.1016/0045-7825(88)90086-2.

[77] Y. M. Xie and G. P. Steven, "A Simple Evolutionary Procedure for Structural Optimization," Comput Struct, vol. 49, no. 5, (Dec 3 1993) pp. 885-896.Doi 10.1016/0045-7949(93)90035-C.

[78] F. Duddeck, S. Hunkeler, P. Lozano, E. Wehrle, and D. Zeng, "Topology optimization for crashworthiness of thin-walled structures under axial impact using hybrid cellular automata," Struct Multidiscip O, vol. 54, no. 3, (Sep 2016) pp. 415-428.10.1007/s00158-016-1445-y.

[79] J. G. Fang, G. Y. Sun, N. Qiu, N. H. Kim, and Q. Li, "On design optimization for structural crashworthiness and its state of the art," Struct Multidiscip O, vol. 55, no. 3, (Mar 2017) pp. 1091-1119.10.1007/s00158-016-1579-y.

[80] G. Y. Sun, G. Y. Li, M. Stone, and Q. Li, "A two-stage multi-fidelity optimization procedure for honeycomb-type cellular materials," Comp Mater Sci, vol. 49, no. 3, (Sep 2010) pp. 500-511.10.1016/j.commatsci.2010.05.041.

[81] K. Deb, A. Pratap, S. Agarwal, and T. Meyarivan, "A fast and elitist multiobjective genetic algorithm: NSGA-II," Ieee T Evolut Comput, vol. 6, no. 2, (Apr 2002) pp. 182-197.Pii S 1089-778x(02)04101-2Doi 10.1109/4235.996017.

[82] M. H. Luxner, J. Stampfl, and H. E. Pettermann, "Finite element modeling concepts and linear analyses of 3D regular open cell structures," J Mater Sci, vol. 40, no. 22, (Nov 2005) pp. 5859-5866.10.1007/s10853-005-5020-y.

[83] G. Campoli, M. S. Borleffs, S. A. Yavari, R. Wauthle, H. Weinans, and A. A. Zadpoor, "Mechanical properties of open-cell metallic biomaterials manufactured using additive manufacturing," Mater Design, vol. 49, (Aug 2013) pp. 957-965.10.1016/j.matdes.2013.01.071.

[84] G. R. Johnson and W. H. Cook, "Fracture characteristics of three metals subjected to various strains, strain rates, temperatures and pressures," Engineering fracture mechanics, vol. 21, no. 1, 1985) pp. 31-48.

[85] T. Belytschko and L. P. Bindeman, "Assumed strain stabilization of the eight node hexahedral element," Comput Method Appl M, vol. 105, no. 2, 1993) pp. 225-260.

[86] P. Wriggers and T. A. Laursen, *Computational contact mechanics*. Springer, 2006.

[87] I. Ullah, M. Brandt, and S. Feih, "Failure and energy absorption characteristics of advanced 3D truss core structures," Mater Design, vol. 92, (Feb 15 2016) pp. 937-948.10.1016/j.matdes.2015.12.058.

[88] H. R. Zarei and M. Kröger, "Optimization of the foam-filled aluminum tubes for crush box application," Thin Wall Struct, vol. 46, no. 2, (Feb 2008) pp. 214-221.10.1016/j.tws.2007.07.016.

[89] J. G. Fang, Y. K. Gao, G. Y. Sun, Y. T. Zhang, and Q. Li, "Crashworthiness design of foam-filled bitubal structures with uncertainty," Int J Nonlin Mech, vol. 67, (Dec 2014) pp. 120-132.10.1016/j.ijnonlinmec.2014.08.005.

[90] W. Hou, P. He, Y. Yang, and L. Sang, "Crashworthiness optimization of crash box with 3D-printed lattice structures," Int J Mech Sci, vol. 247, 2023) p. 108198.

[91] J. Simpson and Z. Kazancı, "Crushing investigation of crash boxes filled with honeycomb and re-entrant (auxetic) lattices," Thin Wall Struct, vol. 150, 2020) p. 106676.

[92] E. Cetin and C. Baykasoğlu, "Energy absorption of thin-walled tubes enhanced by lattice structures," Int J Mech Sci, vol. 157, 2019) pp. 471-484.

[93] X. Wu, S. Zhang, and J. Shao, "Studies on impact performance of gradient lattice structure applied to crash box," SAE Technical Paper0148-7191, 2018.

[94] Y. Liu *et al.*, "Integrated design and additive manufacturing of lattice-filled multi-cell tubes," Composites Science and Technology, vol. 243, 2023) p. 110252.

[95] K. Gunaydin, "Energy absorption ability of crush boxes filled with strut based and TPMS lattice structures," Journal of the Brazilian Society of Mechanical Sciences and Engineering, vol. 46, no. 11, 2024) p. 634.

[96] E. Gültekin and M. Yahşi, "Dynamic compression and impact analyses of the lattice structures for battery safety," Proceedings of the Institution of Mechanical Engineers, Part D: Journal of Automobile Engineering, vol. 237, no. 5, 2023) pp. 930-940.

[97] L. I. Scurtu, I. Szabo, and M. Gheres, "Numerical analysis of crashworthiness on electric vehicle's battery case with auxetic structure," Energies, vol. 16, no. 15, 2023) p. 5849.

[98] G. Totaro and Z. Gürdal, "Optimal design of composite lattice shell structures for aerospace applications," Aerosp Sci Technol, vol. 13, no. 4-5, (Jun-Jul 2009) pp. 157-164.10.1016/j.ast.2008.09.001.

[99] S. A. Galehdari and H. Khodarahmi, "Design and analysis of a graded honeycomb shock absorber for a helicopter seat during a crash condition," Int J Crashworthines, vol. 21, no. 3, 2016) pp. 231-241.10.1080/13588265.2016.1165440.

[100] G. Özturk and A. Kayran, "Energy Absorption Mechanisms and Crash Analysis of Helicopter Seats," Proceedings of the Asme International Mechanical Engineering Congress and Exposition, 2018, Vol 4b, 2019).

CHAPTER 10

COMPARATIVE ASSESSMENT OF COPPER AND ZINC IN BRAKE FRICTION APPLICATIONS

İLKER SUGÖZÜ[1]
BANU SUGÖZÜ[2]

Introduction

Copper has long been a key functional component in brake friction materials due to its ability to stabilize the friction coefficient, dissipate heat, and reduce noise during braking. Yet, as the environmental consequences of copper emissions become increasingly evident, researchers and manufacturers are compelled to seek sustainable alternatives. Wear debris originating from copper-rich friction composites can accumulate in soil and waterways, contributing to ecotoxicity and affecting aquatic organisms. This concern has accelerated global efforts—both regulatory and scientific—to reduce or replace copper in braking systems (Aranganathan & Bijwe, 2016:79).

[1] Doç. Dr., Mersin Üniversitesi, Makine Mühendisliği Bölümü, Orcid: 0000-0001-8340-8121
[2] Doç. Dr., Mersin Üniversitesi, Makine Mühendisliği Bölümü, Orcid: 0000-0002-7798-2677

In response to these environmental and legislative pressures, zinc and zinc-based materials have emerged as promising substitutes. Recent tribological studies provide important insights into how zinc behaves within friction composites and how its effects compare with those of copper. For example, Yang et al. (2020) systematically evaluated the influence of zinc powder content on phenolic-based brake materials and reported that moderate zinc addition can contribute to stable friction levels and reduced wear. Their findings indicate that zinc participates actively in the formation and maintenance of secondary contact plateaus, which are essential for friction stability. Excessive zinc content, however, may lead to increased wear, highlighting the need for optimized content levels.

Further understanding of zinc's role can be drawn from research on brass additives. Because brass inherently contains variable ratios of copper and zinc, it provides a useful model for studying the interactions between these two metals. Ahmed et al. (2020) demonstrated that altering the Cu/Zn ratio in brass powders influences braking performance, including friction consistency and wear resistance. Their results show that higher zinc fractions can slightly diminish thermal conductivity but may enhance wear resistance under certain loading conditions—supporting the idea that zinc-rich compositions can be viable in copper-reduced formulations.

A more detailed mechanistic understanding of copper–zinc interactions is offered in recent investigations of stiction and corrosion-related adhesion phenomena. Motta et al. (2024) examined how copper and zinc additives contribute to the propensity for stiction in automotive braking systems. Their work revealed that copper tends to intensify adhesive interactions at the pad–disc interface under humid or corrosive conditions, whereas zinc plays a comparatively mitigating role. Such findings underscore zinc's

potential to not only replace copper for environmental reasons but also improve braking performance in challenging operational environments.

The effect of varying copper and zinc proportions has also been explored from a fade and recovery perspective. Balachandran and Ma (2022) studied friction composites incorporating brass with different Cu/Zn ratios and found that higher zinc content can improve fade resistance at elevated temperatures. According to their results, zinc-rich composites show better recovery behavior after severe thermal loading, suggesting that zinc contributes positively to the thermal stability of the friction layer.

Collectively, these studies point toward an evolving paradigm in friction material design: zinc is not merely a passive substitute for copper but an active contributor to tribological behavior, plateau development, fade resistance, and corrosion performance (Kalel et al., 2021:464). As environmental restrictions continue to tighten and the automotive industry prioritizes sustainability, the systematic evaluation of zinc as a copper alternative becomes increasingly essential.

This study builds on these research findings to provide a detailed comparative assessment of copper and zinc in brake friction applications, focusing on their tribological roles and suitability for future composite formulations. The originality of the present work lies in its experimental approach, where copper and zinc are incorporated into friction composites at identical content levels, enabling a direct, controlled, and unbiased comparison of their individual contributions to friction behavior, wear characteristics, and thermal stability. By isolating the effect of each metal under equivalent formulation conditions, this study offers new insights into their functional differences and the potential of zinc as a viable replacement for copper.

Experimental Methods

Four different friction composite formulations were prepared to enable a controlled comparison of copper- and zinc-based additives. The base matrix composition was kept constant across all samples, consisting of phenolic resin as the primary binder (20 wt%), steel wool as the metallic reinforcement (15 wt%), cashew dust (10 wt%), graphite (5 wt%), alumina (5 wt%), silica (5 wt%), and barite as the main filler. The only variables among the formulations were the copper and zinc contents, which were systematically adjusted to create two copper-based (C10 and C20) and two zinc-based (Z10 and Z20) composites. In the C10 and C20 samples, copper was incorporated at 10 wt% and 20 wt%, respectively, while zinc was absent. Conversely, the Z10 and Z20 samples contained zinc at corresponding levels of 10 wt% and 20 wt%, with no copper included. Barite content was slightly varied (20–30 wt%) to maintain a total of 100 wt% for each formulation. This approach allowed the direct assessment of copper and zinc effects under identical matrix conditions, ensuring that observed differences in tribological performance could be attributed specifically to the metallic additives.

The preparation of the friction composites followed a controlled laboratory protocol to ensure uniformity across all formulations. Initially, all raw materials were manually mixed for approximately 10 minutes until a visually homogeneous blend was obtained. The mixed powders were then subjected to a pre-forming step using a hydraulic press. This initial compaction was carried out at room temperature under a pressure of 8 MPa for 2 minutes, producing a stable green body suitable for subsequent hot pressing.

After pre-forming, the specimens were transferred to a heated mold for final consolidation. Hot pressing was performed at 150 °C under a pressure of 13 MPa for 10 minutes, promoting adequate resin flow and strong interfacial bonding between the composite

constituents. Following demolding, the specimens were cooled to room temperature and subsequently surface-finished using abrasive sanding to achieve the required flatness and surface quality for tribological testing. This finishing step ensured that all samples met the dimensional and surface preparation standards necessary for reliable experimental evaluation.

The density of the cured composite samples was determined using the Archimedes displacement method to assess the degree of compaction and overall porosity of the materials. Each specimen was weighed both in air and while submerged in distilled water, allowing the bulk density to be calculated based on buoyant force principles. This method ensured reliable measurement accuracy even for materials with complex internal microstructures. Hardness values were obtained using a Rockwell hardness tester, with a minimum of three readings taken at different locations on each sample to account for potential local heterogeneities in the composite matrix. The average hardness and corresponding standard deviation were reported to characterize the mechanical resistance and surface integrity of the copper- and zinc-based friction materials. All measurements were performed in triplicate to ensure repeatability and statistical reliability.

The thermal swelling behavior of the brake friction composites was evaluated to determine their dimensional stability and structural robustness under elevated temperature conditions. Prior to thermal exposure, the thickness, diameter, and mass of each specimen were precisely measured using a digital micrometer with an accuracy of ±1 μm, a digital caliper, and an analytical balance with a resolution of 0.1 mg. The samples were then placed into a laboratory-scale sintering furnace preheated to 400 °C and held at this temperature for 10 minutes to simulate the thermal loads typically encountered in braking operations.

Following heat treatment, the specimens were allowed to cool naturally to room temperature under ambient laboratory conditions. The same dimensional and mass measurements were repeated using identical instruments to ensure consistency. Changes in thickness, diameter, and mass were recorded and compared to the initial values to determine the degree of thermal swelling or shrinkage. These results provided insight into the thermal stability of the copper- and zinc-containing composites, particularly regarding binder integrity, filler interactions, and potential microstructural degradation under high-temperature exposure.

Tribological performance of the friction materials was examined using a laboratory-scale, computer-controlled brake testing rig equipped with a gray cast iron brake disc, similar to those used in automotive braking systems. The rig allowed precise monitoring and adjustment of all operational parameters throughout each experiment, ensuring high measurement fidelity. All tests were conducted in accordance with the TS 555 standard for brake friction materials, providing a realistic representation of actual braking conditions.

During each test cycle, the coefficient of friction (COF) and interface temperature were continuously recorded to evaluate friction stability, fade resistance, and thermal behavior. Upon completion of each test, the samples were weighed to determine mass loss, from which the wear rate was calculated. The worn surfaces were subsequently examined using scanning electron microscopy (SEM) to identify dominant wear mechanisms, material transfer phenomena, and the formation of secondary contact plateaus. All tribological tests were conducted in triplicate to ensure repeatability and to enable reliable comparison between copper-based and zinc-based composite formulations.

Detailed morphological examinations of the worn surfaces were carried out using scanning electron microscopy (SEM) to

investigate microstructural changes induced by frictional loading. SEM images were analyzed to identify wear mechanisms such as abrasion, adhesion, microcracking, and the presence of tribo-oxidative layers. Special attention was given to the development, distribution, and integrity of secondary contact plateaus, as these features play a critical role in friction stabilization and wear control.

In addition to morphological observations, energy-dispersive X-ray spectroscopy (EDS) was employed to determine the elemental composition of the tribo-layer and transferred materials on both copper- and zinc-containing samples. EDS mapping allowed the identification of metallic particle distribution, oxide formation, and potential differences in tribo-film chemistry associated with the two additives. These analyses provided valuable insights into how copper and zinc influence tribological behavior at the microstructural level.

Results and Discussion

The friction coefficient results for all four formulations (C10, C20, Z10, Z20) are collectively presented in Figure 1, enabling a direct comparison of the tribological behavior of copper- and zinc-based composites under identical test conditions. Based on these curves, the C10 specimen exhibited an average friction coefficient of approximately $\mu = 0.316$, indicating a moderate friction level. Its friction stability of 71.8% aligns with the relatively narrow fluctuation band observed in the plot, reflecting a reasonably steady but not highly robust tribological response. Increasing the copper content to 20 wt.% enhanced the performance substantially: the C20 sample reached an average friction coefficient of $\mu = 0.391$—the highest among all tested materials. Its stability also improved to 78.2%, confirming that copper promotes both higher friction generation and more consistent surface interactions during braking.

For the zinc-based composites, the Z10 specimen recorded an average friction coefficient of μ = 0.321, comparable to C10, but its friction stability was slightly lower at 71.1%. The decline in the friction curve during the later stages of testing suggests that low zinc content may limit the development of a stable tribo-layer, resulting in reduced long-term frictional steadiness. Increasing the zinc content to 20 wt.% significantly improved performance. The Z20 composite achieved an average friction coefficient of μ = 0.392—essentially matching the C20 value—and exhibited the highest friction stability of all materials at 80.1%. This superior stability indicates that higher zinc content enhances the formation and continuity of protective tribo-films, effectively reinforcing surface interaction stability.

Figure 1 Coefficient of friction (COF) variation during braking for C10, C20, Z10, and Z20 composite formulations under identical test conditions

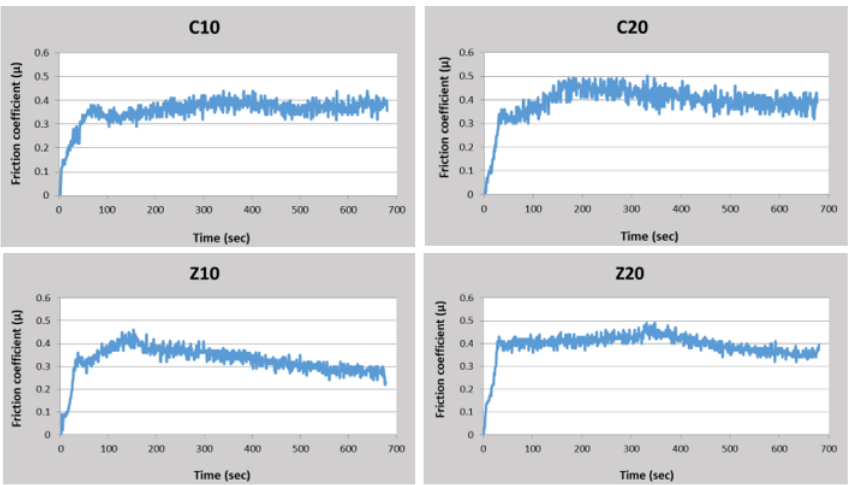

Overall, both copper- and zinc-based composites benefited from increased metallic content, but the zinc-rich Z20 sample demonstrated that zinc can provide friction levels and stability comparable to those of copper. These findings highlight zinc's

potential as a viable and more sustainable alternative for future brake friction formulations, particularly when used at optimized concentrations.

The specific wear ratios of the composites indicate noticeable differences in wear resistance associated with both material type and metallic content. The values ranged from 2.22×10^{-6} cm³/Nm to 2.93×10^{-6} cm³/Nm, demonstrating that all formulations exhibit wear performance within a similar order of magnitude, yet with distinct trends. Among the copper-based samples, C10 showed a wear ratio of 2.32×10^{-6} cm³/Nm, while increasing the copper content to 20 wt.% (C20) unexpectedly led to a higher wear ratio of 2.93×10^{-6} cm³/Nm. This suggests that although C20 exhibited superior frictional properties, its higher metallic loading may have promoted abrasive interactions or less cohesive tribo-layer formation, resulting in increased material loss.

In contrast, the zinc-based samples exhibited slightly lower wear ratios. Z10 presented the lowest wear value of all formulations at 2.22×10^{-6} cm³/Nm, indicating favorable wear resistance at moderate zinc content. The Z20 specimen showed an increased wear ratio of 2.73×10^{-6} cm³/Nm, though still lower than the corresponding copper-rich C20 sample. These findings imply that zinc contributes to more stable tribo-layer formation at lower concentrations, while excessive zinc—similar to copper—may reduce structural integrity under severe sliding conditions. Overall, the wear results suggest that zinc-containing composites maintain competitive wear resistance relative to traditional copper-based materials, with Z10 demonstrating the most advantageous balance between frictional stability and material durability.

The physical and thermomechanical properties of the four formulations, presented in Table 1, reveal clear trends associated with both metallic type and content. Density increased systematically with higher metallic loading, rising from 2.16 g/cm³

for C10 to 2.37 g/cm³ for C20, and from 2.21 g/cm³ for Z10 to a maximum of 2.56 g/cm³ for Z20. This progression reflects the higher intrinsic densities of copper and zinc compared to the polymer–ceramic matrix components. Hardness values exhibited a similar pattern: the C-series increased from 79 HRB (C10) to 89 HRB (C20), while the zinc-based samples rose from 72 HRB (Z10) to 84 HRB (Z20), indicating that the addition of metallic constituents enhances load-bearing capability and structural consolidation.

Thermal expansion behavior also followed an upward trend. The lowest expansion was measured for C10 (0.053), whereas Z20 showed the highest value (0.084), suggesting greater thermal sensitivity at elevated zinc contents. This is consistent with zinc's higher thermal expansion characteristics relative to copper, resulting in more pronounced dimensional changes during heating. Overall, the properties summarized in Table 1 demonstrate that increasing metallic content strengthens the composites mechanically but also elevates their thermal expansion response, with Z20 exhibiting the greatest thermal reactivity despite improved hardness and densification.

Table 1 Physical and thermomechanical properties of C10, C20, Z10, and Z20 composite formulations

Sample code	Density (g/cm^3)	Rockwell hardness (HRB)	Thermal Expansion
C10	2.16	79	0.053
C20	2.37	89	0.071
Z10	2.21	72	0.066
Z20	2.56	84	0.084

The SEM micrographs presented in Figure 2 provide detailed insight into the morphological characteristics and wear-surface evolution of the four composite formulations. In general, all samples exhibit a heterogeneous microstructure composed of resin-rich regions, metallic particles, ceramic abrasives, and fillers; however,

the condition and continuity of the tribo-layer differ markedly depending on copper or zinc content. The C10 and Z10 samples show more fragmented and discontinuous secondary plateaus, indicating that lower metallic content limits the formation of a stable load-bearing tribo-film. These surfaces include exposed fibers, micro-cracks, and local pull-out zones, suggesting less effective compaction and weaker thermal–mechanical stability during braking.

Figure 2 SEM micrographs of the worn surfaces of C10, C20, Z10, and Z20 composites

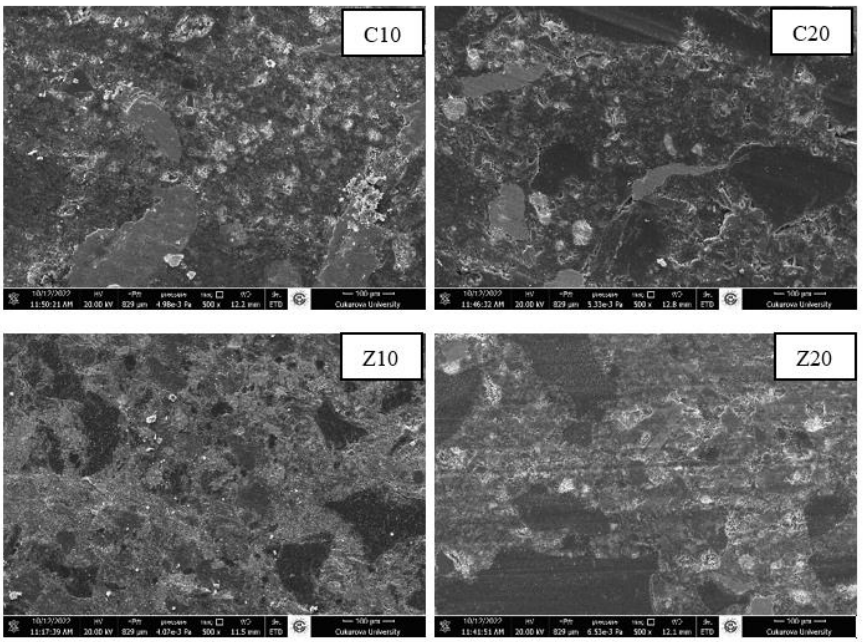

With increased metallic content, the C20 and Z20 surfaces display more cohesive and continuous tribo-layers. In C20, copper particles appear well-embedded within the matrix, forming smoother plateaus that contribute to improved friction stability but also exhibit localized abrasive grooves, consistent with its higher wear rate. In contrast, Z20 shows a relatively uniform distribution of zinc particles

and a more compacted tribo-layer, with fewer micro-cracks and reduced fiber exposure. This morphology corresponds well with the improved friction stability and competitive wear resistance measured experimentally.

Overall, the SEM observations in Figure 2 confirm that higher metallic content—especially zinc at 20 wt.%—promotes the development of more stable and protective tribological films, thereby enhancing braking performance and structural integrity under dynamic loading.

The EDS analyses presented in Figure 3 provide a compositional evaluation of the worn surfaces, offering valuable confirmation of the tribological mechanisms inferred from SEM observations. Across all samples, the dominant detected elements correspond to the principal constituents of the friction composites—carbon and oxygen from the phenolic resin, iron from steel wool, and various ceramic-related elements (such as Al, Si, and Ba) originating from alumina, silica, and barite fillers. However, the distribution and relative intensity of metallic elements (Cu and Zn) vary significantly among the formulations, reflecting their differing roles during tribo-layer formation.

In the copper-based samples (C10 and C20), EDS spectra reveal pronounced copper peaks, particularly in regions associated with compacted secondary plateaus. The C20 sample exhibits a more intense and continuous copper signal, indicating that higher copper content contributes to a denser metallic film on the surface. This observation aligns with the improved friction stability of C20; however, the simultaneous presence of elevated iron and abrasive-related elements suggests that localized three-body abrasion also occurred, consistent with its higher wear rate.

Figure 3 EDS spectra of worn surface regions for C10, C20, Z10, and Z20 composites

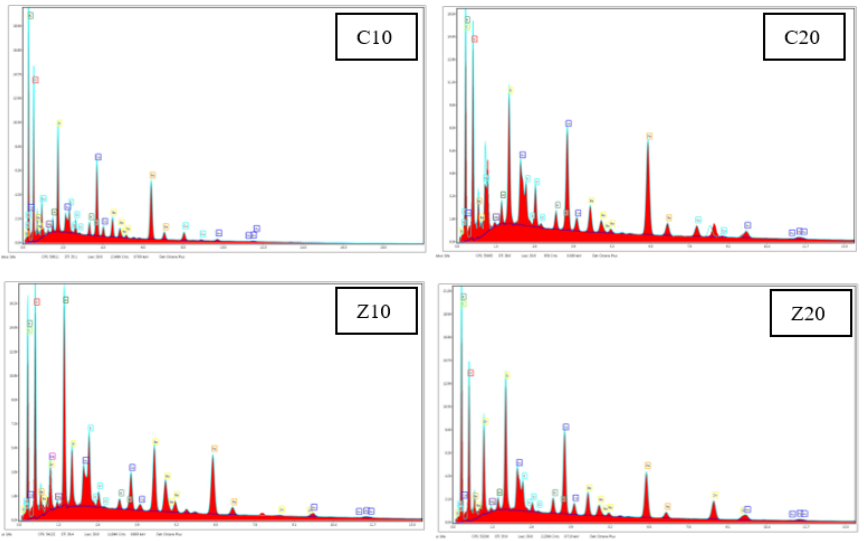

The zinc-based samples (Z10 and Z20) present distinct EDS characteristics. Zinc peaks are clearly visible and more uniformly distributed in Z20, supporting the SEM findings that this formulation develops a relatively coherent and stable tribo-layer. The lower zinc intensity in Z10 correlates with its more fragmented tribological film and reduced friction stability. Additionally, Z20 shows fewer regions with excessive iron or abrasive-element accumulation, indicating reduced abrasive interactions and a more protective tribo-layer, which agrees well with its favorable wear and friction performance.

Overall, the EDS results in Figure 3 confirm that metallic content strongly influences the chemical composition of the tribo-layer. Higher zinc content, in particular, promotes a more uniform and protective surface chemistry compared to copper, positioning zinc-rich composites as promising alternatives for enhanced stability and environmental compatibility in brake friction applications.

References

Aranganathan, N., & Bijwe, J. (2016). Development of copper-free eco-friendly brake-friction material using novel ingredients. *Wear*, *352*, 79-91.

Ahmed, K. A., Mohideen, S. R., Balaji, M. A. S., & Rajan, B. S. (2020). Tribological performance of brass powder with different copper and zinc content in the brake pad. Tribology in Industry, 42(2), 177.

Balachandran, S. R., & MA, S. B. (2022). Varying Cu and Zn composition in brass and its effect on the fade and recovery behavior of the phenolic-based friction composites. Polymer Composites, 43(7).

Kalel, N., Bhatt, B., Darpe, A., & Bijwe, J. (2021). Copper-free brake-pads: A break-through by selection of the right kind of stainless steel particles. *Wear*, *464*, 203537.

Motta, M., Iodice, V., Xicola, A. S., Truccolo, A., Fedrizzi, L., & Andreatta, F. (2024). Role of copper and zinc additives in the stiction phenomenon of automotive braking systems. Materials and Corrosion, 75(8), 1005-1017.

Yang, Y. A. N. G., Liang, L. X., Hong, W. U., & Hui, Q. U. (2020). Effect of zinc powder content on tribological behaviors of brake friction materials. Transactions of Nonferrous Metals Society of China, 30(11), 3078-3092.

CHAPTER 11

PARAMETRIC DESIGN/MODELING IN SOLIDWORKS OF SLIDEWAY

MAHMUT TANDOGAN[1]

Introduction

Old production techniques have evolved into mass production modifications, which may require tiny quantities of various pieces, to fulfil market needs. As a result, it is necessary to develop and manufacture parts with similar but little changing geometric proportions as soon as possible. Design techniques that enable the usage of parameters required to define a shape must be created in order to do this. This necessity has led to the development of design methods known as parametric design. Moreover, a new construction necessitates both static and dynamic calculations even during the design stage, which results in frequent modifications. In this situation, it might be necessary to swiftly redesign an existing product and alter its design considering the findings of engineering investigations (Halkacı & Yiğit, 2004).

The word parametric means the geometric definitions of the design, such as dimensions, can be varied at any time in the design

[1] Assistant Professor, Adıyaman University, Department of Mechanical Engineering, Orcid: 0000-0001-6393-2209

process. In computer aided drawing, a constraint is a relationship that restricts how an entity or collection of objects can behave. Lines that are parallel or perpendicular, lines that are tangent to curves, circles that are concentric, one dimension being smaller than another, or one dimension being a particular multiple of another are some examples of constraints. These constraints led to the start of parametric design applications (Monodero, 2000).

Parametric design types will be applied to the design of slideway of machine tool. Solidworks 2018 software was used to design the parts. The system can be affected by a dimensional change in a component that desired to be designed. While parametric modelling of a single part is supported by many CAD systems, most programs struggle to determine how parts relate to nearby assembly pieces when taking the system into account (Myung & Han, 2001). Extensive attention was taken to ensure that the CAD program used in this study fully supports parametric design during both the part modelling and assembly phases. In solidworks, parametric design can be divided as three main group. These are adding a new configuration, design table applications, using the equation editor.

Types of Parametric Desing in Solidworks

Adding a New Configuration

Firstly, in parametric design concept, names of dimensions are important for easy designing. Normally if click on tick button the name of this dimension will be D1 in Figure 1.

Figure 1. Standard Dimension Name According to Sketch

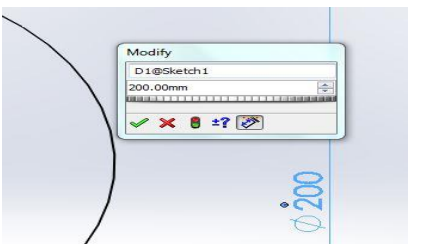

This is not a useful application in parametric design. Because in the parametric design section, dimension names cannot be defined. If the dimension name is renamed according to the drawing of the part configuration as shown in Figure 2, it will be easy to understand the dimension that is related. D1 name in sketch is changed to DiameterInnerHole according to part feature.

Figure 2. Adding New Name

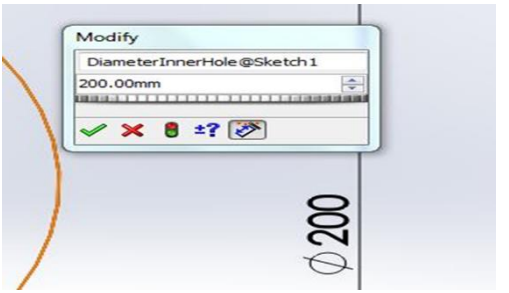

In Solidworks part menu firstly, the Configuration Manager section is clicked then right clicked the *«Name of Part» Configuration(s)* section and clicked the Add Configuration as shown in Figure 3.

Figure 3. Configuration Section in Solidworks Menu

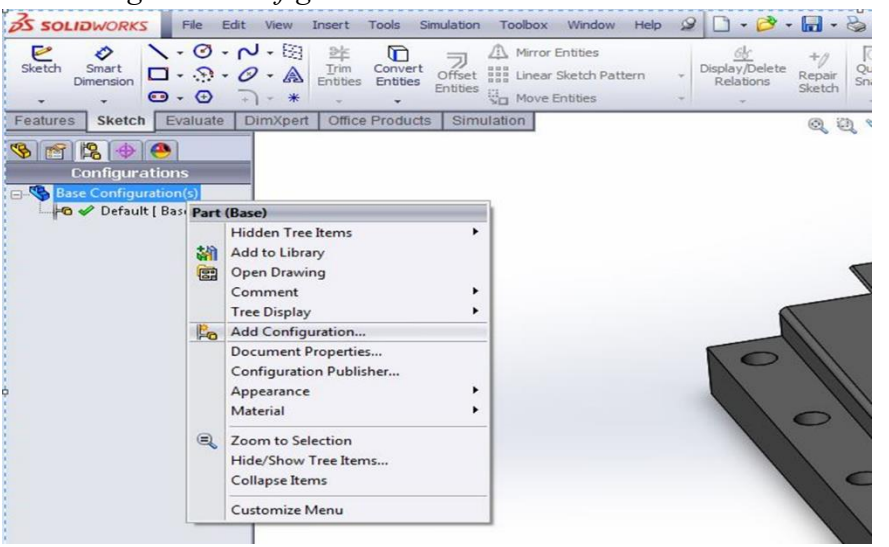

Figure 4. Adding New Configuration Name

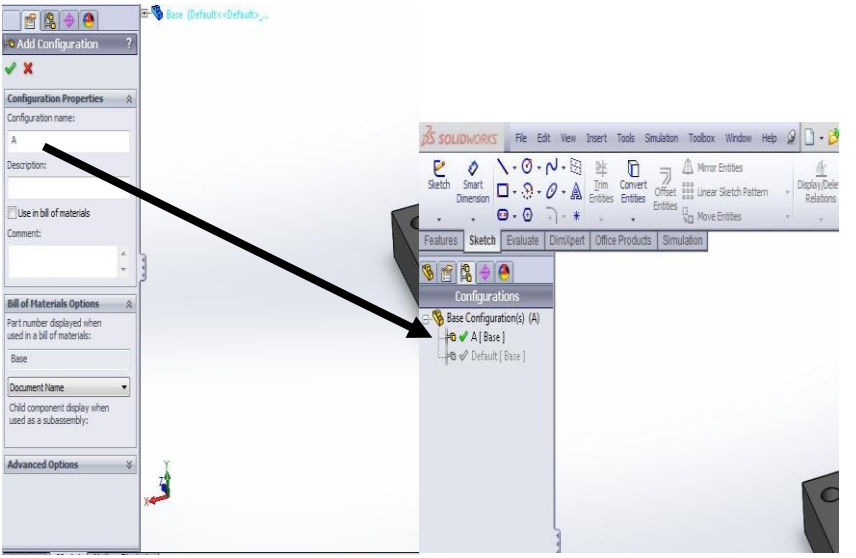

The Length of part (extruded length) in A configuration should be changed. In Default configuration this length is 250 mm in Figure 5.

Figure 5. Default Configuration

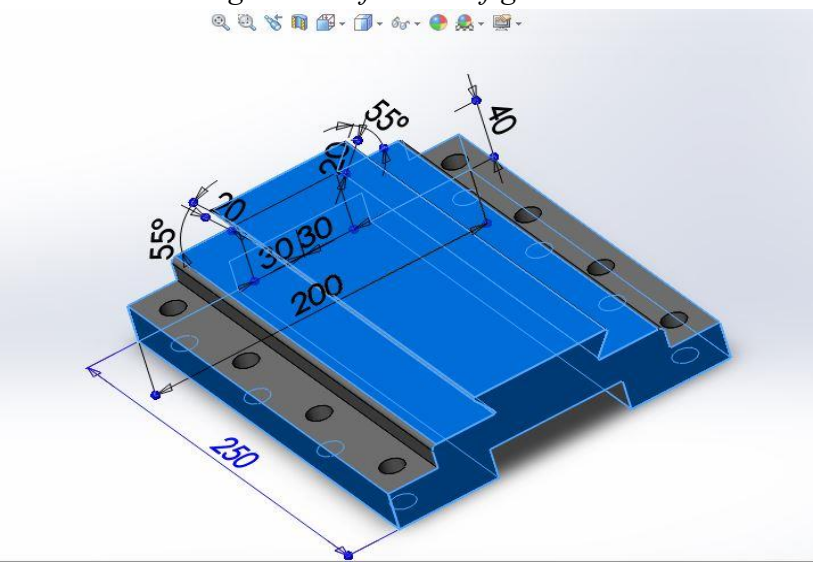

First, the A configuration should be selected then this dimension should be double clicked. Then the showing circle point should be clicked, and this configuration should be selected as in Figure 6.

Figure 6. A Configuration

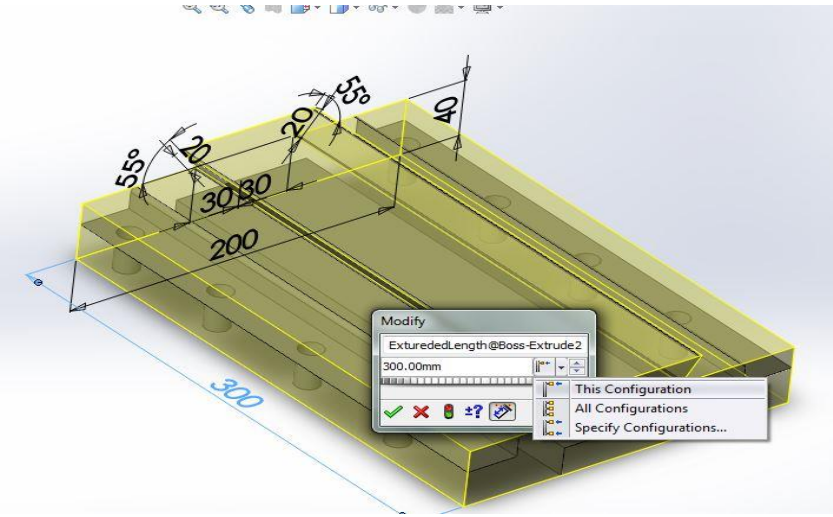

After this, extruded length will be 250 mm and 300 mm for default configuration and A configuration, respectively as shown in Figure 7.

Figure 7. Default and A Configuration

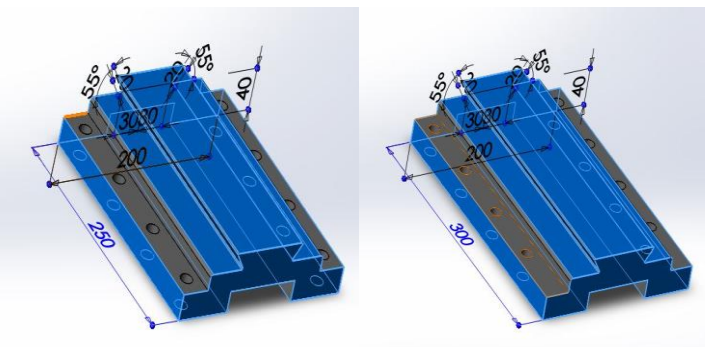

Design Table Features and Applications

Design table is more useful than adding a new configuration property. Because, in design table everything on part can be changed in one section such as any dimension can be changed or any feature can be changed or suppressed/unsuppressed or both. To open design table: click the *Insert* > *Table* > *Design Table* section as in Figure 8.

Figure 8. Desing Table

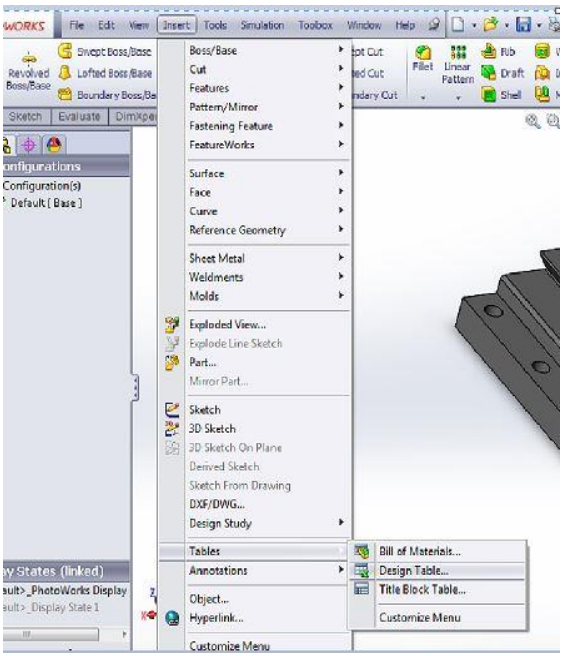

Then, the screen occurs (same as Microsoft Excel screen) as shown in Figure 9.

Figure 9. Desing Table Screen

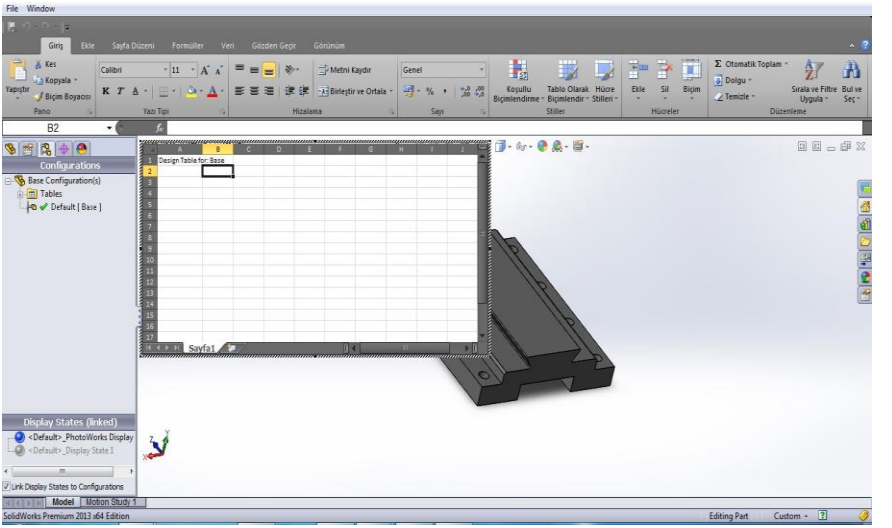

After this, any dimension that you want to change can be selected with one click by clicking the part or from design tree. Left side of column of excel table is name of your configuration. The name of selected dimension appeared in table, and you can modify dimension with number or equations, completely same as Microsoft Excel, shown in Figure 10.

Figure 10. Part Dimension in Desing Table

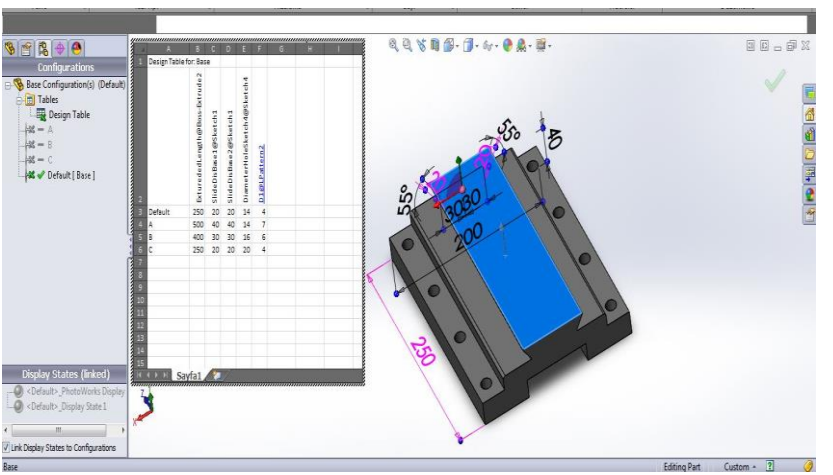

Selected dimensions have different colour. After this, A, B, and C configurations under the Configuration Manager section can be seen clearly.

If any dimension is changed or any feature is added to the part, it should be noted that the design table is aware of this condition. If the design table is opened, it is stated to us that there is any feature on the part. If this is desired to be added, that feature can be selected by us.

Also, in the Design table, any feature of the part can be suppressed. To do this in the Design table, the feature is selected, and if suppression is desired, *«s»* is typed, which means suppressed. If unsuppression is needed in another configuration, then the dimensional number or *«u»*, which means unsuppressed, can be written. In *Slideway Table,* there are any contour to fix the workpiece with other equipment. The suppressing function of design table is shown in Figure 11.

Figure 11. Suppressing Function in Design Table

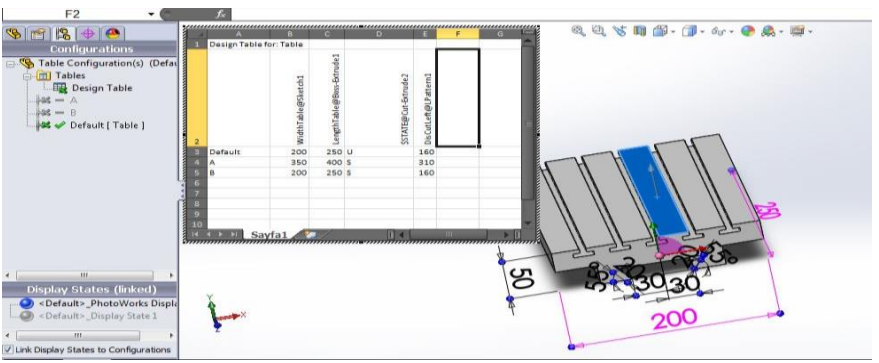

If A configuration was selected, width and length of table increased, and cavities is suppressed as in Figure 12.

Figure 12. A Configuration in Desing Table

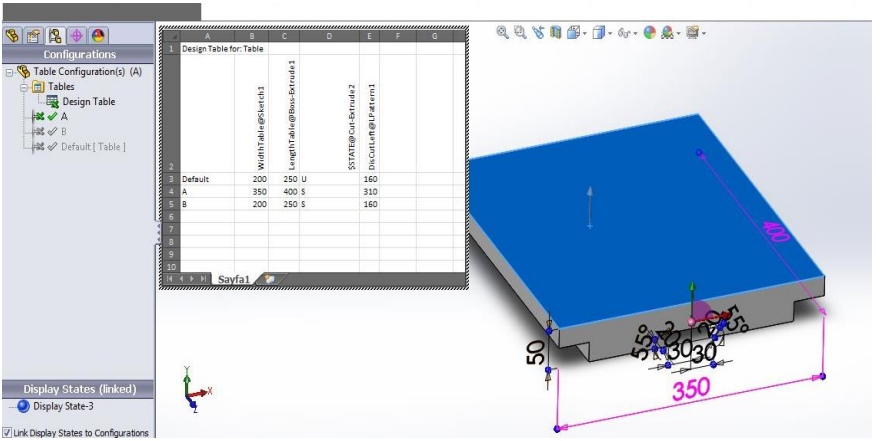

If B is selected, every dimension and feature of table is same as default, but cavities is suppressed as shown in Figure 13.

Figure 13. B Configuration in Desing Table

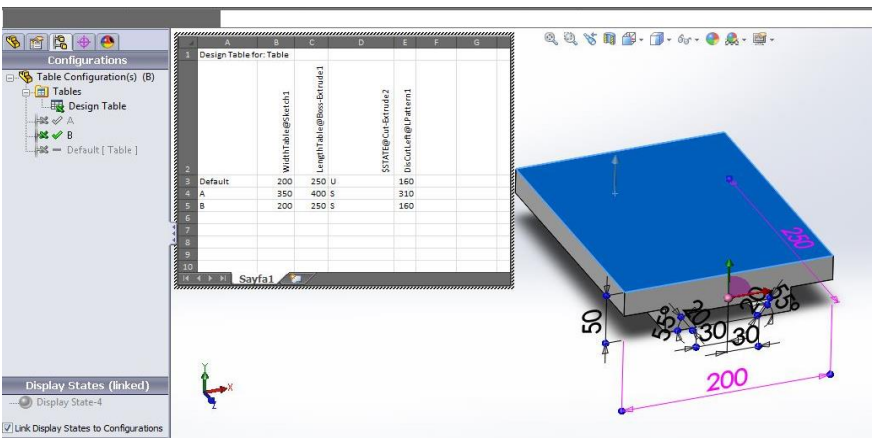

Design table can be used in assembly section in Solidworks. Desing Table using in assembly mode can be achieved by two methods. Firstly, design table is created for each part and separately selected for each part on assembly model. Secondly, any configurations are created for each part and design table is created in assembly model and these configurations are added to this table.

Firstly, design table configurations are created for each part. The three configurations A, B and C on base part and table part was created. Any configuration for any part can be selected separately in the assembled part. In default configurations, the assembled part is shown in Figure 14.

Figure 14. Assembly of Slideway Table

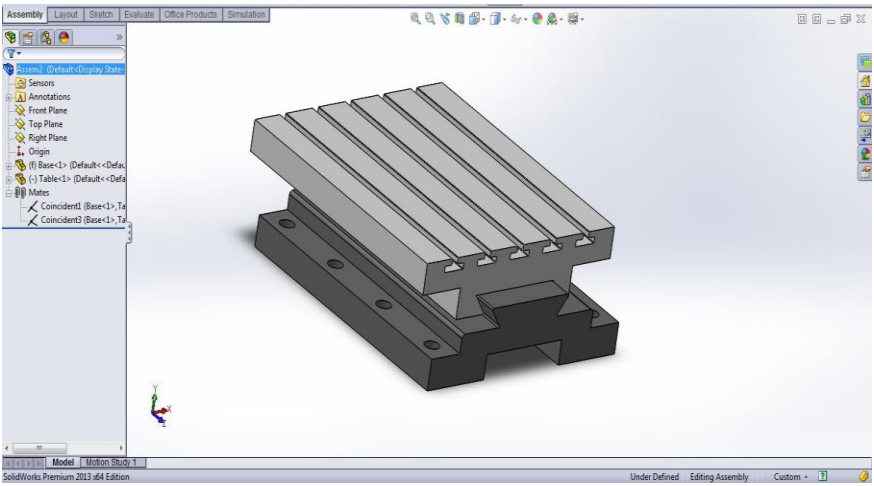

The A configuration for Base and the B configuration for Table should be selected. To accomplish this, any part must be clicked, the *component properties* need to be selected as shown in Figure 15, and then the configuration that is desired should be selected.

A configuration selected for Base in Figure 16. For Table, B configuration is selected (there are any mistakes occurs in assembly tree because we select the A configuration for base. This affects the mate relations after we select the B for table (it has to be recovered by changing mate relations) as shown in Figure 17.

Figure 15. Component Properties in Assembly

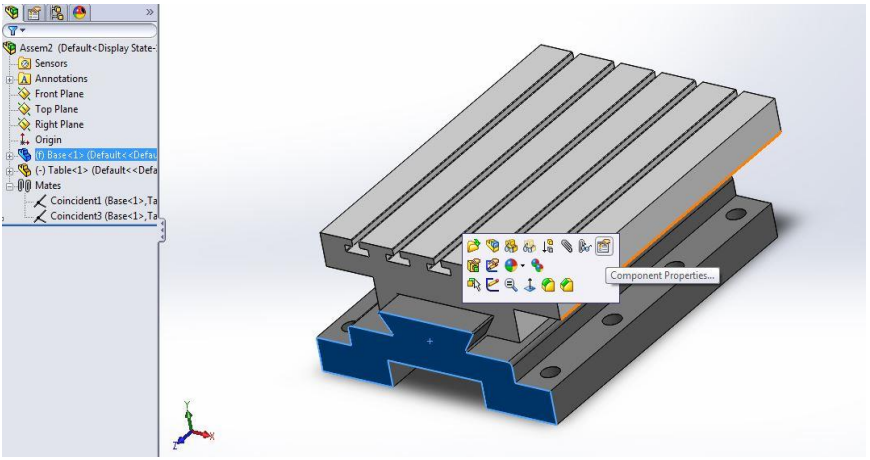

Figure 16. A Configuration for Base in Assembly

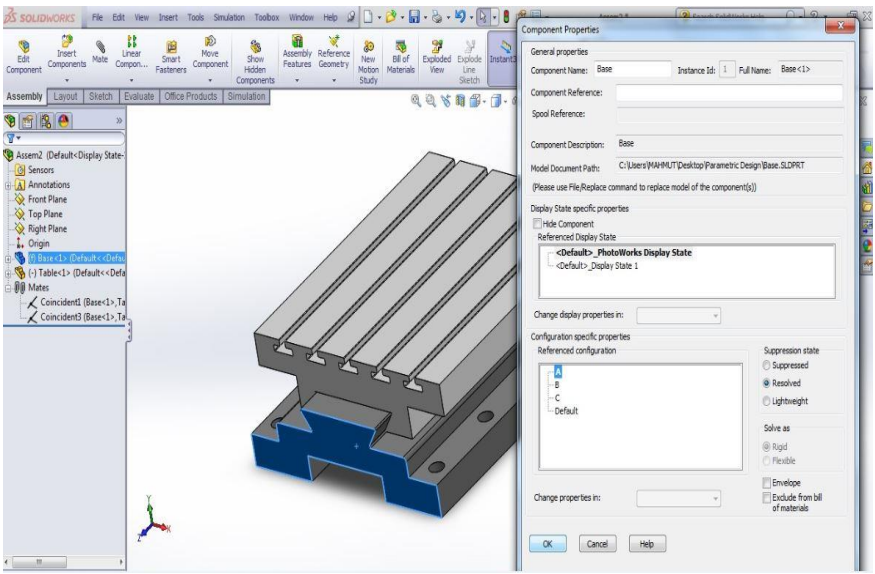

Figure 17. B Configuration for Table in Assembly

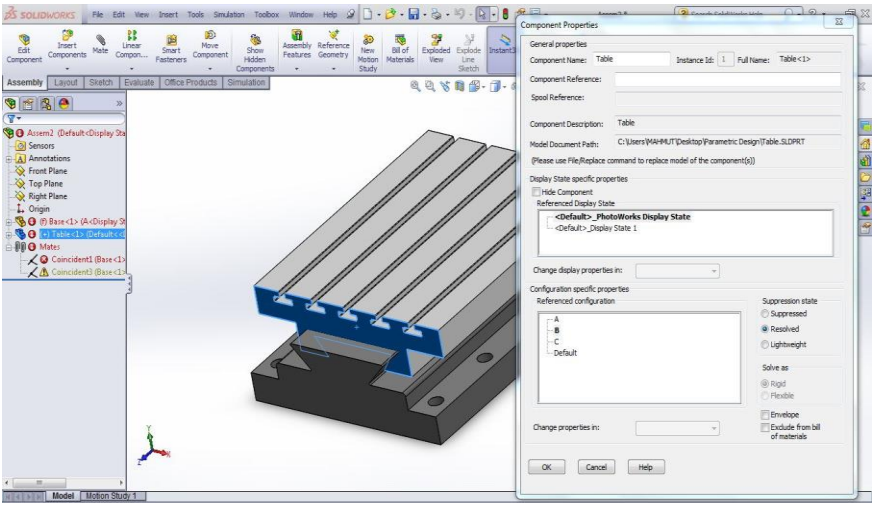

In second way, any configuration is created for each part and design table is created in assembly model. A, B and C configurations is created for Base and Table. In assembly part design table can be created via *insert* > *tables* > *Design table*, as shown in Figure 18.

Figure 18. Desing Table in Assembly

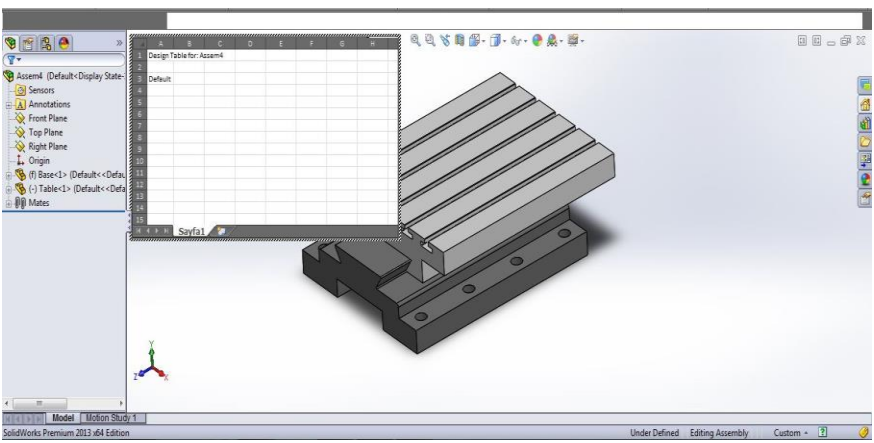

Then, the configuration names must be defined for each part. For this, we must write the « *$configuration@partname<number>*» form must be written to define the configurations. Such as,

$configuration@Base<1>* and *$configuration@Table<1>. After this configuration names for each part and Assembly configurations names for each configuration is shown in Figure 19. After this arrangement, Configuration Manager section design table section appeared.

Figure 19. Desing Table Names in Assembly

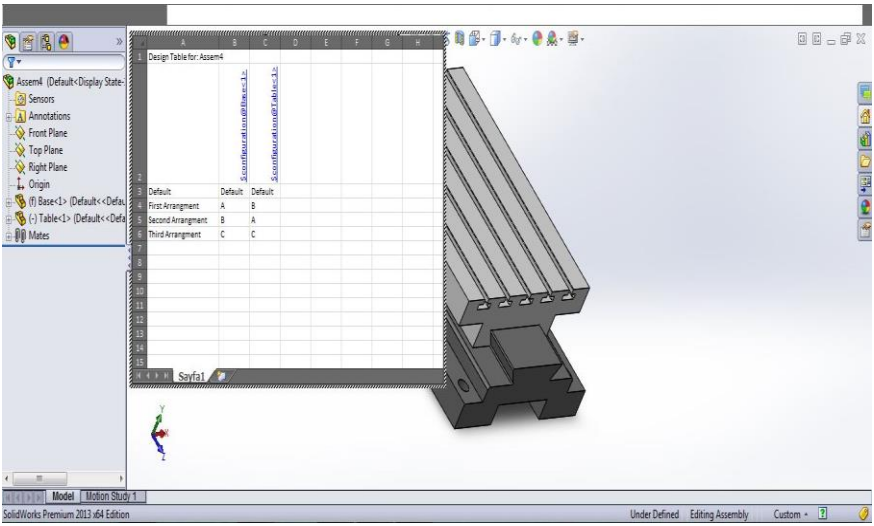

Parametric Design with Equation Editor

Equation Editor is the one of the tools of solidworks. This tool is used to letter or equation assignment to dimensions. For instance, in designing of a part there can be more equal dimensions or there are several relative dimensions. To simplify this, designing *Equation Editor* is a useful tool in solidworks. To activate this tool on solidworks *Tools* > *Equations* is clicked as shown in Figure 20.

In this tool, *Global Variables, Features* or *Equations* can be defined. Let's define the *w* for width *L* for length. Let w equals to L×4/5. To do this, «L» and «w» and its values or equations must be written on Global Variables section, in Figure 21.

Figure 20. Equations in Tool Section on Solidworks

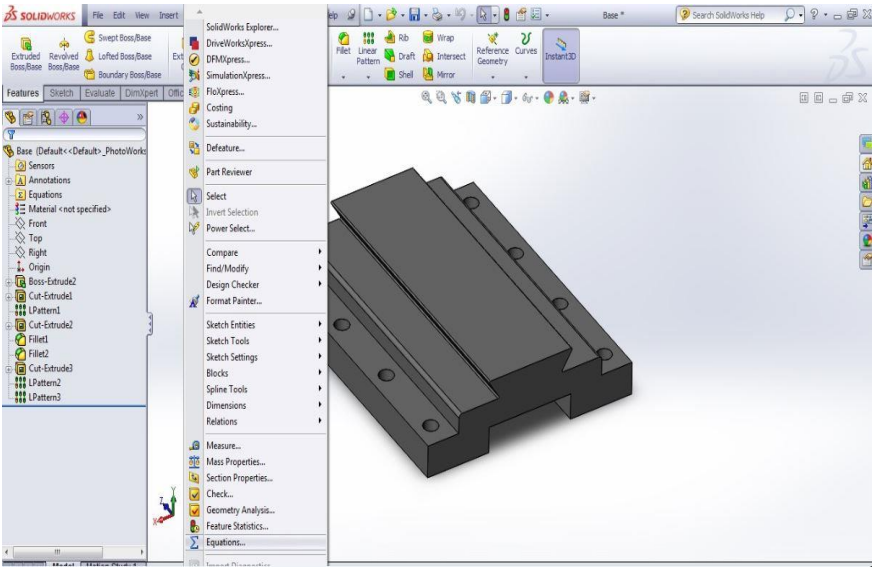

Figure 21. Equations in Solidworks

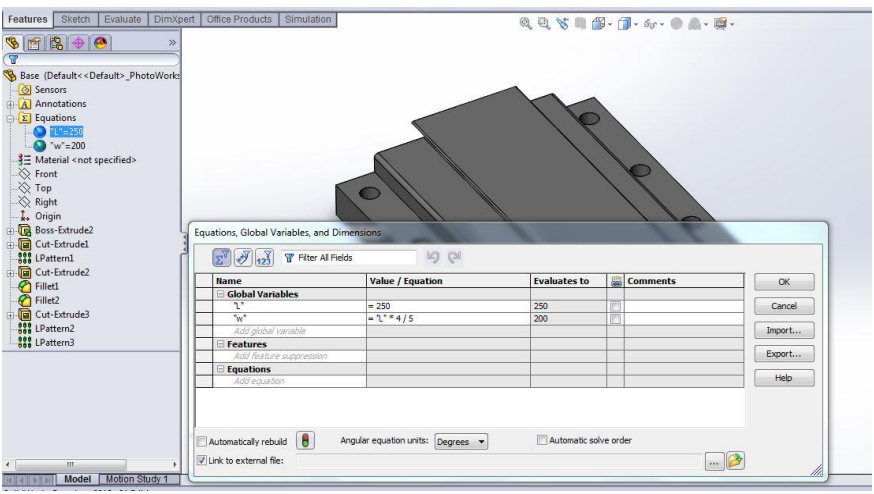

From here, the L and w dimensions must be defined also. In dimensioning instead of writing «250» for any dimension, «L» can be written and every L dimensions will be 250 mm as shown in Figure 22.

Figure 22. L named Dimensions

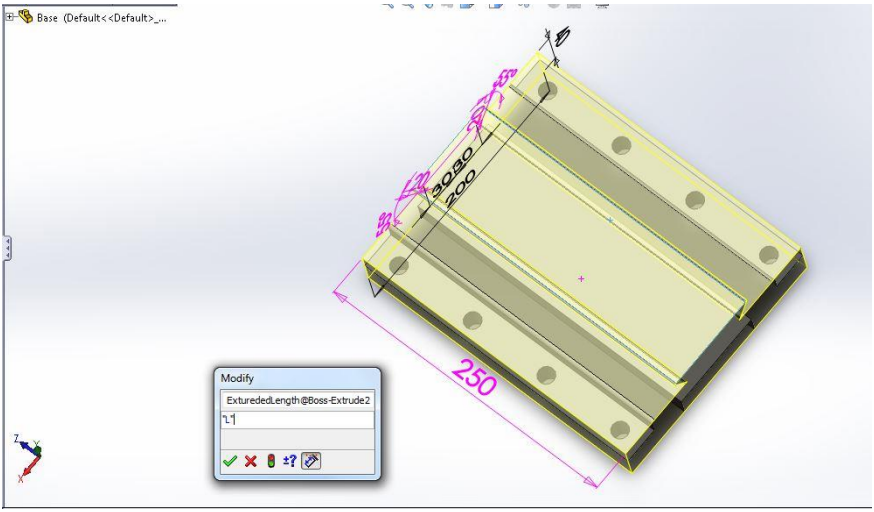

Then instead of writing «200» for any dimension «w» can be written and every w dimensions will be L×4/5 mm as shown in Figure 23. Because the w = L×4/5 was defined in equation editor section.

Figure 23. w Named Dimension

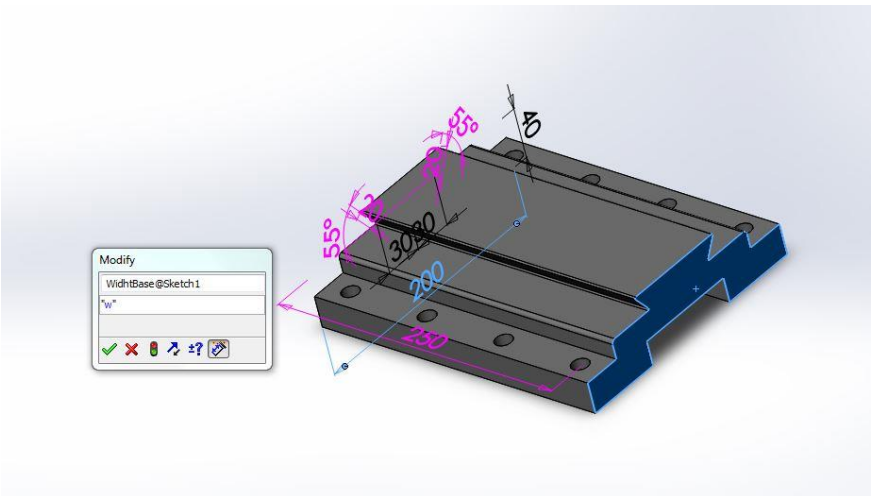

Kaynakça

Halkacı, H. S., & Yiğit, O. (2004). Parametrik Tasarım ve Solidworks CAD Programı ile Bir Uygulama. *Mühendis ve Makina*, pp. 17-24.

Monodero, J. (2000, July). Parametric Design: a Review and Some. *Automation in Construction*, pp. 369-377.

Myung, S., & Han, S. (2001, August). Knowledge-based parametric design of mechanical products based on configuration design method. *Expert Systems with Applications*, pp. 99-107.

CHAPTER 12

WAKE MODELING IN WIND FARMS: THEORY, IMPLEMENTATION, AND POWER PREDICTION

M. ÖZGÜN KORUKÇU[1]

Introduction

Wind energy has emerged as one of the most important renewable energy sources in the global transition toward sustainable and low-carbon power systems. Modern wind turbines are typically deployed in large clusters known as wind farms, where multiple turbines operate collectively to maximize energy extraction from the atmospheric boundary layer. In such farms, the aerodynamic interaction between turbines plays a crucial role in determining overall performance, as upstream turbines generate velocity deficits and increased turbulence intensity in their wakes. These wake effects lead to significant power losses and enhanced structural loading on downstream turbines, directly affecting energy yield, fatigue life, and operational reliability. Therefore, accurate wake modeling and wake interaction analysis are essential for wind farm layout design, performance prediction, and optimization, forming a cornerstone of both wind energy research and industrial wind farm engineering.

[1] Prof. Dr., University of Bursa Uludağ, Department of Mechanical Engineering, Orcid: 0000-0002-4761-4304

In this chapter, the review, theory and implementation of wake calculation with a graphical user interface (GUI) are presented. The developed GUI can generate 20 arbitrary wind turbines and calculate wake interactions among them. For the implementation, the famous Horns Rev I offshore wind farm is used. Wake interactions and the power production of the wind farm at prevailing wind directions are calculated.

Jensen (Jensen, 1983) presented the very first analytical study explicitly addressing wake interactions between wind turbines, marking the foundational work in wind turbine wake calculations. In this pioneering report, a simple linear wake expansion model based on momentum conservation was introduced and validated against full-scale experimental measurements. The study extended the single-turbine wake formulation to multiple interacting turbines, providing the first quantitative estimates of power losses in circular and aligned wind turbine arrays. This work established the conceptual and mathematical basis for all subsequent engineering wake models used in wind farm analysis and optimization.

Katić et al. (Katic et al., 1986) introduced a simple yet influential analytical model for estimating wind farm cluster efficiency based on wake interactions between turbines. Building upon Jensen's earlier single-wake formulation, the study assumed a linearly expanding top-hat wake profile and proposed a quadratic superposition of velocity deficits to model multiple wake interactions. The model explicitly incorporated turbine characteristics and wind-direction statistics, making it suitable for practical wind farm planning. Validation against full-scale measurements from the Nibe wind farm demonstrated that the simplified approach provides results comparable to more complex models while retaining high computational efficiency.

Crespo et al. (Crespo et al., 1999) presented a seminal survey of wind turbine wake and wind farm modeling approaches. The

study reviewed kinematic, field, and distributed roughness models, emphasizing their assumptions and applicability. Wake superposition methods and turbulence effects were critically discussed in the context of multiple-wake interactions. The paper identified key limitations in existing models and outlined directions for future research in wind farm wake modeling.

Göçmen et al. (Göçmen et al., 2016) presented a comprehensive review of wind turbine wake models developed at the Technical University of Denmark (DTU), covering both engineering and high-fidelity approaches. The study compared classical kinematic models, such as Jensen and Larsen, with advanced methods including Dynamic Wake Meandering, RANS, and LES. Model subcomponents, such as wake expansion, wake superposition, and rotor wind speed calculation, were systematically analyzed. Validation against data from the Sexbierum and Lillgrund wind farms demonstrated the strengths and limitations of each approach for operational wind farm analysis.

Shakoor et al. (Shakoor et al., 2016) reviewed wake effect modeling techniques with a particular focus on wind farm layout optimization using Jensen's wake model. The authors showed that the Jensen far-wake model remains attractive due to its simplicity and relatively good accuracy in optimization studies. Different wake models and fitness functions used in layout optimization were compared and discussed. The study highlighted the need for improved optimization techniques when applying simplified wake models to large wind farms.

Rathmann et al. (Rathmann et al., 2007) proposed a wake modeling framework aimed at intermediate and large wind farms that bridges the gap between classical engineering models and large-scale atmospheric approaches. The model is derived from volume and momentum conservation principles and does not require a regular turbine layout. Wake expansion and wake interaction rules

were formulated to estimate mean velocity deficits at downstream turbines. The approach was designed to retain computational efficiency while improving physical consistency for large wind farms.

Bastankhah and Porté-Agel (Bastankhah & Porté-agel, 2014) introduced a new analytical wake model based on conservation of mass and momentum and a Gaussian distribution of velocity deficit. Unlike top-hat wake models, the proposed formulation provides a more realistic representation of the wake velocity field. The model was validated against wind-tunnel measurements and large-eddy simulation data for both model-scale and utility-scale turbines. Results showed improved accuracy in predicting wake velocity deficits and downstream power production.

Baker et al. (Baker et al., 2019) investigated best practices for selecting wake models and optimization algorithms in wind farm layout optimization. Through comparative case studies, the authors demonstrated how both the choice of wake model and optimization strategy influence annual energy production predictions. Gradient-based optimization methods combined with analytical wake models showed superior performance in many scenarios. The study provided practical guidance for balancing model fidelity and computational efficiency in wind farm design.

Gao et al. (Gao et al., 2020) compared the accuracy of several wake models in wind farm layout optimization using a multi-population genetic algorithm. The results indicated that the Jensen model tends to overestimate wind farm power due to underestimated velocity deficits, while Frandsen-type models may underpredict power. A hybrid Jensen–Gaussian wake model demonstrated improved performance under complex wind conditions. The study emphasized the importance of wake model selection in realistic micrositing applications.

Ishihara and Qian (Ishihara & Qian, 2018) proposed a Gaussian-based wake model that explicitly accounts for ambient turbulence intensity and thrust coefficient effects. The model parameters were derived from large-eddy simulation results and validated against wind tunnel experiments. Both velocity deficit and added turbulence intensity were accurately predicted in near- and far-wake regions. The study demonstrated that incorporating turbulence intensity significantly improves wake model robustness.

Niayifar and Porté-Agel (Niayifar & Porté-agel, 2016) developed an analytical wind farm model extending the Gaussian wake formulation to multiple interacting wakes. The model includes turbulence-dependent wake growth and velocity-deficit superposition to predict wind farm power production. Validation against LES data and measurements from the Horns Rev wind farm showed substantial improvement over classical top-hat wake models. The study confirmed the suitability of Gaussian-based analytical models for wind farm-scale power prediction.

Karasu Aşnaz and Yüksel (Karasu Aşnaz & Yüksel, 2018) analyzed power losses due to wake interactions in a real wind farm located in Turkey. Using operational data from an 87 MW wind farm, wake-induced power losses were quantified for individual turbines and the entire farm. The results highlighted the significant impact of turbine placement on energy production and mechanical loading. The study emphasized the importance of wake modeling in wind farm micrositing and performance assessment.

Method

The wake radius grows linearly downstream (Jensen, 1983) .

$$R_w = r(1 + \alpha\frac{x}{r}) \quad (1)$$

r is the rotor radius, α is the wake expansion coefficient, and x is the downstream distance from the turbine.

End points of the wake can be calculated with the given wind direction θ:

$$\begin{aligned} x_{end} &= x_t + Lcos\theta \\ y_{end} &= y_t + Lsin\theta \end{aligned} \tag{2}$$

Wake half-width at maximum distance.

$$\begin{aligned} \Delta x &= \alpha Lcos(\theta + \frac{\pi}{2}) \\ \Delta y &= \alpha Lsin(\theta + \frac{\pi}{2}) \end{aligned} \tag{3}$$

Axial induction factor is obtained from

$$a = 1 - \sqrt{1 - C_T} \tag{4}$$

C_T is the thrust coefficient of the wind turbine.

Downstream distance between turbines. For turbine i, affected by turbine j.

$$x_{ij} = (x_i - x_j)cos\theta + (y_i - y_j)sin\theta \tag{5}$$

The condition for wake influence should be:

$$0 < x_{ij} < L_{wake} \tag{6}$$

The lateral distance from the wake centerline:

$$d_{ij} = \left|(x_i - x_j)sin\theta + (y_i - y_j)cos\theta\right| \tag{7}$$

The wake overlap condition is:

$$d_{ij} \leq R_w(x_{ij}) \tag{8}$$

The velocity deficit caused by turbine *j* on turbine *i* (Jensen, 1983):

$$\delta_{ij} = \frac{2a}{(1+\alpha\frac{x_{ij}}{r})^2} \tag{9}$$

The multiple wake superposition is quadratically found with total velocity deficit at turbine *i* by :

$$\delta_i = \sqrt{\sum_j \delta_{ij}^2} \tag{10}$$

The effective velocity for each turbine is (Katic et al., 1986):

$$U_i = U_0(1-\delta_i) \tag{11}$$

U_0 is the free stream wind velocity.

Turbine swept area:

$$A = \pi r^2 \tag{12}$$

The power output of the turbine *i* (Manwell J.F., McGowan J.G., 2010):

$$P_i = \frac{1}{2}\rho A C_p U_i^3 \tag{13}$$

Where *r* is the air density, and C_p is the power coefficient of the turbine.

The total wind farm power can be calculated with:

$$P_{total} = \sum_{i}^{n} P_i \tag{14}$$

Implemantation

The developed software is designed as a graphical user interface (GUI) and can be implemented for an arbitrary wind farm of 20 turbines and Horns Rev I offshore wind farm. The turbine layout of the Horns Rev wind farm is presented in Figure 1.

In Horns Rev I wind farm, 80 Vestas V80 turbines are used. The most frequent wind directions are SSW, SWW, W, and WWN, which correspond to 210 °, 240°, 270°, and 300°, respectively (Gonzalez-Rodriguez et al., 2022).

Figure 2 shows the main screen of the GUI filled with Horns Rev turbine coordinates (Abdulrahman & Wood, 2019). The user can plot wakes and individual turbine power production by pressing the "Plot Turbines and Wake" and the "View Turbine Data".

In calculations, free wind speed is taken as 10 m/s, density of air 1.225 kg/m³, C_P as 0.495, and C_T as 0.793 (Gonzalez-Rodriguez et al., 2022). Wake expansion coefficient α is taken as 10, and wake length, L, is taken as 2000 m.

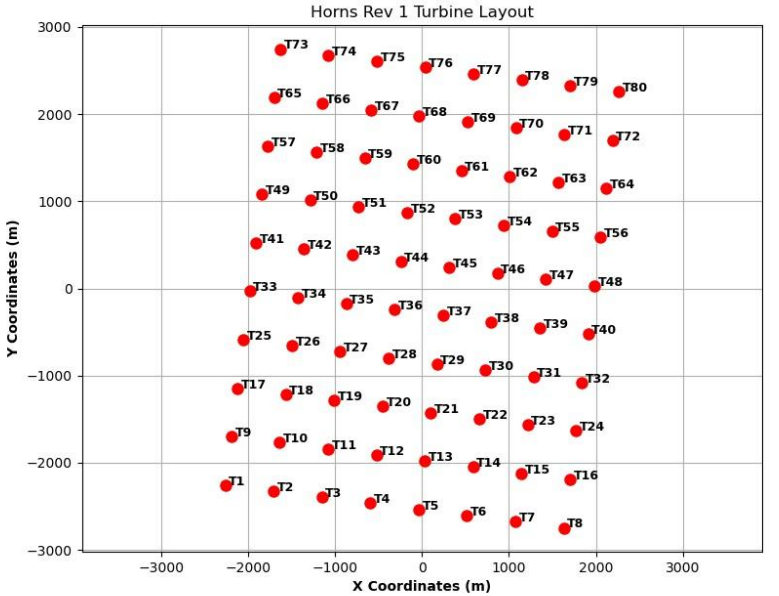

Figure 1 Turbine positions of Horns Rev I offshore wind farm.

Figure 3 shows the turbines and wakes for 210° wind direction. As seen from Figure 3, the turbines affected by the wakes can be clearly seen.

Figure 4 shows the individual and total power output values of the wind turbines. The turbines affected by wakes receive less wind speed and produce less power. In the figure, it can also be seen that turbines are affected by which turbines. As seen from Figure 4, the total power output of the wind farm for 210° wind direction is found as 91.916 MW.

Figures 5-7 show the turbines and wakes for 240°, 270°, and 300° wind directions, respectively. According to the calculations, 79.431 MW, 60.752 MW, and 92.538 MW of power can be produced for 240°, 270°, and 300° wind directions, respectively.

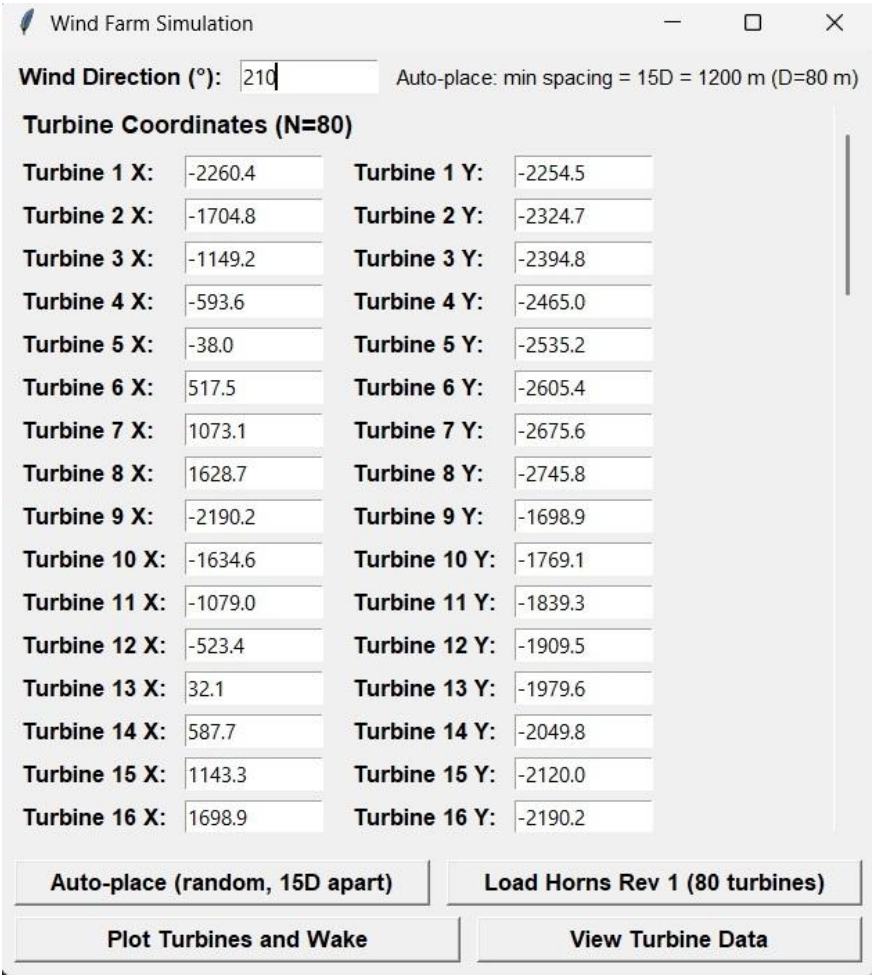

Figure 2 Main screen of the GUI.

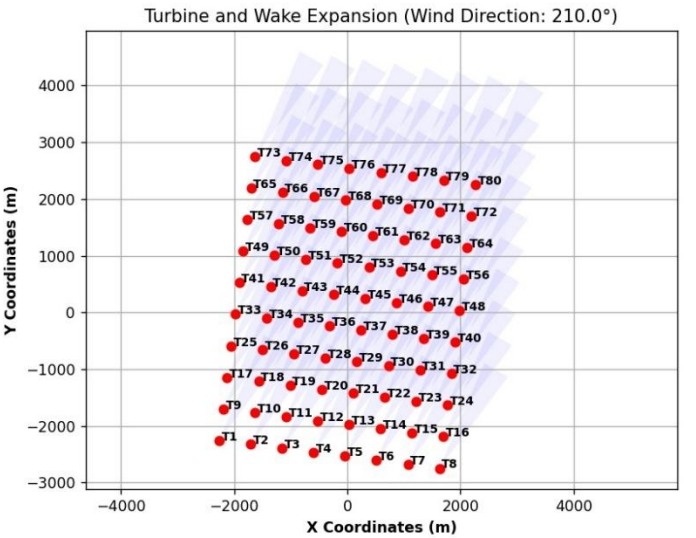

Figure 3 Turbines and wakes for 210 ° wind direction.

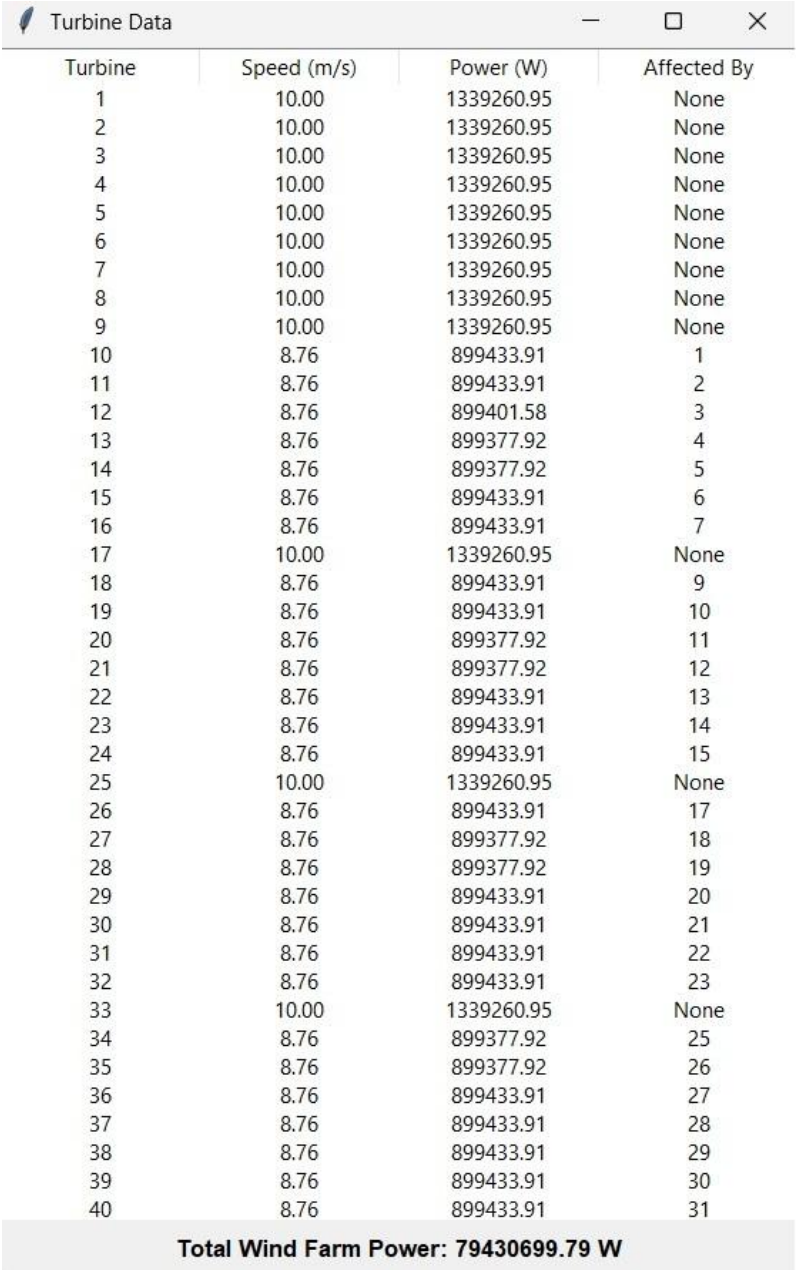

Figure 4 Power output for wind farm.

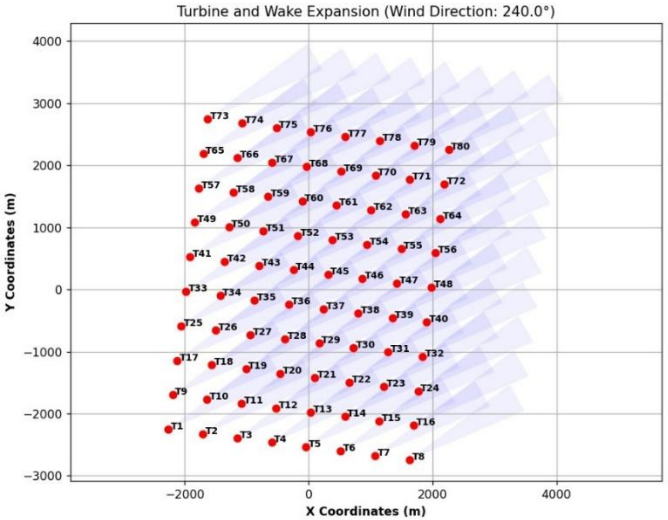

Figure 5 Turbines and wakes for 240 ° wind direction.

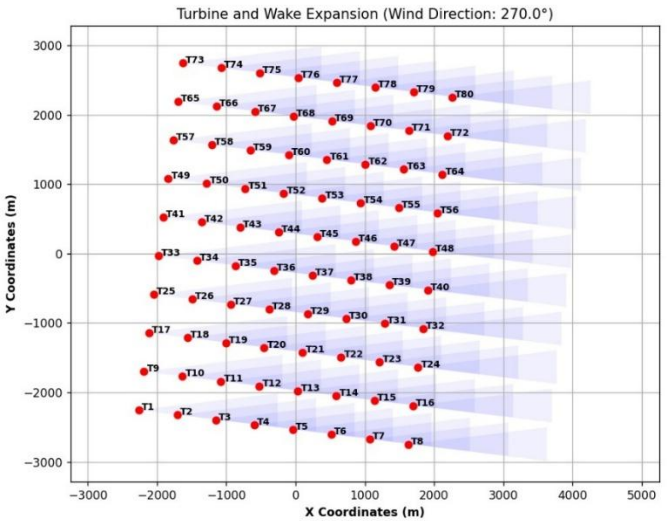

Figure 6 Turbines and wakes for 270 ° wind direction.

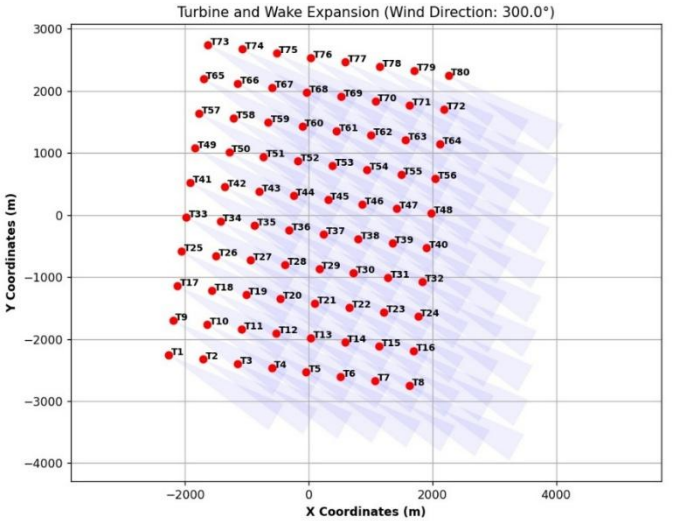

Figure 7 Turbines and wakes for 300 ° wind direction.

Conclusion

This chapter examines wake calculations in wind farms with a particular focus on their impact on power production and wind farm performance assessment. Following a concise review of the existing literature on wind turbine wake modeling, the fundamental theoretical background governing wake formation, expansion, and interaction is presented. Based on this theoretical framework, the power production of the Horns Rev I offshore wind farm is predicted for the most frequently observed wind directions at the site, allowing the influence of wake effects under realistic operating conditions to be systematically evaluated.

To support both analysis and practical implementation, a user-friendly graphical user interface (GUI) has been developed for wake calculations and wind farm power prediction. The GUI enables rapid visualization of turbine layouts, wake interactions, and resulting power losses, while allowing the user to define arbitrary wind directions and turbine positions. In addition to reproducing the

Horns Rev I layout, the interface allows the study of wind farms consisting of up to 20 turbines placed at arbitrary locations, providing flexibility for parametric and layout-based investigations.

The developed GUI serves as a versatile tool for wind farm performance prediction, power production optimization, and educational applications. By combining theoretical wake models with an intuitive graphical environment, the tool facilitates a clearer understanding of wake-induced losses and turbine interactions, making it suitable for both research-oriented studies and classroom demonstrations in wind energy and renewable energy engineering.

References

Abdulrahman, M., & Wood, D. (2019). Wind Farm Layout Upgrade Optimization. *Energies*, *12*(13), 2465.

Baker, N. F., Stanley, A. P. J., Thomas, J. J., Ning, A., & Dykes, K. (2019). Best Practices for Wake Model and Optimization Algorithm Selection in Wind Farm Layout Optimization. *NREL/CP-5000-72935*, *May*.

Bastankhah, M., & Porté-agel, F. (2014). A new analytical model for wind-turbine wakes. *Renewable Energy*, *70*, 116–123. https://doi.org/10.1016/j.renene.2014.01.002

Crespo, A., Hernandez, J., & Frandsen, S. (1999). Survey of Modelling Methods for Wind Turbine Wakes and Wind Farms. *Wind Energy*, *24*(2), 1–24.

Gao, X., Li, Y., Zhao, F., & Sun, H. (2020). Comparisons of the accuracy of different wake models in wind farm layout optimization. *Energy Exploration and Exploitation*, *38*(5), 1725–1741. https://doi.org/10.1177/0144598720942852

Göçmen, T., Laan, P. Van Der, Réthoré, P., Diaz, A. P., Larsen, G. C., & Ott, S. (2016). Wind turbine wake models developed at the technical university of Denmark : A review. *Renewable and Sustainable Energy Reviews*, *60*, 752–769. https://doi.org/10.1016/j.rser.2016.01.113

Gonzalez-Rodriguez, A. G., Serrano-gonzalez, J., Burgos-payan, M., & Riquelme-santos, J. (2022). Complete Dataset to be used as a workb ench to evaluate the profitability of an offshore wind farm. *Data in Brief*, *43*, 108396. https://doi.org/10.1016/j.dib.2022.108396

Ishihara, T., & Qian, G. (2018). Journal of Wind Engineering & Industrial Aerodynamics A new Gaussian-based analytical wake model for wind turbines considering ambient turbulence intensities and thrust coef fi cient effects. *Journal of Wind Engineering & Industrial Aerodynamics*, *177*(August 2017), 275–292. https://doi.org/10.1016/j.jweia.2018.04.010

Jensen, N. O. (1983). A Note on Wind Generator Interaction. *Risoe National Laboratory*, *Risoe-M-24*.

Karasu Aşnaz, M. S., & Yüksel, B. (2018). Bir rüzgar enerji santralindeki rüzgar türbinlerinin yerleşim lerinden kaynaklanan güç kayıplarının hesaplanması. *Journal of Balıkesir University Institute of Science and Technology*, *20*(2), 482–494. https://doi.org/10.25092/baunfbed.485820

Katic, I., Højstrup, J., & Jensen, N. O. (1986). A Simple Model for Cluster Efficiency. *EWEC'86 Proceedings*, *1*, 407–410.

Manwell J.F., McGowan J.G., R. A. L. (2010). *Wind Energy Explained*. Wiley.

Niayifar, A., & Porté-agel, F. (2016). *Analytical Modeling of Wind Farms : A New Approach for Power Prediction*. 1–13. https://doi.org/10.3390/en9090741

Rathmann, O., Frandsen, S., & Barthelmie, R. (2007). *BL3 . 199 Wake Modelling for intermediate and large wind farms*. 1–8.

Shakoor, R., Yusri, M., Raheem, A., & Wu, Y. (2016). Wake effect modeling : A review of wind farm layout optimization using Jensen ' s model. *Renewable and Sustainable Energy Reviews*, *58*, 1048–1059. https://doi.org/10.1016/j.rser.2015.12.229

GEÇİCİ KAPAK

Kapak tasarımı devam ediyor.